

# THÈSE

Pour obtenir le grade de  
**Docteur**

Délivré par l'École Nationale Supérieure de Chimie de Montpellier et l'Universitat Rovira i Virgili

Préparée au sein de l'école doctorale 459 Sciences Chimiques Balard et Escuela de Posgrado y Doctorado

Et des unités de recherche Équipe MACS, Institut Charles Gerhardt Montpellier et Catàlisi Heterogènia, URV Tarragona

Spécialité : Chimie et Physicochimie des Matériaux

Champ Disciplinaire : Chimie théorique, physique, analytique (CNU : 31)

Présentée par **Ana María ANTOLÍN POZUETA**

**Élimination du nitrate dans l'eau potable par catalyse hétérogène et photocatalyse au moyen de nanocatalyseurs AgPt et PdSn supportés sur oxyde de titane**

Supervisée par

Didier TICHIT, Dr., Équipe MACS-Institut Charles Gerhardt Montpellier  
Francesc MEDINA, Prof. Dr., Universitat Rovira i Virgili Tarragona  
Sandra CONTRERAS, Dr., Universitat Rovira i Virgili Tarragona

Soutenue le 16 décembre 2016 devant le jury composé de

Jordi LLORCA, Prof. Dr., Instituto de Técnicas Energéticas	Président
Francisco LÓPEZ, Prof. Dr., Universitat Rovira i Virgili	Examinateur
Vasile HULEA, Prof. Dr., Équipe MACS-Institut Charles Gerhardt	Examinateur

Rapporteurs externes

Verónica Patricia PINOS, Dr., Universidad de Cuenca  
Bárbara Cristina MIRANDA, Dr., Universidad de Costa Rica



## Résumé

En Europe, l'utilisation en agriculture de grandes quantités d'engrais chimiques est la principale cause de contamination des eaux. Les concentrations en nitrate dans l'eau deviennent nuisibles pour les personnes lorsqu'elles dépassent certaines limites car elles sont la cause de méthémoglobinémie, de cancers et agissent comme perturbateurs endocriniens. L'hydrogénéation catalytique hétérogène des nitrates est la méthode de dénitrification la plus connue et la plus efficace due à la grande sélectivité pour les produits non toxiques, azote et eau. La photocatalyse hétérogène a émergé comme une voie très prometteuse de dénitrification du fait de la possibilité d'utiliser la lumière solaire ce qui la rend commercialement compétitive et compatible avec la protection de l'environnement. Les procédés catalytiques conduisent fréquemment à l'obtention des sous-produits toxiques nitrite et ion ammonium, ainsi qu'à des oxydes d'azote gazeux NOx. Dans ce travail ont été utilisés des catalyseurs monométalliques supportés (Ag/P25, Pt/P25), leur mélange physique, et des catalyseurs bimétalliques supportés (Ag-Pt/P25 et Pd-Sn/P25). Le support oxyde de titane ( $TiO_2$ ) P25 est choisi pour développer un catalyseur performant pour la dénitrification à la fois catalytique et photocatalytique permettant d'atteindre les normes requises par l'UE dans l'eau potable ( $50 \text{ mg/L } NO_3^-$ ,  $0.5 \text{ mg/L } NO_2^-$ ,  $0.3 \text{ mg/L } NH_4^+$ ). L'influence des teneurs en métaux (Ag: 0.5 - 4 pds. %; Pt: 2 et 4 pds .%), du précurseur Pt ( $H_2PtCl_6$  (H)/ $K_2PtCl_6$  (K)), de l'ordre d'imprégnation de Ag et Pt et de la morphologie des particules bimétalliques Pd-Sn (nanoparticules et nanobâtonnets) ont été étudiés. Les conditions expérimentales (présence/absence de  $H_2$ ;  $\lambda = 254$  ou  $365 \text{ nm}$ ;  $4W$ ;  $7 \text{ mWcm}^{-2}$ ) ont été également variées et les réactions effectuées dans un réacteur batch en PTFE sous atmosphère inerte et dans des conditions standard (catalyseur :  $0.7 \text{ mg/L}$ ;  $100 \text{ mg/L } NO_3^-$ ;  $500 \text{ r.p.m}$ ). Contrairement à la plupart des études précédentes aucun «piégeur de trous» (expl. acides formique ou oxalique) n'a été utilisé dans nos conditions de réaction, Les analyses ont été effectuées par chromatographie ionique ou photométrie. Les propriétés physico-chimiques des catalyseurs ont été déterminées par DRX, Physisorption de  $N_2$ , MET, DRRUV-Vis, XPS, TPR et chimisorption de  $H_2$ .

Le support  $TiO_2$  P25 est inactif dans les deux procédés non photocatalytique et photocatalytique. Le mélange physique Ag/P25+Pt/P25 conduit à une conversion (~ 56 %) et sélectivité en  $N_2$  (~ 76 %) plus élevées dans les conditions non photocatalytiques que chacun des homologues monométalliques, cependant  $NO_2^-$  and  $NH_4^+$  sont obtenus. Les catalyseurs bimétalliques Ag-Pt(Pt-Ag)/P25 se montrent polyvalents étant actifs dans les procédés non-photocatalytiques et photocatalytiques. Les meilleurs résultats photocatalytiques ont été obtenus sous irradiation

ultraviolette de 365 nm et en présence de H<sub>2</sub> dû à la synergie entre les électrons générés par irradiation et l'hydrogène dissocié sur Pt. Le Pt imprégné en premier conduit à une conversion plus élevée en raison de l'amélioration de l'accessibilité de NO<sub>3</sub><sup>-</sup> aux sites actifs Ag<sup>0</sup> recouvrant partiellement Pt. Toutefois la sélectivité en NO<sub>2</sub><sup>-</sup> est élevée du fait de la faible accessibilité de Pt. Pt imprégné en second décore les ensembles Ag et diminue de ce fait le nombre de sites actifs et la conversion. Le catalyseur bimétallique Pt(4)-Ag(2)/P25(K) conduit au meilleur compromis entre conversion (ca. 45 %) et sélectivité en N<sub>2</sub> (ca. 80 %) dans les conditions photocatalytiques. Ceci est attribué au transfert électronique élevé entre Ag et Pt en forte interaction mis en évidence par XPS. Néanmoins, NO<sub>2</sub><sup>-</sup> et NH<sub>4</sub><sup>+</sup> sont aussi obtenus. Des travaux sont encore nécessaires pour améliorer le rendement en N<sub>2</sub>.

**Mots-clés :** Dénitrification, Eau potable, Catalyse,/Photocatalyse, Oxyde de Titane, Ag-Pt, Pd-Sn.

**Title:** Heterogeneous catalytic and photocatalytic nitrate abatement in drinking water using AgPt and PdSn supported on titania nanocatalysts.

## Abstract

In Europe, the agricultural use of nitrates in chemical fertilizers has been a main source of water contamination. High level of soluble nitrate in water becomes harmful pollutant for people when it exceeds the limit causing methemoglobinemia (blue baby syndrome), cancer or act as endocrine disruptor. Conventional catalytic nitrate reduction processes into N<sub>2</sub> and H<sub>2</sub>O lead to some toxic products (NO<sub>2</sub><sup>-</sup>, NH<sub>4</sub><sup>+</sup>, and NOx gases). Alternatively, photocatalytic nitrate removal using solar irradiation and heterogeneous catalysts is a very promising and ecofriendly route, which has been scarcely performed. In this work monometallic supported catalysts (Ag/P25, Pt/P25), their physical mixture, and bimetallic supported catalysts (Ag-Pt(Pt-Ag)/P25 and Pd-Sn/P25) have been used. The support TiO<sub>2</sub> P25 was chosen to develop both efficient non-photocatalytic and photocatalytic processes able to reach the EU legislation in drinking water (50 mg/L NO<sub>3</sub><sup>-</sup>, 0.5 mg/L NO<sub>2</sub><sup>-</sup>, 0.3 mg/L NH<sub>4</sub><sup>+</sup>). Different compositions of catalyst including, various metal loadings (Ag: 0.5 - 4 wt. %; Pt: 2 and 4 wt. %), Pt precursor (H<sub>2</sub>PtCl<sub>6</sub> (H)/K<sub>2</sub>PtCl<sub>6</sub> (K)), Ag and Pt impregnation order, and morphology of Pd-Sn nanoparticles (spherical and nanorods) have been studied. Different experimental conditions (presence/absence of H<sub>2</sub>; λ = 254 or 365 nm; 4W; 7 mWcm<sup>-2</sup>) have been also evaluated and the experiments performed in a PTFE batch reactor under inert standard operational conditions (0.7 mg/L catalyst; 100 mg/L NO<sub>3</sub><sup>-</sup>; 500 r.p.m). Contrary to most previous studies, any hole scavenger (e.g. formic or oxalic acid) was used in the reaction. Analyses were performed by ionic chromatography or

photometry. Physico-chemical characterizations of the catalysts were done by XRD, N<sub>2</sub>-physisorption, TEM, DRUV-Vis, XPS, TPR and H<sub>2</sub>-Chemisorption in order to explain both the catalytic and photocatalytic performances.

The support TiO<sub>2</sub> P25 was inactive in both processes. The physical mixture Ag(2)/P25+Pt(4)/P25(H) showed better conversion (ca. 56 %) and N<sub>2</sub> selectivity (ca. 76 %) under non-photocatalytic conditions than each monometallic catalyst, however NO<sub>2</sub><sup>-</sup> and NH<sub>4</sub><sup>+</sup> were obtained. Bimetallic Ag-Pt(Pt-Ag)/P25 catalysts exhibit a versatile behavior being active both in the non-photocatalytic and photocatalytic processes. The best photocatalytic conditions were interestingly obtained under the ultraviolet irradiation of 365 nm and in presence of hydrogen. Photocatalytic activity was enhanced in presence of H<sub>2</sub> due to synergetic effect induced by light between photogenerated electrons and dissociation of hydrogen on Pt. Therefore, all bimetallic catalysts based on Ag and Pt were tested under these conditions. Pt impregnated first leads to higher conversion due to improved accessibility of NO<sub>3</sub><sup>-</sup> to active Ag<sup>0</sup> sites partially covering Pt than the opposite impregnation order where the Pt decorates Ag and reduces the number of active sites. However, high NO<sub>2</sub><sup>-</sup> selectivity at the expense of N<sub>2</sub> is obtained in the former case due to low Pt accessibility. The bimetallic catalyst Pt(4)-Ag(2)/P25(K) led to the most interesting conversion (ca. 45%) with the highest selectivity to N<sub>2</sub> (ca. 80%) under photocatalytic conditions. This was assigned to the highest electronic transfer between Ag et Pt particles in close contact revealed by XPS. Nevertheless, NO<sub>2</sub><sup>-</sup> and NH<sub>4</sub><sup>+</sup> are obtained too. Further studies must be done to enhance the catalytic and photocatalytic activity towards desired N<sub>2</sub>.

**Keywords:** Denitration, Drinking water, Catalysis/Photocatalysis, Titania, Ag-Pt, Pd-Sn.

This joint supervision PhD thesis (PMF-PIPF Martí i Franquès-UES Research Grant Programme) was carried out at the Équipe Matériaux Avancés pour la Catalyse et la Santé group (MACS) in the Institut Charles Gerhardt Montpellier (ICGM) of the École Nationale Supérieure de Chimie de Montpellier (ENSCM, Montpellier, France), and at the Catàlisi Heterògenia group (CaTheter) in the Chemical Engineering Department (DEQ) of the Universitat Rovira i Virgili (URV, Tarragona, Spain).

Équipe Matériaux Avancés pour la Catalyse et la Santé (MACS)

Institut Charles Gerhardt

École Nationale Supérieure de Chimie de Montpellier

8, Rue de l'École Normale

34296 Montpellier Cedex 5, France



Département  
de Chimie Physique  
MACS

Catàlisi Heterògenia (CaTheter)

Departament d'Enginyeria Química

Escola Tècnica Superior d'Enginyeria Química

Avinguda Països Catalans, 26

Campus Sescelades

43007 Tarragona, Spain



UNIVERSITAT ROVIRA I VIRGILI



## **ACKNOWLEDGEMENTS**

First of all, I would like to acknowledge to Prof. Dr. Francesc Medina from URV (Tarragona) for giving me the opportunity of working in his research group as a Ph.D. candidate. I would like to thank to Dr. Sandra Contreras for joining us later in this interesting study. Thank you very much to both for all your guidance and patience during these three years. I have also to mention Vanessa Torné, she hired me firstly for doing internships in the group and afterwards proposed me the possibility to become Dr., which I had never imagined.

Secondly, I have to acknowledge to Dr. Didier Tichit from MACS-ICGM (Montpellier) for giving me the chance of working in his group as well. I infinitely thank you for all your guidance throughout this time, contributions, endless encouragement and support (professional and personal).

It has been a real pleasure to work with all of you.

I acknowledge for the financial support to the Spanish Ministry of Economy and Competitiveness (Project CTQ2012-35789-C02-02), URV, ENSCM, AMIC, and Eurorregión Pirineos Mediterráneo.

I have to deeply thank to all my coworkers in both Spanish-French groups, especially the ones that directly helped me and/or highly encouraged, such as Verónica, Susana, Bárbara, Antón, Marwa, Tijani, Ibtihel, Yurani, Dana, Olinda, Erwin, Dan, Thomas, Noelia, Lotfi, Asma and Chiqui. I would like to give my special thanks to Núria Juanpere, Álex Fragoso and Isabelle Girard for the administration issues, and also to Ernest Arce for building up the reactor. Thank you so much for your empathy and efficiency.

To my parents, two elder sisters and closer friends... the way has been hard but you are and you will be always there pushing, believing and giving me strength (no matter the distance).

Gerard, sincerely I could have not make it without you. I have no words enough to express how much gratitude I have for you. Step by step, day by day by my side, let's dream!

¡Muchas gracias! Merci beaucoup!



## PREFACE

The thesis is divided in 6 chapters and 4 annexes.

*Chapter 1* details the general introduction of the topic and objectives of the PhD thesis. The materials and methods used are commented in the *Chapter 2*. In the *Chapters 3* and *4* are shown the synthesis, the characterization techniques results, and the catalytic/photocatalytic nitrate removal in drinking water results related to the Ag and Pt-based catalysts. *Chapter 5* describes the synthesis route and catalytic water denitrification with the Pd-Sn catalysts. This last work is part of the scientific article published in collaboration with the Catalonia Institute for Energy Research (IREC, Barcelona), the Institut de Ciència de Materials de Barcelona (ICMAB, Barcelona), the Institut Català de Nanociència i Nanotecnologia (ICN2, UAB, Barcelona), and the Institució Catalana de Recerca i Estudis Avançats (ICREA, Barcelona). Finally, the *Chapter 6* reports the general conclusions of the research and future recommendations.

In the 4 annexes are detailed the scientific contributions concerned with this thesis (*Annex A*); the publication already submitted (*Annex B*); the Photometer methods used for nitrate, nitrite and ammonium ions detection (*Annex C*); and the planes of the experimental reactor (*Annex D*).

## **CONTENTS**

Summary .....	1
Résumé .....	13
<b>CHAPTER 1: Introduction and Scope.....</b>	<b>27</b>
1.1 Nitrate pollution problem in water .....	29
1.1.1 Normative .....	30
1.2 Nitrate abatement technologies.....	33
1.3 Catalytic and Photocatalytic nitrate reduction .....	35
1.3.1 Catalytic nitrate reduction.....	35
1.3.1.1 Catalysts .....	35
1.3.2 Photocatalytic nitrate reduction .....	38
1.3.2.1 Heterogeneous photocatalysis .....	38
1.3.2.2 Titanium dioxide .....	40
1.3.2.3 Photocatalysts .....	41
1.3.2.4 Optical properties .....	43
1.3.2.5 Reducing agent and hole scavenger .....	43
1.4 Mechanisms .....	46
1.5 Catalyst design.....	50
1.5.1 Metal loading .....	51
1.5.2 Platinum precursor .....	52
1.5.3 Impregnation protocol.....	53
1.5.4 Morphology.....	54
1.6 Objectives and scope of the research.....	54
1.7 References.....	57

<b>CHAPTER 2: Materials and Methods .....</b>	<b>70</b>
2.1 Characterization techniques.....	72
2.1.1 X-Ray Diffraction Powder.....	72
2.1.1.1 Average crystallite size determination .....	74
2.1.2 Nitrogen Physisorption .....	75
2.1.3 Transmission Electron Microscopy .....	77
2.1.4 Diffuse Reflectance UV-Vis Spectroscopy.....	79
2.1.5 X-Ray Photoelectron Spectroscopy .....	80
2.1.6 Temperature-Programmed Reduction by hydrogen.....	82
2.1.7 Hydrogen chemisorption.....	84
2.2 Analytical methods .....	85
2.2.1 Ion Chromatography .....	85
2.2.1.1 Nitrate and nitrite detection.....	88
2.2.1.2 Ammonium detection.....	90
2.2.2 Photometry .....	91
2.3 Experimental set-up and operational conditions.....	93
2.4 Catalytic and photocatalytic behavior calculations .....	96
2.4.1 Nitrate and Nitrite conversions .....	96
2.4.2 Selectivity towards products .....	96
2.4.3 Yield towards products .....	97
2.4.4 Nitrate reduction rates.....	98
2.5 References.....	99

<b>CHAPTER 3: Synthesis and Physicochemical properties of the Ag and Pt/P25 mono- and bimetallic catalysts .....</b>	<b>102</b>
--	------------

3.1 Monometallic catalysts .....	104
3.1.1 Synthesis method .....	104

3.1.2 Characterization .....	107
3.1.2.1 X-Ray Diffraction (XRD) .....	107
3.1.2.2 Nitrogen Physisorption.....	110
3.1.2.3 Transmission Electron Microscopy (TEM).....	113
3.1.2.4 Diffuse Reflectance UV-Vis Spectroscopy (DRUV-Vis) .....	116
3.1.2.5 Temperature-Programmed Reduction by hydrogen (H <sub>2</sub> -TPR) .....	119
3.2 Bimetallic catalysts.....	121
3.2.1 Synthesis method .....	121
3.2.2 Characterization .....	123
3.2.2.1 X-Ray Diffraction (XRD) .....	123
3.2.2.2 Nitrogen Physisorption.....	125
3.2.2.3 Transmission Electron Microscopy (TEM).....	127
3.2.2.4 Diffuse Reflectance UV-Vis spectroscopy (DRUV-Vis).....	130
3.2.2.5 X-Ray Photoelectron Spectroscopy (XPS).....	132
3.2.2.6 Temperature-Programmed Reduction by hydrogen (H <sub>2</sub> -TPR) .....	138
3.3 References.....	142

**CHAPTER 4: Catalytic and Photocatalytic nitrate abatement using Ag and Pt/P25 catalysts .....** **146**

4.1 Experimental conditions and calculations .....	148
4.1.1 Catalytic conditions .....	148
4.1.2 Photocatalytic conditions .....	148
4.2 Aeroxide Titania P25 .....	149
4.3 Monometallic catalysts .....	151
4.3.1 Silver based monometallic catalysts .....	151
4.3.1.1 Effect of silver loading.....	151
4.3.1.2 Effect of pH.....	157

4.3.2 Platinum based monometallic catalysts .....	158
4.3.2.1 Effect of platinum loading and Pt precursor .....	159
4.3.2.2 Photocatalytic nitrite reduction .....	162
4.3.3 Conclusions.....	162
4.4 Bimetallic catalysts.....	163
4.4.1 Effect of Ag-Pt/Pt-Ag impregnation order and catalyst formulation.....	164
4.4.2 Effect of Pt loading and Pt precursor .....	169
4.4.3 Conclusions.....	174
4.5 References.....	176

## **CHAPTER 5: Pd<sub>2</sub>Sn-based catalysts and their water denitration properties..... 179**

5.1 Introduction .....	181
5.2 Experimental section .....	182
5.2.1 Chemicals.....	182
5.2.2 Synthesis of Pd <sub>2</sub> Sn Nanorods.....	182
5.2.2.1 Preparation of Hexadecylammonium Chloride (HDA·HCl).....	183
5.2.3 Synthesis of Pd <sub>2</sub> Sn Spherical NPs for Catalytic Performance Evaluation.....	183
5.2.4 Water Denitration.....	183
5.3 Results and discussion .....	184
5.3.1 Pd-Sn spherical NPs and NRs.....	184
5.3.2 Catalytic nitrate reduction.....	187
5.4 Conclusions .....	192
5.5 Supplementary Information (SI).....	192
5.5.1 Synthesis of Pd Spherical NPs for Catalytic Performance Evaluation.....	192
5.5.2 Characterization techniques .....	192
5.5.2.1 Transmission electron microscopy (TEM) studies.....	192
5.5.2.2 X-ray power diffraction (XRD).....	192

5.5.3 TEM micrograph spherical Pd NPs .....	193
5.5.4 Geometric and crystal structure characterization.....	193
5.5.5 Summary of synthesis conditions of samples presented in Figure 5.2 .....	197
5.5.6 Control experiments.....	197
5.5.7 Estimation of nanorods and nanospheres concentration in NPs/mL .....	201
5.5.8 <i>p</i> -Nitrophenol Reduction.....	201
5.5.8.1 Ligand Exchange with Mercaptopropionic Acid (MPA).....	204
5.6 References.....	205
<b>CHAPTER 6: General conclusions and Future recommendations .....</b>	<b>210</b>
6.1 General conclusions.....	211
6.2 Future recommendations .....	214
<b>ANNEXES.....</b>	<b>216</b>
Annex A: Scientific contributions.....	217
Annex B: Article submitted.....	221
Annex C: Photometer methods .....	245
Annex D: Reactor design .....	252

## **LIST OF FIGURES**

Figure 1.1. The Nitrogen cycle .....	30
Figure 1.2. Groundwater average nitrate concentrations (2004 - 2007) .....	31
Figure 1.3. Nitrate Vulnerable Zones (NVZs) (2000 - 2009) .....	32
Figure 1.4. Surpassing of critical loads for eutrophication due to the deposition of nutrient nitrogen (2010) .....	32
Figure 1.5. Solar spectrum .....	39
Figure 1.6. Photocatalytic process on TiO <sub>2</sub> particle.....	41
Figure 1.7. Diagram of Localized Surface Plasmon Resonance in metal sphere.....	43
Figure 1.8. Possible photocatalytic nitrate and nitrite reduction to ammonia over Ru/TiO <sub>2</sub> and photooxidation of water (production of H <sup>+</sup> radicals) (Ranjit et al. 1995) .....	45
Figure 1.9. General mechanism of nitrate and nitrite reduction by catalyzed hydrogenation .	46
Figure 1.10. Catalytic nitrate and nitrite reduction using Pd-Me (Me: Cu, Sn, In)/Al <sub>2</sub> O <sub>3</sub> catalysts .....	47
Figure 1.11. Schemes of : A) Mechanism for Ag-Pt and Pd-Sn pairs in catalytic nitrate reduction through hydrogenation, B) Additional step for the nitrite reduction.....	49
Figure 1.12. Nitrate removal mechanism on Pd-Sn/NZSM-5 catalyst .....	49
Figure 1.13. Scheme of photocatalytic nitrate reduction using Ag-Pt/TiO <sub>2</sub> nanocatalyst .....	49
Figure 1.14. Diagram of simple catalyst and photocatalyst process .....	50
Figure 2.1. Bragg's law of diffractions .....	73
Figure 2.2. XRD equipment .....	74
Figure 2.3. N <sub>2</sub> -Physisorption adsorption-desorption system scheme .....	75
Figure 2.4. Types of : A) Physisorption isotherms, and B) Hysteresis loops .....	76
Figure 2.5. N <sub>2</sub> -physisorption equipment .....	77
Figure 2.6. TEM scheme .....	78
Figure 2.7. TEM apparatus.....	78
Figure 2.8. Measurement of diffuse reflection using an integration sphere .....	79
Figure 2.9. DRUV-Vis Spectrometer.....	80
Figure 2.10. XPS system scheme .....	81
Figure 2.11. XPS equipment .....	81
Figure 2.12. C1s scan recorded by XPS .....	82
Figure 2.13. Schematic diagram for the TPR analysis .....	83

Figure 2.14. TPR AutoChem II 2920 .....	83
Figure 2.15. H <sub>2</sub> -Chemisorption equipment .....	85
Figure 2.16. Ion Chromatography diagram .....	86
Figure 2.17. General scheme of a suppressor .....	87
Figure 2.18. Ion Chromatography instrument.....	88
Figure 2.19. Nitrate and nitrite chromatograms .....	89
Figure 2.20. Nitrate calibration curve .....	89
Figure 2.21. Nitrite calibration curve .....	90
Figure 2.22. Ammonium chromatogram.....	91
Figure 2.23. Ammonium calibration curve .....	91
Figure 2.24. MultiDirect Lovibond Photometer.....	92
Figure 2.25. Tube tests analyzed by Photometry .....	93
Figure 2.26. Experimental set-up .....	94
Figure 2.27. Spectral curves of the UV-A and UV-C irradiations used.....	95
Figure 3.1. Visual aspect of Aeroxide TiO <sub>2</sub> P25 and of the monometallic catalyst powders	107
Figure 3.2. XRD patterns of P25 and P25 calcined at 400 °C.....	109
Figure 3.3. XRD patterns of: A) Ag(0.5)/P25, B) Ag(1)/P25, C) Ag(1.5)/P25, D) Ag(2)/P25, E) Ag(3)/P25, and F) Ag(4)/P25 .....	109
Figure 3.4. XRD patterns of: A) Pt(2)/P25(H), B) Pt(2)/P25(K), C) Pt(4)/P25(H), and D) Pt(4)/P25(K).....	110
Figure 3.5. Nitrogen adsorption-desorption isotherms of P25, P25 calcined at 400°C and of selected monometallic catalysts .....	111
Figure 3.6. SEM images of: A) P25 and B) P25 400 °C .....	112
Figure 3.7. TEM image of TiO <sub>2</sub> P25: A) before and B) after calcination at 400 °C .....	113
Figure 3.8. TEM image and histogram of Ag(2)/P25 .....	114
Figure 3.9. TEM images and histograms: A) Pt(2)/P25(H) and B) Pt(4)/P25(H) .....	115
Figure 3.10. TEM images and histograms: A) Pt(2)/P25(K) and B) Pt(4)/P25(K) .....	115
Figure 3.11. DRUV-Vis spectra of P25 and P25 calcined at 400°C .....	117
Figure 3.12. DRUV-Vis spectra of P25 calcined at 400°C and: A) Ag(4)/P25, B) Ag(2)/P25, C) Ag(3)/P25, D) Ag(1.5)/P25, E) Ag(1)/P25, and F) Ag(0.5)/P25 .....	118
Figure 3.13. DRUV-Vis spectra of P25 calcined at 400°C and: A) Pt(4)/P25(H), B) Pt(4)/P25(K), C) Pt(2)/P25(H), and D) Pt(2)/P25(K) .....	119
Figure 3.14. H <sub>2</sub> -TPR profiles of: A) Ag(2)/P25, B) Pt(2)/P25(H), C) Pt(2)/P25(K), D) Pt(4)/P25(H), and E) Pt(4)/P25(K).....	120

Figure 3.15. Visual aspect of the bimetallic catalyst powders .....	123
Figure 3.16. XRD patterns of: A) Ag(2)-Pt(2)/P25(H), B) Ag(2)-Pt(2)/P25(K), C) Ag(2)-Pt(4)/P25(H), and D) Ag(2)-Pt(4)/P25(K) .....	124
Figure 3.17. XRD patterns of: A) Pt(2)-Ag(2)/P25(H), B) Pt(2)-Ag(2)/P25(K), C) Pt(4)-Ag(2)/P25(H), and D) Pt(4)-Ag(2)/P25(K) .....	125
Figure 3.18. N <sub>2</sub> adsorption-desorption isotherms of P25, P25 calcined at 400°C and selected bimetallic catalysts Ag(2)-Pt(4)/P25(H) and Pt(4)-Ag(2)/P25(H) .....	126
Figure 3.19. TEM images and histograms: A) Ag(2)-Pt(2)/P25(H) and B) Ag(2)-Pt(4)/P25(H) .....	128
Figure 3.20. TEM images and histograms: A) Ag(2)-Pt(2)/P25(K) and B) Ag(2)-Pt(4)/P25(K) .....	128
Figure 3.21. TEM images and histograms: A) Pt(2)-Ag(2)/P25(H) and B) Pt(4)-Ag(2)/P25(H) .....	129
Figure 3.22. TEM images and histograms: A) Pt(2)-Ag(2)/P25(K), and B) Pt(4)-Ag(2)/P25(K) .....	129
Figure 3.23. DRUV-Vis spectra of P25 calcined at 400°C and of: A) Ag(2)-Pt(4)/P25(H), B) Ag(2)-Pt(2)/P25(H), C) Ag(2)-Pt(2)/P25(K), and D) Ag(2)-Pt(4)/P25(K) .....	131
Figure 3.24. DRUV-Vis spectra of P25 calcined at 400°C and of: A) Pt(4)-Ag(2)/P25(H), B) Pt(2)-Ag(2)/P25(H), C) Pt(4)-Ag(2)/P25(K), and D) Pt(2)-Ag(2)/P25(K) .....	132
Figure 3.25. Survey of the spectra of the selected catalysts .....	133
Figure 3.26. O1s and Ti2p scan of Ag(2)/P25 .....	134
Figure 3.27. Ag3d and Pt4f scans of selected catalysts.....	137
Figure 3.28. H <sub>2</sub> -TPR profiles of monometallic catalysts and Ag-Pt bimetallic catalysts .....	140
Figure 3.29. H <sub>2</sub> -TPR profiles of Pt-Ag bimetallic catalysts.....	140
Figure 4.1. NO <sub>3</sub> <sup>-</sup> conversion and yields (%) toward NO <sub>2</sub> <sup>-</sup> and N <sub>2</sub> , varying the Ag loading (0.5 - 2 wt. %) under P(2)+H <sub>2</sub> condition after 6 h reaction .....	153
Figure 4.2. NO <sub>3</sub> <sup>-</sup> conversion and yields (%) toward NO <sub>2</sub> <sup>-</sup> and N <sub>2</sub> , varying the silver loading (0.5 - 4 wt. %) under P(3)+H <sub>2</sub> after 6 h reaction .....	154
Figure 4.3. NO <sub>3</sub> <sup>-</sup> conversion and selectivity to products (%) measured from Ag(x)/P25 catalysts under P(3)+H <sub>2</sub> condition after 6h reaction .....	154
Figure 4.4. NO <sub>3</sub> <sup>-</sup> , NO <sub>2</sub> <sup>-</sup> and NH <sub>4</sub> <sup>+</sup> concentrations (mg/L) in function of reaction time (h) recorded by the Ag(x)/P25 catalysts under P(2)+H <sub>2</sub> and P(3)+H <sub>2</sub> conditions .....	155
Figure 4.5. NO <sub>3</sub> <sup>-</sup> conversion and selectivity (%) to products measured from Ag(x)/P25 catalysts under P(3)+H <sub>2</sub> condition after 6h reaction .....	160

Figure 4.6. $\text{NO}_3^-$ , $\text{NO}_2^-$ and $\text{NH}_4^+$ concentrations (mg/L) in function of reaction time (h) recorded by Ag(2)-Pt(4)/P25(H), Pt(4)-Ag(2)/P25(H) and physical mixture Ag(2)/P25 + Pt(4)/P25(H) under CAT and P(3)+ $\text{H}_2$ conditions .....	168
Figure 4.7. $\text{NO}_3^-$ conversion and selectivity (%) toward products measured from Ag-Pt/P25 catalysts under P(3)+ $\text{H}_2$ condition after 6 h reaction.....	170
Figure 4.8. $\text{NO}_3^-$ conversion and selectivity (%) toward products measured from Pt-Ag/P25 catalysts under P(3)+ $\text{H}_2$ after 6 h reaction.....	171
Figure 4.9. $\text{NO}_3^-$ conversion and selectivity (%) toward products measured from Ag and Pt-based bimetallic catalysts depending on Pt loading and precursor .....	172
Figure 4.10. $\text{NO}_3^-$ , $\text{NO}_2^-$ and $\text{NH}_4^+$ concentrations (mg/L) in function of reaction time (h) obtained with bimetallic catalysts .....	173
Figure 5.1. a) TEM micrograph of 27 nm long and 9 nm wide $\text{Pd}_2\text{Sn}$ NRs, b) HRTEM micrographs, power spectra, and 3D atomic models of vertically and horizontally aligned $\text{Pd}_2\text{Sn}$ NRs.....	184
Figure 5.2. Tem micrographs of $\text{Pd}_2\text{Sn}$ spherical NPs and NRs with different aspect ratios (AR) .....	185
Figure 5.3. Schematic illustration of the influence of TOP and chloride ions on the shape and size of the $\text{Pd}_2\text{Sn}$ NRs.....	186
Figure 5.4. Mechanism of nitrate reduction by catalyzed hydrogenation to final product A) Ammonia and/or B) Nitrogen .....	187
Figure 5.5. TEM images of $\text{Pd}_2\text{Sn}/\text{P25}$ : a) spherical NPs and b) NRs, supported on $\text{TiO}_2$ P25. Scale bars correspond to 20 nm.....	188
Figure 5.6. $\text{NO}_3^-$ conversion and selectivity (%) toward products measured from $\text{Pd}_2\text{Sn}/\text{P25}$ spherical NPs and $\text{Pd}_2\text{Sn}/\text{P25}$ NRs after 24 h reaction.....	189
Figure 5.7. $\text{NO}_3^-$ , $\text{NO}_2^-$ and $\text{NH}_4^+$ concentrations (mg/L) in function of reaction time (h) obtained with 5% $\text{Pd}_2\text{Sn}/\text{P25}$ spherical NPs and NRs .....	190
Figure 5.8. $\text{NO}_3^-$ conversion and selectivity (%) toward products measured from $\text{Pd}_2\text{Sn}/\text{P25}$ spherical NPs and $\text{Pd}_2\text{Sn}/\text{P25}$ NRs after 6 h reaction.....	191
Figure 5.9. TEM micrograph of spherical Pd NPs .....	193
Figure 5.10. XRD pattern of a) $4.3 \pm 0.2$ nm diameter $\text{Pd}_2\text{Sn}$ spherical NPs, b) $83 \pm 2$ nm wide NRs, c) $276 \pm 28$ nm long and $15 \pm 2$ m wide NRs, d) $603 \pm 65$ nm long and $32 \pm 3$ nm wide NRs, and reference pattern corresponding to orthorhombic $\text{Pd}_2\text{Sn}$ phase Pnma space group .....	193

Figure 5.11. XRD pattern of $276 \pm 28$ nm long and $15 \pm 2$ nm wide NRs and reference pattern corresponding to orthorhombic Pd <sub>2</sub> Sn phase Pmna space group, cubic Pd <sub>3</sub> Sn phase Pm-3m space group, orthorhombic PdSn phase Pnma space group, tetragonal PdSn <sub>2</sub> phase space group, cubic Pd phase Fm-3m space group, and cubic Sn phase Im-3m space group .....	194
Figure 5.12. TEM micrograph of vertically aligned Pd <sub>2</sub> Sn NRs.....	194
Figure 5.13. General STEM-HAADF micrographs showing Pd <sub>2</sub> Sn NRs aligned.....	195
Figure 5.14. Additional images of the 3D structural model of a Pd <sub>2</sub> Sn NR .....	196
Figure 5.15. Additional HRTEM micrographs of orthorhombic Pd <sub>2</sub> Sn NRs .....	196
Figure 5.16. HRTEM micrograph showing several nanoparticles, detail of the red squared nanoparticle and its corresponding power spectrum .....	197
Figure 5.17. TEM micrographs of the Pd <sub>2</sub> Sn obtained from the control experiments. In each TEM image the parameter changed with respect to the standard Pd <sub>2</sub> Sn NR synthesis conditions is pointed out .....	198
Figure 5.18. TEM micrograph of $\sim 600 \pm 60$ nm x $32 \pm 3$ nm Pd <sub>2</sub> Sn NRs.....	199
Figure 5.19. TEM micrographs of the Pd <sub>2</sub> Sn NPs obtained from control experiments. Noted in each TEM image the parameter changed with respect to the standard Pd <sub>2</sub> Sn NR synthesis conditions .....	199
Figure 5.20. TEM micrograph of the Pd NPs obtained when no Sn(acac) <sub>2</sub> and HDA·HCl were added .....	200
Figure 5.21. TEM micrograph of the NPs obtained when no Pn(acac) <sub>2</sub> and HDA·HCl were added .....	200
Figure 5.22. TEM micrograph of the NPs obtained for Pd/Sn ratio equal to 2.....	200
Figure 5.23. Scheme of the p-nitrophenol reaction .....	202
Figure 5.24. Sodium-borohydride-driven degradation of p-nitrophenol over 3 nm Pd and 4.3 nm Pd <sub>2</sub> Sn spheres, 15 x 8 nm Pd <sub>2</sub> Sn NRs, 44 x 10 nm Pd <sub>2</sub> Sn NRs, and 130 x 24 nm Pd <sub>2</sub> Sn NRs .....	203
Figure 5.25. Sodium borohydride-driven degradation of p-nitrophenol over 3 nm Pd (black) and 4.3 nm Pd <sub>2</sub> Sn spheres, 15 nm x 8 nm Pd <sub>2</sub> Sn NRs, 44 nm x 10 nm Pd <sub>2</sub> Sn NRs, and 130 nm x 24 nm Pd <sub>2</sub> Sn NRs .....	203
Figure 5.26. Picture of the solution of Pd <sub>2</sub> Sn NRs before and after MPA treatment.....	204

## **LIST OF TABLES**

Table 1.1. Limit values for N-compounds concentrations in water set by EU policies .....	33
Table 1.2. Standard reduction potentials of Pt, Ag, Pd, Sn and N-compounds .....	37
Table 3.1. Notation of the monometallic catalysts prepared .....	105
Table 3.2. Composition of the aqueous impregnation solutions of the monometallic precursors .....	106
Table 3.3. Specific surface area, pore volume and mean pore diameter of P25, P25 calcined at 400°C and selected monometallic catalysts.....	112
Table 3.4. Mean nanoparticle diameter and number of particles measured in the monometallic catalysts .....	116
Table 3.5. Hydrogen consumption of monometallic catalysts .....	121
Table 3.6. Notation of the bimetallic catalysts prepared .....	122
Table 3.7. Composition of the aqueous impregnation solutions of the bimetallic catalysts..	123
Table 3.8. Specific surface area, pore volume and mean pore diameter of P25, P25 calcined at 400°C and of two selected bimetallic catalysts .....	127
Table 3.9. Mean nanoparticles size and number of particles measured in the bimetallic catalysts .....	130
Table 3.10. BE of Oxygen and Titanium species recorded by XPS .....	134
Table 3.11. BE of silver and platinum species recorded by XPS.....	138
Table 3.12. Pt/Ag atomic ratios of select bimetallics by XPS. ....	138
Table 3.13. Hydrogen consumption of bimetallic catalysts .....	141
Table 4.1. Notation of the experimental conditions .....	149
Table 4.2. Catalytic and photocatalytic activities of Titania P25.....	150
Table 4.3. Catalytic and photocatalytic activities of 0.5 - 4 wt. % Ag/P25 samples under different experimental conditions.....	152
Table 4.4. Pseudo-1 <sup>st</sup> order nitrate reaction rates and correlation coefficients of Ag based monometallic catalysts at P(2)+H <sub>2</sub> condition after 6 h reaction.....	156
Table 4.5. Pseudo-1 <sup>st</sup> order nitrate reaction rates and correlation coefficients of Ag based monometallic catalysts at P(3)+H <sub>2</sub> condition after 6 h reaction.....	156
Table 4.6. Catalytic and photocatalytic nitrate reductions varying the nitrate source, using Ag(2)/P25 catalyst.....	158

Table 4.7. Catalytic and photocatalytic activities of Pt based monometallic catalysts varying the Pt loading and precursor ( $\text{H}_2\text{PtCl}_6 \cdot 6\text{H}_2\text{O}$ / $\text{K}_2\text{PtCl}_6$ ) .....	160
Table 4.8. Pseudo-1 <sup>st</sup> order nitrate reaction rates and correlation coefficients of $\text{Pt}(x)/\text{P}25(\text{H}/\text{K})$ catalysts at $\text{P}(3)+\text{H}_2$ condition after 6 h reaction.....	161
Table 4.9. Comparison performances varying the amount of K loaded at $\text{P}(3)+\text{H}_2$ condition after 6 h reaction .....	161
Table 4.10. Results of photocatalytic nitrite reduction tests varying the Pt loading and the precursor at $\text{P}(3)+\text{H}_2$ condition after 6 h reaction .....	162
Table 4.11. Comparison studies of physical mixture of $\text{Ag}(2)/\text{P}25 + \text{Pt}(4)/\text{P}25(\text{H})$ , and bimetallic $\text{Ag}(2)\text{-}\text{Pt}(4)/\text{P}25$ and $\text{Pt}(4)\text{-}\text{Ag}(2)/\text{P}25$ catalysts, under catalytic and photocatalytic conditions, using $\text{H}_2\text{PtCl}_6 \cdot 6\text{H}_2\text{O}$ as Pt precursor .....	164
Table 4.12. Yields to products of the physical mixture of $\text{Ag}(2)/\text{P}25 + \text{Pt}(4)/\text{P}25$ , and bimetallic $\text{Ag}(2)\text{-}\text{Pt}(4)/\text{P}25$ and $\text{Pt}(4)\text{-}\text{Ag}(2)/\text{P}25$ catalysts, under catalytic and photocatalytic conditions, using $\text{H}_2\text{PtCl}_6 \cdot 6\text{H}_2\text{O}$ as Pt precursor.....	165
Table 4.13. Pseudo-1 <sup>st</sup> order nitrate reaction rates and correlation coefficients of the physical mixture of $\text{Ag}(2)/\text{P}25 + \text{Pt}(4)/\text{P}25(\text{H})$ , and bimetallic $\text{Ag}(2)\text{-}\text{Pt}(4)/\text{P}25$ and $\text{Pt}(4)\text{-}\text{Ag}(2)/\text{P}25$ samples at $\text{P}(3)+\text{H}_2$ condition after 6 h reaction using $\text{H}_2\text{PtCl}_6 \cdot 6\text{H}_2\text{O}$ as Pt precursor .....	167
Table 4.14. Comparison studies of the bimetallic catalysts under photocatalytic conditions at $\text{P}(3)+\text{H}_2$ condition after 6 h reaction .....	169
Table 4.15. Yields to products of the bimetallic catalysts under photocatalytic conditions at $\text{P}(3)+\text{H}_2$ condition after 6 h reaction .....	170
Table 4.16. Pseudo-1 <sup>st</sup> order nitrate reaction rates and correlation coefficients of bimetallic catalysts under photocatalytic conditions at $\text{P}(3)+\text{H}_2$ condition after 6 h reaction .....	174
Table 5.1. Hydrogen chemisorption results for 5 % $\text{Pd}_2\text{Sn}$ spherical NPs and 5 % $\text{Pd}_2\text{Sn}$ NRs .....	189
Table 5.2. Synthesis conditions and geometrical parameters of the $\text{Pd}_2\text{Sn}$ NPs obtained.....	197

## **LIST OF ABBREVIATIONS**

P25: Commercial Aerioxide Titania P25

NPs: Nanoparticles

NRs: Nanorods

VB: Valence band

CB: Conduction band

$e^- - h^+$ : electron-hole pair

BE: Binding energy

LSPR: Localized Surface Plasmon Resonance

UV-A: Ultraviolet irradiation range of 320 - 400 nm

UV-C: Ultraviolet irradiation range of 200 - 280 nm

XRD: X-Ray Diffraction

$N_2$ -physisorption: Nitrogen physisorption

TEM: Transmission Electron Microscopy

DRUV-Vis: Diffuse Reflectance UV-Vis spectroscopy

XPS: X-Photon Spectroscopy

$H_2$ -TPR: Temperature-Programmed Reduction by hydrogen

$H_2$ -Chemisorption: Hydrogen Chemisorption

PTFE: Polytetrafluoroethylene

JCPDS: Joint Committee on Powder Diffraction Standards

Cond: Experimental conditions

CAT: Catalytic or non-photocatalytic conditions

P(2): Photocatalytic conditions using the UV irradiation of 254 nm

P(3): Photocatalytic conditions using the UV irradiation of 365 nm

P(2)+H<sub>2</sub>: Photocatalytic conditions using the UV irradiation of 254 nm and hydrogen flow

P(2)+H<sub>2</sub>: Photocatalytic conditions using the UV irradiation of 365 nm and hydrogen flow

# **Summary**

## ***Introduction***

One of the most pervasive problems affecting people throughout the world is an inadequate access to clean freshwater and sanitation. The global drinking water demand is increasing, therefore regulations on drinking water quality become stricter. In the recent years, the trend of nitrate concentration in groundwater, an important source of potable water, is rising in the European Union (EU) and other countries. Its presence is due to farmer, agricultural and certain industries sources. In Europe, the agricultural use of nitrates in organic and chemical fertilizers has been a mainly source of water contamination. The high soluble and stable nitrate ion ( $\text{NO}_3^-$ ) in water is one of the key chemical that causes large scale health effects through drinking water exposure. High levels of nitrates in water becomes harmful inorganic water pollutant to people and nature when it exceeds the limit ( $> 50 \text{ mg/L } \text{NO}_3^-$  in EU), causing methemoglobinemia, known as “blue baby syndrome”, that affects mostly newborns and reduce the oxygen circulation in the blood. Moreover, it could cause cancer or be an endocrine disruptor. Recently, The European Commission has decided “*to take further steps in legal actions against Spain, Italy, Greece and France for failing to respect the Community Nitrates Directive, which concerns the protection of waters against pollution caused by nitrates from agricultural sources*”.

Among various nitrate abatement technologies (physicochemical, biological, electrochemical and catalytic), heterogeneous catalytic nitrate removal by hydrogenation (reducing agent) is a well-known and established efficient nitrate and nitrite removal technology, due to its high selectivity towards desired harmless products –  $\text{N}_2$ ,  $\text{H}_2\text{O}$  – with the possibility of operating at mild operational conditions. In particular, heterogeneous photocatalysis has emerged as a very promising route for denitration technique due to the possibility of using the solar irradiation, which makes it commercially attractive and environmental friendly. This last technique has been scarcely studied. Nevertheless, these reactions lead frequently to toxic side products, such as nitrite ( $\text{NO}_2^-$ ) – intermediate compound – and ammonia ( $\text{NH}_4^+$ ) – over hydrogenation – ions and  $\text{NO}_x$  gases (Figure 1), which are still a major challenge to overcome for large-scale industrial application in both catalytic and photocatalytic nitrate abatement for drinking water purpose. Thus, more research on highly efficient catalysts is still needed.

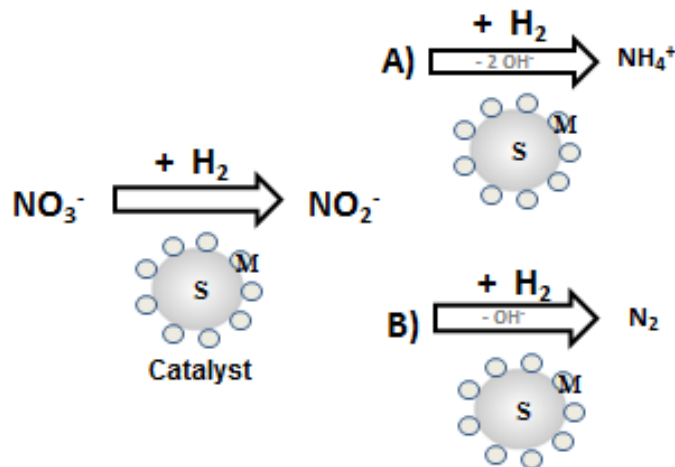


Figure 1. General mechanism of nitrate reduction by catalyzed hydrogenation, where S is the support and M the metal dispersed over the support

Several studies have shown that bimetallic nanoparticles improve the catalytic properties and selectivity in comparison to their monometallic counterparts. They could show properties related to the combination of both individual metals and also new ones due to a synergy between the two metals. Most of the bimetallic catalysts used for denitrification in water reported in literature have been prepared combining a noble metal able to chemisorb hydrogen at ambient temperature (Pt, Pd) and a second promoter metal with redox properties (Ag, Sn). Monometallic catalysts based on noble metals are inactive for nitrate reduction and the presence of promoters is necessary to initiate the reduction reaction (Figure 2).

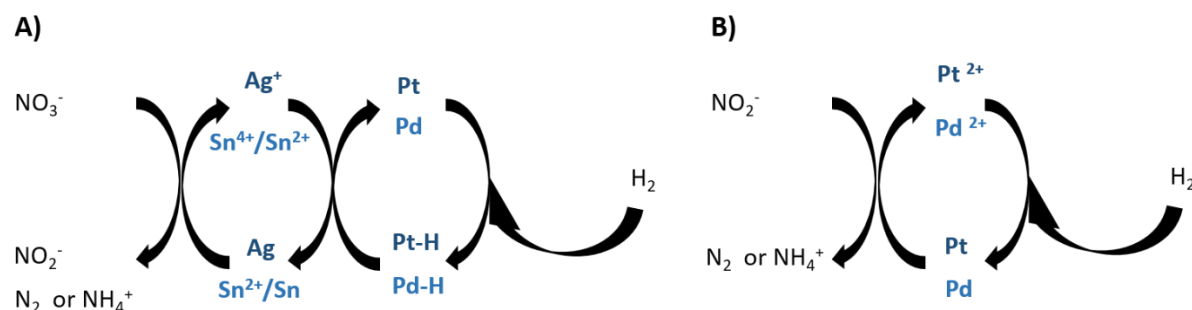


Figure 2. General schemes of : A) Mechanism for Ag-Pt and Pd-Sn pairs in catalytic nitrate reduction through hydrogenation, B) Additional step for the nitrite reduction

The nature of the support is a key parameter of the catalysts formulation able to influence activity and selectivity towards desirable product, and obviously acting on the metals deposition and the diffusion of the species. Among various semiconductor photocatalysts, Titania ( $\text{TiO}_2$ ) is extensively applied for widespread environmental applications among several other oxides, which can be improved by metal(s) doping. Aeroxide Titania P25 (anatase/rutile: ~ 80/20) is commonly used as photocatalyst. Furthermore, physical mixtures of monometallic catalysts have also attracted attention because properly combined they can lead to interesting results.

### ***The objectives of the thesis***

The main objective of our study was to develop an efficient catalyst to accomplish the EU legislation (50 mg/L  $\text{NO}_3^-$ , 0.5 mg/L  $\text{NO}_2^-$ , 0.3 mg/L  $\text{NH}_4^+$ ) in drinking water, evaluating different composition catalysts (metal loading, Pt precursor, Ag and Pt impregnation order, Pd-Sn morphology) and optimal experimental conditions. **The support  $\text{TiO}_2$  P25 was chosen with the aim of using catalysts that could be applied on both non-photocatalytic and photocatalytic processes.** Therefore, we have studied the catalytic nitrate removal through hydrogenation using the bimetallic pair Pd-Sn (5 wt. %  $\text{Pd}_2\text{Sn}/\text{P25}$  spherical Nanoparticles and Nanorods) and Ag-Pt (Ag: 2 wt. %, Pt: 2 and 4 wt. %; Pt precursor:  $\text{H}_2\text{PtCl}_6 \cdot 6\text{H}_2\text{O}$  or  $\text{K}_2\text{PtCl}_6$ ) supported over  $\text{TiO}_2$  P25. Pt and Ag are also known for their properties of acting as electron sinks, avoiding the fast electron-hole recombination in photocatalytic nitrate abatement (Ag: 2 wt. %, Pt: 2 and 4 wt. %; Pt precursor:  $\text{H}_2\text{PtCl}_6 \cdot 6\text{H}_2\text{O}$  or  $\text{K}_2\text{PtCl}_6$ ) under two Ultraviolet irradiations. Ag/P25 (0.5 - 4 wt. %) and Pt/P25(2 and 4 wt. %) monometallic catalysts and physical mixture have been also tested in both processes and compared with their bimetallic catalysts counterparts as an original route scarcely studied to get deeper understanding of the process. The comparative study between the catalytic and photocatalytic behavior of the same catalysts is an original aspect of this work. It is due to the specific composition of the samples that make them potentially active in the two processes. Thus, it was an important feature to establish the part taken by each of these processes.

### ***Synthesis of the catalysts***

The Ag and or Pt supported on P25 catalysts were synthesized by drop-wise wetness impregnation method of the respective metals precursors varying the metal loading, platinum precursor and impregnation order. The calcination temperature was carried out at 400 °C overnight. Afterwards, the desirable amount of catalyst was followed by a chemical reduction with  $\text{NaBH}_4$  in ethanol under continuously stirring, filtered under vacuum, washed several times

with EtOH, and immediately introduced into the reactor to avoid the silver oxidation with the air.

The Pd<sub>2</sub>Sn spherical nanoparticles and nanorods with tuned size were prepared by co-reduction of metal salts in the presence of trioctylphosphine, amine, and chloride ions. Asymmetric Pd<sub>2</sub>Sn nanostructures were achieved by the selective desorption of a surfactant mediated by chlorine ions. The growth mechanism was based on the selective desorption of TOP by chlorine ions. The synthesis of these bimetallic catalysts was done by the IREC Barcelona group. We have evaluated the morphology of the 5 wt. % Pd<sub>2</sub>Sn/P25 spherical NPs and NRs in the catalytic denitration tests.

### ***Characterization of the catalysts***

To discuss the catalytic and photocatalytic performances, various characterization techniques were applied to calculate the physicochemical properties of the catalysts due to their important role in their activity. The X-Ray Diffraction Powder (XRD) and the Nitrogen Physisorption (N<sub>2</sub>-Physisorption) have been used in order to determine their crystallinity structures and textural properties. Transmission Electron Microscopy (TEM) technique was used to show their size and shape. The optical properties are determined through The UV-Vis Spectroscopy using the Kubelka-Munk function (DRUV-Vis). Their atomic environment and different reducibility were determined through X-Ray Photoelectron Spectroscopy (XPS) and Hydrogen Thermal Programmed Reduction (H<sub>2</sub>-TPR). To calculate the metal dispersion (Pd) over the support was used the Hydrogen chemisorption technique (H<sub>2</sub>-Chemisorption).

### ***Catalytic reaction***

Denitration experiments were performed in a polytetrafluoroethylene (PTFE) batch reactor under inert standard operational conditions (Argon stream at 120 mL/min, atmospheric pressure, room temperature). 200 mg of desired catalyst was dispersed in 350 mL milli-Q water solution containing 100 mg/L NO<sub>3</sub><sup>-</sup> (nitrate removal) or 50 mg/L NO<sub>2</sub><sup>-</sup> (nitrite removal), under continuous stirring at 500 r.p.m. The reaction time was 6 h (Ag and/or Pt/P25 catalysts) or 24 h (5 % Pd<sub>2</sub>Sn/P25 catalysts). In the photocatalytic conditions, the ultraviolet irradiations were located on the top of the reactor ( $\lambda = 254$  nm,  $\lambda = 365$  nm; 4 W) with a light intensity of 7 mWcm<sup>-2</sup>. In both, catalytic and photocatalytic conditions, the reactor was covered with aluminum foil to avoid the external light incidence. To establish the catalytic and the photocatalytic contributions in the reduction of NO<sub>3</sub><sup>-</sup>, experiments were done without UV

irradiation in presence of H<sub>2</sub> (catalytic process); under UV irradiation in H<sub>2</sub>-free condition and lastly under UV irradiation and presence of H<sub>2</sub> (photocatalytic process). Contrary to most studies, no hole scavenger was used as hole trapping in the reaction (i.e. formic or oxalic acid), due to possible remnant radicals in the final solution are also potentially risky to human health in water. Samples were withdrawn at a set time, and analyzed by Ionic Chromatography (Ag and/or Pt/P25 catalysts) or Photometry (5 % Pd<sub>2</sub>Sn/P25 catalysts). Performances were evaluated in terms of nitrate and nitrite conversion, selectivity and yields to products, and nitrate reduction rate. Their differences were attributed to their physicochemical properties. The experimental set-up and operational conditions are shown in the following Figure 3.

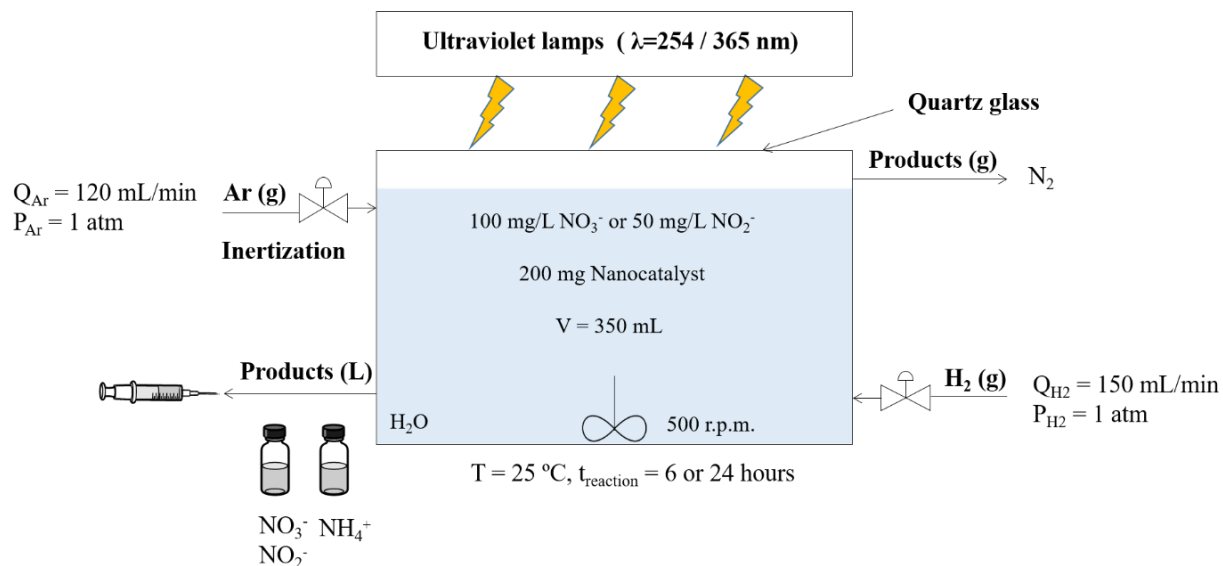


Figure 3. Experimental set-up and operational conditions

## Results

### *Physico-chemical characterization of the catalysts*

The commercial support TiO<sub>2</sub> P25 was tested under non-photocatalytic and photocatalytic conditions, and it has been inactive in both conditions for the removal of nitrate and nitrite in drinking water. It does not present neither nitrate nor nitrite adsorptions. The photolysis effect is not happening too, then all performances were only related to catalysis/photocatalysis processes. Therefore, metal(s) have to be added on the support to enhance the activity and selectivity.

The sodium nitrate as nitrate source in aqueous synthesized solution has been compared with the nitric acid instead for denitration tests under presence of H<sub>2</sub> and presence/absence UV irradiations using the metallic catalyst Ag(2)/P25. The purpose was to decrease the initial pH to observe enhancement of the selectivity towards nitrogen. The use of HNO<sub>3</sub> as nitrate source slightly increased the selectivity towards N<sub>2</sub>, but decreased dramatically the nitrate conversions and the final pH (ca. 2.5). Thus, sodium nitrate and sodium nitrite have been used as nitrate and nitrite sources when applicable.

Metals deposition were observed by XRD and TEM. They are deposited onto the TiO<sub>2</sub> P25 with spherical shape, and they do not influence in the titania's structure. The metals addition does not significantly decrease the surface area of the catalyst, even though in bimetallic catalysts. Higher light absorption properties are proportional with the amount of silver deposited. Higher reducibility is observed in the catalysts impregnated with the chloroplatinic acid than potassium hexachloroplatinate attributed to a higher metal dispersion and smaller particle size (ca. 2 nm lower). Figure 4A and B displays the TEM images of the same bimetallic catalyst varying the impregnation order (same mean diameter particle size (dp) of ca. 2.3 nm), and Figure B and C the TEM images of the same bimetallic catalyst only varying the Pt precursor.

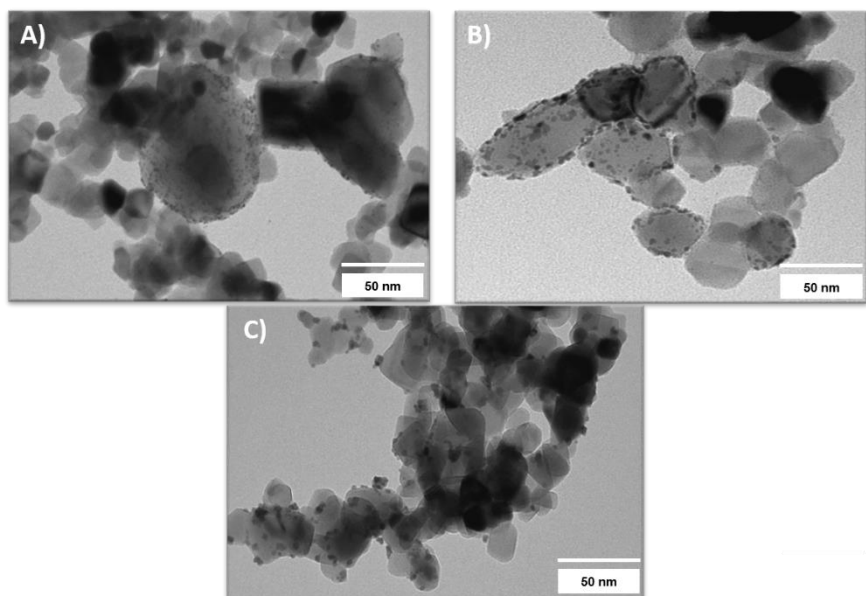


Figure 4. TEM pictures of: A) Ag(2)-Pt(4)/P25(H), dp = 2.1 nm; B) Pt(4)-Ag(2)/P25(H), dp = 2.5 nm; and C) Pt(4)-Ag(2)/P25(K), dp = 3.5 nm

The best photocatalytic conditions were interestingly obtained under the ultraviolet irradiation of 365 nm (closer to visible light) and in presence of pure hydrogen flow. Photocatalytic activity was enhanced in presence of H<sub>2</sub> due to synergetic effect induced by light between photogenerated electrons and dissociation of hydrogen on Pt. Therefore, all bimetallic catalysts were tested under these conditions.

The catalytic tests have been carried out with the monometallic catalysts (Ag/P25, Pt/P25), the physical mixture (Ag/P25 + Pt/P25 = 1/1), and the bimetallics (Ag-Pt/P25, Pt-Ag/P25). They have been tested under purely catalytic (absence of irradiation) and the photocatalytic conditions, and presence of hydrogen in all cases.

### *Activity of monometallic catalysts*

Ag(2)/P25 was the most active monometallic catalyst in terms of nitrate conversion (ca. 60%) and decomposition nitrate rate ( $0.165 \pm 0.065 \text{ h}^{-1}$ ) (Table 1) among the monometallic catalysts based on Ag or Pt with a final pH ~ 7. At higher Ag loading than 2 % the nitrate conversion remains almost similar (48 - 53 %) but the N<sub>2</sub> yield decreases slightly (~ 20.5 %). However, NO<sub>2</sub><sup>-</sup> selectivity is too high (ca. 57 %). Figure 5 shows the effect of Ag loading under UV-A ( $\lambda = 365 \text{ nm}$ ) and hydrogen flow. Pt based monometallic catalysts were almost inactive for the catalytic or photocatalytic reduction of nitrate under the experimental conditions used in this work. Pt-catalysts enhance the selectivity to N<sub>2</sub>, but the NH<sub>4</sub><sup>+</sup> amount is also high. We could conclude that the conversion is improved in presence of H<sub>2</sub> due to a synergetic effect induced by light between photogenerated electrons and H<sub>2</sub>. Therefore, bimetallic catalysts studies with Ag (2 wt. %) and Pt (2 and 4 wt. %) varying the Pt loading and precursor were also performed to enhance the conversion and selectivity. It seems that the 4 wt. % Pt loading enhances the conversion, however the difference is not so high in the monometallic catalysts and has to be studied in the bimetallics as well. On the other hand, the amount of 2 wt. % Ag clearly show the highest conversion and rate to be used in the bimetallic catalysts and physical mixture. Monometallic Ag-catalysts showed higher mean diameter nanoparticle of spherical nanoparticles than Pt-catalysts. The Pt-catalysts impregnated with K<sub>2</sub>PtCl<sub>6</sub>(K) were at about 1 nm bigger than H<sub>2</sub>PtCl<sub>6</sub>·6H<sub>2</sub>O (H), and assigned to worse metal dispersion.

Ag (2 wt. %) and Pt (2 and 4 wt. %) supported on TiO<sub>2</sub> P25 materials synthesized by drop-wise wetness impregnation either as mixture of monometallic catalysts or as co-impregnated catalysts promoted both the non-photocatalytic and the photocatalytic (365 nm UV irradiation;

presence/absence of pure H<sub>2</sub> flow) removal of NO<sub>3</sub><sup>-</sup> from water. In comparison to H<sub>2</sub>-free condition, the photocatalytic activity was highly enhanced in presence of H<sub>2</sub>.

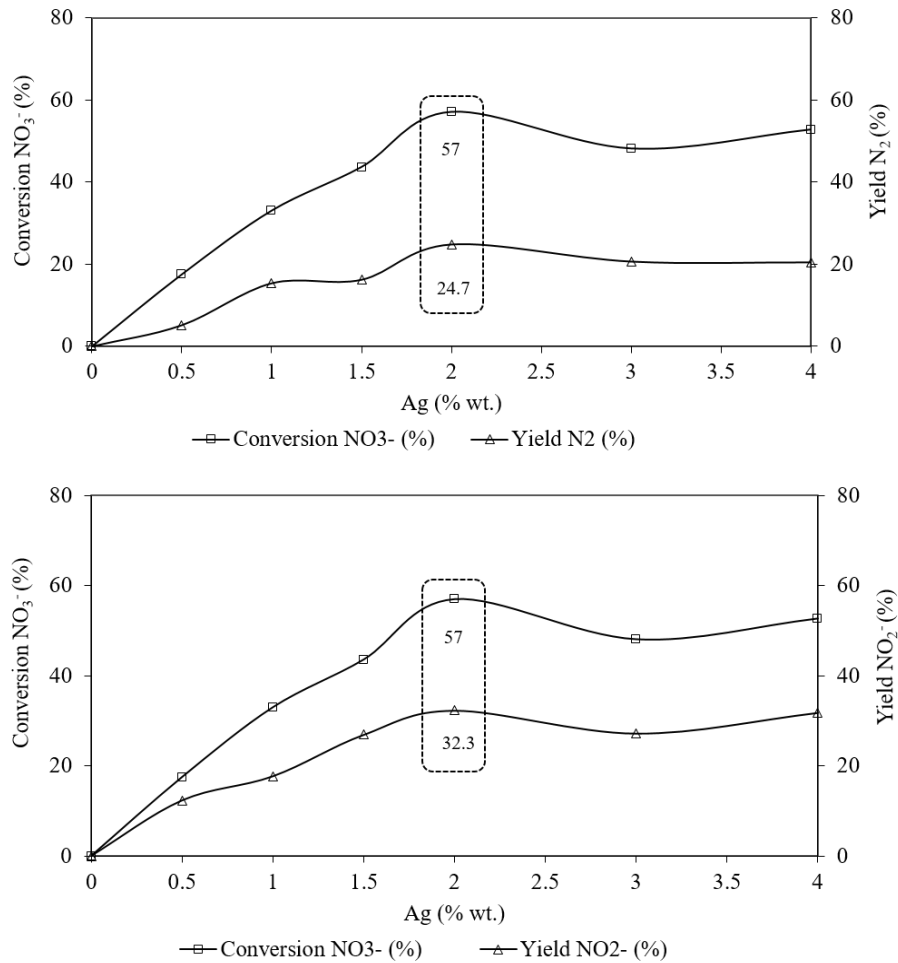


Figure 5. NO<sub>3</sub><sup>-</sup> conversion and yields (%) toward NO<sub>2</sub><sup>-</sup> and N<sub>2</sub>, varying the Ag loading (0.5 - 4 wt. %) under  $\lambda = 365$  nm irradiation and 150 mL/min H<sub>2</sub> flow after 6 h reaction

### Activity of bimetallic catalysts

The impregnated bimetallic samples are highly versatile. They are indeed active both in the catalytic and the photocatalytic processes with a clear influence of the impregnation order and the Pt precursor. Pt impregnated first leads to higher conversion due to improved accessibility of NO<sub>3</sub><sup>-</sup> to Ag<sup>0</sup> sites partially covering Pt, and high NO<sub>2</sub><sup>-</sup> selectivity at the expense of N<sub>2</sub> attributed to low Pt accessibility. Higher synergetic effect by light probably occurs in the most active bimetallic impregnated photocatalysts than in the Ag(2)/P25 + Pt(4)/P25(H) mixture of monometallic catalysts.

In bimetallic catalysts also using  $K_2PtCl_6$  instead of  $H_2PtCl_6 \cdot 6H_2O$  as Pt precursor increases the mean particle size accounting for the decrease of photocatalytic  $NO_3^-$  conversion when Ag is first impregnated (Ag-Pt). When Pt is first impregnated (Pt-Ag), the closer interaction between the metals observed by XPS using  $K_2PtCl_6$  leads to a great improvement of  $N_2$  yield reaching 36 %. It is equivalent to that obtained in the non photocatalytic reaction with Ag(2)-Pt(4)/P25(H), which exhibits higher  $NO_2^-$  selectivity (16 %). However, the samples synthesized with the  $H_2PtCl_6 \cdot 6H_2O$  led to higher reducibility attributed to higher metal dispersion, but generally lower nitrate reduction rates

Table 1 reports the decomposition nitrate reduction rates for Ag and Pt-catalysts.

Table 1. Pseudo-1<sup>st</sup> order nitrate reduction rates and correlation coefficients of Ag and Pt catalysts ( $\lambda = 365$  nm irradiation; 150 mL/min  $H_2$ ; 6 hours)

Catalyst	<b>k</b> ( <b>h<sup>-1</sup></b> )	<b>R<sup>2</sup></b>
Ag(0.5)/P25	0.038 ± 0.010	0.998
Ag(1)/P25	0.074 ± 0.019	0.991
Ag(1.5)/P25	0.069 ± 0.017	0.990
<b>Ag(2)/P25</b>	<b>0.165 ± 0.065</b>	<b>0.987</b>
Ag(3)/P25	0.091 ± 0.038	0.962
Ag(4)/P25	0.097 ± 0.060	0.953
Pt(2)/P25(H)	0.003 ± 0.003	0.987
Pt(2)/P25(K)	0.011 ± 0.006	0.966
Pt(4)/P25(H)	0.005 ± 0.001	0.987
Pt(4)/P25(K)	0.013 ± 0.003	0.976
<u>Ag(2)/P25 + Pt(4)/P25(H)</u>	<u>0.029 ± 0.011</u>	<u>0.983</u>
Ag(2)-Pt(2)/P25(H)	0.076 ± 0.018	0.988
Ag(2)-Pt(2)/P25(K)	0.079 ± 0.013	0.994
Ag(2)-Pt(4)/P25(H)	0.055 ± 0.004	0.999
Ag(2)-Pt(4)/P25(K)	0.073 ± 0.018	0.991
Pt(2)-Ag(2)/P25(H)	0.145 ± 0.034	0.988
Pt(2)-Ag(2)/P25(K)	0.061 ± 0.013	0.999
Pt(4)-Ag(2)/P25(H)	0.065 ± 0.020	0.988
<b>Pt(4)-Ag(2)/P25(K)</b>	<b>0.104 ± 0.022</b>	<b>0.999</b>

The Ag(2)/P25 + Pt(4)/P25(H) physical mixture is more efficient in the non-photocatalytic process with  $N_2$  yield of 42.3 % than in the photocatalytic process ( $Yield_{N_2} = 7.3\%$ ), probably due in this latter case to inhibition by  $H_2$  produced by photoreduction of  $H_2O$  over the Pt/P25 catalyst. This suggests that when Pt is secondly added, it covers the Ag particles, which are the most active in this reaction. It could be concluded that Ag allows the nitrate reduction step to

nitrite, and Pt the nitrite reduction step toward the desirable N<sub>2</sub> gas. This is verified by the possibility of Pt/P25 catalysts to photocatalytic reduce the nitrite to nitrogen, and its ability to dissociate the H<sub>2</sub>. If Ag and Pt are mainly isolated, the nitrate conversion is likely sustained by the H<sub>2</sub> spillover, which is not the best formulation to maximize the conversion and selectivity to N<sub>2</sub>.

The bimetallic catalyst Pt(4)-Ag(2)/P25 impregnated with K<sub>2</sub>PtCl<sub>6</sub> presented the highest photocatalytic activity among all the nanocatalysts synthesized (Conv<sub>NO<sub>3</sub><sup>-</sup></sub> = 45 % and S<sub>N<sub>2</sub></sub> = 80%), with a high 1<sup>st</sup> order nitrate decomposition rate of 0.104 ± 0.022 h<sup>-1</sup> (Table 1). Nevertheless, ammonium levels have to be diminished to be into the European normative limits, as well as the final pH (ca. 9) towards neutral pH. Since the reactions occurs in non-buffered media the final solution pH tends to increase to values higher than the pH<sub>pzc</sub> of Titania P25 (> 6.2).

Nitrate conversion and selectivity to products in percentage of bimetallic catalysts synthesized under the best photocatalytic conditions (P(3)+H<sub>2</sub>) are depicted in Figures 6 (Ag-Pt/P25) and 7 (Pt-Ag/P25).

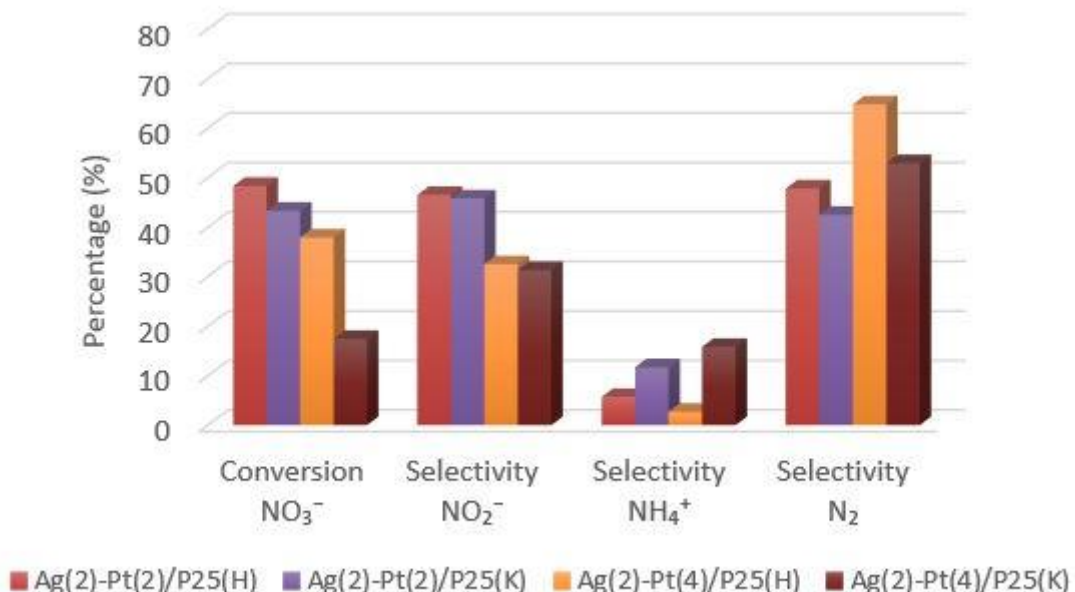


Figure 6. NO<sub>3</sub><sup>-</sup> conversion and selectivity (%) toward products measured from Ag-Pt/P25 catalysts after 6 h reaction

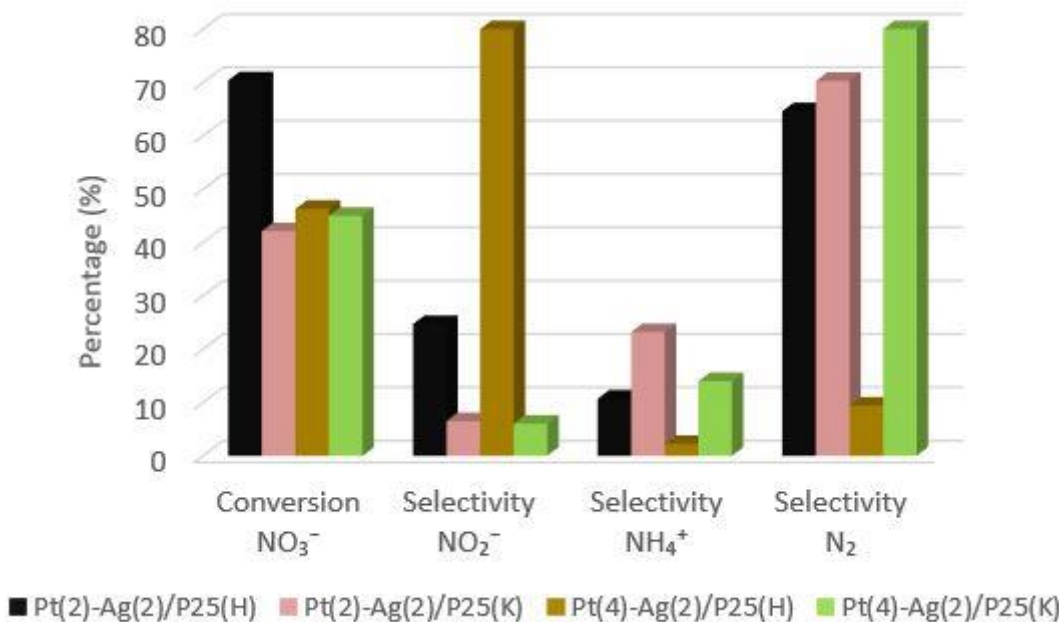


Figure 7.  $\text{NO}_3^-$  conversion and selectivity (%) toward products measured from Pt-Ag/P25 catalysts after 6 h reaction

In the other hand, the 5%  $\text{Pd}_2\text{Sn}/\text{P25}$  spherical NPs and NRs have shown an influence when they were tested under catalytic nitrate conditions and presence of hydrogen flow. The Figure 8 shows the percentages of nitrate conversion and the selectivity to  $\text{N}_2$ ,  $\text{NO}_2^-$  and  $\text{NH}_4^+$  obtained after 24 hours of reaction.

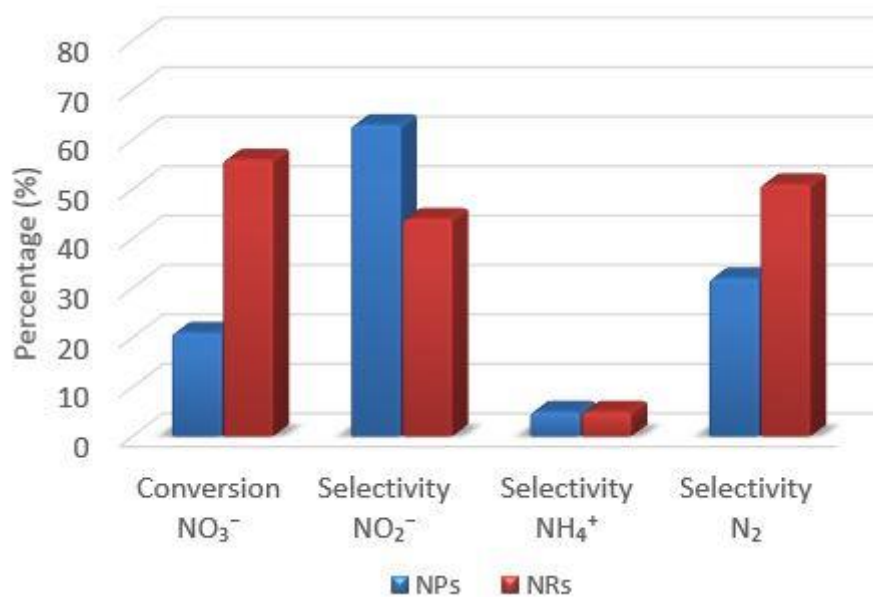


Figure 8.  $\text{NO}_3^-$  conversion and selectivity (%) toward products measured from  $\text{Pd}_2\text{Sn}/\text{P25}$  spherical NPs (blue) and  $\text{Pd}_2\text{Sn}/\text{P25}$  NRs (red), after 24 hours reaction

The selectivity to nitrogen for NRs was higher (51 %) than that for spherical NPs (32 %). Furthermore, the NH<sub>4</sub><sup>+</sup> formation (5 % of selectivity) was lower than other reported Pd–Sn catalysts but still high for the EU legislation. The NRs exhibited a dispersion of 0.37 %, while spherical NPs showed a lower dispersion (0.16 %). These very low values of metal dispersion indicate that the formation of the PdSn alloy inhibits the hydrogen chemisorption. Consequently, the alloy formation could be responsible for the lower selectivity to NH<sub>4</sub><sup>+</sup>, reducing the over-hydrogenation reaction. Besides, the catalyst containing 5% Pd<sub>2</sub>Sn NRs showed much higher catalytic activity than the spherical NPs, at around 3 times higher nitrate conversion was observed. Enhanced catalytic properties when using the 5% Pd<sub>2</sub>Sn/P25 NRs instead of spherical NPs could be associated with the more active surface facets of Pd<sub>2</sub>Sn NRs.

To sum up, the physical mixture Ag(2)/P25 + Pt(4)/P25(H) showed good nitrate conversion of ca. 56 % towards N<sub>2</sub> (S<sub>N2</sub> = ca. 76 %) under non-photocatalytic conditions than monometallic counterparts, however NO<sub>2</sub><sup>-</sup> and NH<sub>4</sub><sup>+</sup> are obtained. Besides, this configuration is not the best to maximize the conversion and selectivity and seems that the migration of NO<sub>2</sub><sup>-</sup> to Pt sites is not effectively achieved. Ag-Pt(Pt-Ag)/P25(H) catalysts show versatility for non-photocatalytic and photocatalytic processes. The bimetallic catalyst Pt(4)-Ag(2)/P25 impregnated with K<sub>2</sub>PtCl<sub>6</sub> led to the best balance between conversion (ca. 45 %) and selectivity to N<sub>2</sub> (ca. 80 %) under photocatalytic conditions ( $\lambda=365$  nm; H<sub>2</sub>) due to closer Ag-Pt interaction and Pt accessibility. However, NO<sub>2</sub><sup>-</sup> and NH<sub>4</sub><sup>+</sup> are analyzed too. Further studies must be done to enhance the catalytic and photocatalytic activity towards desired N<sub>2</sub>.

# Résumé

## ***Introduction***

Un des problèmes les plus préoccupants affectant la population mondiale est le manque d'accès à l'eau potable et à l'hygiène. La demande en eau potable est en augmentation constante et par conséquent la réglementation concernant sa qualité devient de plus en plus stricte. Ces dernières années la concentration en nitrates dans les eaux de surface dans l'Union Européenne (UE) ainsi que dans les autres pays est en forte augmentation. La présence de nitrate à différentes origines parmi lesquelles l'élevage, l'agriculture et l'industrie. En Europe, l'utilisation en agriculture de grandes quantités d'engrais organiques et chimiques est la principale cause de contamination des eaux. L'ion nitrate ( $\text{NO}_3^-$ ) très soluble et stable dans l'eau est un des composés qui occasionne la plus grande variété d'effets nocifs sur la santé des humains exposés par la consommation d'eau contaminée. Les concentrations de nitrate dans l'eau deviennent nuisibles pour les personnes et la nature lorsqu'elles dépassent certaines limites ( $> 50 \text{ mg/L } \text{NO}_3^-$  dans l'UE) car elles sont la cause de méthémoglobinémie suite à sa réduction en nitrite dans les intestins. Ceci est connu sous l'appellation de « syndrome du bébé bleu » qui affecte essentiellement les nouveau-nés en diminuant la circulation d'oxygène dans leur sang. De plus, il peut causer des cancers ou être un perturbateur endocrinien. Récemment la Commission Européenne a décidé « *de franchir une nouvelle étape dans les actions légales contre l'Espagne, l'Italie, la Grèce et la France pour n'avoir pas respecté la Directive sur les Nitrates de la Communauté qui concerne la protection des eaux contre la pollution causée par les nitrates des sources agricoles* ».

Parmi les différentes technologies mises en œuvre pour l'élimination des nitrates (physicochimiques, biologiques, électrochimiques et catalytiques), celle par hydrogénéation catalytique hétérogène (en présence d'un agent réducteur) est la méthode la plus connue et la plus efficace due à la grande sélectivité pour l'obtention de produits non toxiques –azote et eau– avec, de plus, la possibilité d'effectuer la réaction dans des conditions douces. La photocatalyse hétérogène, en particulier, a émergé comme voie très prometteuse de dénitrification du fait de la possibilité d'utiliser la lumière solaire ce qui la rend commercialement compétitive et compatible avec la protection de l'environnement. Cette technologie a été peu étudiée à ce jour. Il faut toutefois noter que les méthodes de dénitrification catalytiques conduisent fréquemment à l'obtention de sous-produits toxiques tels que le nitrite ( $\text{NO}_2^-$ ) – un composé intermédiaire – et

l'ion ammonium ( $\text{NH}_4^+$ ) – obtenu par sur hydrogénéation – ainsi qu'à des oxydes d'azote gazeux  $\text{NO}_x$  (Figure 1), dont l'élimination constitue encore un défi majeur à relever pour aboutir à des applications à l'échelle industrielle des procédés catalytique ou photocatalytique d'élimination des nitrates dans les eaux potables. Par conséquent, des travaux de recherche sont encore nécessaires pour obtenir des catalyseurs hautement performants pour ces procédés.

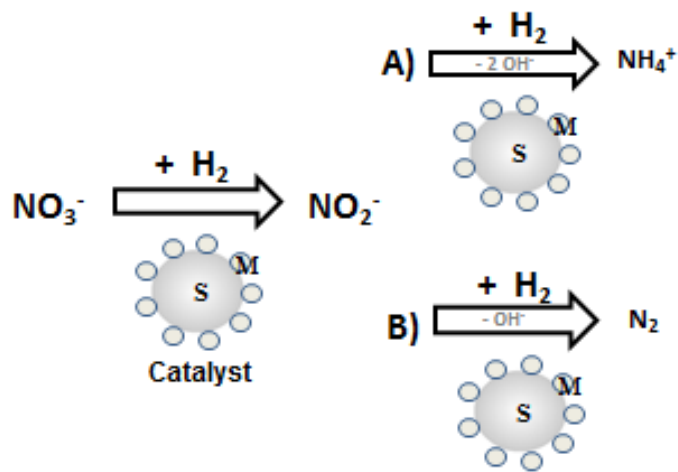


Figure 1. Mécanisme général de la réduction du nitrate par hydrogénéation catalysée, où S est le support et M le métal dispersé sur le support

Concernant les catalyseurs, de nombreuses études ont montré que des nanoparticules bimétalliques sont capables de conduire à de meilleures activités et sélectivités que les particules monométalliques parentes. Elles peuvent en effet manifester des propriétés résultant de la combinaison de celles de chacun des deux métaux constitutifs, mais aussi de nouvelles propriétés dues à un effet de synergie entre ces métaux. Beaucoup des catalyseurs bimétalliques utilisés dans l'élimination des nitrates dans l'eau reportés dans la littérature sont préparés en associant un métal noble, capable de chimisorber l'hydrogène à température ambiante (Pt, Pd) et un second métal, agissant comme promoteur ayant des propriétés redox (Ag, Sn). Les catalyseurs monométalliques à partir de métaux nobles sont inactifs pour la réduction des nitrates et l'addition d'un promoteur est indispensable pour initier la réaction de réduction (Figure 2).

Signalons qu'il a également été montré que des mélanges de catalyseurs monométalliques judicieusement choisis conduisent à des propriétés intéressantes.

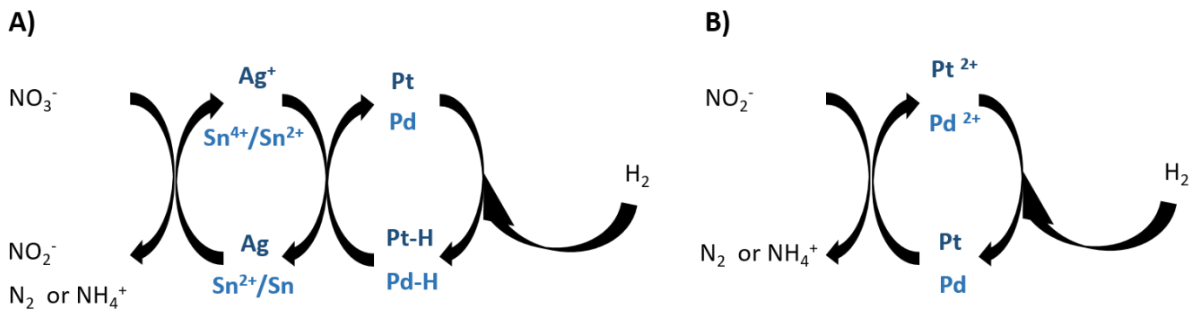


Figure 2. Représentations schématiques de: A) Mécanisme mis en jeu avec les catalyseurs bimétalliques Ag-Pt et Pd-Sn dans la réduction des nitrates par hydrogénéation, B) étape de réduction du nitrite

Par ailleurs, pour les catalyseurs métaux supportés, la nature du support est un paramètre clé de la formulation du catalyseur, susceptible d'influencer l'activité et la sélectivité vers les produits souhaités, agissant par ailleurs aussi sur la dispersion des métaux et la diffusion des espèces à la surface.

Parmi les semi-conducteurs utilisés en photocatalyse, l'oxyde de titane ( $\text{TiO}_2$ ) est le plus largement employé pour les applications relatives aux procédés liés à l'environnement et ses propriétés sont généralement améliorées par l'addition de dopants. Le composé dénommé Aeroxide  $\text{TiO}_2$  P25 (anatase/rutile ~ 80/20) est largement utilisé comme photocatalyseur.

### ***Objectifs de la thèse***

L'objectif principal de ce travail de thèse est de développer un catalyseur performant pour la réduction des nitrates dans l'eau permettant d'atteindre les normes requises par l'UE en ce qui concerne les concentrations des ions nitrate, nitrite et ammonium dans l'eau potable (50 mg/L  $\text{NO}_3^-$ , 0.5 mg/L  $\text{NO}_2^-$ , 0.3 mg/L  $\text{NH}_4^+$ ). Pour cela, sur la base de résultats antérieurs de la littérature, nous avons choisi des catalyseurs bimétalliques Ag-Pt de différentes compositions en faisant varier le contenu en métal, le précurseur de Pt, l'ordre d'imprégnation de Ag et Pt sur le support  $\text{TiO}_2$  P25. Afin d'obtenir des catalyseurs polyvalents pouvant être utilisés à la fois dans un procédé purement catalytique ou photocatalytique nous avons choisi comme préférentiellement le support oxyde de titane.

Nous avons aussi étudié des catalyseurs bimétalliques Pd-Sn en mettant dans ce cas l'accent sur l'influence de la morphologie qui a pu être contrôlée par une méthode de synthèse spécifique. Nous nous sommes également attachés à déterminer les conditions expérimentales optimales de la réaction photocatalytique.

Ceci nous a conduit à synthétiser des particules bimétalliques de type Ag-Pt (Ag: 2 % pds., Pt: 2 et 4 pds. % à partir de précurseurs  $\text{H}_2\text{PtCl}_6 \cdot 6\text{H}_2\text{O}$  ou  $\text{K}_2\text{PtCl}_6$ ) et de type Pd-Sn (5 %  $\text{Pd}_2\text{Sn}/\text{P25}$  Nanoparticles (NPs) sphériques et Nanobâtonnets (NRs)) supportées sur  $\text{TiO}_2$  P25. Pt et Ag sont connus pour se comporter comme capteurs d'électrons empêchant la rapide recombinaison trou-électron lors de l'élimination photocatalytique des nitrates sous irradiation ultraviolette ( $\lambda = 254$  and  $365$  nm).

A titre de comparaison avec leurs homologues bimétalliques, les catalyseurs monométalliques Ag/P25 (0.5 - 4 pds. %) et Pt/P25 (2 et 4 pds. %) ainsi que leurs mélanges physiques ont été testés dans les procédés catalytiques et photocatalytiques ce qui constitue une approche originale rarement développée permettant d'obtenir une compréhension plus approfondie des mécanismes mis en jeu.

Soulignons que l'étude du comportement à la fois catalytique ou photocatalytique d'un catalyseur de même composition est un des aspects originaux de ce travail. Il est rendu possible par la composition qui les rend actifs dans les deux procédés. Il était important lors de la réaction d'établir la part prise par chacun d'entre eux.

### ***Préparation des catalyseurs***

Les précurseurs des catalyseurs Ag et Pt supportés sur  $\text{TiO}_2$  P25 ont été synthétisés par imprégnation des précurseurs métalliques en variant la teneur en cation métallique, le précurseur Pt et l'ordre d'imprégnation de chaque précurseur Ag et Pt. Les catalyseurs ont été obtenus à partir de ces échantillons imprégnés par calcination à  $400^\circ\text{C}$  toute une nuit. Ensuite les catalyseurs ont été réduits chimiquement par un traitement avec le borohydrure de sodium,  $\text{NaBH}_4$ , dans l'éthanol sous agitation permanente et filtrés sous vide. Les échantillons ont subi plusieurs lavages avec l'éthanol et ensuite immédiatement introduits dans le réacteur catalytique pour éviter l'oxydation au contact de l'air.

Des nanoparticules sphériques et des nanobâtonnets de composition  $\text{Pd}_2\text{Sn}$  avec des tailles contrôlées ont été préparés par co-réduction de sels métallique en présence de trioctylphosphine (TOP), amine et ions chlorures. La croissance des nanostructures asymétriques  $\text{Pd}_2\text{Sn}$  a été obtenue par la désorption sélective du tensioactif (TOP) au moyen des ions chlorures. Ces synthèses des composés  $\text{Pd}_2\text{Sn}$  ont été effectuées dans le cadre d'un travail en collaboration par le groupe IREC de Barcelone. La déposition des nanoparticules sphériques et des nanobâtonnets

de Pd<sub>2</sub>Sn sur le support TiO<sub>2</sub> P25 nous a permis d'évaluer l'influence de la morphologie de ces catalyseurs dans la réaction de dénitration.

### ***Caractérisation des catalyseurs***

Afin de pouvoir relier les performances des catalyseurs à leurs caractéristiques physico-chimiques plusieurs caractérisations complémentaires ont été effectuées. La Diffraction des Rayons X (DRX), et la physisorption d'azote à la température de l'azote liquide ont permis de déterminer les propriétés structurales et texturales des matériaux. La microscopie électronique à transmission (MET) a été utilisée pour déterminer la taille et la morphologie des particules.

Les propriétés optiques ont été analysées par spectroscopie UV visible (DRUV-vis) en utilisant la fonction de Kubelka-Munk pour traiter les spectres d'absorption. L'environnement atomiques des différents élément, les réductibilités et la dispersion du métal des catalyseurs ont été déterminés par spectroscopie des photoélectrons X (XPS) et chimisorption d'hydrogène (H<sub>2</sub>-TPR, H<sub>2</sub>-Chimisorption).

### ***Réaction catalytique***

Les réactions catalytiques ont été effectuées dans un réacteur batch en PTFE sous atmosphère inerte et dans des conditions standard (courant d'argon de 120 mL/min, P atmosphérique, température ambiante). 200 mg de catalyseur ont été dispersés dans 350 mL d'eau ultrapure contenant 100 mg/L de NO<sub>3</sub><sup>-</sup> (réduction des nitrates) ou 50 mg/L de NO<sub>2</sub><sup>-</sup> (réduction des nitrites) sous agitation continue à 500 r.p.m. La durée de réaction est 6 h (catalyseurs Ag et/ou Pt/P25) ou 24 h (catalyseurs 5 % pds. Pd<sub>2</sub>Sn/P25). Lors de la réaction photocatalytique la lampe émettant la radiation ultraviolette est située au-dessus du réacteur ( $\lambda = 254$  nm,  $\lambda = 365$  nm; 4 W) avec une intensité de 7 mWcm<sup>-2</sup>. Au cours des réactions catalytiques et photocatalytiques le réacteur est recouvert d'une feuille d'aluminium pour éliminer les effets de la lumière extérieure. De façon à établir les contributions dues respectivement à la réaction catalytique et photocatalytique lors de la réduction des nitrates des expériences ont été réalisées sans irradiation en présence d'hydrogène (procédé catalytique); sous irradiation en absence d'hydrogène et enfin sous irradiation UV et en présence d'hydrogène (procédé photocatalytique). Contrairement à la plupart des études précédentes aucun «piégeur de trous» n'a été utilisé dans nos conditions de réaction (par expl. Acide formique ou oxalique), employés à cause de la présence possible de radicaux dans la solution aqueuse finale et qui présentent un risque potentiel élevé pour la santé humaine. Des échantillonnages ont été prélevés à intervalles

réguliers et analysés par chromatographie ionique (catalyseurs Ag et/ou Pt/P25) ou photométrie (5 % pds. Pd<sub>2</sub>Sn/P25).

Les performances catalytiques ont été suivies par les conversions en nitrates et nitrites, les sélectivités et rendements en produits et les vitesses de décomposition du nitrate. Le dispositif expérimental est représenté sur la Figure 3.

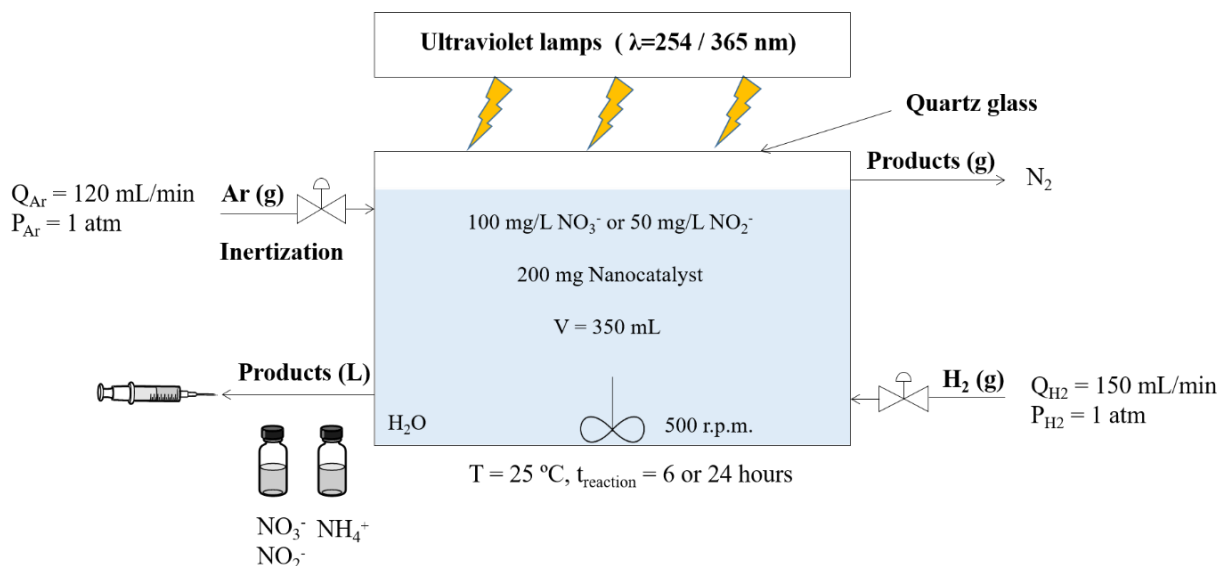


Figure 3. Dispositif expérimental et conditions opératoires

Avant d'effectuer une étude comparative des différents solides dans les conditions catalytiques et photocatalytiques, l'influence d'un certain nombre de paramètre a été examinée.

Le support commercial TiO<sub>2</sub> P25 a été testé dans les conditions catalytiques et photocatalytiques et se révèle dans les 2 cas inactif pour la réduction du nitrate et du nitrite. Il ne conduit à aucune adsorption de nitrate et il ne manifeste pas d'effet photocatalytique. Par conséquent toutes les performances obtenues avec les métaux supportés résultent du dopage du support par les métaux.

Deux sources de nitrate ont été comparées pour les réactions de dénitrification, nitrate de sodium et acide nitrique, en présence d'hydrogène et en présence/absence d'irradiation UV avec le catalyseur Ag(2)/P25 dans le but d'étudier l'influence du pH sur la sélectivité en azote. L'utilisation de HNO<sub>3</sub> comme source de nitrate augmente légèrement la sélectivité en azote

mais décroît fortement la conversion. Par conséquent, dans tout le travail, les nitrate et nitrite de sodium ont été utilisés.

## Résultats

### *Caractérisations physico-chimiques des catalyseurs*

Les principales propriétés des catalyseurs mises en évidence par analyses physico-chimiques sont les suivantes.

Les particules sphériques du support TiO<sub>2</sub> P25 ne sont pas modifiées après déposition des métaux comme observé par DRX et MET. La présence de métaux n'entraîne pas de diminution de la surface spécifique, même dans le cas des catalyseurs bimétalliques.

Les capacités d'absorption de la lumière sont proportionnelles à la quantité d'argent déposé. On observe une plus grande réductibilité des échantillons imprégnés à partir de l'acide chloroplatinique (H<sub>2</sub>PtCl<sub>6</sub>·6H<sub>2</sub>O) qu'à partir de l'hexachloroplatinate de potassium (K<sub>2</sub>PtCl<sub>6</sub>) ce qui est attribué à une plus grande dispersion et à l'obtention de plus petites particules (< 2 nm) dans le premier cas.

Les catalyseurs monométalliques Ag supporté présentent des particules de taille moyenne plus élevées que les catalyseurs au Pt. Par ailleurs la taille des particules est plus élevée d'environ 1 nm lorsque le précurseur est K<sub>2</sub>PtCl<sub>6</sub> plutôt que H<sub>2</sub>PtCl<sub>6</sub>·6H<sub>2</sub>O.

Les Figures 4A et 4B montrent les images MET d'un même catalyseur bimétallique obtenu en variant l'ordre d'imprégnation (même diamètre moyen de particules de 2,3 nm environ) et les Figures B et C celle de ce catalyseur bimétallique obtenu à partir des 2 précurseurs de Pt.

Les caractérisations par XPS montrent que Ag et Pt forment préférentiellement une solution solide lorsque Pt est imprégné en premier avec par ailleurs présence de particules d'argent identiques à celle observées pour les catalyseurs monométalliques Ag(2)/P25. La surface des particules est d'autant plus enrichie en Ag que la teneur en Pt décroît. Lorsqu'Ag est imprégnée en premier ses particules sont probablement décorées par Pt. Dans ce cas les propriétés électroniques du catalyseur Ag(2)-Pt(4)/P25(K) sont proches de celles de Ag(2)/P25. L'utilisation du précurseur K<sub>2</sub>PtCl<sub>6</sub> et l'ordre d'imprégnation Ag-Pt décroît les rapports atomiques de surface Pt/Ag.

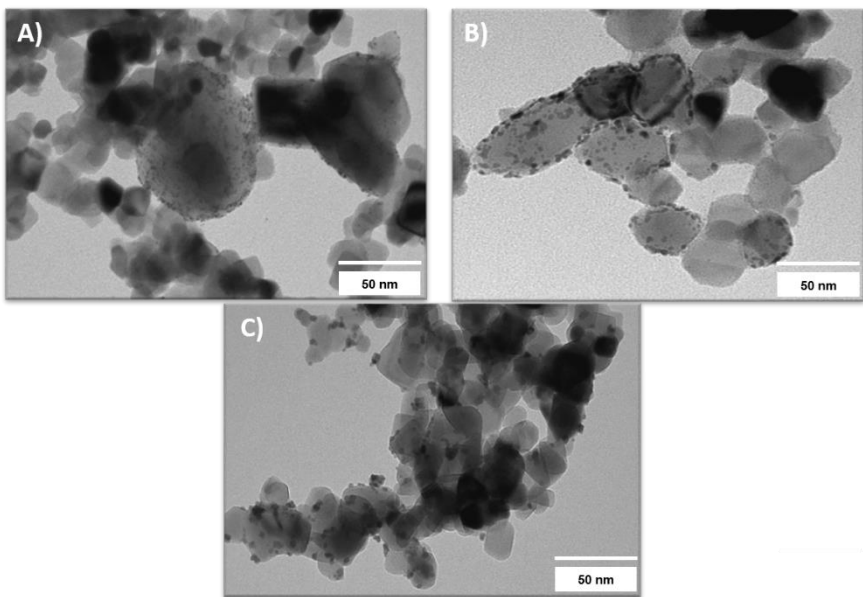


Figure 4. Images MET de: A) Ag(2)-Pt(4)/P25(H),  $d_p = 2.1 \text{ nm}$ ; B) Pt(4)-Ag(2)/P25(H),  $d_p = 2.5 \text{ nm}$ ; and C) Pt(4)-Ag(2)/P25(K),  $d_p = 3.5 \text{ nm}$

Les meilleures performances photocatalytiques ont de façon très intéressantes été obtenues sous irradiation ultraviolette à 365 nm (proche de la lumière solaire) et en présence d'hydrogène. L'activité photocatalytique augmente en présence d'hydrogène dû à un effet de synergie induit par la lumière entre les électrons photogénérés et l'hydrogène dissocié sur le Pt. Par conséquent tous les catalyseurs bimétalliques ont été testés dans de telles conditions.

### ***Activité catalytique***

Les tests ont été effectués sur les catalyseurs monométalliques (Ag/P25, Pt/P25), leur mélange physique ( $\text{Ag}/\text{P25} + \text{Pt}/\text{P25} = 1/1$ ) et les bimétalliques de type Ag/Pt (Ag-Pt/P25, Pt/Ag/P25) et de type  $\text{Pd}_2\text{Sn}$  dans les conditions catalytiques (absence d'irradiation UV) et photocatalytiques, dans tous les cas sous flux d'hydrogène.

### **Activité des catalyseurs monométalliques**

$\text{Ag}(2)/\text{P25}$  (2 % pds Ag) est le catalyseur monométallique conduisant à la conversion du nitrate (~ 60 %) avec une vitesse de décomposition ( $0.165 \pm 0.065 \text{ h}^{-1}$ ) la plus élevée (Table 1) le pH final obtenu étant voisin de 7. A plus haute teneur en Ag la conversion du nitrate demeure similaire (48 - 53 %) mais le rendement en  $\text{N}_2$  décroît légèrement (~ 20.5 %). Toutefois la sélectivité en nitrite est trop élevée (~ 57 %). La Figure 5 montre l'effet de la teneur en Ag lors de la réaction sous irradiation UV – A ( $\lambda = 365 \text{ nm}$ ) en présence d'hydrogène.

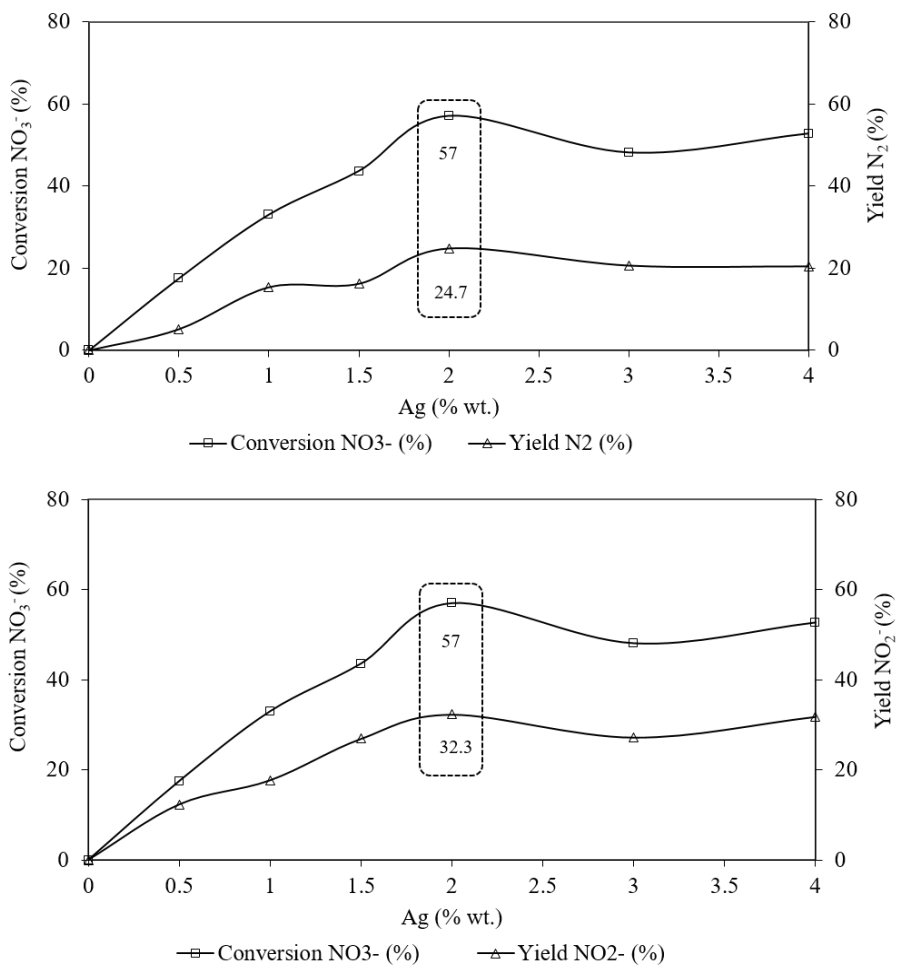


Figure 5. Conversion de  $\text{NO}_3^-$  et rendements (%) en  $\text{NO}_2^-$  et  $\text{N}_2$ , à différentes teneurs en Ag (0.5 - 4 pds. %) sous irradiation  $\lambda = 365 \text{ nm}$  et  $150 \text{ mL/min H}_2$  à 6 h de réaction

Les catalyseurs monométalliques au Pt sont quasiment inactifs dans la réduction catalytique et photocatalytique du nitrate dans les conditions expérimentales utilisées dans ce travail. Ces catalyseurs augmentent la sélectivité en  $\text{N}_2$  mais avec une sélectivité trop élevée en  $\text{NH}_4^+$ .

Les résultats obtenus avec les catalyseurs monométalliques permettent d'envisager une augmentation de l'activité et de la sélectivité avec les catalyseurs bimétalliques contenant à la fois Ag (2 % pd.s) et Pt (2 et 4 % pd.s.; précurseur  $\text{H}_2\text{PtCl}_6 \cdot 6\text{H}_2\text{O}$  ou  $\text{K}_2\text{PtCl}_6$ ).

On observe une tendance à l'augmentation de la conversion dans le catalyseur monométallique contenant 4 % pd.s. de Pt ce qui nous a conduit à étudier l'effet de la teneur en Pt dans le catalyseur bimétallique (2 et 4 % pd.s.). Pour Ag, il a été montré que la teneur de 2 % pd.s. est

optimale dans le catalyseur monométallique ce qui a conduit au choix de cette teneur dans les catalyseurs bimétalliques.

### **Activité des catalyseurs bimétalliques et des mélanges physiques**

Les catalyseurs contenant 2 % pds. Ag et 2 ou 4 % pds. Pt soit sous forme de mélange physique des catalyseurs monométalliques soit bimétalliques sont actifs dans la conversion catalytique et photocatalytique du nitrate (365 nm UV irradiation; présence/absence de H<sub>2</sub>). Par rapport au résultat obtenu en absence de H<sub>2</sub>, l'activité photocatalytique est augmentée en présence de H<sub>2</sub>.

Les catalyseurs bimétalliques imprégnés sont très polyvalents. Ils se comportent en effet à la fois comme catalyseurs et photocatalyseurs avec dans les deux cas une nette influence de l'ordre d'imprégnation et de la nature du précurseur de Pt.

L'imprégnation du Pt en premier conduit à une conversion plus élevée due à une augmentation de l'accessibilité du nitrate au site actif Ag° des ensembles argent recouvrant les particules de Pt. Par ailleurs, on observe une sélectivité élevée en NO<sub>2</sub><sup>-</sup> au détriment de N<sub>2</sub> due à la faible accessibilité du Pt. Un effet de synergie plus élevée due à l'irradiation est probablement obtenu dans les photocatalyseurs bimétalliques imprégnés que dans les mélanges de catalyseurs monométalliques Ag(2)/P25 + Pt(4)/P25(H).

Dans les catalyseurs bimétalliques obtenus à partir du précurseur K<sub>2</sub>PtCl<sub>6</sub>, l'augmentation de la taille moyenne des particules observée en MET par rapport au précurseur H<sub>2</sub>PtCl<sub>6</sub>·6H<sub>2</sub>O explique la diminution de la conversion photocatalytique du nitrate lorsque Ag est imprégné en premier. A l'inverse lorsque Pt est imprégné en premier (Pt-Ag), la forte interaction entre les deux métaux mise en évidence par XPS dans le cas du précurseur K<sub>2</sub>PtCl<sub>6</sub> conduit à une augmentation du rendement en N<sub>2</sub> qui atteint 36 %. Ce rendement est équivalent à celui obtenu dans la réaction purement catalytique avec Ag(2)-Pt(4)/P25(H) qui présente toutefois l'inconvénient de conduire à une sélectivité plus élevée en NO<sub>2</sub><sup>-</sup> (16 %). Les échantillons synthétisés à partir du précurseur H<sub>2</sub>PtCl<sub>6</sub>·6H<sub>2</sub>O sont plus réductibles et conduisent à une vitesse de réduction du nitrate plus élevée due à la plus grande dispersion des particules.

Le mélange physique Ag/P25 + Pt/P25 est plus efficace dans le procédé purement catalytique avec un rendement en N<sub>2</sub> de 42.3 % que dans le procédé photocatalytique où le rendement est de 7.3 %. Ceci est probablement dû à l'inhibition par l'hydrogène produit par photooxidation de H<sub>2</sub>O sur Pt/P25. Ceci suggère que lorsque le Pt est imprégné en second il recouvre les particules d'Ag réputées les plus actives pour la réduction du nitrate.

Dans le Tableau 1 sont reportées les vitesses de réduction du nitrate avec les catalyseurs contenant Ag et Pt.

Tableau 1. Vitesses de pseudo premier ordre de conversion du nitrate et coefficients de corrélation des catalyseurs monométalliques Ag/P25 et Pt/P25 ( $\lambda = 365$  nm irradiation; 150 mL/min H<sub>2</sub>; 6 h)

Catalyst	k (h <sup>-1</sup> )	R <sup>2</sup>
Ag(0.5)/P25	0.038 ± 0.010	0.998
Ag(1)/P25	0.074 ± 0.019	0.991
Ag(1.5)/P25	0.069 ± 0.017	0.990
<b>Ag(2)/P25</b>	<b>0.165 ± 0.065</b>	<b>0.987</b>
Ag(3)/P25	0.091 ± 0.038	0.962
Ag(4)/P25	0.097 ± 0.060	0.953
Pt(2)/P25(H)	0.003 ± 0.003	0.987
Pt(2)/P25(K)	0.011 ± 0.006	0.966
Pt(4)/P25(H)	0.005 ± 0.001	0.987
Pt(4)/P25(K)	0.013 ± 0.003	0.976
Ag(2)/P25 + Pt(4)/P25(H)	0.029 ± 0.011	0.983
Ag(2)-Pt(2)/P25(H)	0.076 ± 0.018	0.988
Ag(2)-Pt(2)/P25(K)	0.079 ± 0.013	0.994
Ag(2)-Pt(4)/P25(H)	0.055 ± 0.004	0.999
Ag(2)-Pt(4)/P25(K)	0.073 ± 0.018	0.991
Pt(2)-Ag(2)/P25(H)	0.145 ± 0.034	0.988
Pt(2)-Ag(2)/P25(K)	0.061 ± 0.013	0.999
Pt(4)-Ag(2)/P25(H)	0.065 ± 0.020	0.988
<b>Pt(4)-Ag(2)/P25(K)</b>	<b>0.104 ± 0.022</b>	<b>0.999</b>

On peut conclure que Ag permet la réduction du nitrate en nitrite et que Pt réduit le nitrite en N<sub>2</sub>. Ceci a été vérifié en effectuant la réduction photocatalytique du nitrite en azote et sa capacité à dissocier l'hydrogène. Si Ag et Pt forment des particules essentiellement isolées la conversion du nitrate est surtout obtenue par épandage de l'hydrogène ce qui n'est pas la meilleure formulation pour obtenir des conversions et des sélectivités élevées est N<sub>2</sub>.

Le catalyseur bimétallique Pt(4)-Ag(2)/P25 imprégné par K<sub>2</sub>PtCl<sub>6</sub> présente l'activité photocatalytique la plus élevée parmi tous les nanocatalyseurs synthétisés dans notre travail (Conv<sub>NO<sub>3</sub></sub> = 45 % and S<sub>N<sub>2</sub></sub> = 80%) avec une vitesse de décomposition de pseudo premier ordre de 0.104 ± 0.022 h<sup>-1</sup> (Tableau 1). Malgré tout, la production d'ammonium doit être diminuée pour correspondre aux normes Européennes, de même que le pH final (~ 9) doit être ramené vers la neutralité. Du fait que la réaction est effectuée dans un milieu non tamponné le pH final

de la solution tend à augmenter à des valeurs plus élevées que le pH<sub>pzc</sub> de l'oxyde de titane P25 (> 6.2) au cours de la réaction. La conversion du nitrate et la sélectivité des produits (exprimées en pourcentages) obtenues pour les catalyseurs bimétalliques manifestant les meilleures performances photocatalytiques sont reportées sur les Figures 6 (Ag-Pt/P25) et 7 (Pt-Ag/P25).

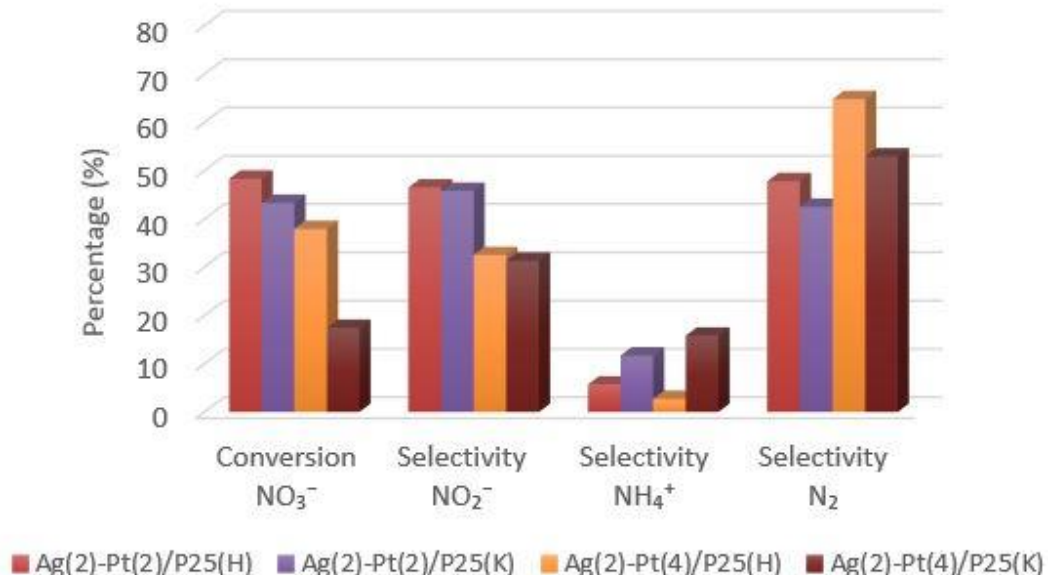


Figure 6. Conversion du nitrate et sélectivité en azote, nitrate et ammonium obtenues avec les catalyseurs Ag-Pt/P25 après 6 h de réaction.

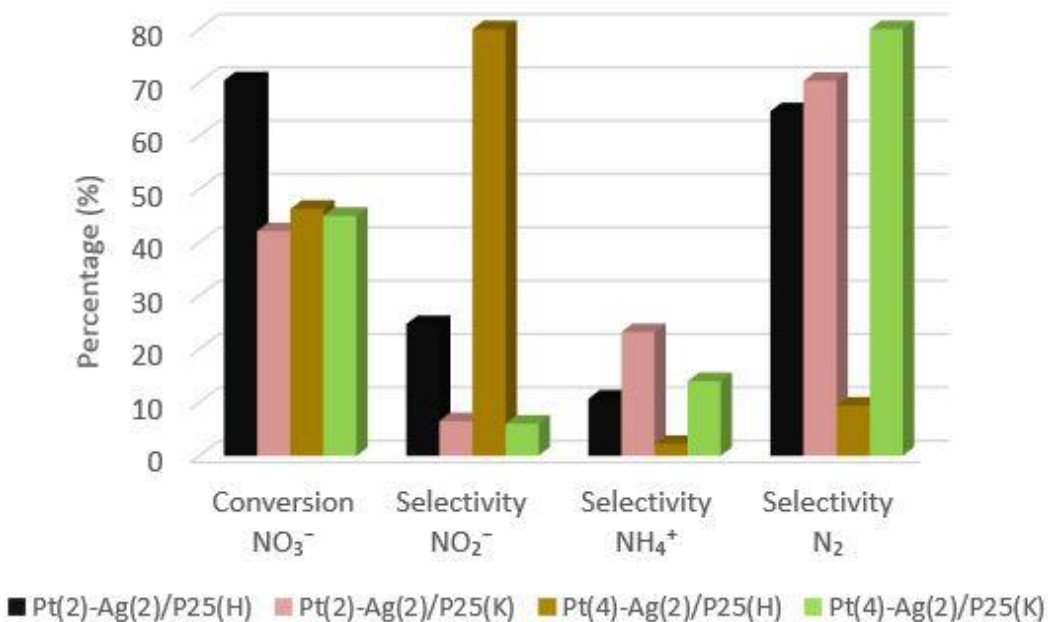


Figure 7. Conversion du nitrate et sélectivité en azote, nitrate et ammonium obtenues avec les catalyseurs Pt-Ag/P25 après 6 h de réaction

Si l'on considère maintenant le catalyseur Pd<sub>2</sub>Sn/P25 les différentes morphologies de type nanoparticules sphériques (NPs) et nanobâtonnets (NRs) ont une influence sur la conversion du nitrate en présence d'hydrogène. Sur la Figure 8 sont reportées la conversion du nitrate et les sélectivités en N<sub>2</sub>, NO<sub>2</sub><sup>-</sup> et NH<sub>4</sub><sup>+</sup> après 24 h de réaction.

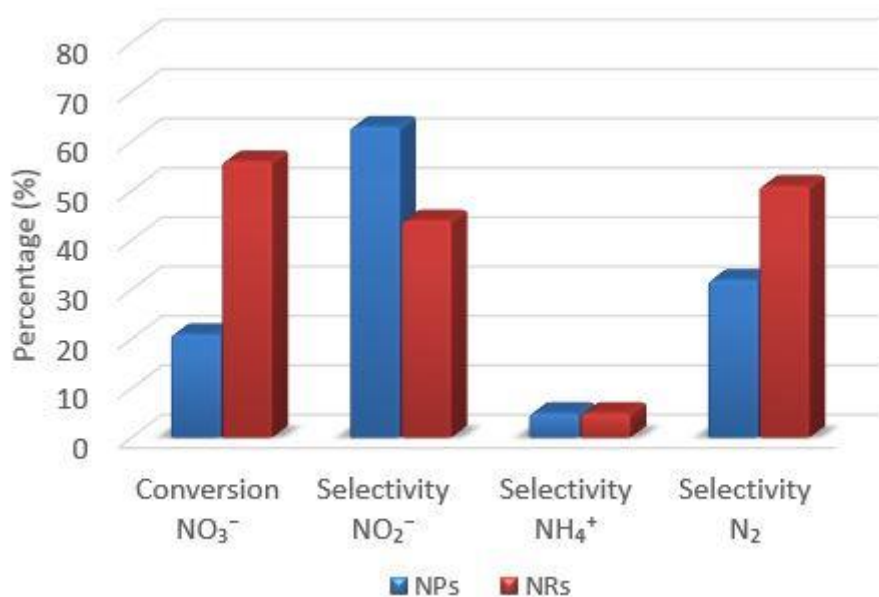


Figure 8. Conversion du nitrate et sélectivité en azote, nitrate et ammonium obtenues avec les nanoparticules sphériques NPs (bleu) et les nanobâtonnets NRs (rouge) du catalyseur Pd<sub>2</sub>Sn/P25 après 24 h de réaction

Les nano bâtonnets conduisent à une sélectivité en N<sub>2</sub> plus élevée (51 %) que les nanoparticules sphériques (32 %). De plus, la formation de NH<sub>4</sub><sup>+</sup> est dans tous les cas plus faible que pour les autres catalyseurs Pd-Sn rapportés dans la littérature mais encore trop élevée pour satisfaire à la législation Européenne. Les nano bâtonnets présentent une dispersion de 0.37 % alors qu'elle est de 0.16% pour les nanoparticules sphériques. Ces faibles valeurs de dispersion des métaux indiquent que la formation d'alliage PdSn inhibe la chimisorption d'hydrogène. Par conséquent, la formation d'alliage serait responsable de la faible sélectivité en NH<sub>4</sub><sup>+</sup> en diminuant la surhydrogénération. Notons que le catalyseur 5 % pds. Pd<sub>2</sub>Sn sous forme de nano bâtonnets est plus actif que celui sous forme de nanoparticules sphériques avec une conversion du nitrate 3 fois plus élevée environ. Ceci peut être associé aux faces exposées qui se révèlent plus actives pour les nano bâtonnets.

En conclusion de ce travail nous avons établi que le mélange physique Ag(2)/P25 + Pt(4)/P25(H) conduit à une conversion plus élevée du nitrate de 56 % environ avec une sélectivité en N<sub>2</sub> de 76 % que les catalyseurs monométalliques dans la réaction catalytique, de dénitration. Toutefois les rendements en NO<sub>2</sub><sup>-</sup> et NH<sub>4</sub><sup>+</sup> sont trop élevés. Le mélange physique de catalyseurs monométalliques ne semble pas optimal afin d'optimiser la conversion et la sélectivité car la migration de NO<sub>2</sub><sup>-</sup> vers les sites Pt° est limitée.

Les catalyseurs bimétalliques Ag-Pt(Pt-Ag)/P25 manifestent une grande polyvalence étant à la fois actifs dans le procédés catalytique et photocatalytique. Parmi ceux-ci le catalyseur Pt(4)-Ag(2)/P25 imprégné avec K<sub>2</sub>PtCl<sub>6</sub> conduit au meilleur résultat photocatalytique avec une conversion de ca. 45 % et la sélectivité la plus élevée en N<sub>2</sub>(ca. 80 %). Ce comportement a été attribué à la forte interaction des particules Pt et Ag mise en évidence par XPS. Toutefois ce catalyseur produit encore des quantités de NO<sub>2</sub><sup>-</sup> et NH<sub>4</sub><sup>+</sup> trop élevées pour conduire à une eau potable. Des études plus approfondies doivent être effectuées afin d'augmenter l'activité catalytique et photocatalytique ainsi que la sélectivité en N<sub>2</sub>.

# CHAPTER 1:

## Introduction and Scope

## **1. Introduction and Scope**

In this chapter the presence of nitrate in water, the current nitrate removal technologies, the catalytic and photocatalytic hydrogenation reactions for its abatement and the objectives of the thesis are exhaustively detailed.

In the section *1.1* of this chapter, the problems induced by the presence of nitrate ion pollutant in ground and surface waters for drinking water are commented, particularly its high risk to human health. In this section is also described the legislation concerned to the harmful nitrates, nitrites and ammonium, especially focused on the European Union countries.

The section *1.2* details the methods existing nowadays for nitrate removal from water.

The section *1.3* describes largely the heterogeneous catalytic nitrate and nitrite reduction towards the non-toxic nitrogen gas through hydrogenation, emphasizing the ecofriendly photocatalytic route. The catalysts used (Ag, Pt, Pd, Sn/TiO<sub>2</sub>) and reducing agent used.

Section *1.4* reports the general catalytic and photocatalytic nitrate reduction mechanisms towards the possible different products.

Section *1.5* shows the catalysts parameters that can be varied for an optimal catalyst design.

The last part of the chapter, *1.6*, details the objectives and main scope of this doctoral thesis.

## 1.1 Nitrate pollution problem in water

Water is the elixir of life, and then a pure and clean water is fundamental to human well-being as well as to natural ecosystems. Ensuring a proper water quality is one of the main goals for the European Union (EU) environmental policy. Nitrogen is an indispensable element to all living organisms, and the nitrogen cycle is one of the most important nutrients for the ecosystems (Figure 1.1). Plants absorb nitrogen from the soil and the animals eat these plants, and when they die are decomposed, so the nitrogen comes back to the soil, where bacteria convert it and the cycle starts again. Nevertheless, normally more nitrogen is applied due to farming activities (fertilizers) than is removed in harvested crops and animal products (livestock manure), which can interrupt the equilibrium of this cycle. Most of this leftover is lost in one hand to the water via nitrate leaching (i.e. excessive application of fertilizers) causing water contamination and eutrophication (excess nutrient load), and on the other hand to the air causing soil acidification and greenhouse gas effects, due to gaseous emissions (ammonia,  $\text{NO}_x$  gases (nitrous oxide and nitrogen oxides) and non-toxic nitrogen gas ( $\text{N}_2$ )). Normally, farming remains are responsible for over 50 % of the total nitrogen release into surface waters. Other important sources are the leaks from septic tanks and sewage, and effluents from certain industries (European Union 2010; Water Health Organization 2011; Velthof et al. 2014).

The high soluble and stable nitrate ion ( $\text{NO}_3^-$ ) in water becomes harmful inorganic water pollutant to people and nature when it exceeds the limit ( $> 10 \text{ mg/L } \text{NO}_3^-$  by the WHO and  $> 50 \text{ mg/L } \text{NO}_3^-$  in EU) (S.I-No.106 2007; Water Health Organization 2011). It is one of the key chemicals that causes large scale health effects through drinking water exposure. Then removing the nitrate in water for drinking water aim is one of the major pursuits since the 80's by the European Union. High levels of soluble nitrates in water cause methemoglobinemia as it can be easily reduced to nitrite in the intestines, known as 'blue baby syndrome', that affects mostly newborns and reduce the oxygen circulation in the blood. Moreover, it could cause cancer or be an endocrine disruptor (Mori et al. 1999; Thompson 2001; Guillette et al. 2005; Mahler et al. 2007). The nitrite ( $\text{NO}_2^-$ ) and ammonium ( $\text{NH}_4^+$ ) ions (Figure 1.1) are also well-known contaminants which must be eliminated as well. They are even more toxic than nitrate. The sum of the three containing-N compounds is called total oxidized nitrogen. Besides, unionized ammonia ( $\text{NH}_3$ ) is also present in water. Ammonia and ammonium can be easily converted one

into the other ( $\text{NH}_3 + \text{H}_2\text{O} \rightarrow \text{NH}_4^+ + \text{OH}^-$ ).  $\text{NH}_4^+$  is from both predominantly present in most natural waters, and is formed under pH values of ca. 8.75.  $\text{NH}_3$  is present at pH higher than ca. 9.75. The sum of ammonia and ammonium (TAM) is expressed as water-quality parameter of ammonium.

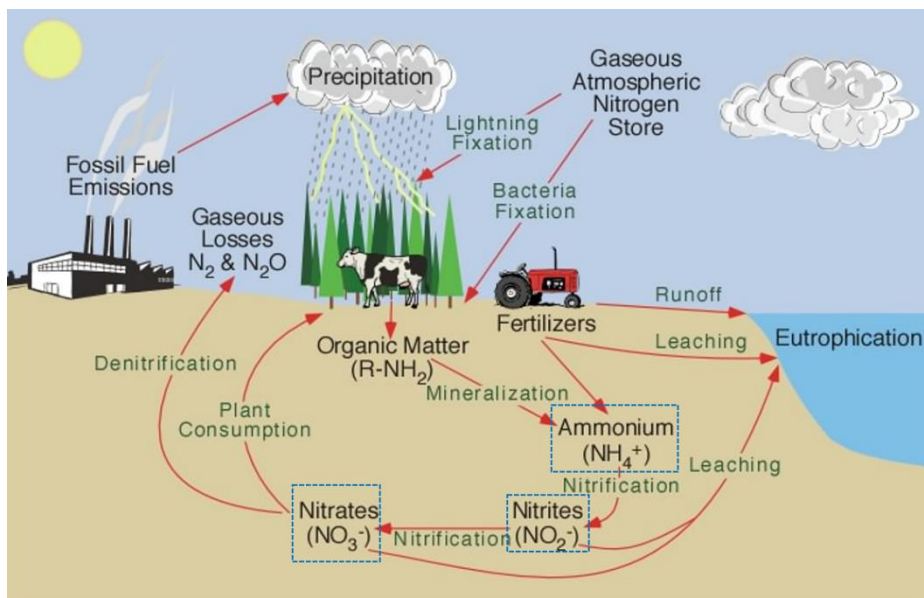


Figure 1.1. The Nitrogen cycle (European Union 2010b)

### 1.1.1 Normative

In Europe, the agricultural use of nitrates in organic and chemical fertilizers has been a main source of water contamination. The 1991 Nitrates Directive (Council Directive 91/676/EEC) (European Commission 1991) is one of the earliest pieces of EU legislation planned at reducing water pollution caused or induced by nitrates and preventing further such pollution in ground and surface waters. The Nitrates Directive requires the EU Member States to determine surface freshwaters and ground waters that surpass or could surpass a nitrate concentration of 50 mg per liter. Moreover, they have to identify surface waters that are eutrophic or could turn into eutrophic. Member States must signalize these areas as nitrate vulnerable zones (NVZs) and establish Action Programs for the protection of these waters from nitrates. For the first time mineral fertilizer consumption registered a progressive reduction in the early 1990s but across all 27 Member States nitrogen consumption has increased by 6 %. At the recent years, nitrates contamination is still continuously rising in EU, and around one third of the EU groundwater

bodies are exceeded. This is more frequently observed (Figure 1.2, groundwater average 40-50 mg/L NO<sub>3</sub>) in the following EU-27 countries (Nitrates Directive EU-27 2004-2007): **Spain (eastern)**, **France (western)**, Italy, Belgium, the Netherlands, Ireland, Germany, Greece, Austria, the UK, Slovakia, Hungary and Denmark (Council 1998; European Union 2010b; European Comission 2012). Recently, The European Commission has decided “*to take further steps in legal actions against Spain, Italy, Greece and France for failing to respect the Community Nitrates Directive, which concerns the protection of waters against pollution caused by nitrates from agricultural sources*” ([http://europa.eu/rapid/press-release\\_IP-96-1217\\_en.htm](http://europa.eu/rapid/press-release_IP-96-1217_en.htm) (2015)).

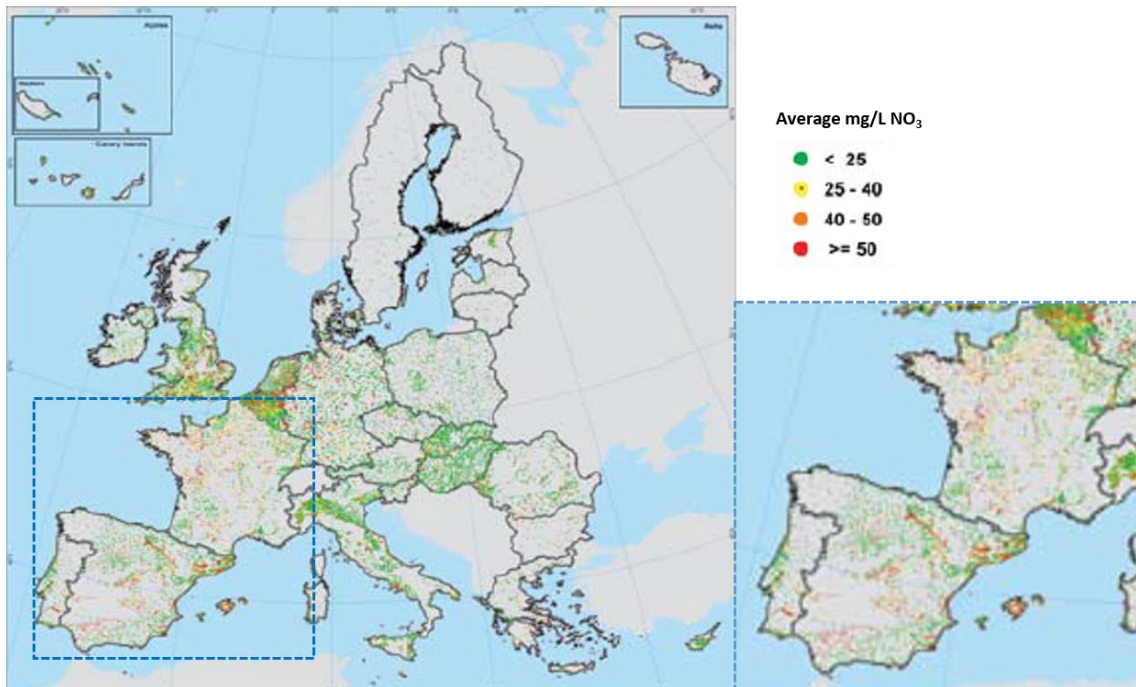


Figure 1.2. Groundwater average nitrate concentrations (2004 - 2007)  
(European Comission 2010)

The nitrate vulnerable zones in EU registered in 2009 and the surpassing of critical loads for eutrophication due to deposition of nutrient nitrogen in 2010 are displayed in Figures 1.3 and 1.4, respectively.

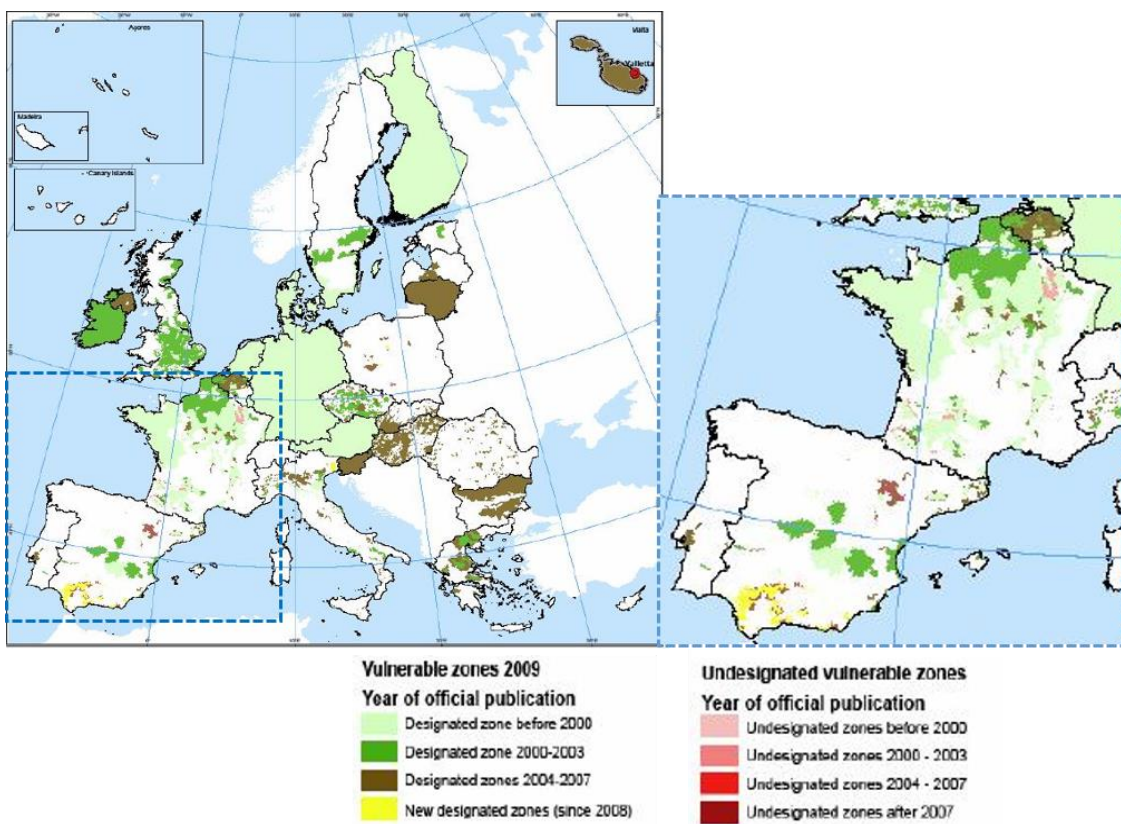


Figure 1.3. Nitrate Vulnerable Zones (NVZs) (2000 - 2009) (European Comission 2010)

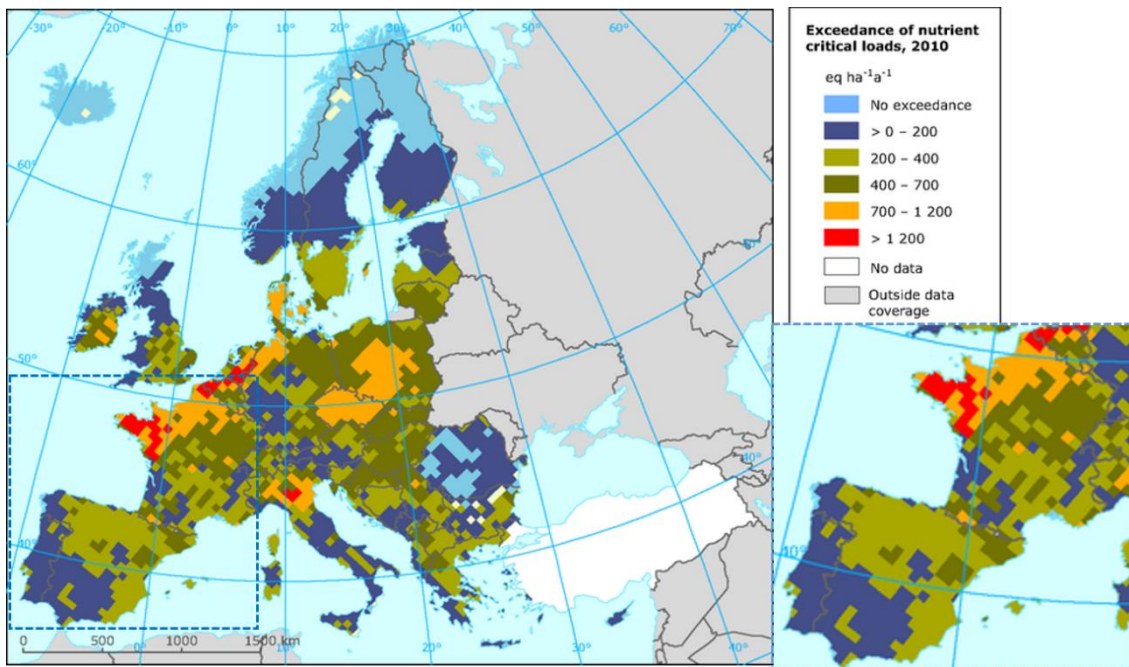


Figure 1.4. Surpassing of critical loads for eutrophication due to the deposition of nutrient nitrogen (2010) (European Union 2010a)

All the possible containing-N pollutants present in drinking water (nitrate, nitrite and ammonium) (Table 1.1) are strictly limited by the European community: 50 mg/L  $\text{NO}_3^-$ , 0.5 mg/L  $\text{NO}_2^-$  and 0.3 mg/L  $\text{NH}_4^+$  (S.I-No.106 2007). On the other hand “*The guidelines for Drinking-water quality*” of The World Health Organization (WHO) are applied for the non-European countries: 10 mg/L  $\text{NO}_3^-$ , 0.03 mg/L  $\text{NO}_2^-$ , and 0.4 mg/L  $\text{NH}_4^+$  (World Health Organization 1996, 2011). It can be observed that  $\text{NO}_2^-$  and  $\text{NH}_4^+$  ions are even much more toxic than  $\text{NO}_3^-$ .

Table 1.1. Limit values for N-compounds concentrations in water set by EU policies (Oenema et al. 2011)

Effects	Indicator	Limit values/ Targets	EU Normative
Adverse effects on humans from nitrates	$\text{NO}_3^-$	50 mg/L in groundwater	Drinking Water Directive (98/83/EC) Nitrates Directive (91/676/EEC) Groundwater Directive (2006/118/EC)
Adverse effects on humans from nitrites	$\text{NO}_2^-$	0.5 mg/L in water used for drinking water*	Drinking Water Directive (98/83/EC) Nitrates Directive (91/676/EEC) Groundwater Directive (2006/118/EC)
Adverse effects on humans from ammonium	$\text{NH}_4^+$	0.3 mg/L	Drinking Water Directive (98/83/EC)
Contamination of groundwater	$\text{NO}_3^-$	50 mg/L	Nitrates Directive (91/676/EEC) Groundwater Directive (2006/118/EC)
Eutrophication of surface waters	$\text{NO}_3^-$	25-50 mg/L	Nitrates Directive (91/676/EEC)
Eutrophication of surface waters	$\text{N}_{\text{total}}$	2-10 mg/L; discharge from sewage treatment plants	Urban Waste Water Directive (91/271/EEC)

\* Further,  $[\text{NO}_3^-]/50 + [\text{NO}_2^-]/3 \leq 1$

## 1.2 Nitrate abatement technologies

Several current methods allow the abatement of nitrate in water for drinking water purpose, which are divided into diverse categories: physicochemical, biological, electrochemical and catalytic for the main ones.

The physicochemical methods - such as ion exchange, reverse osmosis and electrodialysis – are effective, fast and stable for removing the nitrate. However, they only transfer nitrate from water to another concentrate phase that has to be treated with a further process or disposal, and

also which could be expensive. For instance, in reverse osmosis a brine waste is produced (water quality), then a second step must be done to treat the permeate containing the species removed (Kim et al. 2004; Moreno et al. 2005; Ersever et al. 2007; Schoeman 2009).

Biological denitrification is another effective method to remove the nitrate, which is usually applied for wastewater treatments, nevertheless less for drinking water. It can manage high concentrations but the biodegradation processes are: slow, pH and temperature sensitive, producing non-desired products and high turbidity in final water. Furthermore, on the one hand the sludge formed during the process has to be disposed by burning or landfilling it, then increasing the cost operational conditions; and on the other hand operators are exposed to pathogen agents (Ergas et al. 2004; Moreno et al. 2005).

Despite of the fact that the electrochemical processes (i.e. SnO<sub>2</sub> electrode) are very selective to non-toxic products, the electrode is frequently fouled and is costly (energy intensive). Besides it exhibits a low rate of reduction (Duca et al. 2010; Centi et al. 2015).

The conventional heterogeneous catalysis hydrogenation is a very well-known and established efficient nitrate and nitrite abatement technology, due to its high selectivity towards desired harmless products – N<sub>2</sub>, H<sub>2</sub>O – with the possibility of operating at mild operational conditions (room temperature and atmospheric pressure). In particular, photocatalysis has emerged as a very promising route for denitrification technique due to the possibility of using the solar irradiation, which makes it commercially attractive and environmental friendly. This last technique needs still to be developed. These catalytic techniques are largely described in the following section, as this thesis is focused on both of them.

During the last ten years, a wide and exhaustive research has been done in the field of heterogeneous catalytic hydrogenation for denitrification of drinking water in the frame of our Spanish-French collaboration – CaTheter, URV (Tarragona, Spain) and MACS-ICGM, ENSCM (Montpellier, France) – due to the emerging serious nitrate problem that is still remaining nowadays in both countries (*1.1.1*). Thus, in this thesis the research line has been pursued applying new materials (i.e. TiO<sub>2</sub> support) and moving much further using the photocatalysis technique.

## **1.3 Catalytic and Photocatalytic nitrate reduction**

### **1.3.1 Catalytic nitrate reduction**

Conventional catalytic nitrate reduction through hydrogenation is a wide technology used to transform nitrates into nitrogen and water. The contaminated stream is in contact with the heterogeneous catalyst on which the nitrate reacts and is converted to N-compounds in the presence of a reducing agent (normally hydrogen) (Prüss et al. 2000). Since the publications of Vorlop et al. and Hörold et al. almost 30 years ago using noble metal catalysts, the removal of nitrates and nitrites in aqueous solution has been widely studied (Vorlop et al. 1989; Hörold et al. 1993). This reaction leads frequently to toxic side products, such as nitrite ( $\text{NO}_2^-$ ) – intermediate compound – and ammonia ( $\text{NH}_4^+$ ) – over hydrogenation – ions and  $\text{NO}_x$  gases, which is the major challenge to get over.

#### **1.3.1.1 Catalysts**

Since the catalytic nitrate reduction was developed by Vorlop et al. and Hörold et al. several catalyst designs and configurations have been studied among these decades in academia and industry to improve the nitrate reduction into nitrogen using bimetallic catalysts and hydrogen, although, from a practical point of view, the materials tested nowadays are still limited by the formation of ammonia (Batista et al. 1997; Chen et al. 2003; Pintar et al. 2003). Several studies have shown that bimetallic nanoparticles improve the catalytic properties and selectivity in comparison to their monometallic counterparts. They could show properties related to the combination of both individual metals and also new ones due to a synergy between the two metals. Most of the bimetallic catalysts used for denitration in water reported in literature have been prepared combining a noble metal able to chemisorb hydrogen at ambient temperature (Pt, Pd, Rh) and a second promoter metal from groups 11, 12, 13 or 14 easily oxidizable and reducible (redox properties) (Ag, Cu, Sn, In, Au, Zn), supported over various types of supports ( $\text{CeO}_2$ ,  $\text{Al}_2\text{O}_3$ ,  $\text{Fe}_2\text{O}_3$ , HDT, AC). Monometallic catalysts based on noble metals are inactive for nitrate reduction and the presence of promoters is necessary to initiate the reduction reaction (Gauthard et al. 2003; Soares et al. 2008; Barrabés et al. 2006, 2011; Theologides et al. 2011; Aristizábal et al. 2010, 2012, 2014; Zaleska-Medynska et al. 2016). The highest selectivity into nitrogen has been shown by the most used bimetallic pairs in the literature, which are Pd-Cu, Pd-Sn and Pd-In, specially Pd-Cu, but nowadays it is insufficient for the EU legislation of potable water (Hörold et al. 1993; Batista et al. 1997; Deganello et al. 2000; Gauthard et al.

2003; Pintar 2003; Wang et al. 2007; Witońska et al. 2008; Dong et al. 2009). Furthermore, Deganello et al. have proved that copper is detrimental for nitrite reduction because it decreases the activity and increases the ammonium ions formation (Deganello et al. 2000).

The enhancement of the activity by an appropriate bimetallic pair architecture based on Pt with an additional metal is among the promising routes in heterogeneous catalysis for the reduction of nitrate (Zaleska-Medynska et al. 2016). Pt-monometallic catalysts have been clearly established active to reduce selectively nitrite to nitrogen, but are practically inactive for nitrate reduction into nitrite. In addition, Pt is able to dissociate H<sub>2</sub> (Prüssé et al. 2000; Yoshinaga 2002; Gauthard et al. 2003; Sá et al. 2005; Barrabés et al. 2006; Aristizábal et al. 2012;). Silver could be an interesting co-catalyst due to its non-toxicity, antimicrobial properties in water (i.e. *Escherichia coli*), high efficiency, ease composite preparation and relatively low cost when compared with other metals. Besides, Ag-promoted noble metals can have higher activity than classical Cu-promoted catalysts for catalytic reduction, attributed to the Ag<sup>+</sup>/Ag couple redox potential is lower than that of the nitrogen species involved in the reaction. Then, the metallic silver will be able to reduce nitrate into nitrite (Table 1.2) (Epron et al. 2002; Gauthard et al. 2003; Wodka et al. 2010; Aristizábal et al. 2011; Ko et al. 2011; Kowalska et al. 2015). However, it has been shown that the addition of silver as promoter decreases the activity of nitrite reduction due to its inactivity for this reaction, then Ag addition could lead to high nitrite intermediate concentration (Gauthard et al. 2003). Both metals would be reduced by hydrogen completing the catalytic cycle.

Various Pt and/or Ag bimetallic catalysts formed by Pt-Cu, Pd-Ag, Ag-Pt supported on Al<sub>2</sub>O<sub>3</sub> (Gauthard et al. 2003), Pt-Cu on Hydrotalcite (HDT) (Aristizábal et al. 2011), Pt-Cu and Pt-Ag on activated carbon (AC) (Barrabés et al. 2006; Aristizábal et al. 2012) lead to NO<sub>3</sub><sup>-</sup> conversions in a range of ca. 65 to 98 %, however undesirable NO<sub>2</sub><sup>-</sup> and/or NH<sub>4</sub><sup>+</sup> products are produced, which is the main drawback for drinking water. Few other studies related to Ag-containing bimetallic catalysts have been performed. Besides they lead to undesired by-products (Hörold et al. 1993; Witońska et al. 2008; Devadas et al. 2011). Therefore, further studies must be done to implement the efficiency of the interesting Pt-Ag bimetallic pair for the reduction of nitrate.

As commented before, Pd-Sn is another common bimetallic pair used for water denitration (Table 1.2), which leads to interesting results for other type of reactions, like ethanol oxidation (Jou et al. 2010; Du et al. 2012). Garron et al. (Garron et al. 2005) have shown that Pd-Sn/SiO<sub>2</sub>

give rise to higher selectivity and stability but lower activity than the Pd-Sn/Al<sub>2</sub>O<sub>3</sub> catalyst. Besides, both catalysts were synthesized with the same route but differences are found on their metal dispersions and properties. Barbosa et al. (Barbosa et al. 2013) have reported a better catalytic denitration activity for Pd-Sn pair than for Pd-In supported on Al<sub>2</sub>O<sub>3</sub> and cation exchanged resin (Sty-DVB). However, undesirable ammonia has been formed and they concluded that new supports (SiO<sub>2</sub>, HDT, Al<sub>2</sub>O<sub>3</sub>, AC) have to be applied.

Furthermore, physical mixtures of monometallic catalysts have also attracted attention because properly combined they can lead to interesting results (Pintar et al. 1996; Soares et al. 2008, 2011; Aristizábal et al. 2014). Soares et al. (Soares et al. 2011) particularly concluded that mixtures of Pd and Cu or Pt and Cu supported on AC monometallic catalysts can lead to higher activity than the corresponding bimetallic catalysts, probably due to the *in situ* formation of bimetallic pair in aqueous solution attributed to copper leaching. On the other hand, Aristizábal et al. (Aristizábal et al. 2014), reported the highest selectivity to nitrogen over mixture of Pt/AC and Ag/AC catalysts, although with lower nitrate conversion than with the bimetallic pair. This was an incitement to study in our work, physical mixture of Ag/P25 and Pt/P25 monometallic catalysts. This will also allow to establish the role of each metal in the reduction of nitrate.

Table 1.2. Standard reduction potentials of Pt, Ag, Pd, Sn and N-compounds (Fanning 2000; Zaleska-Medynska et al. 2016)

<b>Redox system</b>	<b>E<sup>0</sup> (V)</b>
Pt <sup>2+</sup> /Pt	1.18
Ag <sup>+</sup> /Ag	0.799
Pd <sup>2+</sup> /Pd	0.83
Sn <sup>2+</sup> /Sn	-0.136
Sn <sup>4+</sup> /Sn <sup>2+</sup>	0.15
NO <sub>3</sub> <sup>-</sup> / NO <sub>2</sub> <sup>-</sup>	0.835
NO <sub>3</sub> <sup>-</sup> / NH <sub>4</sub> <sup>+</sup>	0.88
NO <sub>3</sub> <sup>-</sup> / N <sub>2</sub>	1.25

The nature of the support is a key parameter of the catalysts formulation able to influence activity and selectivity, and obviously acting on the metals deposition and the diffusion of the species. Gao et al. and Theologides et al. have interestingly reported that Pd-Cu supported on titania (TiO<sub>2</sub>) diminished more significantly the ammonia production than on other supports such as Al<sub>2</sub>O<sub>3</sub>, FeO<sub>3</sub>, CeO<sub>2</sub>, MgO, Mn<sub>2</sub>O<sub>3</sub>, Cr<sub>2</sub>O<sub>3</sub>, Y<sub>2</sub>O<sub>3</sub>, MoO<sub>2</sub> in the catalytic nitrate reduction reaction (Gao et al. 2003; Theologides et al. 2011), and even increases the nitrate reduction rate (Wehbe et al. 2009). This opens the way to the promising photocatalysis route, replacing a light

inert heterogeneous catalyst for the Titania, which is a very well-known photoactive material. Indeed, in presence of light a photonic pathway of activation takes place and probably makes the energetics of the process more favorable. *Photocatalytic nitrate reduction* has been scarcely performed until now, so more research and development are still needed in this field.

### 1.3.2 Photocatalytic nitrate reduction

#### 1.3.2.1 Heterogeneous photocatalysis

From an environmental point of view, one of the most important challenges of the century is to develop a photocatalyst to harvest the practically endless sources of radiation from sunlight and water. The photoreaction is accelerated in presence of a nanocatalyst due to its high catalytic surface area and short semiconductor-liquid electron pathways for charge and exciting transport. Thus, heterogeneous photocatalysis has attracted the attention of worldwide scientists for its applications in environmental purification and solar energy conversion since the solar light is used, what makes it a sustainable eco-friendly technology. Moreover, differing to other photochemical processes, this technique can be used in a complex mixture of contaminants. This technique was developed by Carey et al in 1976 (Carey et al. 1976) in gaseous and liquid phase, but is in the 90's when it seriously started to be applied as water treatment. It has various advantages for water treatment, like mild operational conditions (ambient temperature and atmospheric pressure); low cost operating conditions; less use of energy, and complete mineralization of parents and their intermediate substances without secondary pollution. This process consists in use of near-ultraviolet (UV) band (shorter than 400 nm,  $\lambda < 400$  nm) and light visible range ( $\lambda = 400 - 750$  nm) of the solar spectrum (Figure 1.5) to photo-excite a semiconductor photocatalyst in contact with water (Gálvez et al. 1985; Chong et al. 2010; Ibhadon et al. 2013; Townsend 2014).

In the last years, various studies have reported a high potential for nitrate reduction in aqueous solution through heterogeneous photocatalysis (Ohtani et al. 1997; Mori et al. 1999; Gao et al. 2003; Zhang et al. 2005; Sá et al. 2009; Wehbe et al. 2009; Gekko et al. 2012; Hirayama et al. 2012; Bem Luiz et al. 2012; Doudrick et al. 2013; Yang et al. 2013; Kobwittaya et al. 2014; Parastar et al. 2013; Shand et al. 2013; Soares et al. 2014; Sowmya et al. 2014; Sun et al. 2016), nevertheless only some of them have shown high nitrate conversion (ca. 98 %) towards nitrogen gas (ca. 100 %) (Kominami et al. 2005; Zhang et al. 2005). Photocatalytic oxidation of pollutants have been extensively studied, contrary to photoreduction.

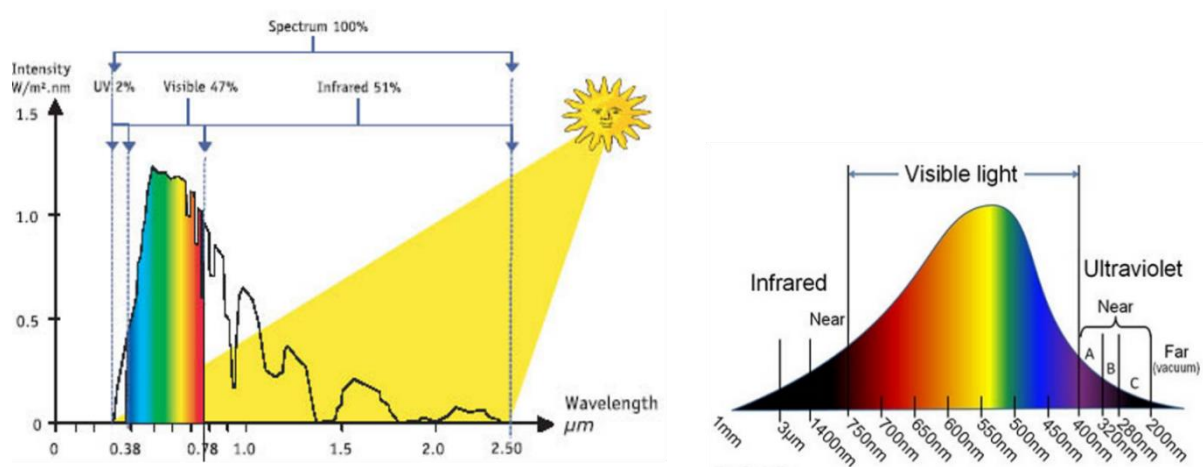


Figure 1.5. Solar spectrum (Sanam Glass 2013; Hydroponic 2016)

Wehbe et al. (Wehbe et al. 2009) have compared for the first time the conventional non-photocatalytic and the photocatalytic nitrate reductions to determine the best of the two processes using Pd-Cu/TiO<sub>2</sub> catalyst under the same conditions [ $\lambda = \sim 365$  nm, H<sub>2</sub> (reducing agent), formic acid (hole scavenger)] and to get deeper understanding of the processes (Wehbe et al. 2009). They concluded that photocatalysis route is more selective. Hirayama et al. [mixture of Pt/TiO<sub>2</sub> and Sn-Pd/Al<sub>2</sub>O<sub>3</sub> catalysts,  $\lambda = 380$  nm, H<sub>2</sub> (reductant), ethanol (hole scavenger), CO<sub>2</sub> (pH control)], (Hirayama et al. 2012) and Soares et al. [Pd-Cu/TiO<sub>2</sub> catalyst,  $\lambda \geq 365$  nm, H<sub>2</sub> as reductant, ethanol as hole scavenger, CO<sub>2</sub> (pH control)] have followed also the same original approach (Soares et al. 2014). It is remarkable that no reduction was observed without hydrogen and photocatalytic routes led also to higher nitrate conversions (ca. 76 %), however the formation of ammonia still occurs. Much further studies must be done to fully understand the process. Thus, in this thesis catalytic (non-photocatalytic) and photocatalytic nitrate reduction routes with hydrogen as reductant have been compared, as both properties of the catalyst should be taken into consideration.

### 1.3.2.2 Titanium dioxide

Among various semiconductor photocatalysts, Titania ( $\text{TiO}_2$ ) is extensively applied for widespread environmental applications among several other oxides, due to its low-cost, strong oxidizing power, biological and chemical inertness (non-toxic), long-term stability, redox efficiency and photosensitivity (Fujishima et al. 2000; Thompson et al. 2006). Depending of the temperature of the thermal treatment the  $\text{TiO}_2$  nanoparticles (NPs) can be composed by three types of phases: anatase, rutile and brokite, however anatase and rutile are the unique phases exhibiting photocatalytic properties. Aerioxide Titania P25 (anatase/rutile: ~ 80/20) is commonly used as photocatalyst. The photocatalytic process takes place on the catalyst surface, then the crystallinity is an important factor (Parastar et al. 2013). The initial process of the photocatalytic inorganic/organic compounds is the photo-electron-hole pairs generation in the semiconductor particles, reacting with substances adsorbed on/near its surface (Legrini et al. 1993; Sun et al. 2016). When a photon of light with sufficient energy equal or higher than the Band gap of the semiconductor ( $E_g$ ) ( $E \geq E_g$ ) hits the titania particle with the appropriate wavelength, this energy ( $h\nu$ ) is adsorbed and used to promote the electron ( $e^-$ ) from the valence band (VB) to the conduction band (CB), thereby creating a hole ( $h^+$ ) in the VB. The holes are considered trapped by the lattice oxygen atoms on the titania's surface, and the trapped hole weakened the bond between the titanium atom and the lattice oxygen atoms. Such oxygen atoms are liberated to create oxygen vacancies. These  $e^-$  and  $h^+$  produced by the light adsorption can either recombine again or migrate to the titania's surface, reacting with other species at the interface, being powerful oxidizing ( $h^+$ ) and reducing ( $e^-$ ) (redox) agents. Hence, the electrons excited to the CB can be transferred to nitrate ions for reduction reactions, and the free holes can oxidize organic species that are adsorbed on the surface or can produce  $\text{OH}^\cdot$  (hydroxyl) radicals when reacting with  $\text{H}_2\text{O}$  or  $\text{OH}^-$  ( $e^- + \text{H}^+ \rightarrow \text{H}^\cdot ; h^+ + \text{OH}^- \rightarrow \text{OH}^\cdot$ ). To prevent the electron-hole recombination, the electrons must be removed rapidly from the titania (acceptor) and the hole could be filled with an electron (i.e. oxidation of a compound called electron donor or hole scavenger) (Mills et al. 1993; Coleman et al. 2005; Zhang et al. 2009; Cheng et al. 2010; Lee et al. 2014). The general photocatalytic process on  $\text{TiO}_2$  particle is shown in Figure 1.6 (based on Herrmann 1999 and Rani et al. 2012).

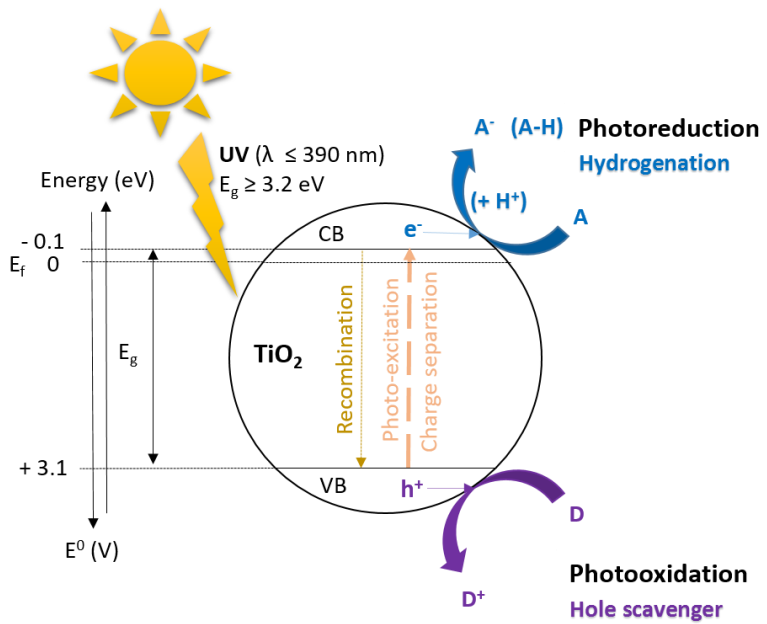


Figure 1.6. Photocatalytic process on  $\text{TiO}_2$  particle:  $E^0$  (redox potential),  $E_g$  (Band gap),  $E_f$  (Fermi level), A (electron acceptor, i.e.  $\text{Pt}^{2+}$ ,  $\text{Ag}^+$ ), D (electron donor, i.e. formate)

Nevertheless, the applications of  $\text{TiO}_2$  are limited due to: its band gap (anatase  $\sim 3.2$  eV and rutile  $\sim 3$  eV), the only UV utilization from solar spectrum (2 - 5 %) and the fast recombination rate between photogenerated electrons and holes limiting the photocatalytic efficiency. Then,  $\text{TiO}_2$  is generally doped with metal ions (acceptor) to prevent the electron-hole recombination and shifting the light absorption into the visible-light range ( $\sim 45$  % of sunlight) by decreasing the band gap of the photocatalyst (Soria et al. 1991; Asahi et al. 2001; Behnajady et al. 2008; Gomathi et al. 2010; Wang et al. 2012; Zhu et al. 2012). Besides, the  $\text{TiO}_2$  has been proven to be practically inactive for nitrate reduction (Bems et al. 1999; Kato et al. 2002; Gao et al. 2003; Sá et al. 2009; Wehbe et al. 2009).

### 1.3.2.3 Photocatalysts

Doping the  $\text{TiO}_2$  particles with noble metals (Au, Pt, Ag, Pd) is a widely effective technique to improve the photocatalytic activity, enhancing the electrochemical behavior of the semiconductor and reducing the electron-hole recombination rate. These metal ions should be in close contact with the surface of the photocatalyst to increase the charge transfer, otherwise the metal ions could operate as recombination centers in the bulk of the photocatalyst particles. If they are in appropriate contact with the surface, they serve as capturing centers in their metal sites for the photogenerated electrons transferred from the titania conduction band, being active centers for photocatalytic reactions. The equilibration of the Fermi level ( $E_f$ ) between the titania

and the metal favors the electron accumulation in the system, which has to be higher than that of metallic NPs. This phenomenon leads to a Schottky barrier formation at the metal/TiO<sub>2</sub> contact region provoking the charge separation (Fujishima et al. 2008; Malato et al. 2009; Ahmed et al. 2010; Anderson 2011; Kočí et al. 2012).

The Pt and Ag noble metals, in addition of their catalytic properties (1.3.1.1), have been reported as perfect electron sinks for TiO<sub>2</sub>, having the higher Schottky barriers – lower Fermi levels - among the metals (Pt presents the maximum). Hence, facilitating the electron-hole separation and promoting a rapid interfacial electron transfer process, which retards the recombination of the photogenerated electrons and holes (Hermann et al. 1993; Kamat 1993; Sclafani et al. 1997). Furthermore, they are good hydrogenation catalysts, promoting the dissociative chemisorbed hydrogen to produce stabilized H<sub>ads</sub>, which are expected to obtain high rates of hydrogen evolution (specially Pt) (Ranjit et al. 1995). Pt/TiO<sub>2</sub> catalyst has been reported to be inactive or low effective in the nitrate photoreduction (Hirayama et al. 2012; Soares et al. 2014), but appears necessary to improve the photocatalytic efficiency in the nitrite photoreduction to nitrogen (Prüssé et al. 2000), possessing higher photonic efficiency than Pd/TiO<sub>2</sub> photocatalyst (Sakthivel et al. 2004). An appropriate composition made of Pt with additional metal enhances the activity, increasing the electronic vacancy in the d-band induced by the bimetallic structures (Yamamoto et al. 2010, Zaleska-Medynska et al. 2016). Silver is among the most largely used dopant in the photocatalytic activity of TiO<sub>2</sub> (Zhang et al. 2007; Behnajady et al. 2008; Doudrick et al. 2013; Sowmya et al. 2014). The photogenerated electrons are transferred from the TiO<sub>2</sub> P25 conduction band to metallic Ag NPs impregnated on TiO<sub>2</sub> P25 (Kočí et al. 2012, Lee et al. 2014). Hole scavengers are used in all cases, being generally the formic and oxalic acid. Sá et al. reported double nitrate reduction rate on Ag/TiO<sub>2</sub> than Fe or Cu/TiO<sub>2</sub> (TiO<sub>2</sub> Hombikat support from Sachtleben Chemie with SA = 49 m<sup>2</sup>g<sup>-1</sup>) (Sá et al. 2009).

Thereupon, bimetallic pair Ag-Pt could be able to enhance the catalytic/photocatalytic activity, combining the property of silver acting as electron-hole separation centers and the ability of Pt to dissociate easily H<sub>2</sub> and reduce NO<sub>2</sub><sup>-</sup> towards N<sub>2</sub>. Ag/TiO<sub>2</sub> catalysts have been reported to have the potential of reducing NO<sub>2</sub><sup>-</sup> as well (Zhang et al. 2007). Recent studies showed that Ag-Pt/TiO<sub>2</sub> is highly efficient in the photo-conversion of CO<sub>2</sub> to CH<sub>4</sub> (Mankidy et al. 2013). To the best of our knowledge, there is no study dealing with the photocatalytic reduction of NO<sub>3</sub><sup>-</sup> with this type of catalyst (Ag-Pt/TiO<sub>2</sub> P25). Nevertheless, it is noteworthy that Pt-Ag/AC or Pt-Ag/Al<sub>2</sub>O<sub>3</sub> catalysts have been reported in our groups for the non photocatalytic NO<sub>3</sub><sup>-</sup> reduction

under H<sub>2</sub> (Aristizábal et al. 2012, 2014), obtaining high nitrate conversion (ca. 90 %) but toxic-side products (nitrite and ammonium) for potable water .

#### 1.3.2.4 Optical properties

The optical properties of the noble metals is originated from the Localized Surface Plasmon Resonance (LSPR) (Figure 1.7). In such metal, a resonant collective excitation of the surface conduction band electrons at the interface is stimulated by the incidence of the light, which is produced when interacting with the electromagnetic field between a positive small and negative real imaginary dielectric constant that is capable of supporting a SPR. Then, a strong band absorption occurs in some part of the electromagnetic spectrum (plasmon resonance wavelength). If the metal is located in the oscillating field of the light irradiation, the electron cloud oscillates. Depending on the size, composition and shape of the metal NPs, the absorption range can be tuned to the desired region of the spectrum. In the bimetallic photocatalysts, it also depends on the metal precursor and metal dispersion (Willets et al. 2007; Zaleska-Medynska et al. 2016).

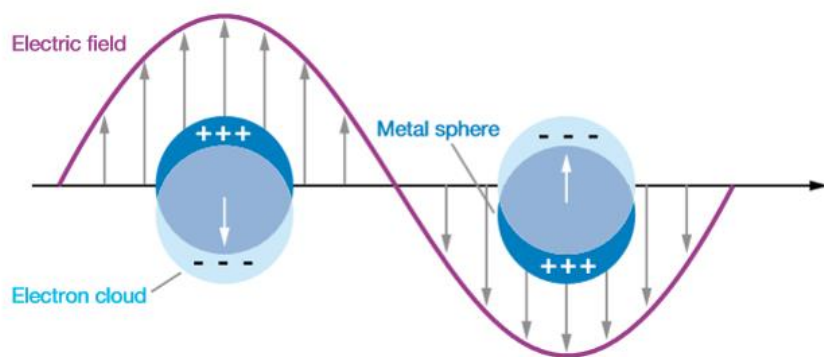


Figure 1.7. Diagram of Localized Surface Plasmon Resonance in metal sphere  
(Willets et al. 2007)

#### 1.3.2.5 Reducing agent and hole scavenger

Hydrogen gas flow is commonly used in non-photocatalytic nitrate reduction like reducing agent. For the photocatalytic reaction, most of the studies are done adding a reducing agent called hole scavenger, which is oxidized by the hole created on the photocatalyst with the purpose of increasing the electron-hole separation, induces pH solution modification to avoid by-products (NH<sub>4</sub><sup>+</sup>) and produces reducing radicals in order to increase the hydrogen evolution rate. Various hole scavengers have been used in the photocatalytic nitrate reduction, such as formic acid (Zhang et al. 2005; Sá et al. 2009; Luiz et al. 2012; Doudrick et al. 2013; Yang et

al. 2013), oxalic acid (Sowmya et al. 2014), benzene (Li et al. 2010), sodium oxalate (Jin et al. 2004; Gekko et al. 2012), acetic acid (Sá et al. 2009), sodium formate (Sá et al. 2009), ethanol (Ranjit et al. 1995), and humic acid (Bems et al. 1999). These hole scavengers have different efficiencies due to the modification of the surface charge of the catalyst and, after dissociation, to the presence of anions competing with  $\text{NO}_3^-$  for adsorption (Zhang et al. 2007; Sá et al. 2009; Barrabés et al. 2011). Their main drawbacks to achieve the requirements for drinking water are the too low pH and the toxic remnant amounts in solution (i.e. formates) (Sá et al. 2009; Doudrick et al. 2013). Formic acid ( $\text{HCOOH}$ ) is the most used because it is effective in terms of nitrate conversion and selectivity towards nitrogen (Bems et al. 1999; Mori et al. 1999; Zhang et al. 2005). Formic acid is directly decomposed into  $\text{H}_2$  and  $\text{CO}_2$  species in presence of a noble metal, which is attractive because  $\text{H}_2$  is a well-known reductant and can be used without hole scavenger as well, leading to higher nitrate reaction rate than formic acid (Sá et al. 2009). Nevertheless, residual formic acid creates problem in drinking water and also can be a carbon nutrient for biofilm growth in water systems (high operational costs) (Doudrick et al. 2013). Besides, the exact role of formic acid as hole scavenger or  $\text{H}_2$  provider is still unknown nowadays with the important drawback of ammonium formation (Wehbe et al. 2009). Perissinoti et al. demonstrated by electron paramagnetic resonance technique (EPR) that no  $\text{H}^\cdot$  was present in the photocatalytic oxidation of formate over  $\text{TiO}_2$  (only the radical  $\text{CO}_2^\cdot-$ ) (Perissinotti et al. 2001), then  $\text{H}^\cdot/\text{H}_2$  is more likely to take place over a hydrogenation co-catalyst as Pd or Pt (Wehbe et al. 2009; Li et al. 2010)

Some studies have been performed with hydrogen gas flow in absence of hole scavenger (Ranjit et al. 1995; Ranjit et al. 1997; Kato et al. 2002). Interestingly, Kato et al. have reported that the photogenerated electrons reduced the nitrate to nitrite ions, and the holes oxidized ammonia to nitrogen over tantalate photocatalysts (Kato et al. 2002). Ranjit et al. have suggested that water can be photodecomposed at slow rate through the photogenerated hole towards  $\text{H}^+ + \frac{1}{2}\text{O}_2$  on the titania producing evolved hydrogen (Figure 1.8) (Ranjit et al. 1995). Lee et al. have also reported a possible photodecomposition of water [ $\text{H}_2\text{O} \rightarrow 2\text{H}^+ + \text{OH}^-$ ;  $2\text{e}^- + \text{H}^+ \rightarrow \text{H}_2$ ;  $2\text{h}^+ + \text{OH}^- \rightarrow 2\text{OH}^-$ ] (Lee et al. 2001). Theoretically,  $\text{TiO}_2$  is thermodynamically able to produce oxygen using water as hole scavenger. Wehbe et al. have performed tests with  $\text{H}_2$  (g) alone and/or in presence of formic acid acting as reductant under catalytic nitrate reduction conditions and/or formic acid as hole scavenger in photocatalytic process using Pd-Cu/ $\text{TiO}_2$  catalysts (Wehbe et al. 2009). They obtained the highest nitrate conversions in dark conditions (no UV, catalytic) applying only  $\text{H}_2$ , and under UV irradiation with the  $\text{H}_2+\text{HCOOH}$  mixture, although higher

ammonium formation than only using H<sub>2</sub> both in presence and absence of UV was observed. It is noteworthy that the reaction was less efficient when using only HCOOH. In general, the reaction was more selective under photocatalytic conditions. Soares et al. demonstrated that without UV irradiation only using H<sub>2</sub> the activity increased by 7% compared to use the mixture of H<sub>2</sub> + CO<sub>2</sub>. Under UV irradiation, the use of H<sub>2</sub> when adding also hole scavenger (formic acid, oxalic acid, ethanol, methanol and humic acid) was essential for the reduction, leading to more electrons availability on the metal NPs, due to photoexcitation of titania. No nitrate conversion was observed without H<sub>2</sub> and the reduction rate was higher under non-photocatalytic than photocatalytic conditions (Soares et al. 2014).

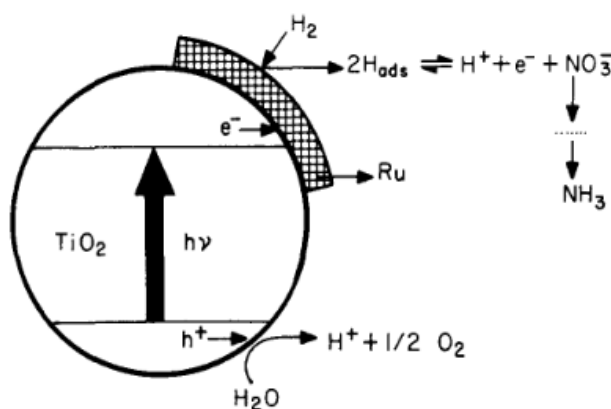


Figure 1.8. Possible photocatalytic nitrate and nitrite reduction to ammonia over Ru/TiO<sub>2</sub> and photooxidation of water (production of H<sup>+</sup> radicals) (Ranjit et al. 1995)

We have performed our studies in absence and presence of H<sub>2</sub> gas flow acting as reductant and without the addition of an organic hole scavenger. Comparison of catalytic and photocatalytic nitrate reduction using Pt and/or Ag supported on Aeroxide TiO<sub>2</sub> P25 support have been achieved. We have also carried out catalytic denitration tests under hydrogen using the bimetallic Pd<sub>2</sub>Sn pair supported on TiO<sub>2</sub> P25, with the aim to establish the influence of their morphology - spherical nanoparticles (NPs) or nanorods (NRs)). This last work has been done in collaboration with the Catalonia Institute for Energy Research (IREC, Barcelona), Institut de Ciència de Materials de Barcelona (ICMAB, Barcelona), Institut Català de Nanociència i Nanotecnologia (ICN2, Barcelona) and Institució Catalana de Recerca i Estudis Avançats (ICREA, Barcelona) (*Chapter 5, article published*).

Despite all the studies done over these years, the mechanisms are still not fully understood and are controversial in the literature. The most generally accepted mechanisms are shown in the next section.

## 1.4 Mechanisms

Hörold et al. reported a general mechanism for catalytic nitrate and nitrite reduction with any heterogeneous hydrogenation catalysts (Figure 1.9) (Hörold et al. 1993). They stated that nitrite could be reduced by various catalysts, however a second metal is needed to activate the catalyst for the nitrate reduction, then a bimetallic catalyst must be used. Nitrate is reduced to the intermediate nitrite and subsequently reduced to the desired non-toxic nitrogen gas or to the non-desired ammonium by-product if the reaction is over-hydrogenated, mostly depending on the second metal added. While the reduction takes place, the metallic sites are oxidized. The formation of ammonium only requires one N-species, nevertheless usually is formed by the meeting of H<sub>2</sub> and N-species on the active sites by a diffusion effect. It has been suggested that the higher the ratio between the Hydrogen and Nitrogen species involved in the coverage of the surface the higher the N<sub>2</sub> selectivity. The selectivity to N<sub>2</sub> is also dependent of the pH of the solution and of the temperature (Tacke et al. 1993; Prüssé et al. 2001).

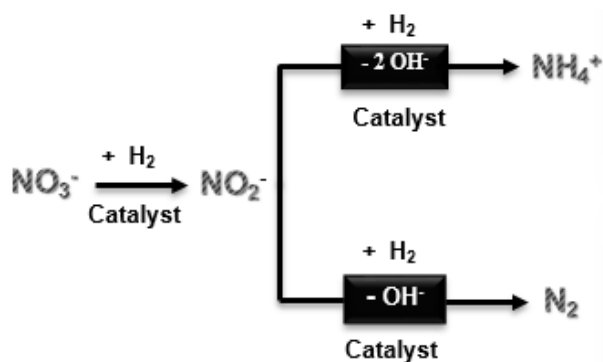


Figure 1.9. General mechanism of nitrate and nitrite reduction by catalyzed hydrogenation  
(Hörold et al. 1993)

The studies of the mechanism have been performed with the Pd-Cu bimetallic pair (Eq. 1.1 (Pd-Cu), Eq. 1.2 and 1.3 (Pd)) (Hörold et al. 1993). Different pathways for nitrogen and ammonium formation have been suggested taking into account the intermediate NO adsorbed ( $\text{NO}_{\text{ads}}$ ) species, as reported by Prüssé et al. using Pd-Me pair over Al<sub>2</sub>O<sub>3</sub> (Figure 1.10), with the possible

release of harmful  $\text{NO}_x$  and  $\text{N}_2\text{O}$  gases intermediates (Prüsse et al. 2000). For the nitrate reduction, an efficient noble metal must be able to dissociate the  $\text{H}_2$  adsorbed on its surface (monoatomic  $\text{H}_{\text{ads}}$ ) (i.e. Pd, Pt) likely on individual particles and not on bimetallic ones, i.e. Pd-Cu. The monoatomic  $\text{H}_{\text{ads}}$  are able to reduce the bimetallic sites by hydrogen spillover between metals (Pd and Cu) and bimetallic ensembles (Pd-Cu) (Leon et al. 1991; Warna et al. 1994; Ilinitch et al. 2000; Prüsse et al. 2000; Prüsse et al. 2001; Barrabés et al. 2006). It is assumed that the reduction of nitrate to nitrite takes place on the bimetallic sites, and afterwards nitrite is reduced to nitrogen. However, there is controversy in the literature about the active sites where the nitrite reduction occurs and which is the first N-intermediate formed (Pintar et al. 1996; Prüsse et al. 2001). To maintain the electroneutrality of the aqueous phase, the converted nitrate ions are replaced by hydroxide ions (Hörold et al. 1993).

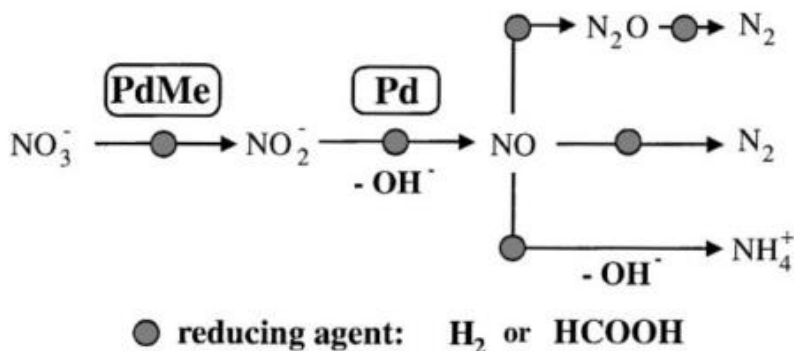
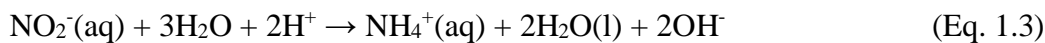
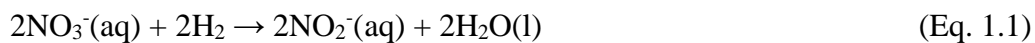
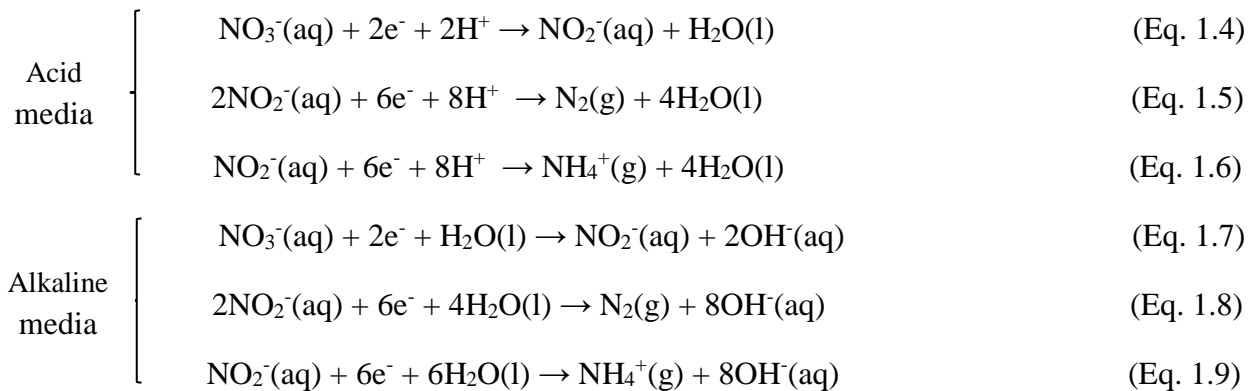
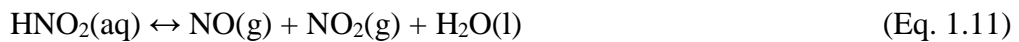
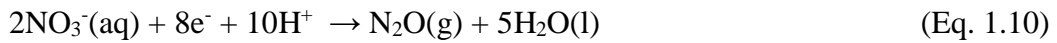


Figure 1.10. Catalytic nitrate and nitrite reduction using Pd-Me (Me: Cu, Sn, In)/ $\text{Al}_2\text{O}_3$  catalysts (Prüsse et al. 2000)

General photocatalytic nitrate and nitrite reductions are shown in Equations 1.4 to 1.9. They show consecutive and parallel reduction reactions, where nitrate is reduced towards nitrite intermediate compound (Eq. 1.4 and 1.7), and it is converted to nitrogen (Eq. 1.5 and 1.8) or into ammonium (Eq. 1.6 and 1.9).



It could be also obtained  $\text{HNO}_2$ ,  $\text{NO}$  and  $\text{N}_2\text{O}$  non-desired products (Eq. 1.10 and 1.11) (Parkt et al. 1988).



Figures 1.11, 1.12 and 1.13 display the possible catalytic and photocatalytic reaction schemes based on the generally accepted reaction mechanism for Pd-Cu pair and on several reports in literature regarding Pt, Pd (noble metal) and Ag, Sn (promoter) bimetallic pairs. Nitrate species are reduced to nitrite by a redox process involving the noble metal and the promoter, while the nitrite species can only be reduced to nitrogen or ammonium on noble metal sites (Epron et al. 2001). The hydrogen chemisorbed on noble metal allows to maintain the promoter in a metallic state. Soares et al. reported that the nitrate and nitrite ions adsorbed on the Pd-Cu metals could be reduced by the photogenerated electrons trapped on the metal NPs, and that the electrons are able to be transferred from Pd to oxidized Cu attributed to higher Fermi level. Then, the ammonium formation would be unfavored. They also concluded that the ammonium formation only occurs from the hydrogen adsorbed on the noble metal sites (Pd) (Soares et al. 2014).

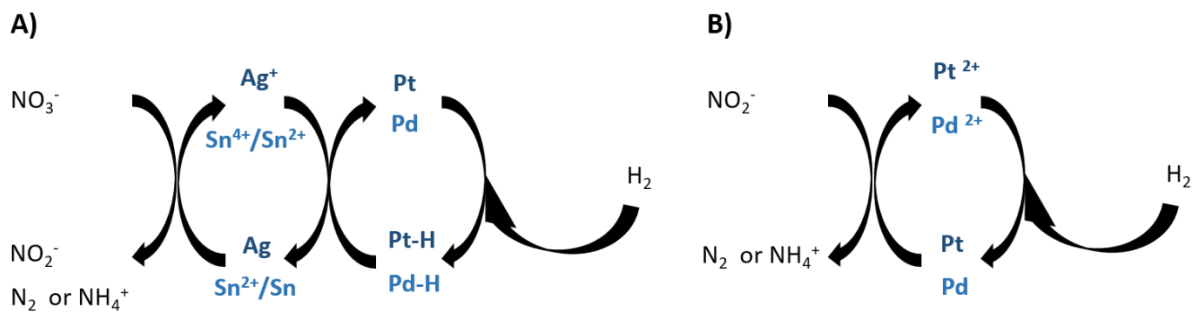


Figure 1.11. Schemes of : A) Mechanism for Ag-Pt and Pd-Sn pairs in catalytic nitrate reduction through hydrogenation, B) Additional step for the nitrite reduction  
(modified from Barrabés et al. 2006)

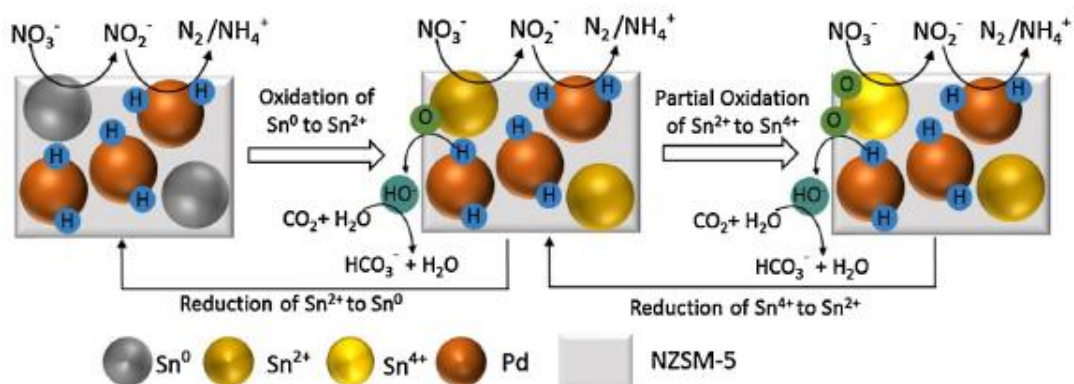


Figure 1.12. Nitrate removal mechanism on Pd-Sn/NZSM-5 catalyst (Hamid et al. 2016)

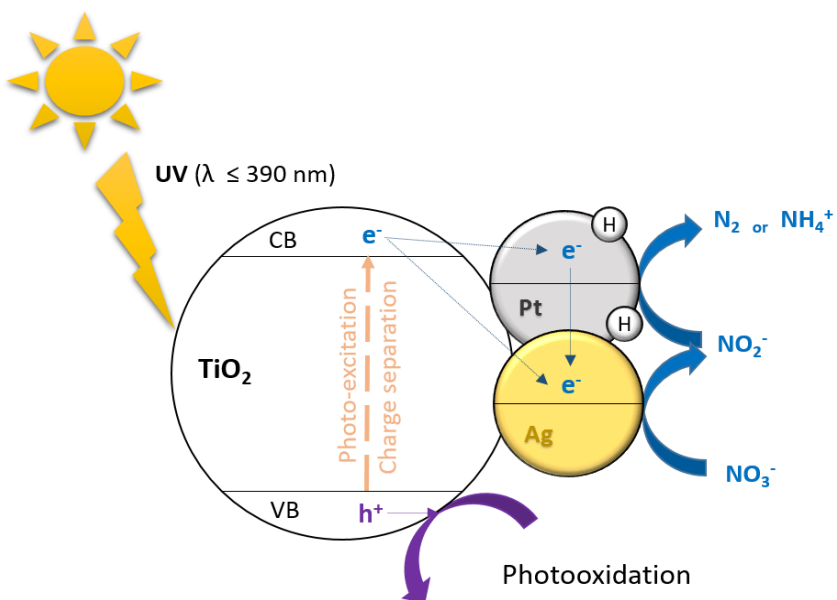


Figure 1.13. Scheme of photocatalytic nitrate reduction using Ag-Pt/TiO<sub>2</sub> nanocatalyst  
(modified from Soares et al. 2014)

It has to be taken into account that the active sites of a catalyst differ from those of a photocatalyst. The active sites from a catalyst refer to those where the substrates are transformed into a desired or undesired product. In a photocatalyst, the active sites are referring to those which after irradiation of the metals by the light are able to adsorb it. The activity from a catalytic and a photocatalytic process can be taken as the estimated reaction rate per active site, and could be compared (Figure 1.14) (Pichat PhD thesis 2013).

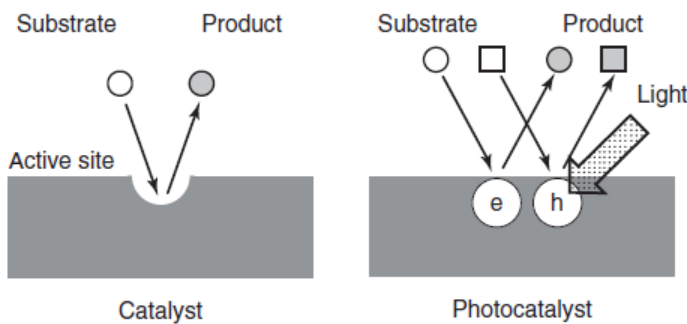


Figure 1.14. Diagram of simple catalyst and photocatalyst process (Pichat PhD thesis 2013)

## 1.5 Catalyst design

Several studies have been focused on the study of various catalyst design parameters, as they are key factors of the catalytic/photocatalytic activity and selectivity towards N<sub>2</sub>. Important parameters regarding a catalyst are on the one hand those related to the synthesis conditions like:

- The nature of the support (Gao et al. 2003; Theologides et al. 2011), the metal loading (Ohtani et al. 1997; Deganello et al. 2000; Yoshinaga 2002; Pulido Melián et al. 2012; Mankidy et al. 2013),
- The nature of the metal precursor(s) (El-Biyyadh et al. 1989; Scardi et al. 1993; Iida et al. 2006; Kanda et al. 2009; Christodoulakis et al. 2009; Aristizábal et al. 2011; Chattopadhyay et al. 2016),
- The impregnation order of the precursors in the case of bimetallic catalysts (Batista et al. 1997; Aristizábal et al. 2014),
- The pH of the solution (Ohtani et al. 1987; Doudrick et al. 2013),

- The synthesis route (photodeposition, wetness impregnation, chemical reduction, sol-gel method) (Prüsse et al. 2000; Wang et al. 2005; Zhang et al. 2007; Behnajady et al. 2007; Abou El-Nour et al. 2010; Han et al. 2012; Kobwittaya et al. 2014).

And on the other hand, those related to the activation conditions (calcination temperature, reducing agent) (Yu et al. 2003; Tang et al. 2004; Mulfinger et al. 2007). Besides, structural and textural parameters such as particle size (Mafune et al. 2000; Zielińska et al. 2009; Wang et al. 2016) and morphology (Luo et al. 2015; Zaleska-Medynska et al. 2016) are also very relevant. The selectivity to N<sub>2</sub> could be also affected by diffusion limitations in the catalytic systems (Warna et al. 1994; Ilinitch et al. 2000).

In the present work we have studied the influence of: the metal(s) loading (Ag: from 0.5 to 4 wt. %; Pt: 2 and 4 wt. %) supported on TiO<sub>2</sub> P25; the nature of the platinum precursor (H<sub>2</sub>PtCl<sub>6</sub>·6 H<sub>2</sub>O or K<sub>2</sub>PtCl<sub>6</sub>); the impregnation order of the metals in the case of the bimetallic Ag-Pt samples (Ag-Pt, Pt-Ag); and the particles morphology in the case of the bimetallic Pd-Sn samples (Pd<sub>2</sub>Sn/P25 spherical NPs and NRs), on the nitrate conversion and reduction rate, the selectivity and the yield of products.

### **1.5.1 Metal loading**

The amount of doping ion is one of the crucial parameters when designing a catalyst. It is necessary to define the optimum amount leading to high activity and selectivity, being a cost-effective process. The metal loading strongly affects the metal dispersion and particle size (Ohtani et al. 1997; Pulido Melián et al. 2012). Based on previous studies reported in literature on catalytic and photocatalytic nitrate reduction, silver loading from 0.5 - 4 wt. % and platinum loading of 2 and 4 wt. % have been chosen.

Indeed, metal-supported samples with loadings in a range of 0.1 - 4 wt.% for Ag (Zhang et al. 2005; Sá et al. 2009; Aristizábal et al. 2012; Doudrick et al. 2013; Parastar et al. 2013) and 1 - 5 wt. % for Pt (Li et al. 2010; Aristizábal et al. 2010, 2012) have been reported. Doudrick et al. (0.5 - 5 wt. % Ag/TiO<sub>2</sub>) reported higher nitrite and ammonium formation when increasing the Ag loading, however with lower nitrate reduction rate (optimum Ag at 1 wt. %) (Doudrick et al. 2013).

Furthermore, the increasing of the amount of metals, such as silver, increases the visible absorbance capacity of the photocatalysts (Krejcikova et al. 2012). Metals should be close to

the surface of the photocatalyst for a better charge transfer. Higher metal loading provides more active sites for nitrate reduction, although excessive doping ions will cover and occupy more active sites on the surface of the titania decreasing the activity, N<sub>2</sub> selectivity and photoinduced efficiency. It has to be taken into consideration also that big particles will enrich more electrons and become new recombination centers of photogenerated electron-holes, as well as the formation of clusters leading to inefficient electrons storage may occur (Zhang et al. 2007; Li et al. 2010; Takai et al. 2011; Luiz et al. 2012).

Moreover, a good balance between the metal amounts deposited in the bimetallic pair has to be found. For instance, Li et al. have concluded that in the 5 % Pt-(0.83 - 2.5 wt. %)Cu/TiO<sub>2</sub> catalysts the nitrate reduction to nitrite enhances when the Cu content is increased, whereas this increase is detrimental for nitrogen selectivity (Li et al. 2010). Aristizábal et al. recorded the highest nitrate conversion at 1.5 wt. % Ag and 3 wt. % Pt over AC but with high ammonium yield (ca. 80 %), then leading to a poor N<sub>2</sub> selectivity (ca. 10 - 25 %) (Aristizábal et al. 2012).

The metal loading for the spherical nanoparticles (NPS) and nanorods (NRs) fully synthesized by the IREC group was fixed at 5 wt. % Pd<sub>2</sub>Sn supported on TiO<sub>2</sub> P25 (*Chapter 5*). This bimetallic pair has been reported at a range of Pd (1 - 5 wt. %) and Sn (0.6 - 3.4 %) (Yoshinaga 2002; Barbosa et al. 2013; Hamid et al. 2016).

### **1.5.2 Platinum precursor**

Another main parameter to take into account is the nature of the precursor, as it directly influences the surface metal chemistry and dispersion over the support, thus having strong impact on the activity and selectivity (Hörold et al. 1993; Yoshinaga 2002). The influence of different Pt precursors has been studied in nitrate removal. The Pt nanoparticles are normally prepared from water-soluble metal salts, like H<sub>2</sub>PtCl<sub>6</sub>, K<sub>2</sub>PtCl<sub>6</sub>, K<sub>2</sub>PtCl<sub>4</sub>, PtCl<sub>2</sub>, Pt(NH<sub>3</sub>)<sub>4</sub>(NO<sub>3</sub>)<sub>2</sub>, Pt(NH<sub>3</sub>)<sub>4</sub>Cl<sub>2</sub>, Pt(NH<sub>3</sub>)<sub>4</sub>(OH)<sub>2</sub>, and Pt(AcAc)<sub>2</sub> (Scardi et al. 1993; Qi et al. 1998; Bönnemann et al. 2002; Gauthard et al. 2003; Chen et al. 2004; Iida et al. 2006; Marie et al. 2007; Aristizábal et al. 2012). The most common Pt precursor used in the case of catalysts for nitrate removal is the H<sub>2</sub>PtCl<sub>6</sub> (chloroplatinic acid), giving rise to high selectivity towards nitrogen (Barrabés et al. 2006).

Comparing Pt precursors, Aristizábal et al. reported higher metal dispersion and selectivity using H<sub>2</sub>PtCl<sub>6</sub> than Pt(NH<sub>3</sub>)<sub>4</sub>(NO<sub>3</sub>)<sub>2</sub>, but also higher selectivity to harmful nitrogen species (Aristizábal et al. 2012). Other differences in the properties of catalysts synthesized with both

precursors were observed (particle size, metals dispersion) (Aristizábal et al. 2014). Therefore, several properties depending on the precursor used influence the production of toxic side-products, and more research is still needed to determine its role.  $K_2PtCl_6$  (potassium hexachloroplatinate) is a Pt precursor normally used in electrocatalysis assigned to a slight solubility in cold water unlike most Pt salts, then is suitable for the electrochemically-mediated Pt NPs preparation (Kim et al. 2013). El-Biyyadah et al. introduced for the first time the  $K_2PtCl_6$  precursor in the impregnation instead of conventional  $H_2PtCl_6$  in the catalyst synthesis (El-Biyyadah et al. 1989). Despite of being used in many other studies, i.e. water gas-shift (Iida et al. 2006), selective tetrahedral nanocrystals preparation (Yu et al. 2003), and Pt-doped  $TiO_2$  pillared clay to enhance photocatalytic degradation of Methyl Orange dye (Ding et al. 2008), to the best of our knowledge,  $K_2PtCl_6$  has not been used in the catalyst synthesis impregnation for nitrate and nitrite abatement in drinking water.

The comparison of the performance of catalysts impregnated with  $H_2PtCl_6 \cdot 6H_2O$  and  $K_2PtCl_6$  have been already carried out in few studies (Scardi et al. 1993; Kanda et al. 2009), but not for catalytic nitrate removal application. Thus, we have synthesized and performed comparative studies using these two platinum precursors in the nitrate removal towards nitrogen gas (*Chapter 3 and 4*).

### **1.5.3 Impregnation protocol**

The impregnation protocol is very important in the preparation of bimetallic catalysts performed either by impregnating the two metal precursors simultaneously or successively onto the support. For example when the promoter precursor (i.e. Ag, Cu) is impregnated over the monometallic catalyst (i.e. Pd, Pt) it is randomly located on the support or over the noble metal. Previous studies have suggested that the two metals have to be in close contact in order to obtain high catalytic activities in denitration reaction. The intimate contact between the two metals instead of the formation of an alloy favors the nitrate conversion. Nevertheless, there is controversy in literature whether alloy or close contact between the NPs is favorable to enhance the conversion towards nitrogen (Epron et al. 2001; Gauthard et al. 2003; Sá et al. 2005; Aristizábal et al. 2011).

The addition order of the two Pt precursors has been varied in our research to determine its influence on physical-chemical properties and activities of the catalysts. Aristizábal et al. studied for first time the influence of both impregnation orders with the AgPt bimetallic pair in

catalytic nitrate removal. They observe in the case of Pt-Ag order (Pt first and Ag second) higher nitrate conversion, higher Pt contact with Ag, and larger particles sizes (same Pt precursor), although higher ammonium formation and lower reducibility than in the case of the Ag-Pt order (Aristizábal et al. 2014).

#### **1.5.4 Morphology**

The shape and size of the nanoparticles influences the exposed surface facets and the active sites thus acting on the catalytic performance. The control of the nanoparticles geometry is very limited with the conventional impregnation protocols. New synthetic routes of Pd-based bimetallic nanoparticles have been developed to by-pass this problem (Wang et al. 2010; Yang et al. 2011; Gao et al. 2013), especially in the case of Pd-Sn bimetallic pair studied for water catalytic denitrification (Garron et al. 2005; Dodouche et al. 2009; Devadas et al. 2011; Barbosa et al. 2013). In the present work, we show a synthetic route to obtain highly dispersed Pd<sub>2</sub>Sn spherical nanoparticles and nanorods with tuned size and morphology done by the IREC group. The aim was to evaluate the influence of these morphology parameters in the water denitrification reaction (*Chapter 5, article published*).

### **1.6 Objectives and scope of the research**

One of the most pervasive problems affecting people throughout the world is an inadequate access to clean freshwater and sanitation. The global drinking water demand is increasing, therefore regulations on drinking water quality become stricter. Concretely, high nitrate consumption in drinking water has a high impact in human health. Among various nitrate abatement technologies, heterogeneous catalytic and photocatalytic nitrate removal by hydrogenation are well-known ecofriendly and cost-efficient technologies. However, the formation of products even more toxic than nitrate (nitrite and ammonia) are still a major challenge for large-scale industrial application.

Several researches have been done on catalytic nitrate abatement trough hydrogenation in the frame of our Spanish-French collaboration groups with the aim of improving this process. The main scope of this thesis was to develop a catalyst and/or photocatalyst able to accomplish the European Legislation applied on nitrate, nitrite and ammonium ions concentrations in drinking

water. Based on our wide knowledge, this led us to investigate a system associating the monometallic Ag/P25 and Pt/P25 catalysts and also bimetallic Ag-Pt(Pt-Ag)/P25 catalysts under catalytic and photocatalytic conditions performed in a batch reactor (*Chapters 3 and 4*). The aim was thus to evaluate the versatile character of these types of catalysts in order to conceive highly adaptable denitration processes. Besides, the Pd-Sn/P25 spherical nanoparticles and nanorods prepared in collaboration were also tested under catalytic water denitration in order to determine the influence of the morphology of the catalyst (*Chapter 5*).

The specific objectives of the thesis were:

1) The optimization of the catalyst design parameters, which includes:

- To study the effect of silver (0.5 - 4 wt. %.) and platinum loadings (2 and 4 wt. %) impregnated onto TiO<sub>2</sub> P25 support on the activity and selectivity in the catalytic and photocatalytic nitrate reduction.
- To investigate the effect of the Pt precursor used (H<sub>2</sub>PtCl<sub>6</sub>·6H<sub>2</sub>O and K<sub>2</sub>PtCl<sub>6</sub>) on the photocatalytic activity.
- To determine the incidence of the impregnation order of both noble metals (Ag, Pt) in the bimetallic pair (Ag-Pt and Pt-Ag) on the catalytic and photocatalytic nitrate removal.
- To determine the influence of the morphology (spherical NPs or Nanorods) of the 5 wt. % Pd<sub>2</sub>Sn/P25 catalysts on the denitration activity.

2) The optimization of the experimental conditions (T = 25 °C, P = 1 atm, t<sub>reaction</sub> = 6 h):

- To choose the proper nitrate source affecting the initial pH solution (NaNO<sub>3</sub> or HNO<sub>3</sub>) in terms of nitrate conversion, selectivity towards N<sub>2</sub> and final pH.
- To study the influence of the absence or presence of hydrogen as reducing agent.
- The influence of the ultraviolet irradiation wavelength ( $\lambda$  = 254 nm or 365 nm) implementation on the photocatalytic activity and selectivity to N<sub>2</sub>.

- 3) A comparison of the performances of the physical mixture of Ag and Pt monometallic catalysts and of the bimetallic catalysts in the catalytic and photocatalytic nitrate and nitrite abatements.
- 4) To study the ability of the catalysts to perform both catalytic and photocatalytic denitration process.
- 5) To explain the catalytic and photocatalytic performances based on the physicochemical properties obtained by various characterization techniques: XRD, N<sub>2</sub>-physisorption, TEM, DRUV-Vis, XPS, H<sub>2</sub>-TPR and H<sub>2</sub>-Chemisorption.

## **1.7 References**

[http://europa.eu/rapid/press-release\\_IP-96-1217\\_en.htm](http://europa.eu/rapid/press-release_IP-96-1217_en.htm) (22/10/2015)

- Abou, E.N., M.M. Kholoud, A. Eftaiha, A. Al-Warthan, and R. A. A. Ammar. 2010. “Synthesis and Applications of Silver Nanoparticles.” *Arabian Journal of Chemistry* 3(3):135–40.
- Ahmed, S., M. G. Rasul, W. N. Martens, R. Brown, and M. A. Hashib. 2010. “Heterogeneous Photocatalytic Degradation of Phenols in Wastewater: A Review on Current Status and Developments.” *Desalination* 261(1–2):3–18.
- Anderson, J. A. 2011. “Photocatalytic Nitrate Reduction over Au/TiO<sub>2</sub>.” *Catalysis Today* 175(1):316–21.
- Aristizábal, A., N. Barrabés., S. Contreras, M. Kolafa, D. Tichit, F. Medina, and J. Sueiras. 2010. “Pt/CuZnAl Mixed Oxides for the Catalytic Reduction of Nitrates in Water: Study of the Incidence of the Cu/Zn Atomic Ratio.” *Physics Procedia* 8:44–48.
- Aristizábal, A., S. Contreras, N. Barrabés, D. Tichit, F Medina. 2011. “Catalytic Reduction of Nitrates in Water on Pt Promoted Cu Hydrotalcite-Derived Catalysts: Effect of the Pt-Cu Alloy Formation.” *Applied Catalysis B: Environmental* 110:58–70.
- Aristizábal, A., S. Contreras, N. J. Divins, J. Llorca, and F. Medina. 2012. “Pt-Ag/activated Carbon Catalysts for Water Denitration in a Continuous Reactor: Incidence of the Metal Loading, Pt/Ag Atomic Ratio and Pt Metal Precursor.” *Applied Catalysis B: Environmental* 127:351–62.
- Aristizábal, A., S. Contreras, N. J. Divins, J. Llorca, and F. Medina. 2014. “Effect of Impregnation Protocol in the Metallic Sites of Pt-Ag/activated Carbon Catalysts for Water Denitration.” *Applied Surface Science* 298:75–89.
- Asahi, R., T. Mikawa, T. Ohwaki, K. Aoki, and Y. Taga. 2001. “Visible Light Photocatalysis in Nitrogen-Doped Titanium Oxides.” *Science* 293(July):269–71.
- Barbosa, D. P., P. Tchiéta, M. Do Carmo Rangel, and F. Epron. 2013. “The Use of a Cation Exchange Resin for Palladium-Tin and Palladium-Indium Catalysts for Nitrate Removal in Water.” *Journal of Molecular Catalysis A: Chemical* 366:294–302.
- Barrabés, N., J. Just, A. Dafinov, F. Medina, F. L. G. Fierro, JE. Sueiras, P. Salagre, and Y. Cesteros. 2006. “Catalytic Reduction of Nitrate on Pt-Cu and Pd-Cu on Active Carbon Using Continuous Reactor: The Effect of Copper Nanoparticles.” *Applied Catalysis B: Environmental* 62(1–2):77–85.
- Barrabés, N., and J. Sá. 2011. “Catalytic Nitrate Removal from Water, Past, Present and Future Perspectives.” *Applied Catalysis B: Environmental* 104:1–5.

- Batista, J., A. Pintar, and M. Ceh. 1997. "Characterization of Supported Pd-Cu Bimetallic Catalysts by SEM, EDXS, AES and Catalytic Selectivity Measurements." *Catalysis Letters* 43(1–2):79–84.
- Behnajady, M. A., N. Modirshahla, N. Daneshvar, and M. Rabbani. 2007. "Photocatalytic Degradation of an Azo Dye in a Tubular Continuous-Flow Photoreactor with Immobilized TiO<sub>2</sub> on Glass Plates." *Chemical Engineering Journal* 127(1–3):167–76.
- Behnajady M.A., N. Modirshahla, M. Shokri, and B. Rad. 2008. "Enhancement of Photocatalytic Activity of TiO<sub>2</sub> Nanoparticles by Silver Doping: Photodeposition versus Liquid Impregnation Methods." *Global Nest Journal* 10(1):1–7.
- Bems, B., F. C. Jentoft, and R. Schlögl. 1999. "Photoinduced Decomposition of Nitrate in Drinking Water in the Presence of Titania and Humic Acids." *Applied Catalysis B: Environmental* 20(2):155–63.
- Bönnemann, H., N. Waldöfner, H. G. Haubold, and T. Vad. 2002. "Preparation and Characterization of Three-Dimensional\nPt Nanoparticle Networks." *Chem. Mater.* 14(3):1115–20.
- Carey, J.H., J. Lawrence, and H.M. Tosine. 1976. *Bulletin of Environmental Contamination and Toxicology*, 16(6), 697-701 (1976).
- Centi, G., and S. Perathoner. 2015. "Remediation of Water Contamination Using Catalytic Technologies Remediation of Water Contamination Using Catalytic Technologies." 41(MARCH 2003):15–29.
- Chattopadhyay, J., T. S. Pathak, D. Pak, and R. Srivastava. 2016. "Metal Hollow Sphere Electrocatalysts." *Korean Journal of Chemical Engineering* 33(5):1514–29.
- Chen, J., T. Herricks, M. Geissler, and Y. Xia. 2004. "Single-Crystal Nanowires of Platinum Van Be Dynthesized by Vontrolling the Reaction Rate of a Polyol Process." *Journal of the American Chemical Society* 126(35):10854–55.
- Chen, Y. X., Y. Zhang, and G. H. Chen. 2003. "Appropriate Conditions or Maximizing Catalytic Reduction Efficiency of Nitrate into Nitrogen Gas in Groundwater." *Water Research* 37(10):2489–95.
- Cheng, B., Y. Le, and J. Yu. 2010. "Preparation and Enhanced Photocatalytic Activity of Ag@TiO<sub>2</sub> Core-Shell Nanocomposite Nanowires." *Journal of Hazardous Materials* 177(1–3):971–77.
- Chong, M. N., B. Jin, C. W. K. Chow, and C. Saint. 2010. "Recent Developments in Photocatalytic Water Treatment Technology: A Review." *Water Research* 44(10):2997–3027.

- Christodoulakis, K. E., D. Palioura, S. H. Anastasiadis, and M. Vamvakaki. 2009. "Metal Nanocrystals Embedded within Polymeric Nanostructures: Effect of Polymer-Metal Compound Interactions." *Topics in Catalysis* 52(4):394–411.
- Coleman, H. M., K. Chiang, and R. Amal. 2005. "Effects of Ag and Pt on Photocatalytic Degradation of Endocrine Disrupting Chemicals in Water." *Chemical Engineering Journal* 113(1):65–72.
- Council, T. H. E., O. F. The, and European Union. 1998. "COUNCIL DIRECTIVE 98/83/EC of 3 November 1998 on the Quality of Water Intended for Human Consumption." *Official Journal of the European Communities* L 330:32–54.
- Deganello, F., L. F. Liotta, A. Macaluso, A. M. Venezia, and G. Deganello. 2000. "Catalytic Reduction of Nitrates and Nitrites in Water Solution on Pumice-Supported Pd-Cu Catalysts." *Applied Catalysis B: Environmental* 24(3–4):265–73.
- Devadas, A., S. Vasudevan, and F. Epron. 2011. "Nitrate Reduction in Water: Influence of the Addition of a Second Metal on the Performances of the Pd/CeO<sub>2</sub> Catalyst." *Journal of Hazardous Materials* 185(2–3):1412–17.
- Ding, X., T. An, G. Li, S. Zhang, J. Chen, J. Yuan, H. Zhao, H. Chen, G. Sheng, and J. Fu.. 2008. "Preparation and Characterization of Hydrophobic TiO<sub>2</sub> Pillared Clay: The Effect of Acid Hydrolysis Catalyst and Doped Pt Amount on Photocatalytic Activity." *Journal of Colloid and Interface Science* 320(2):501–7.
- Dodouche, I., D. Pereira Barbosa, M. do Carmo Rangel, and F. Epron. 2009. "Palladium-Tin Catalysts on Conducting Polymers for Nitrate Removal." *Applied Catalysis B: Environmental* 93(1–2):50–55.
- Dong, D., and Z. Lin Wang. 2009. "Fundamental Theory of Transmission Electron Microscopy." Nanoscience Research group. School of Materials Science and Engineering. Georgia Tech College.
- Doudrick, K., T. Yang, K. Hristovski, and P. Westerhoff. 2013. "Photocatalytic Nitrate Reduction in Water: Managing the Hole Scavenger and Reaction by-Product Selectivity." *Applied Catalysis B: Environmental* 136–137:40–47.
- Doudrick, K., O. Monzón, A. Mangonon, K. Hristovski, and P. Westerhoff. 2012. "Nitrate Reduction in Water Using Commercial Titanium Dioxide Photocatalysts (P25, P90, and Hombkat UV100)." (August):852–61.
- Du, W. X., K. E. Mackenzie, D. F. Milano, N.A. Deskins, D. Su, and X. Teng . 2012. "Palladium-Tin Alloyed Catalysts for the Ethanol Oxidation Reaction in an Alkaline Medium." *ACS Catalysis* 2:287–97.
- Duca, M., S. Khamseh, S. C. S. Lai, and Marc T. M. Koper. 2010. "The Influence of Solution-Phase HNO<sub>2</sub> Decomposition on the Electrocatalytic Nitrite Reduction at a Hemin-Pyrolytic Graphite Electrode." *Langmuir* 26(14):12418–24.

- El-Biyyadh, A., M. Guerin, C. Kappenstein, D. Bazin, and H. Dexpert. 1989. "Pt and Ir/Al<sub>2</sub>O<sub>3</sub> Catalysts: Study of the Impregnation Reaction with New Precursors." 158:172–73.
- Epron, F., F. Gauthard, and J. Barbier. 2002. "Influence of Oxidizing and Reducing Treatments on the Metal-Metal Interactions and on the Activity for Nitrate Reduction of a Pt-Cu Bimetallic Catalyst." *Applied Catalysis A: General* 237(1–2):253–61.
- Epron, F., F. Gauthard, C. Pinéda, and J. Barbier. 2001. "Catalytic Reduction of Nitrate and Nitrite on Pt–Cu/Al<sub>2</sub>O<sub>3</sub> Catalysts in Aqueous Solution: Role of the Interaction between Copper and Platinum in the Reaction." *Journal of Catalysis* 198(2):309–18.
- Ergas, S. J., and D. E. Rheinheimer. 2004. "Drinking Water Denitrification Using a Membrane Bioreactor." *Water Research* 38(14–15):3225–32.
- Ersever, I., and V. Ravindran. 2007. "Biological Denitrification of Reverse Osmosis Brine Concentrates: {II.} Fluidized Bed Adsorber Reactor Studies." *Journal of Environmental European Comission. 2010. "On Implementation of Council Directive 91/676/EEC Concerning the Protection of Waters against Pollution Caused by Nitrates from Agricultural Sources Based on Member State Reports for the Period 2004-2007." SEC(2010).*
- European Comission. 2012. "EU Water Legislation. The Nitrates Directive." Cooperation with national judges and prosecutors in the field of EU Environmental Law.
- European Commission. 1991. "Council Directive 91/676/EEC Concerning the Protection of Waters against Pollution Caused by Nitrates from Agricultural Sources." Official Journal of the European Communities L 375(31.12.1991):1–8.
- European Union. 2010a. "Exceedances of Critical Loads for Eutrophication due to the Deposition of Nutrient Nitrogen in 2000 and 2010."
- European Union. 2010b. "The EU Nitrates Directive." 1–4.
- Fanning, J. C. 2000. "The Chemical Reduction of Nitrate in Aqueous Solution." *Coordination Chemistry Reviews* 199(May):159–79.
- Fujishima, A., T. N. Rao, and D. A. Tryk. 2000. "Titanium Dioxide Photocatalysis." *Journal of Photochemistry and Photobiology C: Photochemistry Reviews* 1(1):1–21.
- Fujishima, A., X. Zhang, and D. A. Tryk. 2008. "TiO<sub>2</sub> Photocatalysis and Related Surface Phenomena." *Surface Science Reports* 63(12):515–82.
- Gálvez, J. B., S. Malato Rodríguez, C. A. Estrada Gasca, E. R. Bandala, S. Gelover, and T. Leal. 1985. "Purificación de Aguas Por Fotocatálisis Heterogénea: Estado Del Arte." 1–5.

- Gao, Q., Y. M. Ju, D. An, M. R. Gao, C. H. Cui, J. W. Liu, H. P. Cong, and S. H. Yu. 2013. “Shape-Controlled Synthesis of Monodisperse PdCu Nanocubes and Their Electrocatalytic Properties.” *ChemSusChem* 6(10):1878–82.
- Gao, W., N. Guan, J. Chen, X. Guan, R. Jin, H. Zeng, Z. Liu, and F. Zhang. 2003. “Titania Supported Pd-Cu Bimetallic Catalyst for the Reduction of Nitrate in Drinking Water.” *Applied Catalysis B: Environmental* 46(2):341–51.
- Garron, A., K. Lázár, and F. Epron. 2005. “Effect of the Support on Tin Distribution in Pd-Sn/Al<sub>2</sub>O<sub>3</sub> and Pd-Sn/SiO<sub>2</sub> Catalysts for Application in Water Denitration.” *Applied Catalysis B: Environmental* 59(1–2):57–69.
- Gauthard, F., F. Epron, and J. Barbier. 2003. “Palladium and Platinum-Based Catalysts in the Catalytic Reduction of Nitrate in Water: Effect of Copper, Silver, or Gold Addition.” *Journal of Catalysis* 220(1):182–91.
- Gekko, H., K. Hashimoto, and H. Kominami. 2012. “Photocatalytic Reduction of Nitrite to Dinitrogen in Aqueous Suspensions of Metal-Loaded Titanium(iv) Oxide in the Presence of a Hole Scavenger: An Ensemble Effect of Silver and Palladium Co-Catalysts.” *Physical Chemistry Chemical Physics* 14(22):7965.
- Gomathi Devi, L., and K. M. Reddy. 2010. “Enhanced Photocatalytic Activity of Silver Metallized TiO<sub>2</sub> Particles in the Degradation of an Azo Dye Methyl Orange: Characterization and Activity at Different pH Values.” *Applied Surface Science* 256(10):3116–21.
- Guillette, L. J., and T. M. Edwards. 2005. “Is Nitrate an Ecologically Relevant Endocrine Disruptor in Vertebrates?” *Integrative and comparative biology* 45(1):19–27.
- Hamid, S., M. A. Kumar, and W. Lee. 2016. “Highly Reactive and Selective Sn-Pd Bimetallic Catalyst Supported by Nanocrystalline ZSM-5 for Aqueous Nitrate Reduction.” *Applied Catalysis B: Environmental* 187:37–46.
- Han, Y., J. Zhou, W. Wang, H. Wan, Z. Xu, S. Zheng, and D. Zhu. 2012. “Enhanced Selective Hydrodechlorination of 1,2-Dichloroethane to Ethylene on Pt-Ag/TiO<sub>2</sub> Catalysts Prepared by Sequential Photodeposition.” *Applied Catalysis B: Environmental* 125:172–79.
- Herrmann, J. M. 1999. “Heterogeneous Photocatalysis: Fundamentals and Applications to the Removal of Various Types of Aqueous Pollutants.” *Catalysis Today* 53:115–29.
- Hirayama, J., R. Abe, and Y. Kamiya. 2014. “Combinational Effect of Pt/SrTiO<sub>3</sub>:Rh Photocatalyst and SnPd/Al<sub>2</sub>O<sub>3</sub> Non-Photocatalyst for Photocatalytic Reduction of Nitrate to Nitrogen in Water under Visible Light Irradiation.” *Applied Catalysis B: Environmental* 144(3):721–29.

- Hirayama, J., H. Kondo, Y. K. Miura, R. Abe, and Y. Kamiya. 2012. "Highly Effective Photocatalytic System Comprising Semiconductor Photocatalyst and Supported Bimetallic Non-Photocatalyst for Selective Reduction of Nitrate to Nitrogen in Water." *Catalysis Communications* 20(3):99–102.
- Hörold, S., K. D. Vorlop, T. Tacke, and M. Sell. 1993. "Development of Catalysts for a Selective Nitrate and Nitrite Removal from Drinking Water." *Catalysis Today* 17:21–30.
- Hydroponic. 2016. <http://www.homemadehydroponic.net/visiblelightspectrumplus/>
- Ibhadon, A., and P. Fitzpatrick. 2013. "Heterogeneous Photocatalysis: Recent Advances and Applications." *Catalysts* 3:189–218.
- Iida, H., K. Kondo, and A. Igarashi. 2006. "Effect of Pt Precursors on Catalytic Activity of Pt/TiO<sub>2</sub> (Rutile) for Water Gas Shift Reaction at Low-Temperature." *Catalysis Communications* 7(4):240–44.
- Ilinitch, O. M., L. V. Nosova, V. V. Gorodetskii, V. P. Ivanov, S. N. Trukhan, E. N. Gribov, S. V. Bogdanov and F. P. Cuperus. 2000. "Catalytic Reduction of Nitrate and Nitrite Ions by Hydrogen: Investigation of the Reaction Mechanism over Pd and Pd-Cu Catalysts." *Journal of Molecular Catalysis A: Chemical* 158(1):237–49.
- Jin, R., W. Gao, J. Chen, H. Zeng, F. Zhang, Z. Liu, and N. Guan. 2004. "Photocatalytic Reduction of Nitrate Ion Drinking Water by Using Metal-Loaded MgTiO<sub>3</sub>-TiO<sub>2</sub> Composite Semiconductor Catalyst." *Journal of Photochemistry and Photobiology A: Chemistry* 162(2–3):585–90.
- Jou, L. H., J. K. Chang, T. J. Whang, and I. Wen Sun. 2010. "Electrodeposition of Palladium–Tin Alloys from 1-Ethyl-3-Methylimidazolium Chloride–Tetrafluoroborate Ionic Liquid for Ethanol Electro-Oxidation." *Journal of The Electrochemical Society* 157(8):D443.
- Kamat, P. V. 1993. "Photochemistry on Nonreactive and Reactive (Semiconductor) Surfaces." *Chemical Reviews* 93:267–300.
- Kanda, Y., A. Seino, T. Kobayashi, Y. Uemichi, and M. Sugioka. 2009. "Catalytic Performance of Noble Metals Supported on Mesoporous Silica MCM-41 for Hydrodesulfurization of Benzothiophene." *Journal of the Japan Petroleum Institute* 52(2):42–50.
- Kato, H., and A. Kudo. 2002. "Photocatalytic Reduction of Nitrate Ions over Tantalate Photocatalysts." *Physical Chemistry Chemical Physics* 4(12):2833–38.
- Kim, J., and M. M. Benjamin. 2004. "Modeling a Novel Ion Exchange Process for Arsenic and Nitrate Removal." *Water Research* 38(8):2053–62.
- Kim, K. T., S. H. Jin, S. C. Chang, and D. S. Park. 2013. "Green Synthesis of Platinum Nanoparticles by Electroreduction of a K<sub>2</sub>PtCl<sub>6</sub> Solid-State Precursor and Its Electrocatalytic Effects on H<sub>2</sub>O<sub>2</sub> Reduction." *Bulletin of Korean Chemistry Society* 34(12):2–4.

- Ko, S., C. K. Banerjee, and J. Sankar. 2011. "Photochemical Synthesis and Photocatalytic Activity in Simulated Solar Light of Nanosized Ag Doped TiO<sub>2</sub> Nanoparticle Composite." *Composites Part B: Engineering* 42(3):579–83.
- Kobwittaya, K., and S. Sirivithayapakorn. 2014. "Photocatalytic Reduction of Nitrate over TiO<sub>2</sub> and Ag-Modified TiO<sub>2</sub>." *Journal of Saudi Chemical Society* 18:291–98.
- Kočí, K., S. Krejčíková, O. Šolcová, and L. Obalová. 2012. "Photocatalytic Decomposition of N<sub>2</sub>O on Ag-TiO<sub>2</sub>." *Catalysis Today* 191(1):134–37.
- Kominami, H., T. Nakaseko, Y. Shimada, A. Furusho, H. Inoue, S. Y. Murakami, Y. Kera, and B. Ohtani. 2005. "Selective Photocatalytic Reduction of Nitrate to Nitrogen Molecules in an Aqueous Suspension of Metal-Loaded titanium(IV) Oxide particles". *Chem. Commun.* 2933–35.
- Kowalska, E., Z. Wei, B. Karabiyik, A. Herissan, M. Janczarek, M. Endo, A. Marlowska-Szczupak, H. Remita, and B. Ohtani . 2015. "Silver-Modified Titania with Enhanced Photocatalytic and Antimicrobial Properties under UV and Visible Light Irradiation." *Catalysis Today* 252:136–42.
- Krejcikova, S., L. Matejova, K. Koci, L. Obalova, Z. Matej, L. Capek, and O. Solcova. 2012. "Preparation and Characterization of Ag-Doped Crystalline Titania for Photocatalysis Applications." *Applied Catalysis B: Environmental* 111–112:119–25.
- Lee, D. S., and Y. W. Chen. 2014. "Nano Ag/TiO<sub>2</sub> Catalyst Prepared by Chemical Deposition and Its Photocatalytic Activity." *Journal of the Taiwan Institute of Chemical Engineers* 45(2):705–12.
- Lee, S. G., S. Lee, and H. I. Lee. 2001. "Photocatalytic Production of Hydrogen from Aqueous Solution Containing CN<sup>-</sup> as a Hole Scavenger." *Applied Catalysis A: General* 207(1–2):173–81.
- Legrini, O., E. Oliveros, and A. M. Braun. 1993. "Photochemical Processes for Water Treatment." *Chemical Reviews* 93(2):671–98.
- Leon y Leon, C., and M. Albert Vannice. 1991. "Adsorption and Catalytic Properties of Pd/SiO<sub>2</sub>, Cu/SiO<sub>2</sub>, and Pd-Cu/SiO<sub>2</sub> Systems. I. Hydrogen, Carbon Monoxide and Oxygen Adsorption on Pd/SiO<sub>2</sub> and Cu/SiO<sub>2</sub>." *Applied Catalysis* 69(1):269–90.
- Li, L., Z. Xu, F. Liu, Y. Shao, J. Wang, H. Wan, and S. Zheng. 2010. "Photocatalytic Nitrate Reduction over Pt-Cu/TiO<sub>2</sub> Catalysts with Benzene as Hole Scavenger." *Journal of Photochemistry and Photobiology A: Chemistry* 212(2–3):113–21.
- Luiz, D. De Bem, S. L. Floriani Andersen, C. Berger, H. J. José, and R. De Fátima Peralta Muniz Moreira. 2012. "Photocatalytic Reduction of Nitrate Ions in Water over Metal-Modified TiO<sub>2</sub>." *Journal of Photochemistry and Photobiology A: Chemistry* 246:36–44.

- Luo, Z., M. Ibáñez, A. M. Antolín, A. Genç, A. Shavel, S. Contreras, F. Medina, J. Arbiol, and A. Cabot. 2015. “Size and Aspect Ratio Control of Pd<sub>2</sub>Sn Nanorods and Their Water Denitration Properties.” *Langmuir* 31(13):3952–57.
- Mafune, F., J. Kohno, Y. Takeda, T. Kondow, and H. Sawabe. 2000. “Formation and Size Control of Silver Nanoparticles by Laser Ablation in Aqueous Solution.” *Journal of Physical Chemistry B* 104(39):9111–17.
- Mahler, R. L., A. Colter, and R. Hirnyck. 2007. “Nitrate and Groundwater.” *Cis* 1–4.
- Malato, S., P. Fernández-Ibáñez, M. I. Maldonado, J. Blanco, and W. Gernjak. 2009. “Decontamination and Disinfection of Water by Solar Photocatalysis: Recent Overview and Trends.” *Catalysis Today* 147(1):1–59.
- Mankidy, B. D., B. Joseph, and V. K. Gupta. 2013. “Photo-Conversion of CO<sub>2</sub> Using Titanium Dioxide: Enhancements by Plasmonic and Co-Catalytic Nanoparticles.” *Nanotechnology* 24(40):405402.
- Marie, J., S. Berthon-Fabry, M. Chanetet, E. Chainet, R. Pirard, N. Cornet, and P. Achard. 2007. “Platinum Supported on Resorcinol-Formaldehyde Based Carbon Aerogels for PEMFC Electrodes: Influence of the Carbon Support on Electrocatalytic Properties.” *Journal of Applied Electrochemistry* 37(1):147–53.
- Mills, A., R. H. Davies, and D. Worsley. 1993. “Water Purification by Semiconductor Photocatalysis.” *Chemical Society Reviews* 22(6):417.
- Moreno, B., M. A. Gómez, J. González-López, and E. Hontoria. 2005. “Inoculation of a Submerged Filter for Biological Denitrification of Nitrate Polluted Groundwater: A Comparative Study.” *Journal of Hazardous Materials* 117(2–3):141–47.
- Mori, T., J. Suzuki, K. Fujimoto, M. Watanabe, and Y. Hasegawa. 1999. “Reductive Decomposition of Nitrate Ion to Nitrogen in Water on a Unique Hollandite Photocatalyst.” *Applied Catalysis B: Environmental* 23(4):283–89.
- Mulfinger, L., S. D. Solomon, M. Bahador, A. V. Jeyarajasingam, S. A. Rutkowsky, and C. Boritz. 2007. “Synthesis and Study of Silver Nanoparticles.” *Journal of Chemical Education* 84(2):322–25.
- Neyertz, C., F. A. Marchesini, A. Boix, E. Miró, and C. A. Querini. 2010. “Catalytic Reduction of Nitrate in Water: Promoted Palladium Catalysts Supported in Resin.” *Applied Catalysis A: General* 372(1):40–47.
- Oenema, O., A. Bleeker, N. A. Braathen, M. Budnakova, K. Bull, P. cermak, M. Geupel, K. Hicks, R. hoft, N. Kozlova, A. Leip, T. Spranger, L. Valli, G. Velthof, and W. Winiwarter. 2011. “Nitrogen in Current European Policies.” *The European Nitrogen Assessment* 62–81.

- Ohtani, B., K. Iwai, S.I. Nishimoto, and S. Sato. 1997. "Role of Platinum Deposits on Titanium (IV) Oxide Particles : Structural and Kinetic Analyses of Photocatalytic Reaction in Aqueous Alcohol and Amino Acid Solutions." *Society* 101(Iv):3349–59.
- Ohtani, B., Y. Okugawa, S. I. Nishimoto, and T. Kagiya. 1987. "Photocatalytic Activity of TiO<sub>2</sub> Powders Suspended in Aqueous Silver Nitrate Solution. Correlation with pH-Dependent Surface Structures." *Journal of Physical Chemistry* 91:3550–55.
- Organization, World Health. 2006. "Guidelines for Drinking-Water Quality." 1.
- Parastar, S., S. Nasseria, S. Hemmati Borjia, M. Fazlzadehb, A. Hossein Mahvia, A. Hossein Javadic, and M. Gholami. 2013. "Application of Ag-Doped TiO<sub>2</sub> Nanoparticle Prepared by Photodeposition Method for Nitrate Photocatalytic Removal from Aqueous Solutions." *Desalination and Water Treatment* 51(January 2014):7137–44.
- Parkt, J. Y., and Y. N. Lee. 1988. "Solubility and Decomposition Kinetics of Nitrous Acid in Aqueous Solution." *Journal of Physical chemistry* 92(23):6294–6302.
- Perissinotti, L. L., M. A. Brusa, and M. A. Grela. 2001. "Yield of Carboxyl Anion Radicals in the Photocatalytic Degradation of Formate over TiO<sub>2</sub> Particles." *Langmuir* 17(26):8422–27.
- Pichat PhD Thesis. 203. Photocatalysis and water purification: from fundamentals to recent applications. Chapter 2.
- Pintar, A.. 2003. "Catalytic Processes for the Purification of Drinking Water and Industrial Effluents." *Catalysis Today* 77(4):451–65.
- Pintar, A., J. Batista, J. Levec, and T. Kajiuchi. 1996. "Kinetics of the Catalytic Liquid-Phase Hydrogenation of Aqueous Nitrate Solutions." *Applied Catalysis B: Environmental* 11(1):81–98.
- Prüsse, U., M. Hähnlein, J. Daum, and K. D. Vorlop. 2000. "Improving the Catalytic Nitrate Reduction." *Catalysis Today* 55(2):79–90.
- Prüsse, U., and K. D. Vorlop. 2001. "Supported Bimetallic Palladium Catalysts for Water-Phase Nitrate Reduction." *Journal of Molecular Catalysis A: Chemical* 173(1–2):313–28.
- Pulido Melián, E., O. González Díaz, J. M. Doña Rodríguez, G. Colón, J. A. Navío, M. Macías, and J. Pérez Peña. 2012. "Effect of Deposition of Silver on Structural Characteristics and Photoactivity of TiO<sub>2</sub>-Based Photocatalysts." *Applied Catalysis B: Environmental* 127:112–20.
- Qi, Z., and P. G. Pickup. 1998. "High Performance Conducting Polymer Supported Oxygen Reduction Catalysts." *Chemical Communications* (21):2299–2300.
- Rani, M., N. Gupta, and B. Pal. 2012. "Superior Photodecomposition of Pyrene by Metal Ion-Loaded TiO<sub>2</sub> Catalyst under UV Light Irradiation." *Environmental Science and Pollution Research* 19:2305–12.

- Ranjit, K. T., T. Varadarajan, and B. Viswanathan. 1995. "Photocatalytic Reduction of Nitrite and Nitrate Ions to Ammonia on Ru/TiO<sub>2</sub> Catalysts." *Journal of Photochemistry and Photobiology A: Chemistry* 89:67–68.
- Ranjit, K. T., and B. Viswanathan. 1997. "Photocatalytic Reduction of Nitrite and Nitrate Ions to Ammonia on M/TiO<sub>2</sub> Catalysts." *Journal of Photochemistry and Photo*
- S.I-No.106. 2007. "European Communities Drinking Water Regulations."
- Sá, J., C. Alcaraz Agüera, S. Gross, and J. A. Anderson. 2009. "Photocatalytic Nitrate Reduction over Metal Modified TiO<sub>2</sub>." *Applied Catalysis B: Environmental* 85(3–4):192–200.
- Sá, J., and H. Vinek. 2005. "Catalytic Hydrogenation of Nitrates in Water over a Bimetallic Catalyst." *Applied Catalysis B: Environmental* 57(4):247–56.
- Sakthivel, S., M.V. Shankar, M. Palanichamyb, Banumathi Arabindoob, D.W. Bahnemann, and V. Murugesanb. 2004. "Enhancement of Photocatalytic Activity by Metal Deposition: Characterisation and Photonic Efficiency of Pt, Au and Pd Deposited on TiO<sub>2</sub> Catalyst." *Water Research* 38(13):3001–8.
- Scardi, P., and U. Trento. 1993. "XRD Characterization of Highly Dispersed Metal Catalysts on Carbon Support." *J. Mater. Res.* 8:1829–35.
- Sclafani A., M.N. Mozzanegra, J. M. Herrmann. 1997. "Influence of Silver Deposits on the Photocatalytic Activity of Titania." *Journal of Catalysis* 120:117–20.
- Sclafani A., J. M. Herrmann. 1998. "Influence of metallic silver and of platinum-silver bimetallic deposits on the photocatalytic activity of titania (anatase and rutile) in organic and aqueous media". *J. Photochem. Photobiol. A: Chem.* 113 (1998) 181–188.
- Schoeman, J. J. 2009. "Nitrate-Nitrogen Removal with Small-Scale Reverse Osmosis, Electrodialysis and Ion-Exchange Units in Rural Areas." *Water SA* 35(5):721–28.
- Shand, M., and J. A. Anderson. 2013. "Aqueous Phase Photocatalytic Nitrate Destruction Using Titania Based Materials: Routes to Enhanced Performance and Prospects for Visible Light Activation." *Catalysis Science & Technology* 3(4):879.
- Soares, O. S. G. P., M. F. R. Pereira, J. J. M. Órfão, J. L. Faria, and C. G. Silva. 2014. "Photocatalytic Nitrate Reduction over Pd–Cu/TiO<sub>2</sub>." *Chemical Engineering Journal* 251:123–30.
- Soares, O. S. G. P., J. J. M. Orfao, and M. F. R. Pereira. 2008. "Activated Carbon Supported Metal Catalysts for Nitrate and Nitrite Reduction in Water." *Catalysis Letters* 126(3–4):253–60.
- Soares, O. S. G. P., J. J. M. Órfão, and M. F. R. Pereira. 2011. "Nitrate Reduction with Hydrogen in the Presence of Physical Mixtures with Mono and Bimetallic Catalysts and Ions in Solution." *Applied Catalysis B: Environmental* 102(3–4):424–32.

Sanam Glass. 2013. <http://clonet.net/designs/sanam/solar-spectrum/>

Soria, J. J. C. Conesa, V. Augugliaro, M. Schiavello, and A. Sclafani. 1991. "Dinitrogen Photoreduction to Ammonia over Titanium Dioxide Powders Doped with Ferric Ions." *The Journal of Physical Chemistry* 95(1):274–82.

Sowmya, A., and S. Meenakshi. 2014. "Photocatalytic Reduction of Nitrate over Ag-TiO<sub>2</sub> in the Presence of Oxalic Acid." *Journal of Water Process Engineering* 4–11. Retrieved

Sun, D., W. Yang, L. Zhou, W. Sun, Q. Li, and J. K. Shang. 2016. "The Selective Deposition of Silver Nanoparticles onto {101} Facets of TiO<sub>2</sub> Nanocrystals with Co-Exposed {001}/{101} Facets, and Their Enhanced Photocatalytic Reduction of Aqueous Nitrate under Simulated Solar Illumination." *Applied Catalysis B: Environmental* 182:85–93.

Tacke, T., and K.D. Vorlop, *Chemie Ingenieur Technik*, 1993. 65(12): p.1500-1502.

Takai, A., and P. V. Kamat. 2011. "Capture, Store, and Discharge. Shuttling Photogenerated Electrons across TiO<sub>2</sub>-Silver Interface." *ACS Nano* 5(9):7369–76.

Tang, X., B. Zhang, Y. Li, Y. Xu, Q. Xin, and W. Shen. 2004. "Structural Features and Catalytic Properties of Pt/CeO<sub>2</sub> Catalysts Prepared by Modified Reduction-Deposition Techniques." *Catalysis Letters* 97(3–4):163–69.

Theologides, C. P., P. G. Savva, and C. N. Costa. 2011. "Catalytic Removal of Nitrates from Waters in a Continuous Flow Process: The Remarkable Effect of Liquid Flow Rate and Gas Feed Composition." *Applied Catalysis B: Environmental* 102(1–2):54–61.

Thompson, T. S. 2001. "Nitrate Concentrations in Private Rural Drinking Water Supplies in Saskatchewan, Canada." *Bulletin of Environmental Contamination and Toxicology* 66(1):64–70.

Thompson, T. L., and J. T. Yates. 2006. "Surface Science Studies of the Photoactivation of TiO<sub>2</sub>". *New Photochemical Processes.*" *Chemical Reviews* 106(412):4428–53.

Townsend, T. K. 2014. "Inorganic Metal Oxide Nanocrystal Photocatalysts for Solar Fuel Generation from Water." 7426(2012):7420–26.

Velthof, G. L., J. P. Lesschen, and J. Webb. 2014. "Measuring the Impacts of the Nitrates Directive on Nitrogen Emissions." 16.

Vorlop, K.D., and T. Tacke. 1989. *Chem. Ing. Tech.* 61, 836.

Wang, G., L. Xu, J. Zhang, T. Yin, and D. Han. 2012. "Enhanced Photocatalytic Activity of TiO<sub>2</sub> Powders (P25) via Calcination Treatment." *International Journal of Photoenergy* 2012.

Wang, H., Y. Liu, M. Li, H. Huang, H. M. Xu, R. J. Hong, and H. Shen. 2010. "Multifunctional TiO<sub>2</sub> Nanowires-Modified Nanoparticles Bilayer Film for 3D Dye-Sensitized Solar Cells." *Optoelectronics and Advanced Materials, Rapid Communications* 4(8):1166–69.

- Wang, H., X. Qiao, J. Chen, and S. Ding. 2005. "Preparation of Silver Nanoparticles by Chemical Reduction Method." *Colloids and Surfaces A: Physicochemical and Engineering Aspects* 256(2–3):111–15.
- Wang, Y., J. Qu, H. Liu, and C. Z. Hu. 2007. "Adsorption and Reduction of Nitrate in Water on Hydrotalcite-Supported Pd-Cu Catalyst." *Catalysis Today* 126(3–4 SPEC. ISS.):476–82.
- Wang, Y., X. Wang, B. Sun, S. Tang, and X. Meng. 2016. "Concentration-Dependent Morphology Control of Pt-Coated-Ag Nanowires and Effects of Bimetallic Interfaces on Catalytic Activity." *Journal of Materials Science and Technology* 32(1):41–47.
- Warna, J., I. Turunen, T. Salmi, and T. Maunula. 1994. "Kinetics of Nitrate Reduction Reactor." *Chemical Engineering Science* 49(248):5763–73.
- Wehbe, N., M. Jaafar, C. Guillard, J. M. Herrmann, S. Miachon1, E. Puzenat, and N. Guilhaume. 2009. "Comparative Study of Photocatalytic and Non-Photocatalytic Reduction of Nitrates in Water." *Applied Catalysis A: General* 368:1–8.
- Willets, K. A., and R. P. Van Duyne. 2007. "Localized Surface Plasmon Resonance Spectroscopy and Sensing." *Annual review of physical chemistry* 58(October):267–97.
- Wisniewski, C., F. Persinb , T. Cherifb , R. Sandeauxb , A. Grasmicka, and C. Gavach. 2001. "Denitrification of Drinking Water by the Association of an Electrodialysis Process and a Membrane Bioreactor: Feasibility and Application." *Desalination* 139(1–3):199–205.
- Witońska, I., S. Karski, J. Rogowski, and N. Krawczyk. 2008. "The Influence of Interaction between Palladium and Indium on the Activity of Pd-In/Al<sub>2</sub>O<sub>3</sub> Catalysts in Reduction of Nitrates and Nitrites." *Journal of Molecular Catalysis A: Chemical* 287(1–2):87–94.
- Wodka, D., E. Bielanska, R. P. Socha, M. Elzbieciak-Wodka, J. Gurgul, P. Nowak, P. Warszynski, and I. Kumakiri. 2010. "Photocatalytic Activity of Titanium Dioxide Modified by Silver Nanoparticles." *ACS Applied Materials and Interfaces* 2(7):1945–53.
- World Health Organization. 1996. "Ammonia in Drinking-Water. Background Document for Development of WHO Guidelines for Drinking-Water Quality." Health San Francisco 2.
- World Health Organization. 2011. "Nitrate and Nitrite in Drinking-Water: WHO Guidelines for Drinking-Water Quality." 1–31.
- World, Chem. Mater. 5 (1993) 280.
- Yamamoto, T. A., T. Nakagawa, S. Seino, and H. Nitani. 2010. "Bimetallic Nanoparticles of PtM (M = Au, Cu, Ni) Supported on Iron Oxide: Radiolytic Synthesis and CO Oxidation Catalysis." *Applied Catalysis A: General* 387(1–2):195–202. Retrieved
- Yang, T., K. Doudrick, and P. Westerhoff. 2013. "Photocatalytic Reduction of Nitrate Using Titanium Dioxide for Regeneration of Ion Exchange Brine." *Water Research* 47(3):1299–1307.

- Yang, X., J. Hu, J. Fu, R. Wu, and B. E. Koel. 2011. "Role of Surface Iron in Enhanced Activity for the Oxygen Reduction Reaction on a Pd<sub>3</sub>Fe(111) Single-Crystal Alloy." *Angewandte Chemie - International Edition* 50(43):10182–85.
- Yoshinaga, Y. 2002. "Hydrogenation of Nitrate in Water to Nitrogen over Pd–Cu Supported on Active Carbon." *Journal of Catalysis* 207(1):37–45.
- Yu, J. G. Jimmy C., H. G. Yu, B. Cheng, X. J. Zhao, and W. K. Ho. 2003. "The Effect of Calcination Temperature on the Surface Microstructure and Photocatalytic Activity of TiO<sub>2</sub> Thin Films Prepared by Liquid Phase Deposition." *The Journal of Physical Chemistry B* 107(50):13871–79.
- Yu, Y. T., and B. Q. Xu. 2003. "Selective Formation of Tetrahedral Pt Nanocrystals from K<sub>2</sub>PtCl<sub>6</sub>/PVP." *Chinese Science Bulletin* 48(23):2589–93.
- Zaleska-Medynska, A., M. Marchelek, M. Diak, and E. Grabowska. 2016. "Noble Metal-Based Bimetallic Nanoparticles: The Effect of the Structure on the Optical, Catalytic and Photocatalytic Properties." *Advances in Colloid and Interface Science* 229:80–107.
- Zhang, F., R. Jin, J. Chen, C. Shao, W. Gao, L. Li, and N. Guan. 2005. "High Photocatalytic Activity and Selectivity for Nitrogen in Nitrate Reduction on Ag/TiO<sub>2</sub> Catalyst with Fine Silver Clusters." *Journal of Catalysis* 232:424–31.
- Zhang, F., Y. Pi, J. Cui, Y. Yang, X. Zhang, and N. Guan. 2007. "Unexpected Selective Photocatalytic Reduction of Nitrite to Nitrogen on Silver-Doped Titanium Dioxide." *Journal of Physical Chemistry C* 111(9):3756–61.
- Zhang, H., and G. Chen. 2009. "Potent Antibacterial Activities of Ag / TiO<sub>2</sub> Nanocomposite Powders Synthesized by a One-Pot Sol - Gel Method." 2(852):2905–10.
- Zhu, S., S. Liang, Q. Gu, L. Xie, J. Wang, Z. Ding, and P. Liu. 2012. "Effect of Au Supported TiO<sub>2</sub> with Dominant Exposed {001} Facets on the Visible-Light Photocatalytic Activity." *Applied Catalysis B: Environmental* 119–120:146–55.
- Zielińska, A., E. Skwarek, A. Zaleska, M. Gazda, and J. Hupka. 2009. "Preparation of Silver Nanoparticles with Controlled Particle Size." *Procedia Chemistry* 1(2):1560–66.

CHAPTER 2:

# Materials and Methods

## 2. Materials and Methods

The different characterization techniques and the methods for the analysis of ions (nitrate, nitrite, and ammonium) have been extensively described in this chapter.

The first part (2.1) details the fundamentals and operational conditions of every characterization technique applied on the fresh catalyst powder to determine their physicochemical properties due to their important role in their activity. The X-Ray Diffraction Powder (XRD) and the Nitrogen Physisorption ( $N_2$ -Physisorption) have been used to determine their crystallinity structures and textural properties. Their morphologies were observed by Transmission Electron Microscopy (TEM) technique. The UV-Vis Spectroscopy was used to obtain their diffuse reflectance using the Kubelka-Munk function (DRUV-Vis) in order to know the light absorption range. Their atomic environment and reducibility were analyzed through X-Ray Photoelectron Spectroscopy (XPS) and Temperature-Programmed Reduction by hydrogen ( $H_2$ -TPR). Hydrogen chemisorption ( $H_2$ -Chemisorption) was applied to calculate the metal dispersion and metal (Pd) surface area over the support. The physicochemical properties obtained by all these characterization techniques for the monometallic and bimetallic catalysts synthesized in this thesis are broadly described in *Chapters 3* and *Chapter 5*.

The second part of this chapter (2.2) explains the fundamental aspects of the ionic analysis (nitrate, nitrite and ammonium) using the Ion Chromatography (Ag and/or Pt/P25 catalysts) or the Photometry ( $Pd_2Sn/P25$  catalysts) techniques, which are comparable. The catalytic and photocatalytic activities of the monometallic and bimetallic catalysts are largely commented in the *Chapter 4* (Ag and or Pt/P25) and *Chapter 5* ( $Pd_2Sn/P25$ ).

The third part (2.3) describes the experimental set-up and operational conditions under the catalytic and photocatalytic nitrate and nitrite abatement in water have been carried out.

The last part of the chapter (2.4) shows the calculation of the parameters used for the comparison of the catalytic and photocatalytic behaviors presented by the different monometallic and bimetallic catalysts: nitrate and nitrite conversions; nitrate reduction rate; selectivity and yields to products.

## 2.1 Characterization techniques

The physicochemical properties of each catalyst (structure, morphology, surface area, chemical state...) allow us to acquire a very precious and relevant information to understand the catalytic and photocatalytic behavior, which is essential for a meaningful comparison of the catalysts. Therefore, various characterization techniques were applied and are extensively described in the following sections of this chapter.

A physical adsorption is the result of a weak solid-gas interaction. The physical attraction is the result from nonspecific, relatively weak Van der Waal's forces and adsorption energy usually not exceeding 80 kJ/mol. Physically adsorbed molecules may diffuse on the surface of the adsorbent molecules and normally are not bound to a specific location on the surface, then is easily reversed. Physical adsorption occurs on all surfaces under favorable temperature and pressure conditions, resulting in adsorbed molecules that create multiple layers. Nevertheless, the chemisorption adsorption is highly selective and occurs only between certain adsorptive and adsorbent species. The chemisorption only takes place when the active surface was never in contact with the adsorbed molecules. The chemical adsorption isotherm gives information about the active surface of the catalyst, proceeding until the metal is saturated by the gas in a single-layer process (irreversible). Both physical and chemical adsorptions may occur on the surface at the same time, a layer of molecules may be physically adsorbed on top of an underlying chemisorbed layer. Then, the same surface could display physisorption at one temperature and chemisorption at a higher temperature. For instance, at liquid N<sub>2</sub> temperature (77 °K) the N<sub>2</sub> gas is adsorbed physically on iron, but it is adsorbed chemically at 800 °K to form iron nitride, as the energy level is too high for physical adsorption bonds (Webb 2003).

### 2.1.1 X-Ray Diffraction Powder

The X-Ray Diffraction (XRD) is a characterization method used for the identification of the different crystalline phases and the determination of certain structural properties, such as the disposition of the atoms, the grain size, the preferred orientation and the identification of defects in the structure. The solid studied with this technique should be crystalline enough to diffract X-rays, being the amount of powder higher than 1% for its analysis. Each crystalline plane diffracts at a different angle, which corresponds to a unique element or compound pattern, then the substances can be differentiated one for the others within the catalysts. These patterns are collected and stored in the database as standards for comparison.

An electron in an alternating electromagnetic field will oscillate with the same frequency as the field. The X-ray beam is generated by a cathode ray tube and is filtered to create monochromatic radiation, which is focused to the sample. When the X-ray beam hits an atom, the electrons around the atom start to oscillate with the same frequency as the incident beam (Figure 2.1). Mostly, in all directions destructive interference will be observed, which means that the combining waves are out of phase and there is no resultant energy leaving the catalyst. Nevertheless, the atoms in a crystal are organized in a regular pattern, and constructive interference will be obtained in only few directions. The waves will be in phase and there will be well defined X-ray beams leaving the sample at various directions. Thus, a diffracted beam may be described as a beam composed of a large number of reflected or scattered rays reinforcing one to the other (Thermo ARL 1999). The conditions in which a constructive interference is observed is described by the Bragg's Law. The interaction of the incident rays with the catalyst analyzed produces constructive interference, and a diffracted ray at the same diffraction angle, which is described by the relationship of the Bragg's law (Eq. 2.1) (Van Holde et al. 2006).

$$n\lambda = 2ds\sin\theta \quad (\text{Eq. 2.1})$$

Where :  $n$  is the interference order ;  $\lambda$  is the X-Ray wavelength, measured in Ångström ( $\text{\AA}$ ) – equivalent to the distance between the atoms of a solid ;  $d$  is the distance between two diffraction planes; and  $\theta$  the diffraction angle.

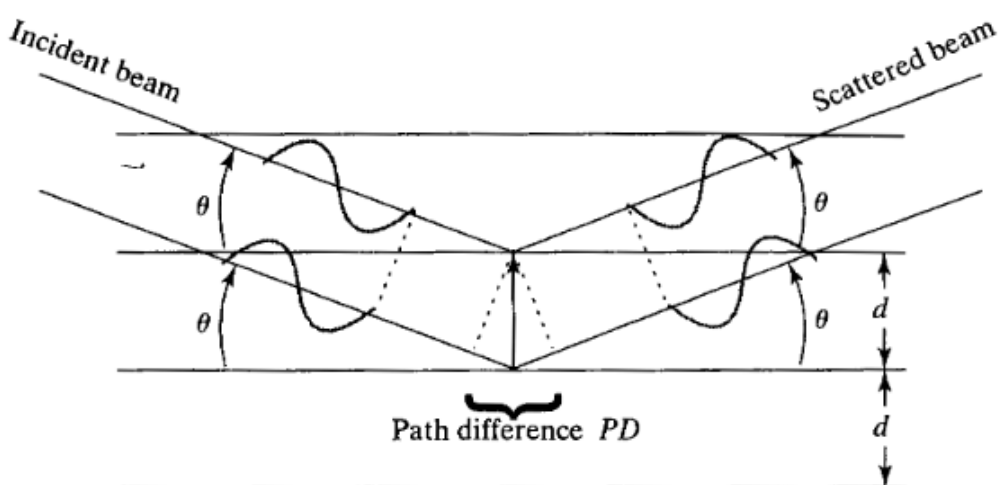


Figure 2.1. Bragg's law of diffractions (Van Holde et al. 2006)

The XRD analyses have been recorded with a Bruker D8 Advance Diffractometer using monochromatic X-ray Cu-K $\alpha$  radiation ( $\lambda_{\alpha} = 1.54184 \text{ \AA}$ , 40 kV, 50 mA) with a Bragg-Brentano configuration and equipped with a Bruker Lynx Eye detector (Figure 2.2) and the EVA software. The diffractions were performed between 0 - 60° (2 $\theta$ ), with an angular size of 0.0197°. The data acquisition was every 0.2 s, in 100 mg of sample.



Figure 2.2. XRD equipment

#### 2.1.1.1 Average crystallite size determination

The XRD analyses allow to calculate the average crystallite size of the catalysts. The most used method is the Scherrer equation (Monshi et al. 2012), which relates the average crystallite size of the particles to the width of a peak in the diffraction pattern (Eq. 2.2):

$$D = \frac{0.9\lambda}{\beta \cos\theta} \quad (\text{Eq. 2.2})$$

Where:  $D$  is the average crystallite size of the catalyst,  $\lambda$  is the X-Ray wavelength,  $\beta$  is the full width at half maximum (FWHM) of the peak, and  $\theta$  the diffraction angle of the peak (Bragg angle).

### 2.1.2 Nitrogen Physisorption

Gas adsorption measurements are normally applied for determining the specific surface area and the porosity of several solid materials, like catalysts, adsorbents and ceramics. The measurements of the adsorption at the gas/solid interface is an essential part of wide investigations on the nature and behavior of solid surfaces (Sing et al. 1985). The Brunauer-Emmett-Teller (BET) method applied to the adsorption isotherm is the most commonly used for the surface area determination.

200 mg of each sample was previously outgassed during 5 h at a temperature of 120 °C with Helium stream to remove all the possible physisorbed species from the surface of the catalysts. Then, the specific surface areas ( $S_{BET}$ ) of the catalysts were determined applying the BET method to the  $N_2$  adsorption isotherm at 77 °K. The pore volume ( $V_{Pore}$ ) (nm or Å) and average pore diameters ( $\bar{\phi}_{Pore}$ ) (nm or Å) of the selected catalysts were determined through the Barrett-Joyner-Halenda (BJH) method (Barrett et al. 1951) giving the pore size distribution plots from the adsorption isotherms. A scheme of the experimental system is detailed in Figure 2.3 (static volumetric gas adsorption), which integrates a vacuum system to work at high vacuum conditions (at least at  $10^{-4}$  torr) meantime the pressure is increased until the adsorbate saturation, in order to ensure very accurate results.

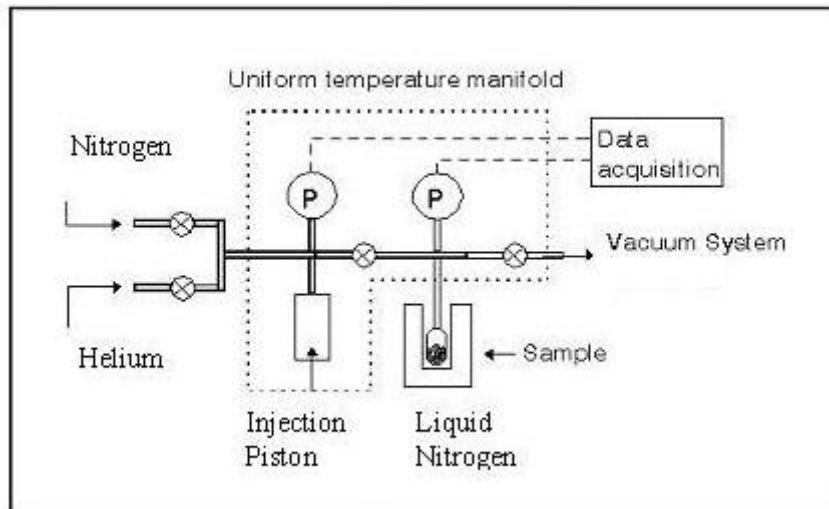


Figure 2.3.  $N_2$ -Physisorption adsorption-desorption system scheme (Univ. of Oxford 2008)

The pores are classified according to their widths (IUPAC) depending on the pores access: micropores ( $< 2$  nm), mesopores ( $2 - 50$  nm), and macropores ( $> 50$  nm). The Brunauer-

Deming-Teller (BDDT) classification for the types of adsorption isotherms and hysteresis loops of solid materials are depicted in Figure 2.4.

The types of isotherms are:

- Type I: microporous solids with the exposed surface residing almost exclusively inside the micropores.
- Type II: non-porous surface.
- Type III: only in certain porous adsorbents (i.e. krypton on polymethylmethacrylate). Weak adsorbent-absorbate interaction.
- Type IV: porous adsorbents with pores in the range 2 - 50 nm.
- Type V: Weak adsorbent-absorbate interaction, presenting pores in the range 2 - 50 nm.
- Type VI: stepwise multilayer adsorption on a uniform non-porous surface (i.e. isotherms obtained with argon or krypton on graphitized carbon blacks at liquid nitrogen temperature).

The types of hysteresis loops are:

- Type H1: is often associated to porous materials with narrow distributions of pore size.
- Type H2: many porous adsorbents presents this type of hysteresis (i.e. inorganic oxide gels and porous glasses).
- Type H3: mesoporous materials with plate-like particles giving rise to slit-shaped pores, which are narrow.
- Type H4: microporous solids with narrow slit-like pores.

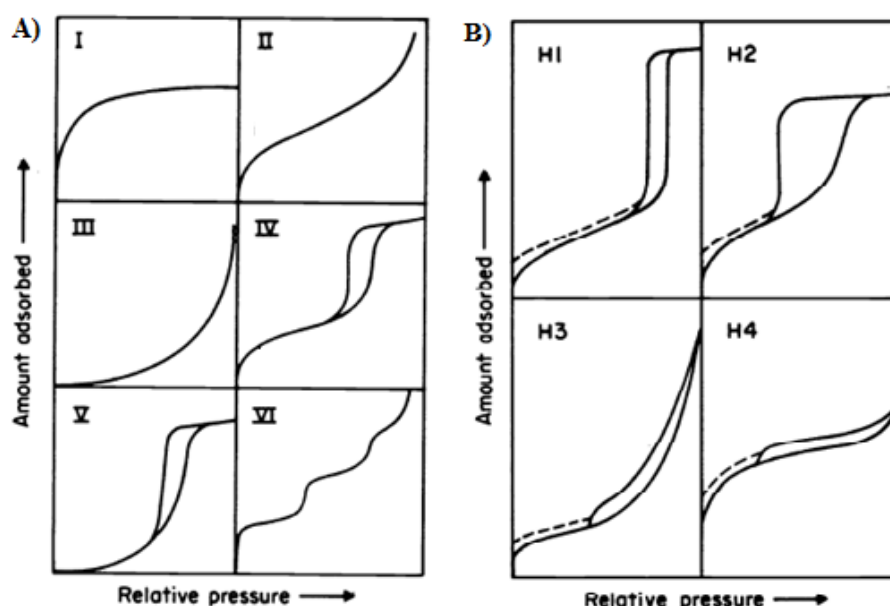


Figure 2.4. Types of : A) Physisorption isotherms, and B) Hysteresis loops (Sing et al. 1985)

The nitrogen physisorption studies have been performed in a Quadasorb equipped with a Flovac Degasser (Quantachrome) (Figure 2.5).



Figure 2.5. N<sub>2</sub>-physisorption equipment

### 2.1.3 Transmission Electron Microscopy

The Transmission Electron Microscopy (TEM) provides information about the morphology of the catalysts, such as the particles sizes, shapes and visual distributions of the particles over the support. The source of illumination is a stable electron beam (~ 100 - 200 kV of electron energy) focused by the objective lens. It is produced in the upper part of the equipment and passes through the objective aperture, where it is introduced the sample supported on a copper grid in a sample holder (specimen). The specimen produces diffracted or scattered electrons that are used for creating the images (intermediate lens), which are magnified with the projector lenses. The diffraction pattern and image are created at the back focus plane and image plane of the objective lens. This mode of operation recognizes in a narrow range the crystallites. The system works at a high vacuum, reaching at least 10<sup>-5</sup> torr (Knözinger et al. 2009; Kiely 2010). The scheme of the system is displayed in Figure 2.6.

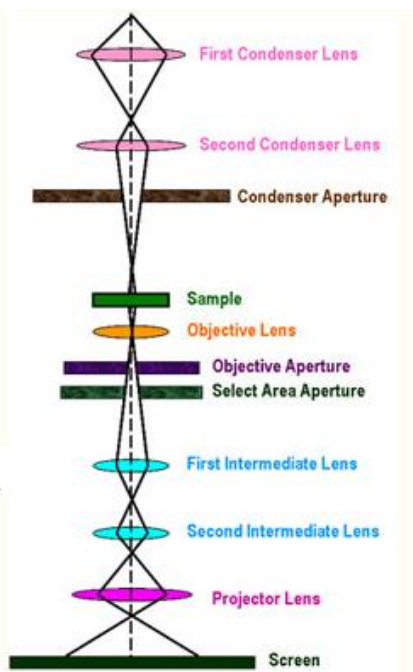


Figure 2.6. TEM scheme (Dong et al. 2009)

In this research, the TEM characterizations were operated in a Jeol 1200 EXII apparatus at an electron beam of 120 kV. It is equipped with a numeric camera that integrates a CCD sensor of 11 MP with a point resolution of 0.4 nm (SIS Olympus, Quemesa) (Figure 2.7). The amount of the sample introduced was lower than 100 mg. This TEM displays a good quality on the images, as it has high resolution with a broad range of grey-scale values, and a precise and uniform relation between the brightness and illumination (Nils Hasselmo Hall EM lab 2007).



Figure 2.7. TEM apparatus

The diameter sizes of the metal nanoparticles were measured with the Measure IT software directly on the images obtained with the TEM.

### 2.1.4 Diffuse Reflectance UV-Vis Spectroscopy

The Diffuse Reflectance Spectroscopy gives information about the optical absorption properties of the solids, in our case in the ultraviolet and visible light ranges (DRUV-Vis). The reflectance spectrum is converted to the absorption spectrum applying normally the Kubelka-Munk (K-M) function (Eq. 2.3 and 2.4). This theory assumes that a plane-parallel layer of thickness is able of both absorbing ( $K$ ) and scattering radiation ( $s$ ). The solid is irradiated with a diffuse monochromatic radiation in an integrating sphere, where is located the sample, or the reference, in a quartz cell. Therefore, we are able to achieve an optical absorption spectra of the absorbents presented in an opaque solid sample taking into account the diffusion phenomenon recorded in the detector. As in practice important deviations from the theory could occur at  $R_\infty < 0.6$ , a “white” reference solid is used as standard spectrum – Barium sulfate ( $\text{BaSO}_4$ ) for UV-Vis radiation – for the calibration procedure, which possess a known scattering coefficient at the various wavelengths (Figure 2.8) (Jentoft 2004; Torrent et al. 2008; Wodka et al. 2010; Doudrick et al. 2013).

$$f(R_\infty(\lambda)) = \frac{(1-R_\infty)^2}{2R_\infty} = \frac{k}{s} \quad (\text{Eq. 2.3})$$

$$R_\infty = \frac{R}{R_{\text{BaSO}_4}} \quad (\text{Eq. 2.4})$$

Where:  $k$  is the molar absorption coefficient (absorption),  $s$  is the scattering coefficient (diffusion),  $R$  is the reflectance recorded,  $R_\infty$  is the absolute reflectance, and  $\lambda$  is the absorbance wavelength.

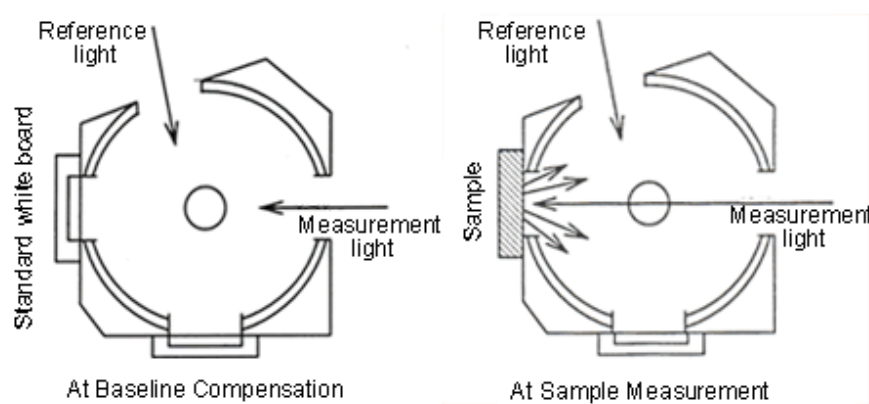


Figure 2.8. Measurement of diffuse reflection using an integration sphere (Shimadzu 2016)

The DRUV-Vis spectra were registered in the wavelength range of 300 - 800 nm at a scan speed of 60 nm/min in a Perkin Elmer LAMBDA 40 UV/VIS spectrometer equipped with an integrating sphere accessory (Figure 2.9), and treated with the UV WinLab software. The BaSO<sub>4</sub> powder (Aldrich) was used as reference. The sample (< 100 mg) was deposited in a quartz cell of 0.1 mm (Quartz SUPRASIL, Hellma).



Figure 2.9. DRUV-Vis Spectrometer

### 2.1.5 X-Ray Photoelectron Spectroscopy

The X-Ray Photoelectron Spectroscopy technique (XPS), also known as Electron Spectroscopy for Chemical Analysis (ESCA), is an equipment extensively used to quantitatively investigate the chemical composition of surfaces. This technique allows to obtain the identification of each element and its chemical state by measuring the binding energies of the electrons correlated to the different atoms, as well as the chemical environment of the atoms, i.e. electronic state composition of the constituents in the surface region, bonding geometry of the molecules to the surface.

The surface region is normally irradiated with low energy X-rays sources (Al anode or twin anode of Al and Mg) in order to provoke the photoelectric effect. The difference between the X-ray energy source and the photoelectron energies gives the binding energies of the core level electrons (BE). The number of emitted electrons measured by the electron detector are function of their kinetic energy value. The sample has to be able to support ultra-high vacuum conditions ( $\leq 10^{-7}$  torr), to minimize the XPS error, as the only binding energies are detected from the

electrons escaped into the vacuum of the instrument (Univ of Illinois 2005; Smart et al. 2009; Diplas 2013). A simple scheme of the XPS equipment is shown in Figure 2.10.

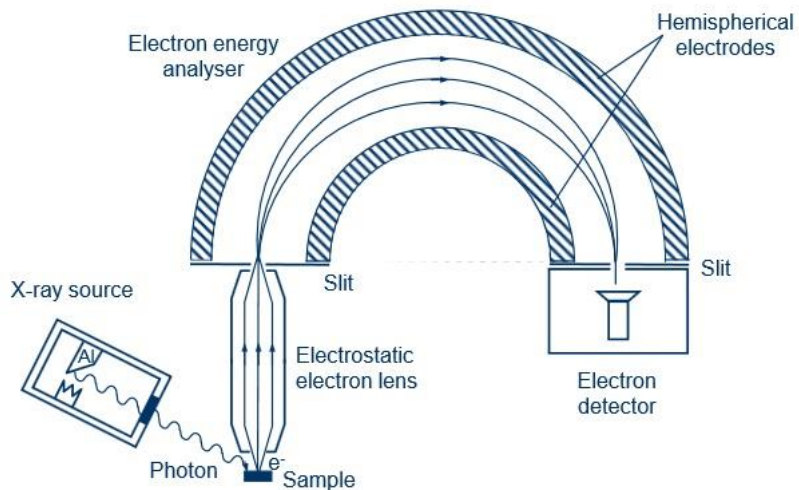


Figure 2.10. XPS system scheme (Diplas 2013)

The XPS spectrum of selected catalysts were achieved with the ESCALAB 250 spectrometer (0.1% atomic sensitivity) equipped with a thermo electrode and the Advantage software for obtaining the spectrum and their analysis (Figure 2.11). A 400  $\mu\text{m}$  surface was irradiated with monochromatic  $\text{K}\alpha$  photon source ( $h\nu$ ), provided by an Al anode of 1486.6 eV.



Figure 2.11. XPS equipment

The binding energies (BE) are referenced to the carbon 1s signal at 284.8 eV and the load is compensated by an electron beam of -2 eV. The Figure 2.12 displays the C1s spectra applied to all samples.

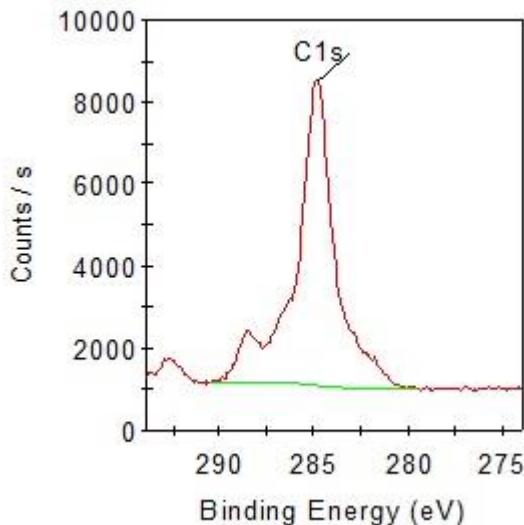


Figure 2.12. C1s scan recorded by XPS

### 2.1.6 Temperature-Programmed Reduction by hydrogen

Through the characterization technique called Temperature Programmed Reduction (TPR) can be determined the number of reducible species that are existing in the solid catalyst surface analyzed. The only restriction for the sample measured by TPR is to content reducible metals. This technique also reports the temperature at which the reduction takes place.

In a typical TPR analysis, a constant reducing gas mixture flow containing hydrogen in an inert carrier gas (nitrogen or argon) is passed through the sample, typically at ambient temperature, situated on a quartz reactor in a furnace (Figure 2.13). Meantime, the temperature is raised linearly (thermocouple), then the hydrogen consumption as a function of temperature and the changes in the concentration of the gas mixture are recorded and monitored by the thermal conductivity detector (TCD). A cold trap is frequently installed before the TCD's cell to trap the water that may be produced (water condensation), obtaining a better stability in the baseline without noise. The useful information given by the TPR can improve the catalyst pretreatment conditions, especially in the metal oxide reduction temperature step. The total hydrogen consumed is calculated from the area under the peak, which is directly proportional to the

volume of gas reacted. Generally, the higher the interaction between the metal and the support the higher is the reduction temperature (Micromeritics 2009; NPTEL 2014).

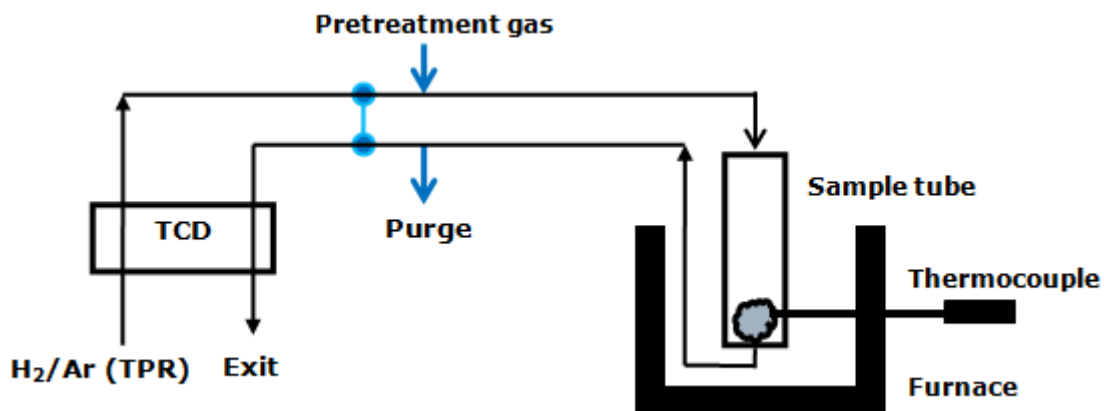


Figure 2.13. Schematic diagram for the TPR analysis (NPTEL 2014)

The hydrogen consumption of various catalysts (H<sub>2</sub>-TPR) before their chemical reduction step with NaBH<sub>4</sub> were measured in an AutoChem II 2920 V 4.03 (Micromeritics) equipped with a TCD (Figure 2.14). 200 mg of sample was located in a quartz reactor and reduced in a 20 ml/min of 10 % vol. H<sub>2</sub>/Ar stream (Argon as carrier gas). The analysis were performed at a temperature range from -50 to 400°C at a linear heating rate of 10 °C/min.



Figure 2.14. TPR AutoChem II 2920 (Micromeritics 2009)

### 2.1.7 Hydrogen chemisorption

Hydrogen chemisorption ( $H_2$ -Chemisorption) is based in the formation of a strong chemical bond between the active metal surface and the adsorbate molecules. These analyses are used to calculate the quantity of “active” metal that is available for reaction, the metallic surface area and the hydrogen chemisorbed by measuring the gas adsorbed selectively on the metal at the monolayer coverage per weight (gram) of the catalyst. Measurements are done without taking into account the non-metal species (i.e. support) and under static vacuum. They are carried out under proper experimental conditions and stoichiometry of the reaction ( $H_2$ /Metal) in order to determine the available metallic surface area in the catalyst. The pressure of the hydrogen is continuously increased until the catalytic surface is saturated with the monolayer of the gas. Usually, the hydrogen is considered to be dissociated on the metal surface atom ( $M_s$ ) (Eq. 2.5). The metal dispersion ( $\gamma$ ) in percentage (Eq. 2.6) describes the ratio of the number of active metal atoms available ( $N_s$ ) for reaction to the total number of metal atoms in the catalyst material ( $N_T$ ) (Pinna 1998; Webb 2003).



$$\gamma = (N_s/N_T) \times 100 \quad (\text{Eq. 2.6})$$

The metal dispersion (%), metallic surface area ( $m^2 g^{-1}$ ) and  $H_2$  chemisorbed ( $cm^3 g^{-1}$ ) over the titania of selected samples were determined by  $H_2$ -Chemisorption. The studies were performed with a Micromeritics ASAP 2010 system (Accelerated Surface Area and Porosimetry System) (Figure 2.15). The Micromeritics ASAP 2010 consists of an analyzer equipped with two sample preparation ports and one analysis port, a control module, and an interface controller which promotes the operation to be controlled. As the equipment contains two independent vacuum system, one for the samples and the other for the analyses, allows both processes to concur without interruption. This equipment is equipped with a software to carry out automatic analysis and record different analytical reports in an easy and accurate way (Micromeritics 2006). The  $H/Pd$  hydrogen adsorption stoichiometry factor has been considered as 1 (Berndt et al. 2001), and the catalyst sample introduced was 600 mg. The study consisted on one cycle of Helium (inertization), two cycles of  $O_2$  flow at 350°C (oxidation, 35 min) followed by two cycles of  $H_2$  flow at 350 °C (reduction, 125 min) Afterwards, the chemisorption (hydrogen adsorption) analysis took place at 100°C. The temperature heating linear rate was at 10 °C/min.



Figure 2.15. H<sub>2</sub>-Chemisorption equipment

## 2.2 Analytical methods

The concentrations of the nitrates (NO<sub>3</sub><sup>-</sup>), nitrites (NO<sub>2</sub><sup>-</sup>) and ammonium (NH<sub>4</sub><sup>+</sup>) ions in the ultrapure water were analyzed by Ion Chromatography (Pt and Ag photocatalysts denitration experiments, *Chapter 4*) or Photometry (Pd<sub>2</sub>Sn NPs denitration experiments, *Chapter 5*) analytical techniques (18.2 Ω). Both analytical methods are commented above. According to the EU Normative for drinking water, the nitrates, nitrites and ammonium ions should be lower than 50 mg/L, 0.5 mg/L and 0.3 mg/L, respectively (S.I-No.106 2007). Before the analysis, samples were filtered (0.45 μm PTFE filter) to avoid any damage of the equipment or contamination due to the presence of solid particles.

### 2.2.1 Ion Chromatography

Among several standard methods capable of analyzing the concentration of different analytes (anions and cations) in water at the same time, the Ion Chromatography is one of the most used nowadays, due to its high sensitivity and effectiveness. This technique is a liquid chromatographic technique in which ionic and strongly polar species are able to be separated and detected (DIONEX 2012).

An ion chromatographic system is normally constituted by the following elements (Figure 2.16): an injection port; a pump; a guard column to prevent damage in the column; a column for ion separation (anions or cations retention times); an eluent to ensure the transport of the species; and a detection cell. A conductivity suppressor is usually used in the system to remove the background signal from eluent and the noise associated with this signal, then a regenerator (Regen) current flows through this suppressor to ensure the desired analytes detection (Thermo Scientific 2015).

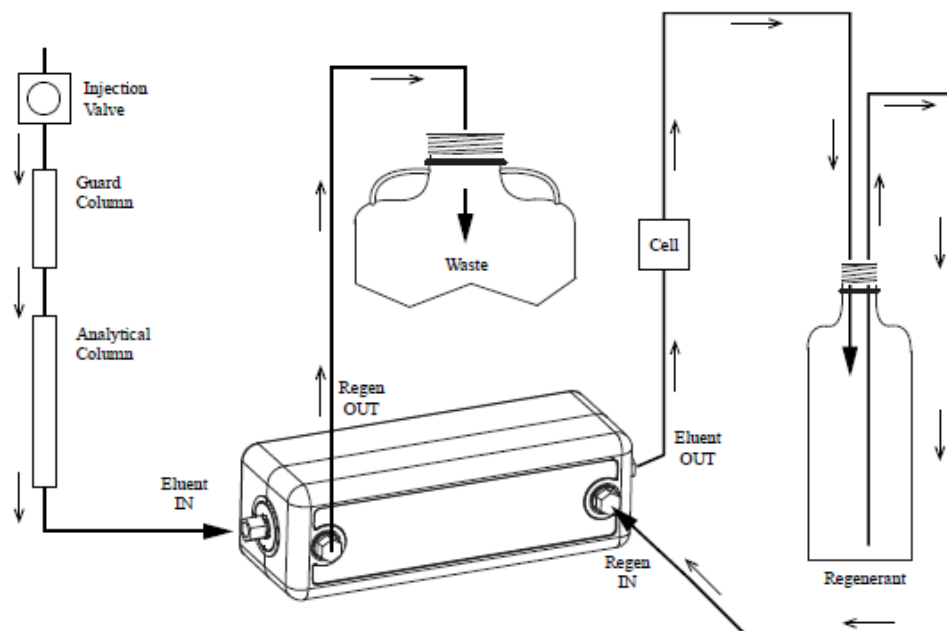


Figure 2.16. Ion Chromatography diagram (Thermo Scientific 2015)

The eluent flows to the pump, after it is supplied to a sensor that measures the pressure of the system, and through a pulsation damper to record the minor variations of the pump pressure to minimize noise background. The eluent is then injected into the injection valve. As we have seen, a suppressor is used to cancel the conductivity of the eluent, and thus only measure the ions to be analyzed. Afterwards, the sample is inserted into the injection loop (injection port). The eluent passes through the injection loop bringing the sample into the eluent stream. The mixture sample/eluent is pumped through the guard column (or precolumn) which retains impurities, and after to the proper column where the ions are separated by an ion exchange process. The guard column is installed before the column to prevent sample contaminants from eluting onto the analytical column, which is easier and cheaper to replace. The mixture sample/eluent is then sent to the suppressor, which suppresses the conductivity of the eluent

and increases the conductivity of the analytes (Figure 2.17). A regenerant (Regen) stream is sent continuously at the same rate as the eluent. The mixture sample/eluent flows through the conductivity cell where the analytes are detected. A signal is generated and is sent to a software.

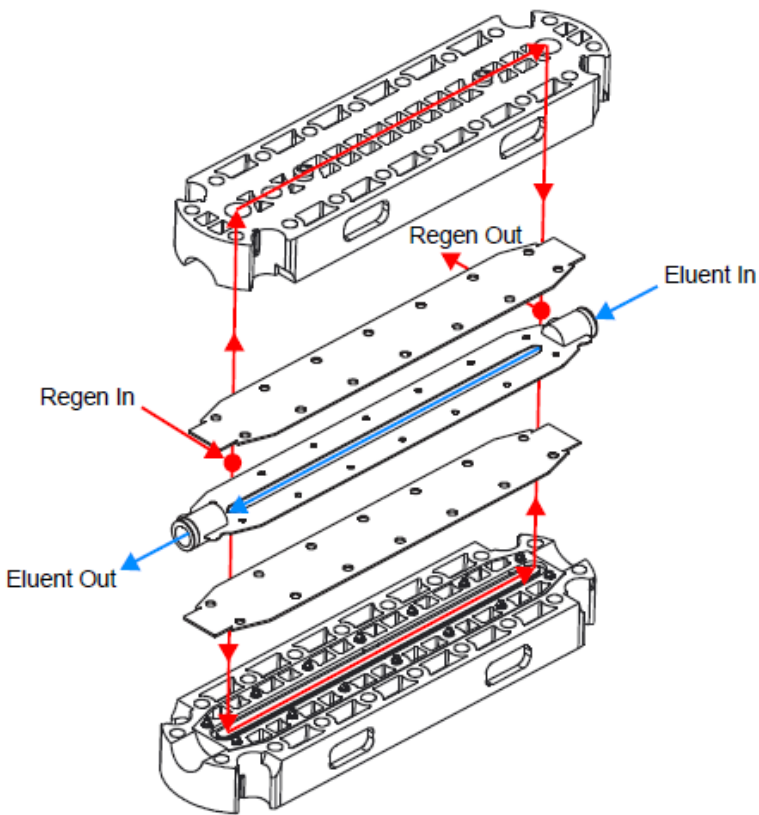


Figure 2.17. General scheme of a suppressor (Thermo Scientific 2015)

The DIONEX ICS-900 (Thermo Fisher) integrated with the Chromeleon 7 software was used for  $\text{NO}_3^-$ ,  $\text{NO}_2^-$  and  $\text{NH}_4^+$  ions analysis. The system works at isocratic flow and suppressed conductivity detection. The Ion Chromatography instrument and its different elements are displayed in Figure 2.18.



Figure 2.18. Ion Chromatography instrument

Nitrate, nitrite and ammonium measurements related to their concentration and calibration curves through Ion Chromatography are detailed in the followings sections.

#### 2.2.1.1 Nitrate and nitrite detection

For the  $\text{NO}_3^-$  and  $\text{NO}_2^-$  ions detection the guard column (DIONEX IonPac<sup>TM</sup> AG9-HC RFIC<sup>TM</sup> 4 x 50 mm, Thermo Scientific), anionic column (DIONEX IonPac<sup>TM</sup> AS9-HC RFIC<sup>TM</sup> 4 x 250 mm, Thermo Scientific) and anionic suppressor (DIONEX ACRS 500 4 mm, Thermo Scientific) are used. The eluent solution is 9 mM  $\text{Na}_2\text{CO}_3$  (0.5 M, Thermo Scientific) and the regenerant solution 25 mM  $\text{H}_2\text{SO}_4$  (2 N, Thermo Scientific), at constant 0.9 mL/min flow for both solutions.

The anionic guard column and column are formed by a 9  $\mu\text{m}$  diameter macroporous resin bed (ethylvinylbenzene crosslinked with 55 % divinylbenzene) and an anion exchange layer functionalized with quaternary ammonium groups. The chemical suppressor is a neutralization reaction and a selective desalting process performed across a couple of cation exchange membranes, which promotes the selective exchange of cations. Sodium ions from eluent are continuously exchanged for hydronium ions from the regenerant acid, being the  $\text{Na}^+$  ions constantly removed by the regenerant acid stream from the suppressor, thus effecting continuous suppression (Thermo Scientific 2001).

## Chapter 2: Materials and Methods

The retention times for  $\text{NO}_3^-$  and  $\text{NO}_2^-$  are c.a. 16.3 min and 10.8 min, respectively. Calibrations curves match linear type with a correlation coefficient of  $R^2 = 0.991$  (0 - 100 mg/L  $\text{NO}_3^-$ ) and  $R^2 = 0.995$  (0 - 50 mg/L  $\text{NO}_2^-$ ). Examples of a nitrate (100 mg/L) and nitrite (50 mg/L) chromatograms and their calibration curves are shown in Figures 2.19, 2.20 and 2.21.

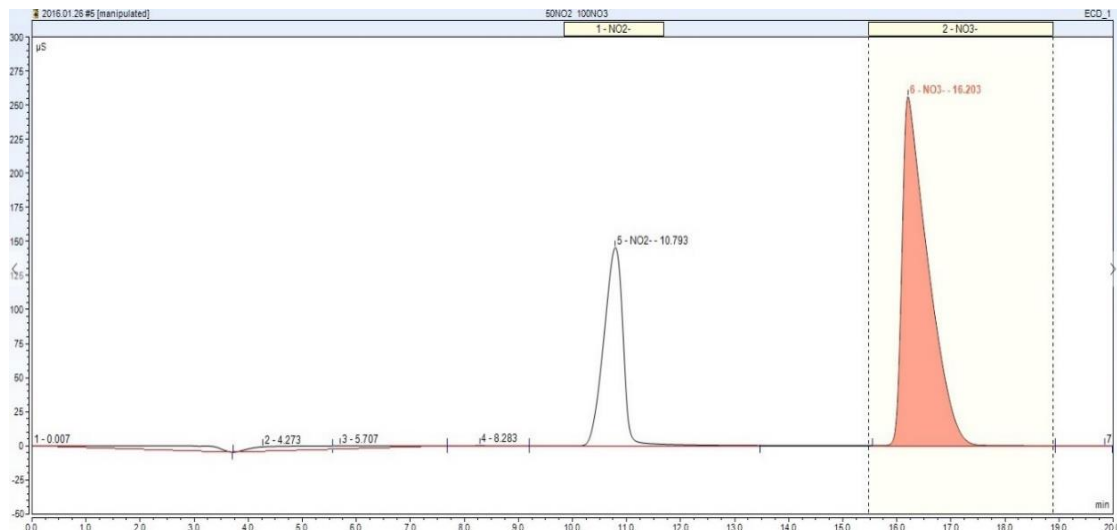


Figure 2.19. Nitrate and nitrite chromatograms

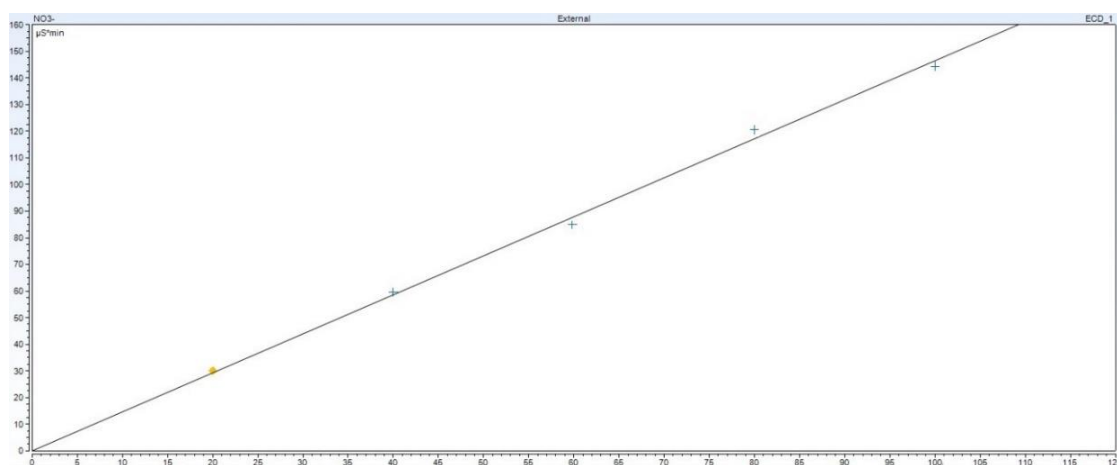


Figure 2.20. Nitrate calibration curve

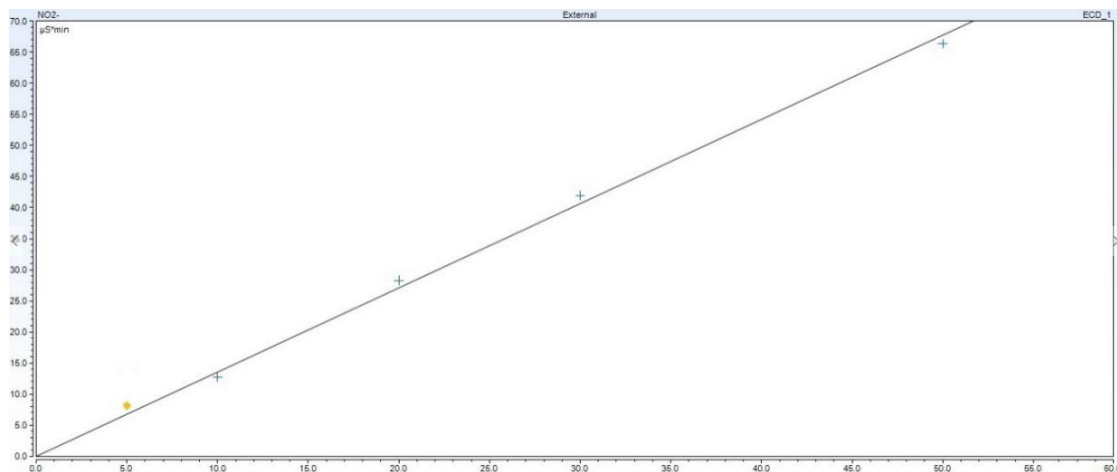


Figure 2.21. Nitrite calibration curve

### 2.2.1.2 Ammonium detection

For the ammonium ion detection is used the cationic suppressor system of guard column (DIONEX IonPac™ CG12A RFIC™ 4 x 50 mm, Thermo Scientific), cationic column (DIONEX IonPac™ CS12A RFIC™ 4 x 250 mm, Thermo Scientific) and cationic suppressor (DIONEX CCRS 500 4 mm, Thermo Scientific). The eluent solution is 20 mM CH<sub>4</sub>SO<sub>3</sub> (Sigma-Aldrich) and 100 mM C<sub>16</sub>H<sub>37</sub>NO (1.5 M, Acros Organics) as regenerant solution. The flow for both solutions in the analysis was 1 mL/min.

The cationic guard column and column are composed by 8.5 µm resin bed and a cationic layer of carboxylic/phosphonic acid. A pair of anion exchange membranes are located on the cationic suppressor to facilitate the selective exchange of anions. The methanesulfonate anions from the eluent are constantly exchanged for hydroxide ions from the regenerant stream, which are removed by the regenerant from the suppressor, and then effecting a continuous suppression (Thermo Scientific 2010).

The retention time for NH<sub>4</sub><sup>+</sup> is c.a. 5.5 min. The calibration curve fits quadratic second order type with a correlation coefficient of R<sup>2</sup>= 0.999 (0 - 6 mg/L NH<sub>4</sub><sup>+</sup>). Examples of an ammonium (3 mg/L) chromatogram and its calibration curve are displayed in Figures 2.22 and 2.23, respectively.

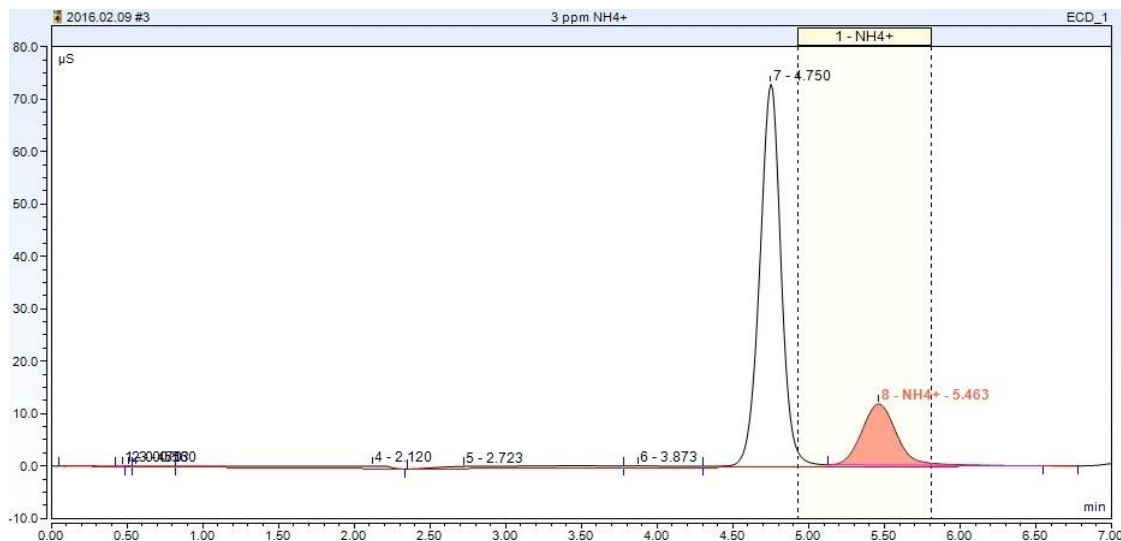


Figure 2.22. Ammonium chromatogram

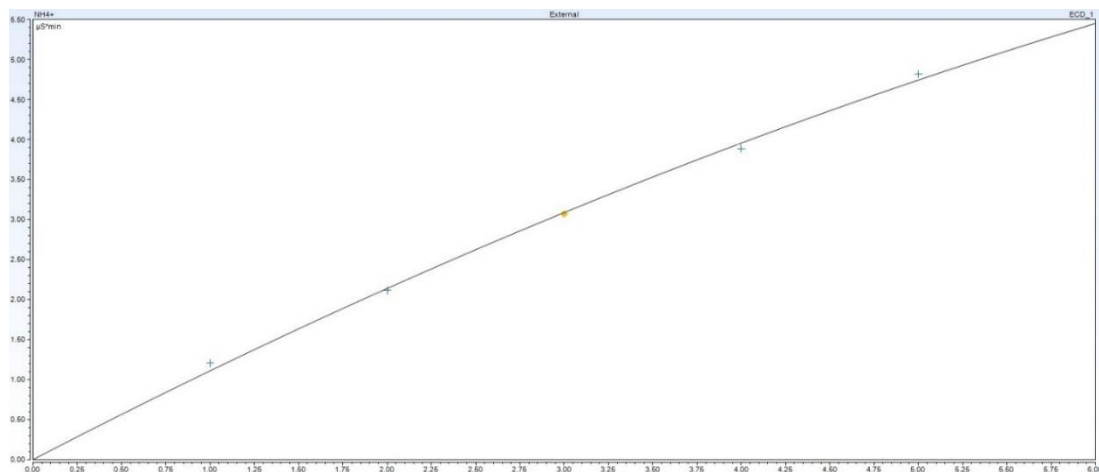


Figure 2.23. Ammonium calibration curve

## 2.2.2 Photometry

The photometry is the measurement of electromagnetic radiation weighted by the human eye's response, and this response changes with each wavelength. In photometry, the word 'luminous' is used to express that measurements were used with a detection system (photometer) that has a spectral response similar to that of a human eye. Internationally-agreed standard observer functions are therefore used to provide a consistent measurement base for photometry; the two most widely used are the  $V(\lambda)$  function, which applies for photopic vision (typical day-time

light levels) and the V'( $\lambda$ ) for scotopic vision (low lighting levels). At intermediate light levels (mesopic or ‘twilight’ levels, such as found on lit roads at night) (NPL 2007).

The  $\text{NO}_3^-$ ,  $\text{NO}_2^-$  and  $\text{NH}_4^+$  ions detection have been done with the MultiDirect (Lovibond) Photometer (Figure 2.24). The MultiDirect (Lovibond) is a fast and simple microprocessor-controlled photometer equipped with a range of pre-programmed methods based on the proven range of Lovibond® tablet reagents, liquid reagents, tube tests and high stable and soluble powder reagents (VARIO Powder Packs). This equipment is a filter photometer that uses interference filters at 6 different wavelengths ( $\lambda = 430, 530, 560, 580, 610$  and  $660\text{ nm}$ ). The unique design of the optics allows the automatic selection of the required wavelength without any moving parts. This and the dual beam technology utilizing an internal reference channel, guarantees the highest accuracy. The concentration function can be used to measure from 2 to 14 known standards. On the basis of the concentrations/absorption pairs obtained, the photometer will calculate a linear interpolation between the measured points (Tintometer-Group 2009).



Figure 2.24. MultiDirect Lovibond Photometer

Blank tube tests (addition of ultrapure water) are compared with the respective ion detection tubes. They are placed in the sample chamber. Figure 2.25 displays the pairs of each tube tests for sample analysis -  $\text{NO}_3^-$  (slight yellow),  $\text{NO}_2^-$  (pink) and  $\text{NH}_4^+$  (green) -, being the blank tube test located on the left side per couple. The detailed methods used for the ions detection are recorded on the Photometer and shown in the *Annex C*, where the procedure to follow for the preparation of the blank and samples tube tests are explained (Lovibond 2009).

The specifications for each analysis are the following:

- Nitrate detection: 1 mL of sample; 1 - 30 mg/L N;  $\lambda = 430$  nm; Method: Chromotropic acid; VARIO Powder reagent: Nitrate Chromotropic;  $t_{\text{reaction}} = 5$  min.
- Nitrite detection: 2 mL of sample; 0.01 - 0.5 mg/L N;  $\lambda = 560$  nm; Method: N-(1-Naphthyl)-ethylendiamine; VARIO Powder reagent: Nitrite LR tablet;  $t_{\text{reaction}} = 10$  min.
- Ammonium detection: 2 mL of sample; 0.02 - 0.5 mg/L N;  $\lambda = 660$  nm; Method: Salicylate; VARIO Powder reagent: Ammonia Salicylate and Ammonia Cyanurate;  $t_{\text{reaction}} = 20$  min.

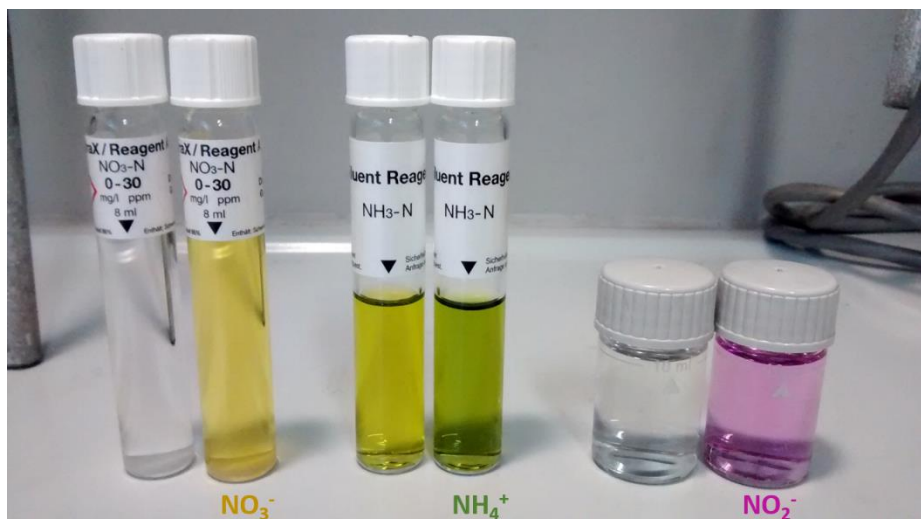


Figure 2.25. Tube tests analyzed by Photometry

### 2.3 Experimental set-up and operational conditions

The catalytic and photocatalytic removal of NO<sub>3</sub><sup>-</sup> and NO<sub>2</sub><sup>-</sup> from aqueous solution were performed in a polytetrafluoroethylene (PTFE) batch reactor under inert standard operational conditions (P = 1 atm, T = 25 °C) (Figure 2.26). In all reactions, 200 mg of each catalyst were dispersed in 350 mL ultrapure water solution, containing an initial water solution of 100 mg/L NO<sub>3</sub><sup>-</sup> (nitrate removal) or 50 mg/L NO<sub>2</sub><sup>-</sup> (nitrite removal), and remained in suspension by a continuous stirring at 500 r.p.m., as already published in our previous work (Luo et al. 2015). The reaction time ( $t_{\text{reaction}}$ ) was 6 hours (Ag,Pt-catalysts, *Chapter 4*), or 24 hours (Pd<sub>2</sub>Sn catalysts, *Chapter 5*). The synthesized nitrate solution fed to the reactor has been 100 mg/L due

to this concentration is commonly found in contaminated groundwater in Europe according to the last EC reports (European Comission 2010). 50 mg/L initial nitrite solution was used because this concentration was the highest obtained among our results. Before the catalyst was introduced into the reactor, the initial solution was purged 10 min with a constant Argon flow ( $Q_{Ar} = 120 \text{ mL/min}$ ) to remove the oxygen (Luiz et al. 2012), and then to avoid reoxidation of the system. The two 4W medium mercury maximum ultraviolet irradiations ( $\lambda=254 \text{ nm}$  (UV-C) and  $\lambda=365 \text{ nm}$  (UV-A)) are located on the top of the reactor. Their light intensity is 7 mW.cm<sup>-2</sup> and spectral curves are depicted in Figure 2.27. In both catalytic and photocatalytic conditions, the reactor was covered with aluminum foil to avoid the external natural light incidence.

The reactor design and detailed specifications were made with the SolidWorks software, and are provided in the *Annex D*.

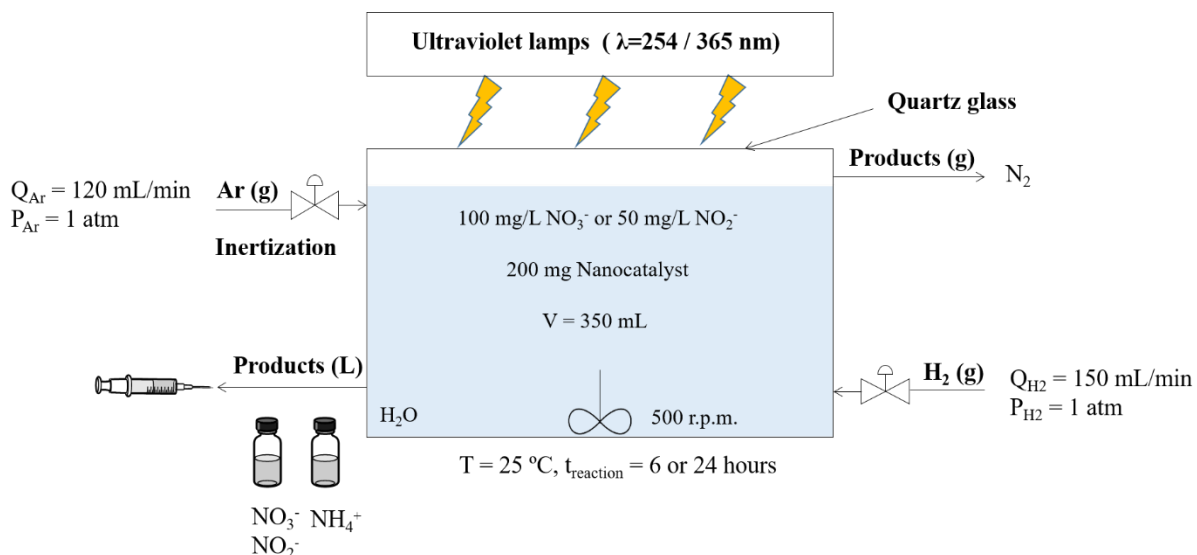


Figure 2.26. Experimental set-up

Sodium nitrate ( $NaNO_3$ ) was generally used as the nitrate source and sodium nitrite ( $NaNO_2$ ) as nitrite source. There was no pH adjustment after addition of the catalyst in the initial solution; thereupon there was not any control on it during reaction and it was measured at the end of the reaction (Final pH).

Conventional catalytic nitrate reduction processes into  $N_2$  and  $H_2O$  lead to some toxic intermediates and by-products, such as  $NO_2^-$  and  $NH_4^+$  (Hörold et al. 1993), thus liquid samples

were withdrawn at the beginning of the reaction and once per hour to analyze the  $\text{NO}_3^-$ ,  $\text{NO}_2^-$  and  $\text{NH}_4^+$  ions by Ion chromatography/Photometer. Several studies proved the existence of  $\text{N}_2$  as the only product gas in these types of reactions and catalysts by Gas chromatography-MS over titania (Zhang et al. 2005; Sá et al. 2009; Wehbe et al. 2009; Doudrick et al. 2013) or over other supports, such as carbon active, alumina and ceria (Barrabés et al. 2011; Aristizábal et al. 2014).

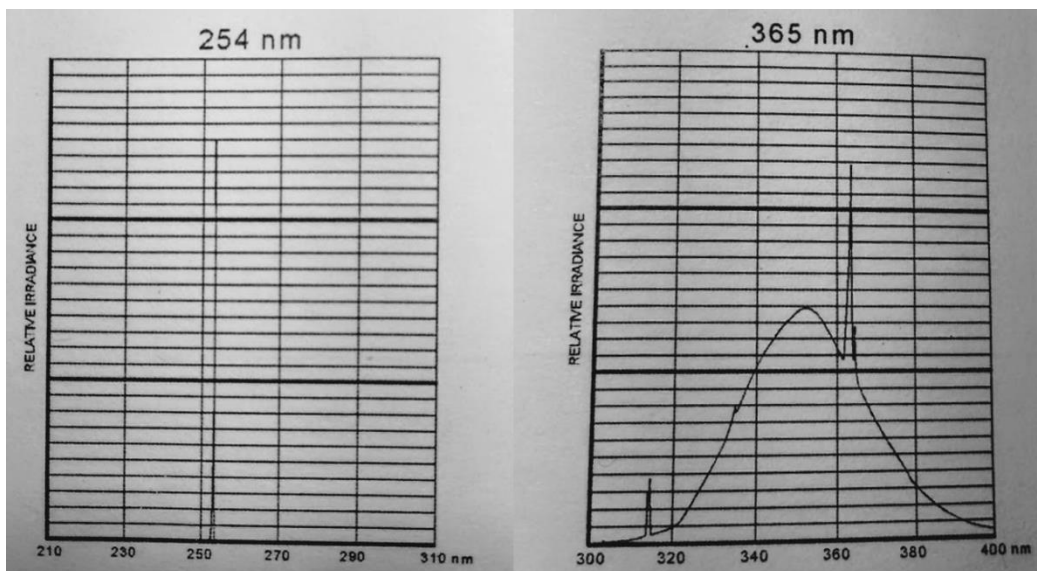


Figure 2.27. Spectral curves of the UV-A and UV-C irradiations used

Due to the high importance of removing completely the oxygen from the system, catalytic nitrate reductions were performed with the same catalyst ( $\text{Ag}(2 \text{ wt. \%})/\text{P}25$ ) in presence of a constant and pure hydrogen flow ( $Q_{\text{H}_2} = 150 \text{ mL/min}$ ), in order to ensure a perfect inertization. Three routes of inertization were tested ( $Q_{\text{Ar}} = 120 \text{ mL/min}$ ):

- A constant Ar flow was applied for 10 min in the initial  $\text{NO}_3^-$  solution before the catalyst introduction into the reactor, and then continuously kept until the reaction finished.
- A constant Ar flow was applied for 10 min in the initial  $\text{NO}_3^-$  solution before the catalyst introduction into the reactor. Afterwards, it was only applied before and after taking sample every hour for a proper liquid mixture of products and to maintain the inertization in the system.

- The initial  $\text{NO}_3^-$  solution before its introduction into the reactor was sonicated for 15 min (Sá et al. 2009), then purged with Ar initially for 10 min, and later before and after taking each sample.

No difference was shown in the catalytic activities and selectivities between the three routes, therefore in this work the last option was used for all catalytic and photocatalytic processes.

## 2.4 Catalytic and photocatalytic behavior calculations

The catalytic and photocatalytic calculated data is shown in the following sections:

### 2.4.1 Nitrate and Nitrite conversions

Nitrate and nitrite conversion (Conv) in percentage are calculated by the following equations:

$$\text{Conv}_{\text{NO}_3^-} = \frac{[\text{NO}_3^-]_0 - [\text{NO}_3^-]_i}{[\text{NO}_3^-]_0} \times 100 \quad (\text{Eq. 2.7})$$

$$\text{Conv}_{\text{NO}_2^-} = \frac{[\text{NO}_2^-]_0 - [\text{NO}_2^-]_i}{[\text{NO}_2^-]_0} \times 100 \quad (\text{Eq. 2.8})$$

Where:  $i$  points out the concentration of the substance (nitrate or nitrite) at the moment of taking sample, and  $0$  the concentration at initial time.

### 2.4.2 Selectivity towards products

The selectivity (Sel.) in percentage from nitrate (Eq. 2.9 - 2.11) and nitrite (Eq. 2.12 - 2.14) reduction towards the respective products are calculated by the equations shown below:

$$\text{Sel}_{\text{NO}_2^-} = \frac{[\text{NO}_2^-]_i}{[\text{NO}_3^-]_0 - [\text{NO}_3^-]_i} \times 100 \quad (\text{Eq. 2.9})$$

$$\text{Sel}_{\text{NH}_4^+} = \frac{[\text{NH}_4^+]_i}{[\text{NO}_3^-]_0 - [\text{NO}_3^-]_i} \times 100 \quad (\text{Eq. 2.10})$$

$$Sel_{N_2} = 100 - (Sel_{NO_2^-} + Sel_{NH_4^+}) \quad (\text{Eq.2.11})$$

$$Sel_{NO_3^-} = \frac{[NO_3^-]_i}{[NO_2^-]_0 - [NO_2^-]_i} \times 100 \quad (\text{Eq.2.12})$$

$$Sel_{NH_4^+} = \frac{[NH_4^+]_i}{[NO_2^-]_0 - [NO_2^-]_i} \times 100 \quad (\text{Eq.2.13})$$

$$Sel_{N_2} = 100 - (Sel_{NO_3^-} + Sel_{NH_4^+}) \quad (\text{Eq.2.14})$$

Where:  $i$  points out the concentration of the substance (nitrate or nitrite) at the moment of taking sample, and  $0$  the concentration at initial time.

#### 2.4.3 Yield towards products

The yields (Yield) to  $NO_2^-$ ,  $NH_4^+$  and  $N_2$  (Eq. 2.15 - 2.17) from nitrate reduction, and towards  $NO_3^-$ ,  $NH_4^+$  and  $N_2$  (Eq. 2.18 – 2.20) from photocatalytic nitrite reduction tests, are calculated by the equations shown below:

$$Yield_{NO_2^-} = \frac{\text{Conv}_{NO_3^-}}{100} \times Sel_{NO_2^-} \quad (\text{Eq. 2.15})$$

$$Yield_{NH_4^+} = \frac{\text{Conv}_{NO_3^-}}{100} \times Sel_{NH_4^+} \quad (\text{Eq. 2.16})$$

$$Yield_{N_2} = 100 - (Yield_{NO_2^-} + Yield_{NH_4^+}) \quad (\text{Eq. 2.17})$$

$$Yield_{NO_3^-} = \frac{\text{Conv}_{NO_2^-}}{100} \times Sel_{NO_3^-} \quad (\text{Eq. 2.18})$$

$$Yield_{NH_4^+} = \frac{\text{Conv}_{NO_2^-}}{100} \times Sel_{NH_4^+} \quad (\text{Eq. 2.19})$$

$$Yield_{N_2} = 100 - (Yield_{NO_3^-} + Yield_{NH_4^+}) \quad (\text{Eq. 2.20})$$

#### **2.4.4 Nitrate reduction rates**

The nitrate reduction rates from the nanocatalysts were fitting pseudo-first order kinetics at a constant initial nitrate concentration of 100 mg/L. The equation used for their calculations was the following (Li et al. 2002; Ko et al. 2011; Sowmya et al. 2014):

$$\ln \frac{C_0}{C_t} = kt \quad (\text{Eq. 2.21})$$

Where:  $k$  is the pseudo-first photocatalytic reaction constant ( $\text{h}^{-1}$ ),  $t$  the time of UV irradiation (h),  $C_0$  the initial nitrate concentration (mg/L), and  $C_t$  the nitrate concentration after a time  $t$  of UV irradiation.

## 2.5 References

- Aristizábal, A., S. Contreras, N. J. Divins, J. Llorca, and F. Medina. 2014. “Effect of Impregnation Protocol in the Metallic Sites of Pt-Ag/activated Carbon Catalysts for Water Denitration.” *Applied Surface Science* 298:75–89.
- Barrabés, N., and J. Sá. 2011. “Catalytic Nitrate Removal from Water, Past, Present and Future Perspectives.” *Applied Catalysis B: Environmental* 104:1–5.
- Barrett, E. P., L. G. Joyner, and P. P. Halenda. 1951. “The Determination of Pure Volume and Area Distributions in Porous Substances. I. Computations from Nitrogen Isotherms.” Contribution from the multiple fellowship of Baugh and sons Company, Mellox Institute. 1896(1948).
- Berndt, H., I. Mönnich, B. Lücke, and M. Menzel. 2001. “Tin Promoted Palladium Catalysts for Nitrate Removal from Drinking Water.” *Applied Catalysis B: Environmental* 30(1):111–22.
- DIONEX. 2012. “Ion Chromatography.”
- Diplas, Spyros. 2013. “X-Ray Photoelectron Spectroscopy - An Introduction.” MENA3100. SINTEF. University of Oslo.
- Dong, D., and Z. Lin Wang. 2009. “Fundamental Theory of Transmission Electron Microscopy.” Nanoscience Research group. School of Materials Science and Engineering. Georgia Tech College.
- Doudrick, K., T. Yang, K. Hristovski, and P. Westerhoff. 2013. “Photocatalytic Nitrate Reduction in Water: Managing the Hole Scavenger and Reaction by-Product Selectivity.” *Applied Catalysis B: Environmental* 136–137:40–47.
- European Comission. 2010. “On Implementation of Council Directive 91/676/EEC Concerning the Protection of Waters against Pollution Caused by Nitrates from Agricultural Sources Based on Member State Reports for the Period 2004-2007.” SEC(2010).
- Hirayama, J., H. Kondo, Y. K. Miura, R. Abe, and Y. Kamiya. 2012. “Highly Effective Photocatalytic System Comprising Semiconductor Photocatalyst and Supported Bimetallic Non-Photocatalyst for Selective Reduction of Nitrate to Nitrogen in Water.” *Catalysis Communications* 20(3):99–102.
- Van Holde, K. E., W. Curtis Johnson, and P. Shing Ho. 2006. “Principals of Physical Biochemistry.”
- Hörhold, S., K. D. Vorlop, T. Tacke, and M. Sell. 1993. “Development of Catalysts for a Selective Nitrate and Nitrite Removal from Drinking Water.” *Catalysis Today* 17:21–30.

- Jentoft, F. 2004. "Diffuse Reflectance IR and UV-Vis Spectroscopy. Modern Methods in Heterogeneous Catalysis."
- Kiely, C. 2010. "Electron Microscopy: New Views of Catalysts." Nature Publishing Group 9(4):296–97.
- Knözinger, H., and K. Kochloefl. 2009. "Heterogeneous Catalysis and Solid Catalysts." Ullmann's Encyclopedia of Industrial Chemistry 1:2–110.
- Ko, S., C. K. Banerjee, and J. Sankar. 2011. "Photochemical Synthesis and Photocatalytic Activity in Simulated Solar Light of Nanosized Ag Doped TiO<sub>2</sub> Nanoparticle Composite." Composites Part B: Engineering 42(3):579–83.
- Li, F. B., F. B. Li, X. Z. Li, and X. Z. Li. 2002. "The Enhancement of Photodegradation Efficiency Using Pt-TiO<sub>2</sub> Catalyst." Chemosphere 48:1103–11.
- Lovibond. 2009. "Photometer System Multidirect." Instruction Manual.
- Luiz, D. De Bem, S. L. Floriani Andersen, C. Berger, H. J. José, and R. De Fátima Peralta Muniz Moreira. 2012. "Photocatalytic Reduction of Nitrate Ions in Water over Metal-Modified TiO<sub>2</sub>." Journal of Photochemistry and Photobiology A: Chemistry 246:36–44.
- Luo, Z., M. Ibáñez, A. M. Antolín, A. Genç, A. Shavel, S. Contreras, F. Medina, J. Arbiol, and A. Cabot. 2015. "Size and Aspect Ratio Control of Pd<sub>2</sub>Sn Nanorods and Their Water Denitration Properties." Langmuir 31(13):3952–57.
- Micromeritics. 2006. ASAP 2020 Operator's Manual.
- Micromeritics. 2009. AutoChem 2920 Automated Catalyst Characterization System Operator's Manual.
- Monshi, A., M. Reza Foroughi, and M. Reza Monshi. 2012. "Modified Scherrer Equation to Estimate More Accurately Nano-Crystallite Size Using XRD." World J. Nano Sci. Eng. 2(3):154.
- Nils Hasselmo Hall EM lab. 2007. "Jeol 1200-EX II Instructions." 1–16.
- NPL. 2007. "Principles of Photometry Throwing Light on the Use and Abuse of Luxmeters."
- NPTEL. 2014. "Catalyst Characterization - Thermal Analysis." MHRD project. Government of India.
- Pinna, F. 1998. "Supported Metal Catalysts Preparation." Catalysis Today 41(1–3):129–37.
- S.I-No.106. 2007. "European Communities Drinking Water Regulations."
- Sá, J., C. Alcaraz Agüera, S. Gross, and J. A. Anderson. 2009. "Photocatalytic Nitrate Reduction over Metal Modified TiO<sub>2</sub>". Applied Catalysis B: Environmental 85:192–200.
- Shimadzu. 2016. "Diffuse Reflectance Measurement."

- Sing, K. S. W. 1985. "Reporting Physisorption Data for Gas/solid Systems with Special Reference to the Determination of Surface Area and Porosity (Recommendations 1984)." *Pure and Applied Chemistry* 57(4):603–19.
- Smart, R., S. McIntyre, and I. Bello. 2009. "X - Ray Photoelectron Spectroscopy." Department of Physics and Material Science. City university of Hong Kong.
- Soares, O. S. G. P., M. F. R. Pereira, J. J. M. Orfao, J. L. Faria, and C. G. Silva. 2014. "Photocatalytic Nitrate Reduction over Pd-Cu/TiO<sub>2</sub>." *Chemical Engineering Journal* 251:123–30.
- Sowmya, A., and S. Meenakshi. 2014. "Photocatalytic Reduction of Nitrate over Ag-TiO<sub>2</sub> in the Presence of Oxalic Acid." *Journal of Water Process Engineering* 4–11.
- Thermo ARL. 1999. "Basics of X-Ray Diffraction. Introduction to Powder/ Polycrystalline Diffraction." Chapter7.
- Thermo Scientific. 2001. "IonPac ® AS9-SC and AS9-HC Anion-Exchange Columns."
- Thermo Scientific. 2010. "Product Manual for Dionex IonPac™ CS12A and CG12A Columns 031132-09."
- Thermo Scientific. 2015. "Dionex CRS 500. Product Manual."
- Tintometer-Group. 2009. "MultiDirect Lovibond Photometer." (July):62–65.
- Torrent, J., and V. Barrón. 2008. "Diffuse Reflectance Spectroscopy." Soil Science Society of American, 677S. Madison, USA. Chapter 13.
- Univ. of Illinois. 2005. "X-Ray Photoelectron Spectroscopy ( XPS )." Center for microanalysis of materials. Frederick Seitz Material Research Laboratory. University of Illinois, USA.
- Webb, P. A. 2003. "Introduction to Chemical Adsorption Analytical Techniques and Their Application to Catalysis." Micromeritics Instrument Corp., Norcross, Georgia (January).
- Wehbe, N., M. Jaafar, C. Guillard, J. M. Herrmann, S. Miachon, E. Puzenat, and N. Guilhaume. 2009. "Comparative Study of Photocatalytic and Non-Photocatalytic Reduction of Nitrates in Water." *Applied Catalysis A: General* 368:1–8.
- Wodka, D., E. Bielanska, R. P. Socha, M. Elzbieciak-Wodka, J. Gurgul, P. Nawek, P. Warszynski, and I. Kumakiri. 2010. "Photocatalytic Activity of Titanium Dioxide Modified by Silver Nanoparticles." *ACS Applied Materials and Interfaces* 2(7):1945–53.
- Zhang, F., R. Jin, J. Chen, C. Shao, W. Gao, L. Li, and N. Guan. 2005. "High Photocatalytic Activity and Selectivity for Nitrogen in Nitrate Reduction on Ag/TiO<sub>2</sub> Catalyst with Fine Silver Clusters." *Journal of Catalysis* 232:424–31.

## CHAPTER 3:

**Synthesis and Physicochemical  
properties of the Ag and Pt/P25  
mono- and bimetallic catalysts**

### **3. Synthesis and Physicochemical properties of the Ag and Pt/P25 mono- and bimetallic catalysts**

The main scope of this research (deeply detailed in the *Chapter 1*) is to develop a bimetallic catalyst impregnated over the support Aerioxide Titania P25 (P25) to reduce the nitrate ion from water towards non-toxic nitrogen gas to obtain drinking water accomplishing the European Union Normative (50 mg/L  $\text{NO}_3^-$ , 0.5 ppm  $\text{NO}_2^-$ , 0.3 ppm  $\text{NH}_4^+$ ) (S.I-No.106 2007). The water treatment used for this purpose is the classical heterogeneous catalytic process and, less classical, the photocatalytic process using pure hydrogen flow as the reducing agent under standard operational conditions (room temperature, atmospheric pressure).

In this chapter, the preparation and the physicochemical properties of several monometallic (Ag or Pt) and bimetallic (Ag-Pt, Pt-Ag) supported on  $\text{TiO}_2$  P25 nanocatalysts are described. Various main parameters have been modified to study their influence on the catalytic and photocatalytic activities.

The first part (3.1) describes the synthesis and the physicochemical properties of the monometallic catalysts based on silver or platinum onto P25 – Ag/P25 or Pt/P25 – which have been prepared in order to determine the specific role of each noble metal in the catalytic/photocatalytic nitrate reaction. The following parameters have been varied: the noble metal loading (Ag: from 0.5 to 4 wt. %; Pt: 2 and 4 wt. %), and the platinum precursors ( $\text{H}_2\text{PtCl}_6 \cdot 6\text{H}_2\text{O}$  and  $\text{K}_2\text{PtCl}_6$ ).

The second part (3.2) details the synthesis and the physicochemical properties of the bimetallic catalysts based on both noble metals over the P25 – Ag-Pt/P25 and Pt-Ag/P25 –. In these bimetallic catalysts we have varied: the platinum loading (2 and 4 wt. %), the platinum precursors ( $\text{H}_2\text{PtCl}_6 \cdot 6\text{H}_2\text{O}$  and  $\text{K}_2\text{PtCl}_6$ ), and the impregnation order of both metals (Ag-Pt and Pt-Ag). The silver amount was fixed at 2 wt. % because at this loading the monometallic catalyst Ag/P25 shows the best catalytic behavior (*Chapter 4*).

Several characterization techniques have been applied on the fresh catalysts powders to study their physicochemical properties for a deeper understanding of their activity. The chemical structure and textural properties of the samples have been studied through X-Ray Diffraction (XRD) and the Nitrogen physisorption ( $\text{N}_2$ -Physisorption) techniques. The Transmission Electron Microscopy (TEM) was used to observe the morphology of the samples and determine

the metal nanoparticles size. The optical absorption properties have been analyzed through the diffuse reflectance UV-Vis Spectroscopy (DRUV-Vis). The X-Ray Photoelectron Spectroscopy (XPS) allowed us to determine the chemical state of the different elements within the materials. The differences in the reducibility of the catalysts have been analyzed using the Temperature-Programmed Reduction by hydrogen (H<sub>2</sub>-TPR) technique. In *Chapter 2* all these catalyst characterization techniques and the operational conditions used in each equipment for the different measurements are detailed.

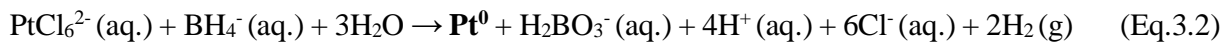
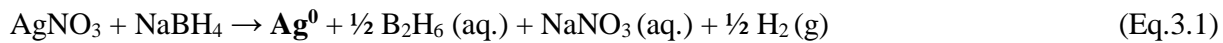
### **3.1 Monometallic catalysts**

In this section we report the synthesis method and the physicochemical properties of all the monometallic catalysts (Ag, Pt).

#### 3.1.1 Synthesis method

The heterogeneous catalysts were synthesized using the well-known technique of wise-drop incipient wetness impregnation of Aeroxide P25 powder (Acros Organics) with the respective precursors: AgNO<sub>3</sub> (65%, Johnson Matthey), H<sub>2</sub>PtCl<sub>6</sub>·6H<sub>2</sub>O (Alfa Aesar) or K<sub>2</sub>PtCl<sub>6</sub> (Aldrich). The precursor impregnation was followed by a chemical reduction with sodium borohydride (NaBH<sub>4</sub>, Aldrich) to obtain the metal NPs over the support. The chemical reduction method is still one of the most common methods applied, using typically the sodium borohydride as reducing agent among several others, i.e. hydrazine, formic acid, citric acid, hydrogen (Han et al. 2012; Sridharan et al. 2013; Li et al. 2014; Calderón-Magdaleno et al. 2014; Zaleska-Medynska et al. 2016), because it could be used either in aqueous or non-aqueous media (Ghosh Chaudhuri et al. 2012), and also because it possess a high reducing potential (from 0.48 eV at pH = 0 to -1.24 eV at pH = 14). In the chemical reduction process, an electron transfer from the reducing agent – electron donor – to the metal ion – electron acceptor – occurs (Zaleska-Medynska et al. 2016). In this catalyst synthesis method, different parameters are very important, i.e. temperature, metal precursors, reducing agents (Tang et al. 2004).

The most probable chemical reduction mechanisms by NaBH<sub>4</sub> of metal precursors AgNO<sub>3</sub> (Eq. 3.1) (Mulfinger et al. 2007; Rashid et al. 2013), H<sub>2</sub>PtCl<sub>6</sub>·6H<sub>2</sub>O (Eq. 3.2) (Coutanceau et al. 2012) and K<sub>2</sub>PtCl<sub>6</sub> (Eq. 3.3), are the following:



Various monometallic catalysts (Table 3.1) based on Ag or Pt over the support Aeroxide TiO<sub>2</sub> P25 (P25) (Figure 3.1) have been prepared varying the Ag and Pt metal loading (from 0-5 to 4 wt. %) and the Pt precursor (H<sub>2</sub>PtCl<sub>6</sub>·6H<sub>2</sub>O/K<sub>2</sub>PtCl<sub>6</sub>). The catalysts are noted as:

- Ag(x)/P25, where x = 0.5, 1, 1.5, 2, 3 and 4 wt. %.
- Pt(x)/P25(H or K), where x = 2 and 4 wt. %; (H) = H<sub>2</sub>PtCl<sub>6</sub>·6H<sub>2</sub>O or (K) = K<sub>2</sub>PtCl<sub>6</sub>.

Table 3.1. Notation of the monometallic catalysts prepared

Catalyst	Ag (wt.%)	Pt (wt.%)	Pt precursor		K (wt.%)
			H <sub>2</sub> PtCl <sub>6</sub> ·6H <sub>2</sub> O	K <sub>2</sub> PtCl <sub>6</sub>	
Ag(0.5)/P25	0.5	-	-	-	-
Ag(1)/P25	1	-	-	-	-
Ag(1.5)/P25	1.5	-	-	-	-
Ag(2)/P25	2	-	-	-	-
Ag(3)/P25	3	-	-	-	-
Ag(4)/P25	4	-	-	-	-
Pt(2)/P25(H)	-	2	X	-	-
Pt(2)/P25(K)	-	2	-	X	-
Pt(4)/P25(H)	-	4	X	-	-
Pt(4)/P25(K)	-	4	-	X	-
Ag(2)/P25+Pt(4)/P25(H)	2	4	X	-	-
K(2)/P25	-	-	-	-	2
K(4)/P25	-	-	-	-	4

The detailed preparation protocols are described below.

In the case of the Ag(x)/P25 catalysts, W g AgNO<sub>3</sub> (Table 3.2) was dissolved in 0.5 mL of ultrapure water and deposited drop by drop over 2 g of TiO<sub>2</sub> P25. The obtained powder was dried at 100 °C overnight, and then calcined at 400 °C overnight, getting the metal oxides and avoiding the utilization of P25 – thermal transformation of TiO<sub>2</sub> into rutile phase (Viswanathan et al. 2009).

Preparation of the Pt(x)/P25(H or K) monometallic catalysts (Table 3.2) followed the same impregnation protocol using aqueous solutions of Y g of H<sub>2</sub>PtCl<sub>6</sub>·6H<sub>2</sub>O or Z g of K<sub>2</sub>PtCl<sub>6</sub> dissolved in 0.5 mL of ultrapure water.

Afterwards, the desirable amount of catalyst was stirred in 20 ml of EtOH (absolute PRS, Panreac) and 20 mg of NaBH<sub>4</sub>, previously stirred in 5 ml of EtOH, was drop-wise added. The solution color turns out to dark yellow (Ag) and grey (Pt). Thereupon, catalyst is filtered under vacuum (Cellulose acetate filter, 0.45 µm) and washed with EtOH several times. As Ag gets oxidized fast, the catalyst was immediately introduced inside the reactor or characterized (Figure 3.1).

Moreover, potassium monometallic catalysts (at 2 and 4 wt. %) (Table 3.1 and 3.2) were prepared following exactly the same protocol as described before, using KCl (Aldrich) as K precursor. These K-based monometallics were synthesized for the sake of comparison in the photocatalytic nitrate reduction tests.

Table 3.2. Composition of the aqueous impregnation solutions of the monometallic precursors

Catalyst	Ag (W g)	Pt	K (g)
		H <sub>2</sub> PtCl <sub>6</sub> ·6H <sub>2</sub> O (Y g)	K <sub>2</sub> PtCl <sub>6</sub> (Z g)
Ag(0.5)/P25	0.016	-	-
Ag(1)/P25	0.031	-	-
Ag(1.5)/P25	0.047	-	-
Ag(2)/P25	0.063	-	-
Ag(3)/P25	0.094	-	-
Ag(4)/P25	0.126	-	-
Pt(2)/P25(H)	-	0.084	-
Pt(2)/P25(K)	-	-	0.101
Pt(4)/P25(H)	-	0.168	-
Pt(4)/P25(K)	-	-	0.203
Ag(2)/P25+Pt(4)/P25(H)	0.063	0.168	-
K(2)/P25	-	-	0.076
K(4)/P25	-	-	0.152

The visual aspect of TiO<sub>2</sub> P25 and of the Ag or Pt-monometallic catalysts is shown in the Figure 3.1.

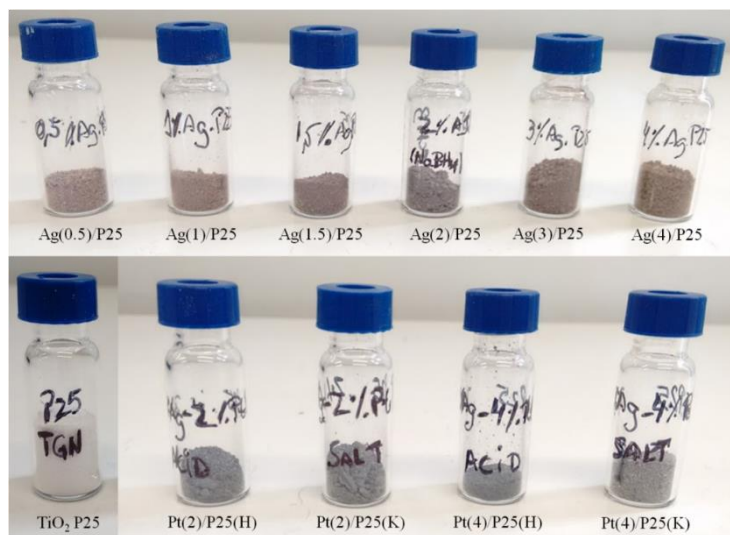


Figure 3.1. Visual aspect of Aeroxide  $\text{TiO}_2$  P25 and of the monometallic catalyst powders

### 3.1.2 Characterization

#### 3.1.2.1 X-Ray Diffraction (XRD)

The powder XRD patterns allow determining the nature of the crystalline phases present in the  $\text{TiO}_2$  P25 (P25) and P25 calcined at 400 °C (P25 400 °C), which corresponds to the calcination temperature in the catalyst synthesis, and in the monometallic samples.

As expected P25 and P25 400 °C (ca. 80 anatase/20 rutile, % w/w) (Figure 3.2), and the reduced monometallic catalysts (Figures 3.3 and 3.4) show in the 10 – 70  $2\theta$  range the characteristic peaks of the anatase (JCPDS 021-1272) and rutile (JCPDS 021-1274) crystalline phases.

- Anatase:  $2\Theta = 25.28^\circ, 36.95^\circ, 37.04^\circ, 37.80^\circ, 38.58^\circ, 48.08^\circ, 48.18^\circ, 53.89^\circ, 54.04^\circ, 55.06^\circ, 55.21^\circ, 62.69^\circ, 62.86^\circ, 68.76^\circ, 68.96^\circ$ .
- Rutile:  $2\Theta = 27.45^\circ, 27.52^\circ, 30.87^\circ, 36.09^\circ, 36.18^\circ, 41.23^\circ, 41.33^\circ$ .

The average crystallite sizes of the anatase and rutile phases before and after calcination at 400 °C were determined according to the Scherrer equation (Eq. 3.4):

$$D = \frac{0.9\lambda}{\beta \cos\theta} \quad (\text{Eq. 3.4})$$

Where:  $D$  is the average crystallite size of the catalyst,  $\lambda$  is the X-Ray wavelength,  $\beta$  is the full width at half maximum (FWHM) of the peak and  $\theta$  the diffraction angle of the peak (Bragg angle) (*Chapter 2, section 2.1.1.1*).

This equation relates the average crystallite size of the particles to the width of a peak in the diffraction pattern. In this case, it relates the average crystallite sizes to the width of the anatase (101) and rutile (110) characteristic peaks (Sakthivel et al. 2004; Qiu et al. 2006; Wang et al. 2012). The average crystallite size for anatase and rutile phase were denoted as Da and Dr, respectively.

There is practically no change in the nature of the crystalline phases after calcinations of P25 at 400°C, however, some peaks are slightly narrowed, which is attributed to a small increase in the crystallite sizes from Da = 22.1 nm and Dr = 36 nm in P25 to Da = 22.4 nm and Dr = 40.7 nm in P25 400 °C, as reported by Wang et al. (Wang et al. 2012). This will be further confirmed by a slight decrease in surface area obtained by nitrogen physisorption (3.1.2.2).

No additional peaks due to metallic particles are observed for Ag- (JCPDS 065-2871) and Pt-containing (JCPDS 004-0802) monometallic catalysts because of the too low sensitivity of XRD analysis at such metal loadings (< 5 wt. %) and/or the low size and high dispersion of the metallic particles (Matos et al. 2012; Talat-Mehrabad et al. 2015). Moreover, Ag and Pt additions do not interfere in the structure of P25, pointing out that the metal NPs are deposited onto the support and not dissolved in it (Lee et al. 2014). This has been observed by the TEM technique as well (3.1.2.3). Therefore, the addition of different silver (Figure 3.3) or platinum (Figure 3.4) loadings do not influence the structure of the support.

Characteristic peaks of K<sub>2</sub>PtCl<sub>6</sub> precursor (JCPDS 070-1346) are present in the XRD pattern of the sample Pt(4)/P25(K) (Figure 3.4), indicating that oxidized Pt is present, as further confirmed by XPS analysis (3.2.2.5).

- K<sub>2</sub>PtCl<sub>6</sub>: 2θ = 15.73°, 18.18°, 25.82°, 45.53°.

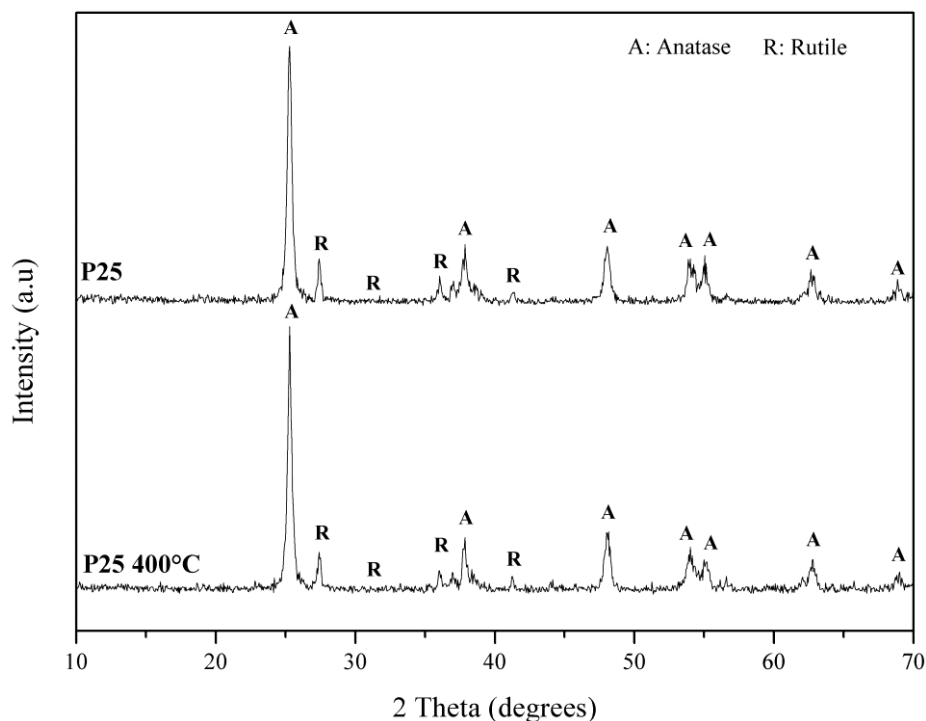


Figure 3.2. XRD patterns of P25 and P25 calcined at 400 °C

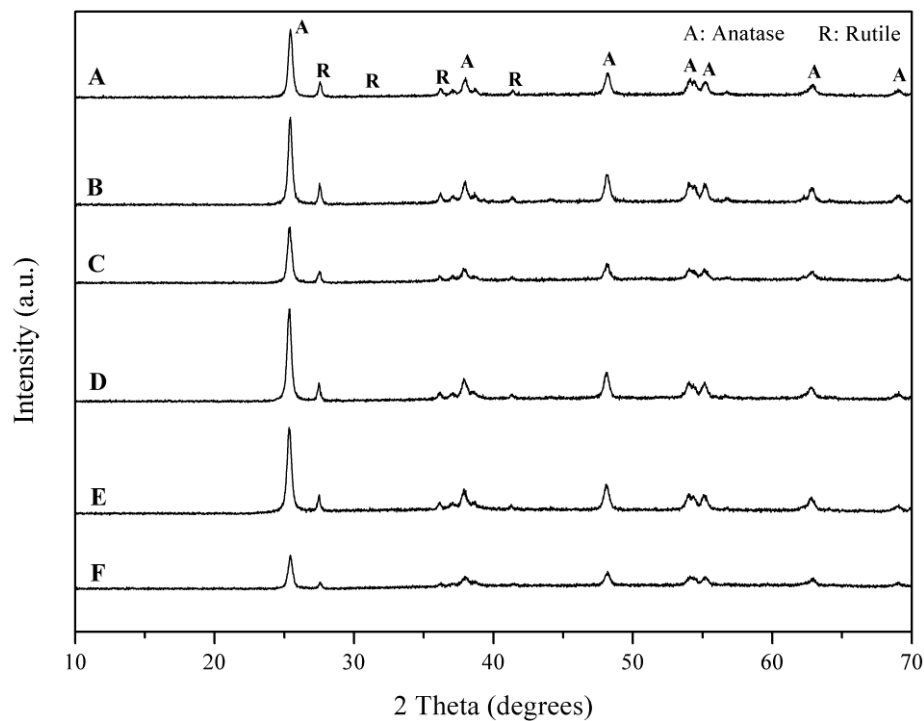


Figure 3.3. XRD patterns of: A) Ag(0.5)/P25, B) Ag(1)/P25, C) Ag(1.5)/P25, D) Ag(2)/P25, E) Ag(3)/P25, and F) Ag(4)/P25

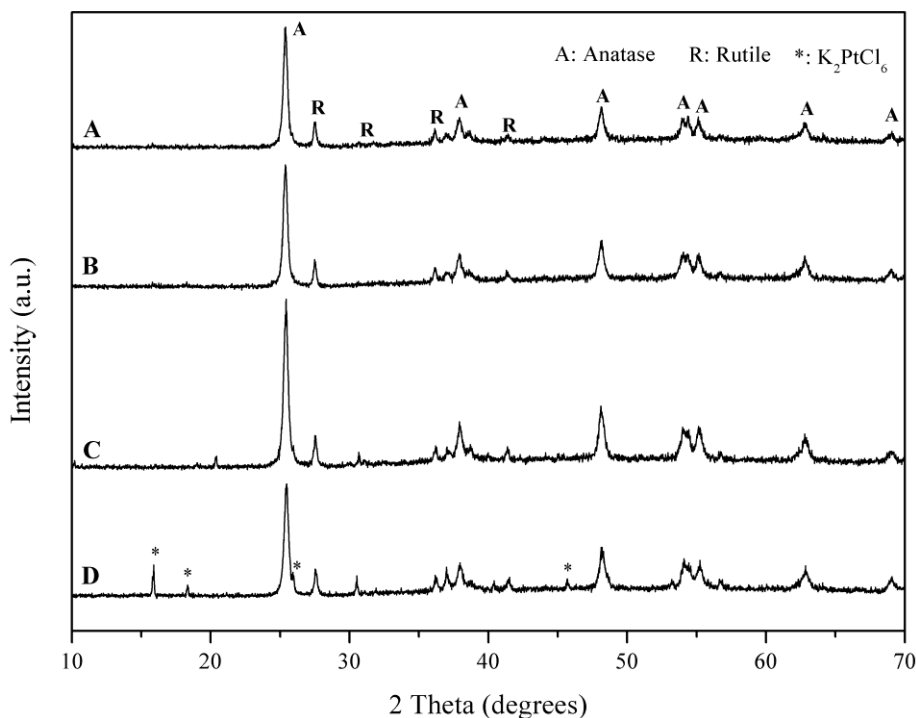


Figure 3.4. XRD patterns of: A) Pt(2)/P25(H), B) Pt(2)/P25(K), C) Pt(4)/P25(H), and D) Pt(4)/P25(K)

### 3.1.2.2 Nitrogen Physisorption

The nitrogen adsorption-desorption isotherms were done on selected reduced samples (Figure 3.5) in order to determine their surface areas ( $S_{BET}$ ) (BET method), pore volumes ( $V_{Pore}$ ) and average pore diameters ( $\bar{\phi}_{Pore}$ ) (BJH method) (Table 3.3).

The  $TiO_2$  P25 support before and after thermal treatment at 400 °C, and the selected monometallic samples exhibit a type H3 hysteresis loop according to BDDT classification, (Sing et al. 1985; Wang et al. 2012), characteristic of materials with mesopores (2 - 50 nm), whatever the nature and the load of noble metal (Ag, Pt) impregnated. Furthermore, as the hysteresis loop approaches a relative pressure  $P/P_0 \approx 1$ , the samples exhibit large mesopores and macropores due to interparticle condensation (> 50 nm) (Tsai et al. 2004; Yu et al. 2011; Wang et al. 2012).

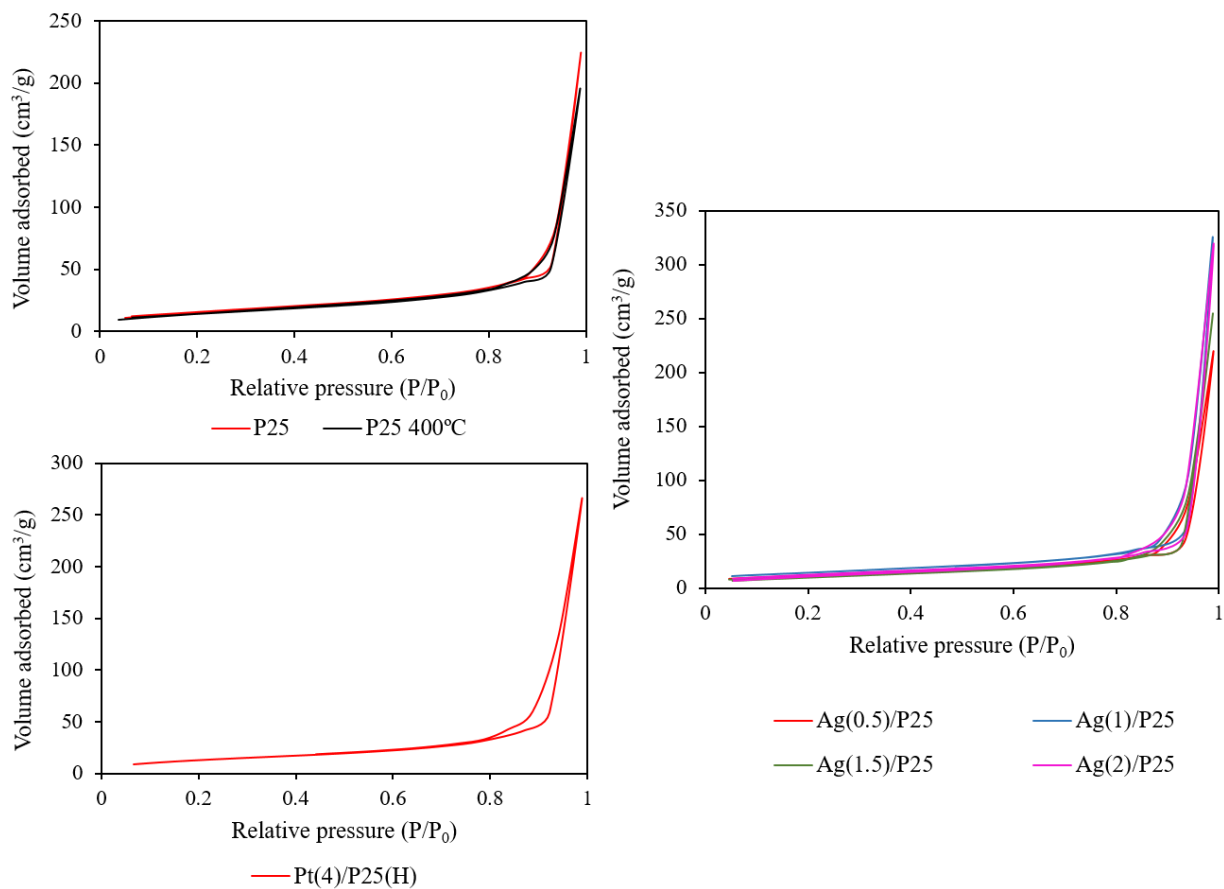


Figure 3.5. Nitrogen adsorption-desorption isotherms of P25, P25 calcined at 400°C and of selected monometallic catalysts

The surface area for  $\text{TiO}_2$  P25,  $55 \text{ m}^2\text{g}^{-1}$ , decreases to  $50 \text{ m}^2\text{g}^{-1}$  after calcination at  $400^\circ\text{C}$ , which is in agreement with literature data. Viswanathan et al. reported that the BET surface area slightly decreases - ca. 7 % - when increasing the calcination temperature of P25 until  $500^\circ\text{C}$  (Viswanathan et al. 2009). Wang et al. observed a decrease in surface area associated to an increase in the average crystallite size when calcined at  $400^\circ\text{C}$  (from 31.7 to 33.8 nm) (Wang et al. 2012). The Scanning Electron Microscopy (SEM) images of P25 and P25 calcined at  $400^\circ\text{C}$  reported by Wang et al. (Figure 3.6.) show that this decrease is not significant.

Table 3.3. Specific surface area, pore volume and mean pore diameter of P25, P25 calcined at 400°C and selected monometallic catalysts

Catalyst	$S_{BET}$ ( $\text{m}^2\text{g}^{-1}$ )	$V_{\text{Pore}}$ ( $\text{cm}^3\text{g}^{-1}$ )	$\varnothing_{\text{Pore}}$ (nm)
P25	55	0.3	33
P25 400 °C	50	0.3	33
Ag(0.5)/P25	41	0.3	26
Ag(1)/P25	49	0.5	26
Ag(1.5)/P25	39	0.4	26
Ag(2)/P25	45	0.5	25
Pt(4)/P25(H)	50	0.4	26

After impregnation of the metals onto P25, the surface areas of the catalysts are in the range of 42 to 50  $\text{m}^2\text{g}^{-1}$ , and their pore volume is about 0.4  $\text{cm}^3\text{g}^{-1}$  with a mean pore diameter of 26 nm. There is a tendency toward a larger decrease of the BET area with Ag (2 - 22 %), except for Ag(1)/P25 (2 %), than with Pt (Pt(4)/P25(H)). Pulido Melián et al. demonstrated that increasing the amount of impregnated silver onto P25 from 0.1 to 5 % wt. led to larger crystallite sizes, and then to a decrease of the surface area from 49 to 41  $\text{m}^2\text{g}^{-1}$  (Pulido Melián et al. 2012).

A decrease of the mean pore diameter (ca. 21 - 24 %) is also observed in comparison to P25 400 °C, while no decrease of the pore volume is observed. This could account for deposition of metallic species or NaBH<sub>4</sub> in the chemical reduction step at the entry of the pores, blocking them partially (Xu et al. 2015). In summary, there is only a small influence of the metals impregnated on the textural properties of the support (Iliev et al. 2006).

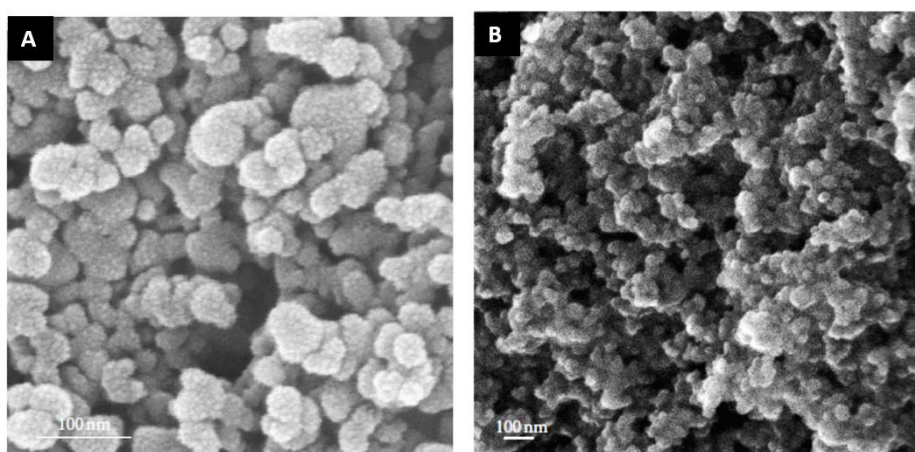


Figure 3.6. SEM images of: A) P25 and B) P25 400 °C (Wang et al. 2012)

### 3.1.2.3 Transmission Electron Microscopy (TEM)

The morphology of bare  $\text{TiO}_2$  P25, P25 400 °C, Ag(2)/P25, Pt(2)/P25(H), Pt(4)/P25(H), Pt(2)/P25(K) and Pt(4)/P25(K) were analyzed by TEM and the images are displayed in Figures 3.7 to 3.10. The mean particle diameter of the monometallic samples are reported in Table 3.4.

The TEM images of bare  $\text{TiO}_2$  P25 and of P25 400 °C display spherical-shape particles ranging from 20 to 70 nm (Figure 3.7). P25 is composed of anatase and rutile crystalline phases (anatase: rutile, ca. 80:20), however they are not distinguishable by TEM. Moreover, it can be observed that the particles are randomly superimposed resulting in black regions, making more difficult to detect the metal NPs when they are deposited on them (black dots over P25).

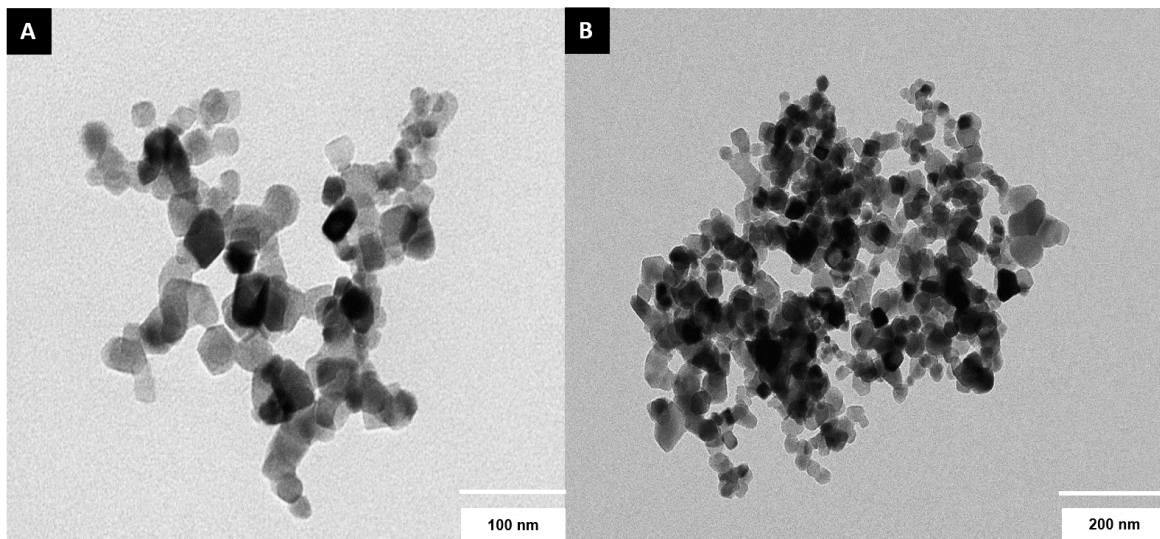


Figure 3.7. TEM image of  $\text{TiO}_2$  P25: A) before and B) after calcination at 400 °C

In the Ag(2)/P25 catalyst (Figure 3.8) the Ag spherical-shape NPs are heterogeneously distributed on the surface of P25 particles with an average crystallite size of 3.1 nm, showing the largest mean particle diameter among monometallic catalysts (Table 3.4).

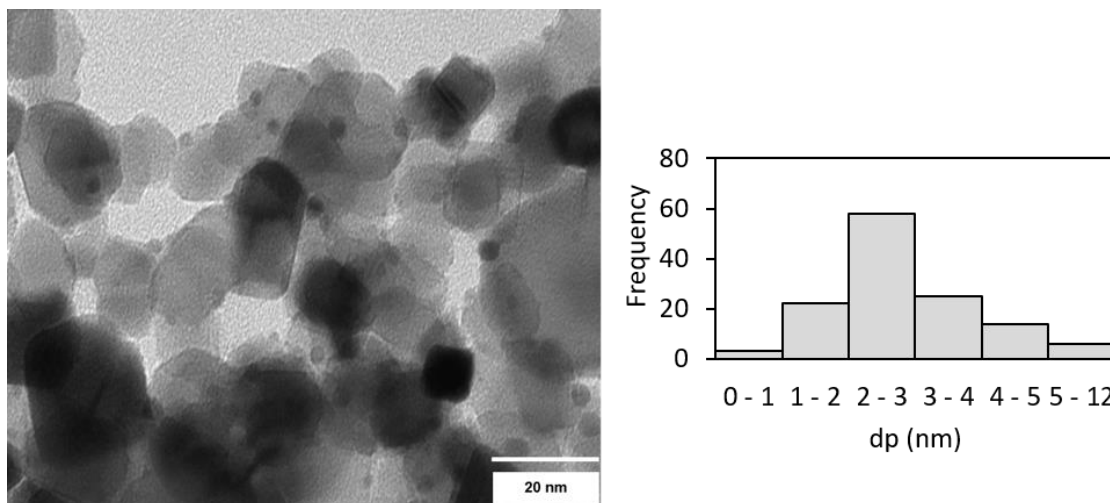


Figure 3.8. TEM image and histogram of Ag(2)/P25

The TEM images of the Pt-monometallic catalysts are displayed in Fig. 3.9 and 3.10 for the  $\text{H}_2\text{PtCl}_6 \cdot 6\text{H}_2\text{O}$  and  $\text{K}_2\text{PtCl}_6$  precursors, respectively.

The behavior of the monometallic Pt-containing catalysts differs slightly depending on the precursor. Using  $\text{K}_2\text{PtCl}_6$  (K), the Pt NPs present an average size of 2.2 nm (Figure 3.10), and the NPs are larger and more agglomerated (higher standard deviation) than using  $\text{H}_2\text{PtCl}_6 \cdot 6\text{H}_2\text{O}$  (H) precursor, which leads to higher dispersion with an average particle size of 1.4 nm (Figure 3.9). Besides, in this latter case (H), the Pt particles are found on the overall surface of the support but with a preferential distribution at the boundaries of the particles. If the amount of platinum is raised from 2 to 4 wt. %, higher quantity of NPs are observed as expected.

Due to the composition of P25, the metal particles are mostly deposited on the anatase phase as previously demonstrated by Sclafani et al. (Sclafani et al. 1997, 1998). The influence of the precursor on the Pt dispersion can be explained based on the IEP - Isoelectric point - for  $\text{TiO}_2$  P25 of  $\sim 6.2$  (Suttiponparnit et al. 2011) and the pH of aqueous  $\text{H}_2\text{PtCl}_6 \cdot 6\text{H}_2\text{O}$  and  $\text{K}_2\text{PtCl}_6$  solutions of ca. 1 and 2, respectively. The electrostatic interaction between  $[\text{PtCl}_6]^{2-}$  species and  $\text{TiO}_2$  is higher and the dispersion is enhanced using  $\text{H}_2\text{PtCl}_6 \cdot 6\text{H}_2\text{O}$  (Kanda et al. 2009). Moreover, the chlorine-containing mobile species  $[\text{Pt}_y\text{O}_x\text{Cl}_y]$  also probably formed increase the Pt dispersion onto the support (Antos et al. 2004).

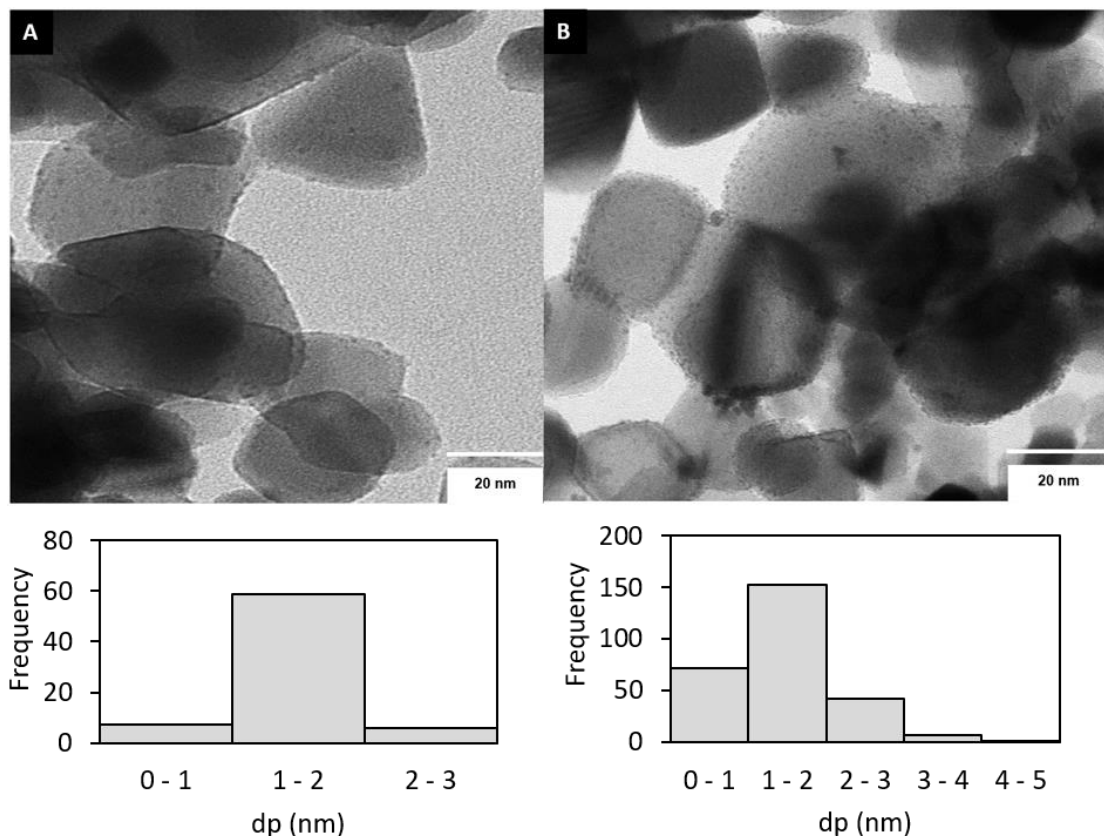


Figure 3.9. TEM images and histograms: A) Pt(2)/P25(H) and B) Pt(4)/P25(H)

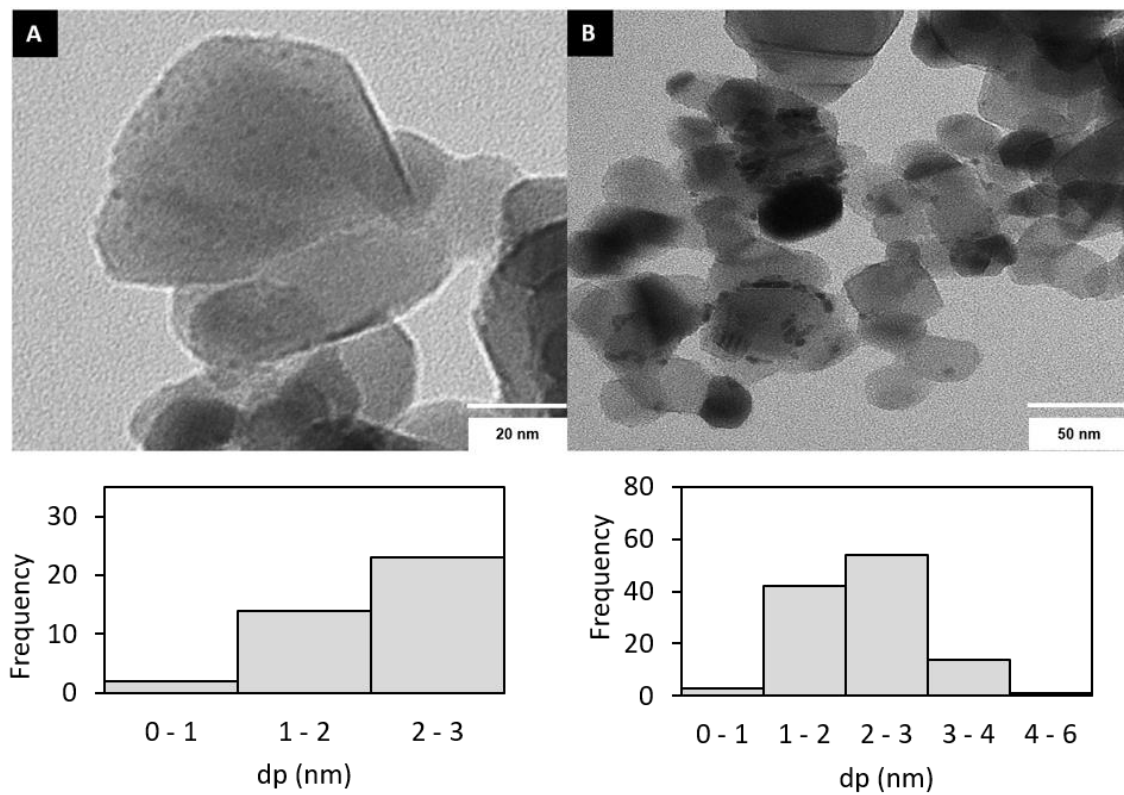


Figure 3.10. TEM images and histograms: A) Pt(2)/P25(K) and B) Pt(4)/P25(K)

In Table 3.4 are reported the number of particles measured to calculate the mean nanoparticle diameters and their standard deviation in the monometallic catalysts.

Table 3.4. Mean nanoparticle diameter and number of particles measured in the monometallic catalysts

Catalyst	Mean dp (nm)	Std deviation (nm)	Particles number
Ag(2)/P25	3.1	± 1.8	129
Pt(2)/P25(H)	1.3	± 0.4	72
Pt(2)/P25(K)	2.1	± 0.4	39
Pt(4)/P25(H)	1.5	± 0.7	275
Pt(4)/P25(K)	2.2	± 0.8	114

### 3.1.2.4 Diffuse Reflectance UV-Vis Spectroscopy (DRUV-Vis)

The DRUV-Visible light characterization technique for each fresh monometallic catalyst was realized in order to measure their optical absorption properties in the spectral range 250 - 800 nm. Reflectance spectra were converted to the absorbance spectra using the Kubelka-Munk function (K-M) (Eq. 3.5 and Eq. 3.6) to calculate the DRUV-Vis spectrums (Wodka et al. 2010; Doudrick et al. 2013) :

$$f(R_\infty(\lambda)) = \frac{(1-R_\infty)^2}{2R_\infty} = \frac{k}{s} \quad (\text{Eq. 3.5})$$

$$R_\infty = \frac{R}{R_{\text{BaSO}_4}} \quad (\text{Eq. 3.6})$$

Where:  $k$  is the molar absorption coefficient,  $s$  is the scattering coefficient,  $R$  is the reflectance recorded,  $R_\infty$  is the absolute reflectance, and  $\lambda$  is the absorbance wavelength. The  $\text{BaSO}_4$  is the reference powder of the measures (*Chapter 2, section 2.1.4*).

The light absorption of  $\text{TiO}_2$  generally increases with the calcination temperature (Yu et al. 2006; Wang et al. 2012). The DRUV-Vis spectra of  $\text{TiO}_2$  P25 powders before and after thermal treatment at 400 °C are shown in Figure 3.11. Both spectra exhibit broad absorption bands below 400 nm attributed to charge-transfer transitions between the oxygens and the titanium ions (Krejckova et al. 2012). A significant increase of absorption at wavelengths below 400 nm is observed for the P25 calcined at 400 °C compared with the uncalcined P25, which could be related to the absorption of light caused by the excitation of the electrons from the valence to the conduction band - band transition - of Titania. This red shift indicates a decrease in the

band gap energy (Wang et al. 2012). The differences in the light absorptions are assigned to the change of crystallite sizes, which were obtained by XRD (3.1.2.1), because they do not present any change in the structure phases.

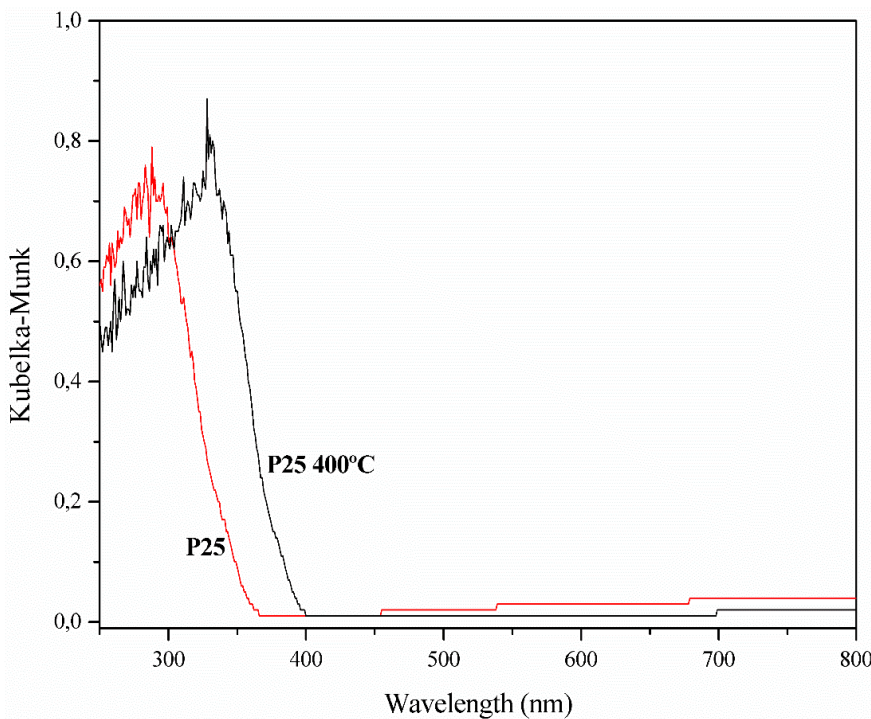


Figure 3.11. DRUV-Vis spectra of P25 and P25 calcined at 400°C

The DRUV-Vis spectra of Ag(x)/P25 catalysts varying the silver loading from 0.5 to 4 wt. % compared to that of P25 calcined at 400 °C - the calcination temperature in the catalysts preparation - are displayed in the Figure 3.12. The absorption peak until ~ 400 nm are ascribed to the band transition of P25 400 °C. Compare to P25 400 °C, the Ag-containing catalysts show an enhanced light absorption capability from ca. 400 to 800 nm, which means that are absorbing light in the entire visible light range and that they can be used as photocatalysts. This light absorption can be explained by the localized surface resonance plasmon (LSPR) effect characteristic of the silver particles, which is an oscillation of the free electron density of the electrons confined in the conduction band of metal NPs by the electric field of electromagnetic wave (*Chapter 1, section 1.2.3.4*) (Gomathi et al. 2010; Wodka et al. 2010). The absorption bands present a maximum centered at around 500 nm. These maximum absorption bands have been reported at various positions in the literature, i. e. 370, 440 and 530 nm (Sobana et al. 2006; Rupa et al. 2009; Pulido Melián et al. 2012) . Higher amount of silver impregnated on P25 led to more intense and broadened peaks, and also smaller blue shifts, demonstrating that

the higher the silver impregnated the higher the LSPR effect of silver NPs. Pulido Melián et al. demonstrated that higher impregnated Ag deposition (from 0.5 to 5 %) over P25 led to slight decrease in the energy band gaps (from 3.08 to 2.94 eV) (Pulido Melián et al. 2012), attributed to localized energy levels in the titania band gap introduced by the metallic particles. Therefore, the electrons can be excited from the valence band to these levels at lower energies than to the conduction band of the titania. To sum up, the absorption in the visible light range increases with the Ag loading on the support.

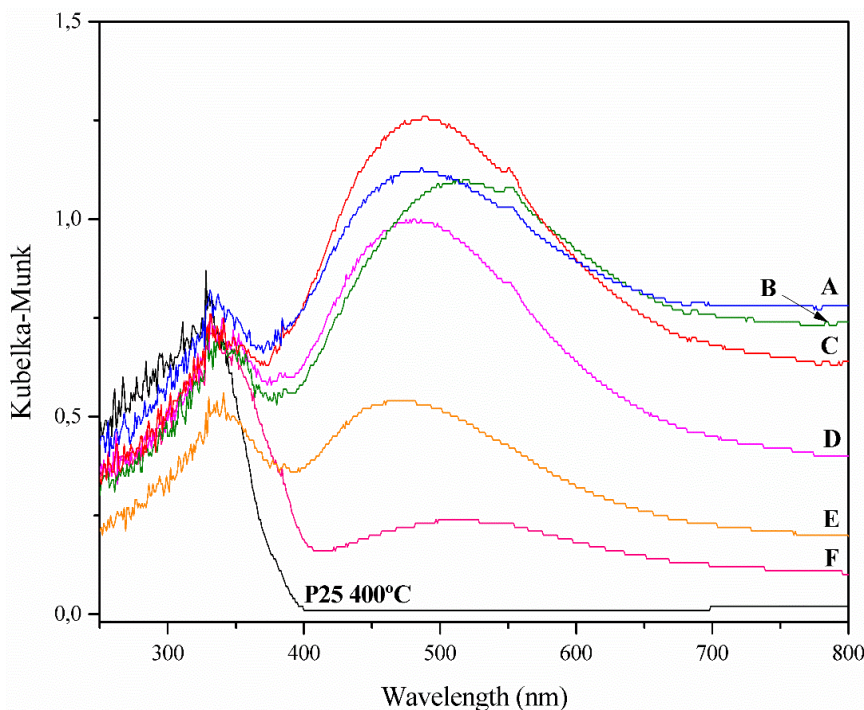


Figure 3.12. DRUV-Vis spectra of P25 calcined at 400°C and: A) Ag(4)/P25, B) Ag(2)/P25, C) Ag(3)/P25, D) Ag(1.5)/P25, E) Ag(1)/P25, and F) Ag(0.5)/P25

The Figure 3.13 shows the DRUV-Vis spectra of P25 calcined at 400 °C and of the Pt(x)/P25 catalysts varying the Pt loading (2 and 4 wt. %) and precursor. The absorption peak ranging from ~ 400 - 700 nm is due to Pt NPs (Li et al. 2002). There is no significant enhancement of absorption with the Pt(2)-monometallic catalysts, which display very similar optical spectra than P25 400 °C. When the Pt loading is 4 %, a weak optical absorption is observed centered at ca. 550 nm ( $\text{Pt}^0$  and  $\text{Pt}^{2+}$ ), especially in the Pt(4)/P25(H) catalyst. Higher Pt loadings led to more intense and wider peaks like in the case of Ag-based monometallic catalysts commented before. Furthermore, the type of Pt precursor used in the catalyst preparation seems to have an influence. More intense and broadened absorption bands are recorded when using

$\text{H}_2\text{PtCl}_6 \cdot 6\text{H}_2\text{O}$  instead of  $\text{K}_2\text{PtCl}_6$ . This is attributed to the higher dispersion and smaller mean particle sizes (ca. 1.4 nm and 2.2 nm, respectively) observed previously by TEM (3.1.2.3).

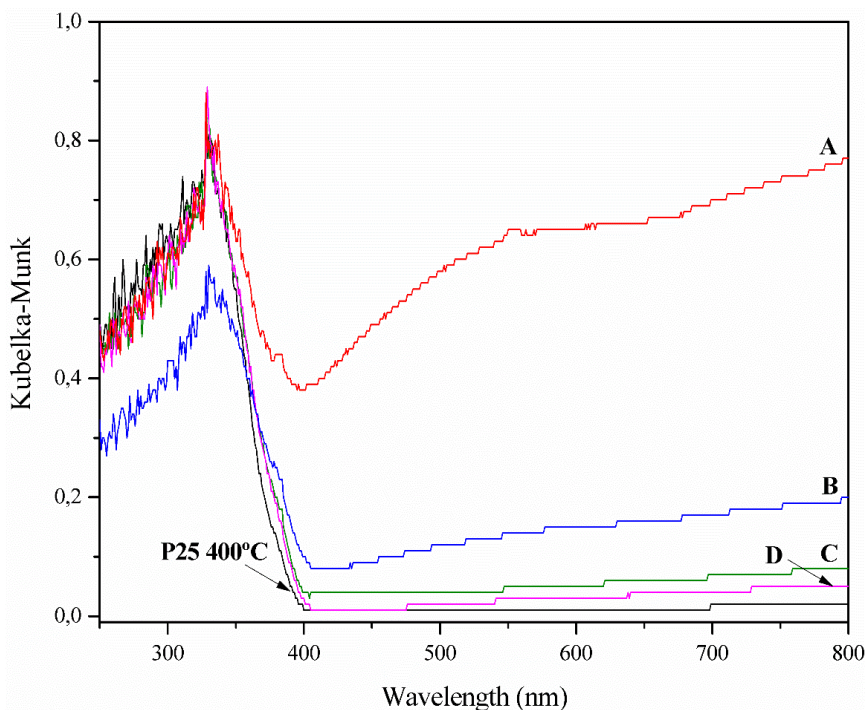


Figure 3.13. DRUV-Vis spectra of P25 calcined at 400°C and: A) Pt(4)/P25(H), B) Pt(4)/P25(K), C) Pt(2)/P25(H), and D) Pt(2)/P25(K)

### 3.1.2.5 Temperature-Programmed Reduction by hydrogen (H<sub>2</sub>-TPR)

The hydrogen consumption of selected monometallic catalysts was analyzed by TPR to determine the differences in the reducibility of the samples. The TPR profiles of the monometallic catalysts in the temperature range -50 °C to 400 °C are exhibited in Figure 3.14, and their hydrogen consumptions in the Table 3.5. The reduction of bulk oxygen of  $\text{TiO}_2$  has been demonstrated to occur at  $T > 600$  °C (Ou et al. 2007; Zhang et al. 2012).

$\text{Ag}(2)/\text{P25}$  catalyst presents a weak peak at ~ 100 °C attributed to  $\text{AgNO}_3$  reduction and also suggesting that an easily reducible silver oxide was present in the catalyst (Nanba et al. 2012; Aristizábal et al. 2014). No other shoulders are present in the TPR profile. Besides, the H<sub>2</sub> consumption registered from this catalyst ( $0.14 \text{ mmol.g}^{-1}$ ) was the lowest among all catalysts. Thus, it could be assumed that almost all  $\text{AgNO}_3$  is photoreduced to  $\text{Ag}^0$  during the catalyst impregnation (Aristizábal et al. 2014). Accordingly, no silver oxide has been detected by XRD (3.1.2.1) and XPS (3.2.2.5).

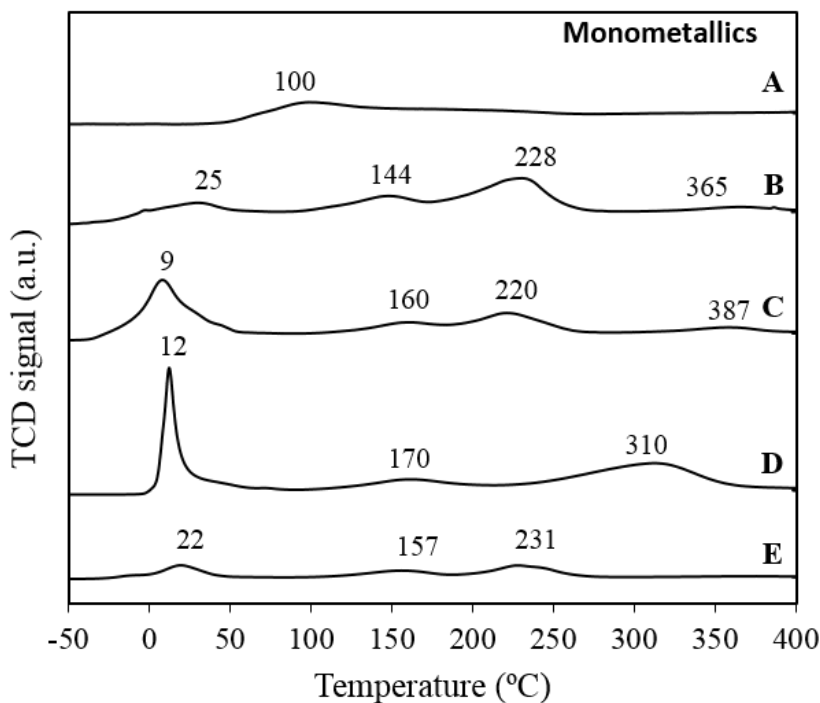


Figure 3.14. H<sub>2</sub>-TPR profiles of: A) Ag(2)/P25, B) Pt(2)/P25(H), C) Pt(2)/P25(K), D) Pt(4)/P25(H), and E) Pt(4)/P25(K)

The Pt(2)-catalysts impregnated with the two types of platinum precursors show four peaks. The first peak below 50 °C (at 9 °C (H) or 25 °C (K)) is due to Pt species poorly interacting with the support. The three peaks above 50 °C are at similar temperatures, around 152 °C, 224 °C and 376 °C. They are related to particles interacting more strongly with the support, and particularly those at T ~ 152 °C and 376 °C to some PtO<sub>x</sub> species as reported in the literature (Panagiotopoulou et al. 2006).

In Pt(4)-catalysts, three peaks are obtained. The first peak below 50 °C (at 12 °C (H) or 22 °C (K)) assigned to Pt particles poorly interacting with the support is in the same temperature range than with 2 wt. % Pt (9 or 25 °C). In contrast to the Pt(2)-catalysts, only two peaks are observed above 50 °C. Those are very broad showing a large distribution of Pt<sup>0</sup> particles differently interacting with the support. It can be noted, at this Pt loading (4 wt. %), a lower reducibility of the Pt particles obtained from H<sub>2</sub>PtCl<sub>6</sub>·6H<sub>2</sub>O than from K<sub>2</sub>PtCl<sub>6</sub>, the peak at high temperature is being shifted from 231 °C to 310 °C.

Remarkably, the peak at T = 12 °C owing to the H<sub>2</sub>PtCl<sub>6</sub>·6H<sub>2</sub>O precursor was the highest, attributed to highly dispersed Pt<sup>0</sup> particles as demonstrated by TEM in the reduced samples

(3.1.2.3). The TPR of the Pt-containing catalysts show a reduction in different steps with a majority of  $\text{Pt}^0$  particles formed around room temperature (Ou et al. 2007).

The  $\text{H}_2$  consumptions are much more significant when increasing the Pt loading from 2 % (ca. 30 mmol $^{-1}$ ) to 4 % with also a higher platinum reducibility. The Pt(4)/P25(H) catalyst presented the highest hydrogen consumption (0.95 mmol $^{-1}$ ) increasing of 227.6 % in comparison to Pt(2)/P25(H). An increase of the 40.6 % is observed when going from Pt(2)/P25(K) to Pt(4)/P25(K). The shift toward lower temperature of the reduction peak above 200 °C and the decrease of the hydrogen consumption observed in Pt(4)/P25(K) might be related to the larger mean particle size obtained with this sample (~ 2.2 nm) observed by TEM (3.1.2.3) and to the presence of residual  $\text{K}_2\text{PtCl}_6$  detected by XRD (3.1.2.1).

Table 3.5. Hydrogen consumption of monometallic catalysts

Catalyst	$\text{H}_2$ TPR (mmol/g)
Ag(2)/P25	0.14
Pt(2)/P25(H)	0.29
Pt(2)/P25(K)	0.32
Pt(4)/P25(H)	0.95
Pt(4)/P25(K)	0.45

## 3.2 Bimetallic catalysts

In this section we report the synthesis method and the physicochemical properties of the bimetallic catalysts.

### 3.2.1 Synthesis method

The bimetallic catalysts were synthesized by drop-wise wetness-incipient impregnation method followed by a chemical reduction step using  $\text{NaBH}_4$  as reducing agent. This method of synthesis was the same than that used for the monometallic catalysts largely described in the paragraph 3.1.1. The chemical reduction is broadly used for the synthesis of bimetallic pair NPs to obtain core-shell or alloyed NPs with different shapes, such as cubes, spheres flower-like or wires (Zaleska-Medynska et al. 2016).

Numerous bimetallic catalysts (Table 3.6) based on Ag and Pt supported onto Aerioxide  $\text{TiO}_2$  P25 were prepared varying the Pt loading (2 and 4 wt. %), the Pt precursor and also the impregnation order of both noble metals (Ag-Pt, Pt-Ag). The Ag load was fixed at 2 wt. %. The

impregnation order was varied as detailed in Table 3.6, where the notation Ag(2)-Pt(x) means that Ag was firstly impregnated and Pt secondly, using  $\text{H}_2\text{PtCl}_6 \cdot 6\text{H}_2\text{O}$  or  $\text{K}_2\text{PtCl}_6$  precursors. Notation Pt(x)-Ag(2) corresponds to the reverse impregnation order of the Pt and Ag salts.

The bimetallic catalysts are named as:

- Ag(2)-Pt(x)/P25(H or K); or
- Pt(x)-Ag(2)/P25(H or K)

Where: x = 2 and 4 wt. %; (H) =  $\text{H}_2\text{PtCl}_6 \cdot 6\text{H}_2\text{O}$  or (K) =  $\text{K}_2\text{PtCl}_6$ .

Table 3.6. Notation of the bimetallic catalysts prepared

Catalyst	Pt (wt.%)	Pt precursor		Impregnation order	
		$\text{H}_2\text{PtCl}_6 \cdot 6\text{H}_2\text{O}$	$\text{K}_2\text{PtCl}_6$	1)	2)
Ag(2)-Pt(2)/P25(H)	2	X	-		
Ag(2)-Pt(2)/P25(K)	2	-	X		
Ag(2)-Pt(4)/P25(H)	4	X	-	Ag	Pt
Ag(2)-Pt(4)/P25(K)	4	-	X		
Pt(2)-Ag(2)/P25(H)	2	X	-		
Pt(2)-Ag(2)/P25(K)	2	-	X		
Pt(4)-Ag(2)/P25(H)	4	X	-	Pt	Ag
Pt(4)-Ag(2)/P25(K)	4	-	X		

In a typical preparation, the Ag(2)-Pt(x)/P25(H or K) catalyst was obtained by firstly drop-wise impregnation of 2 g of  $\text{TiO}_2$  P25 powder by an aqueous solution of 0.063 g  $\text{AgNO}_3$  in 0.5 mL of  $\text{H}_2\text{O}$ , then dried overnight at 100 °C. On this dried powder, a solution (Table 3.7) of Y g of  $\text{H}_2\text{PtCl}_6 \cdot 6\text{H}_2\text{O}$  or Z g of  $\text{K}_2\text{PtCl}_6$  in 0.5 mL of  $\text{H}_2\text{O}$  was secondly drop-wise added, after dried again at 100 °C overnight. Afterwards, the powder was calcined at 400 °C overnight. For the Pt(x)-Ag(2)/P25(H or K) catalysts the procedure followed was the same as mentioned before but with reverse precursors impregnation. The precursors impregnation was followed by a chemical reduction with sodium borohydride ( $\text{NaBH}_4$ ) to obtain the metal NPs over the support. Thus, the desirable amount of catalyst was stirred in 20 ml of EtOH and 20 mg of  $\text{NaBH}_4$ , previously stirred in 5 ml of EtOH, was drop-wise added. Later, catalyst is filtered under vacuum and washed with EtOH several times. The final catalyst powder colors are grey (Figure 3.15). Once the catalyst is filtered, it is immediately introduced into the reactor to avoid silver oxidation.

Table 3.7. Composition of the aqueous impregnation solutions of the bimetallic catalysts.

Catalyst	Pt	
	$\text{H}_2\text{PtCl}_6 \cdot 6\text{H}_2\text{O}$ (Y g)	$\text{K}_2\text{PtCl}_6$ (Z g)
Ag(2)-Pt(2)/P25(H)	0.084	-
Ag(2)-Pt(2)/P25(K)	-	0.101
Ag(2)-Pt(4)/P25(H)	0.168	-
Ag(2)-Pt(4)/P25(K)	-	0.203
Pt(2)-Ag(2)/P25(H)	0.084	-
Pt(2)-Ag(2)/P25(K)	-	0.101
Pt(4)-Ag(2)/P25(H)	0.168	-
Pt(4)-Ag(2)/P25(K)	-	0.203

The visual aspect of the Ag-Pt and Pt-Ag bimetallic catalysts synthesized are displayed in the Figure 3.15.

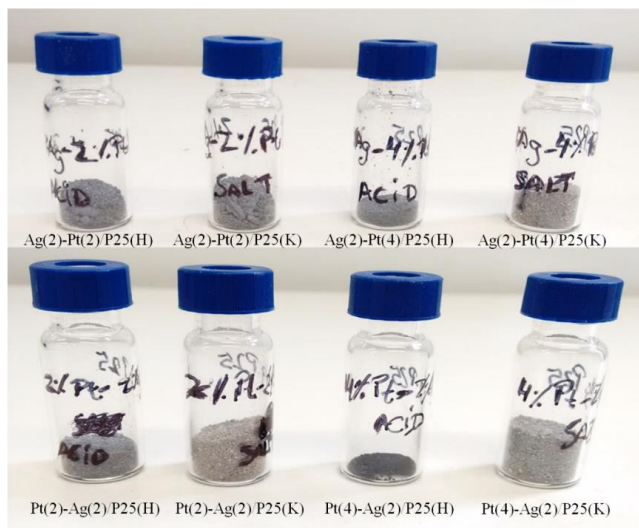


Figure 3.15. Visual aspect of the bimetallic catalyst powders

### 3.2.2 Characterization

#### 3.2.2.1 X-Ray Diffraction (XRD)

The crystalline phases present in the P25, P25 calcined at 400 °C and the bimetallic samples have been identified by XRD.

The XRD patterns of the support P25 and P25 400 °C (ca. 80 anatase/20 rutile, % w/w) were previously presented in Figure 3.2. and their average crystallite sizes calculated using the Scherrer equation in previous section 3.1.2.1.

The XRD patterns of the reduced Ag(2)-Pt(x)/P25 and Pt(x)-Ag(2)/P25 bimetallic catalysts are reported in Figures 3.16 and 3.17, respectively. Each XRD pattern presents the characteristic peaks of anatase (JCPDS 021-1272) and rutile (JCPDS 021-1274) crystalline phases, as observed for the monometallic catalysts.

Similarly to the monometallic catalysts (Figures 3.3 and 3.4, 3.1.2.1), no peaks related to Ag or Pt NPs are observed for the bimetallic catalysts due to the too low sensitivity of the XRD analysis at such metal loadings and/or to the low size and high dispersion of the particles. The characteristic peaks of the anatase and rutile phases of the P25 support are also not modified, suggesting that the metal NPs are deposited onto the surface of P25 (Matos et al. 2012; Lee et al. 2014; Talat-Mehrabad et al. 2015), as suggested by TEM too (3.2.2.3). The platinum loading has also no influence on the catalyst crystallinity.

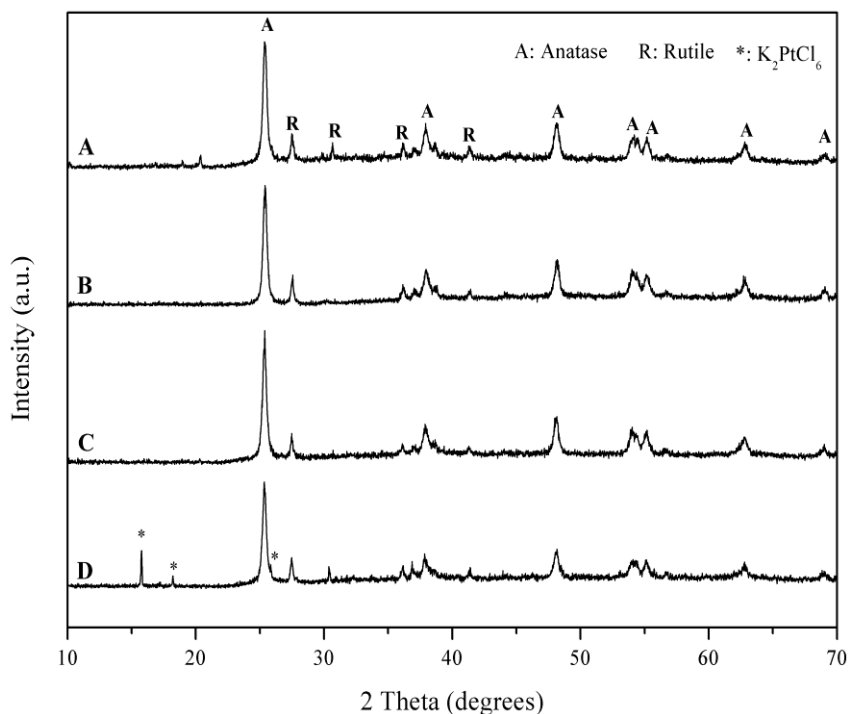


Figure 3.16. XRD patterns of: A) Ag(2)-Pt(2)/P25(H), B) Ag(2)-Pt(2)/P25(K),  
C) Ag(2)-Pt(4)/P25(H), and D) Ag(2)-Pt(4)/P25(K)

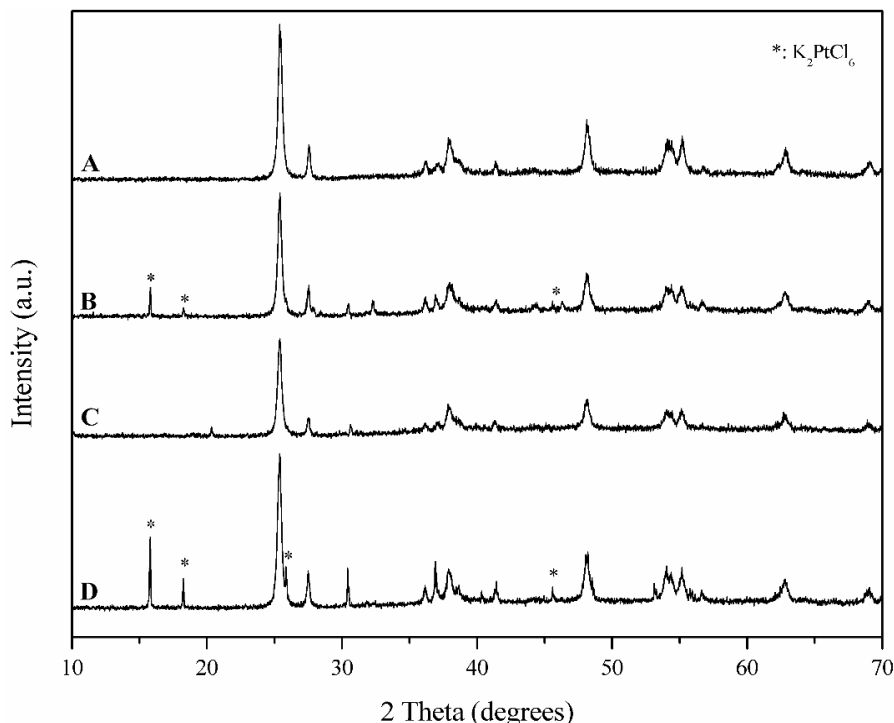


Figure 3.17. XRD patterns of: A) Pt(2)-Ag(2)/P25(H), B) Pt(2)-Ag(2)/P25(K),  
C) Pt(4)-Ag(2)/P25(H), and D) Pt(4)-Ag(2)/P25(K)

XRD patterns of the samples impregnated with the  $\text{K}_2\text{PtCl}_6$  show the characteristic peaks of this precursor (JCPDS 070-1346,  $2\theta = 15.73^\circ, 18.18^\circ, 25.82^\circ, 45.53^\circ$ ), as presented in the monometallic Pt(4)/P25(K) sample. The peaks are more intense when the amount of platinum increases from 2 to 4 wt. %, indicating that oxidized Pt is also present. In addition, the peaks of  $\text{K}_2\text{PtCl}_6$  are more intense when platinum was impregnated first (Pt-Ag samples) over the support. This statement is confirmed by XPS (3.2.2.5).

### 3.2.2.2 Nitrogen Physisorption

The  $\text{N}_2$  adsorption-desorption isotherms and the textural properties (surface area ( $S_{\text{BET}}$ )) (BET method), pore volume ( $V_{\text{Pore}}$ ) and pore diameter ( $\phi_{\text{Pore}}$ ) (BJH method)) of selected bimetallic catalysts are reported in Figure 3.18 and Table 3.8. Whatever the metal impregnation order,  $\text{H}_2\text{PtCl}_6$  was used as Pt precursor in both selected samples. Like P25 (before and after calcination at  $400^\circ\text{C}$ ) and the selected monometallic catalysts commented in section 3.1.2.2., the catalyst Ag(2)-Pt(4)/P25(H) exhibits a type H3 hysteresis loop indicating the presence of mesopores (2 - 50 nm), while Pt(4)-Ag(2)/P25(H) is close to a H4 hysteresis loop (BDDT classification, Sing et al. 1985), which suggests, in addition, the presence of internal mesoporous. Therefore, the metal impregnation order (Ag-Pt, Pt-Ag) influences slightly the

nature of the mesopores in the materials. The H3 and H4 hysteresis loops approach a relative pressure  $P/P_0 \approx 1$ , suggesting the existence of large pores between the particles ( $> 50$  nm) (Tsai et al. 2004; Yu et al. 2011; Wang et al. 2012).

These bimetallic catalysts exhibit similar textural properties than the previous monometallic ones. Compared to the P25 400 °C support the BET surface area decreases the 12 - 16 %, maybe accounting for deposition of metallic species or NaBH<sub>4</sub> after the chemical reduction step at the entry of the pores, blocking them partially (Xu et al. 2015). The selected bimetallic samples present a pore volume of 0.4 cm<sup>3</sup>g<sup>-1</sup> and a mean pore diameter of ~ 26 nm. Therefore, the impregnation order of the noble metals has only a slight influence on the type of mesopores of the bimetallic catalysts.

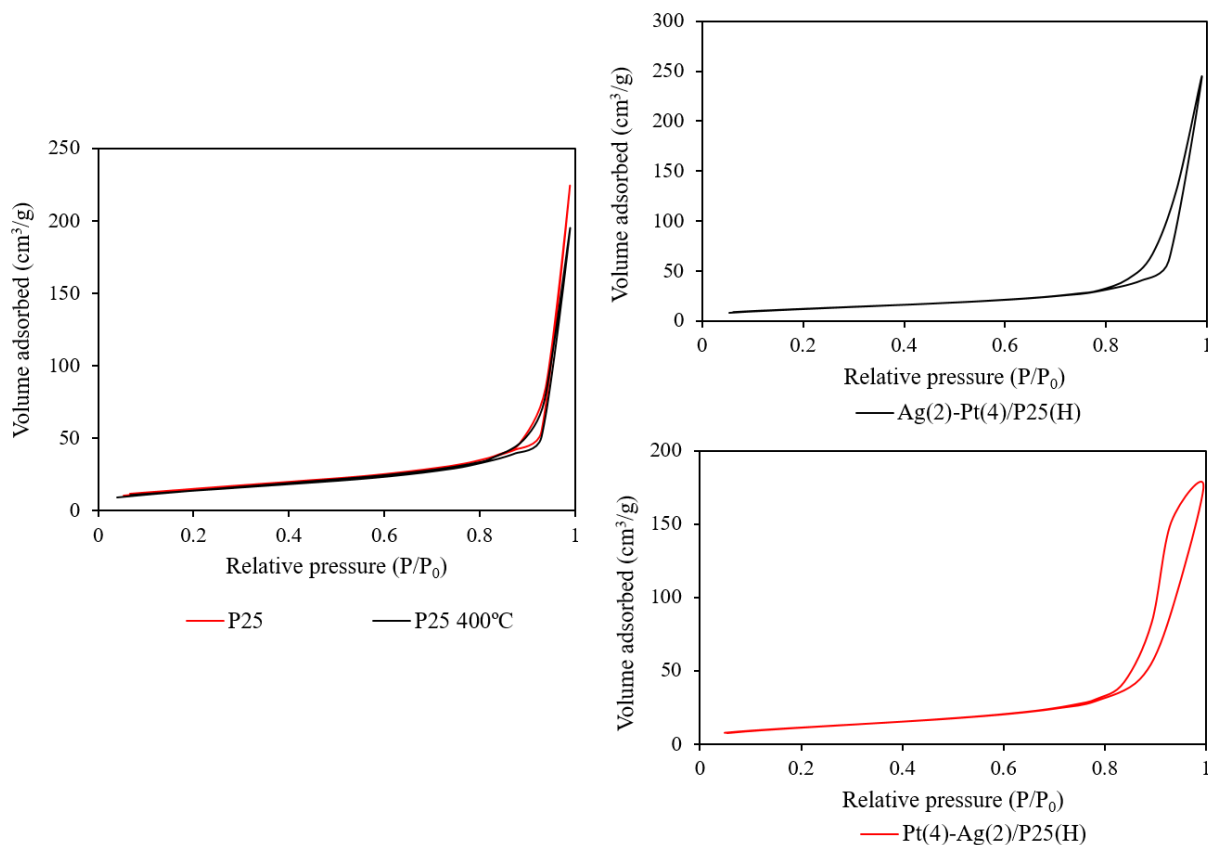


Figure 3.18. N<sub>2</sub> adsorption-desorption isotherms of P25, P25 calcined at 400°C and selected bimetallic catalysts Ag(2)-Pt(4)/P25(H) and Pt(4)-Ag(2)/P25(H)

The textural properties are shown in Table 3.8.

Table 3.8. Specific surface area, pore volume and mean pore diameter of P25, P25 calcined at 400°C and of two selected bimetallic catalysts

Catalyst	$S_{BET}$ ( $\text{m}^2\text{g}^{-1}$ )	$V_{\text{Pore}}$ ( $\text{cm}^3\text{g}^{-1}$ )	$\varnothing_{\text{Pore}}$ (nm)
P25	55	0.3	33
P25(400°C)	50	0.3	33
Ag(2)-Pt(4)/P25(H)	44	0.4	26
Pt(4)-Ag(2)/P25(H)	42	0.4	26

### 3.2.2.3 Transmission Electron Microscopy (TEM)

The morphology and particles sizes of reduced bimetallic catalysts were analyzed by TEM. Analysis were performed on samples where the impregnation order of noble metals (Ag-Pt, Pt-Ag), the platinum precursor ( $\text{H}_2\text{PtCl}_6 \cdot 6\text{H}_2\text{O}$  or  $\text{K}_2\text{PtCl}_6$ ) and the amount of platinum loading (2 or 4 wt. %) are different. The morphologies and the mean nanoparticle diameters of bare  $\text{TiO}_2$  P25 and selected monometallic catalysts for comparison are shown and commented in section 3.1.2.3. The metal NPs are observed in the images as black dots over the support P25, and their mean sizes are reported in Table 3.9.

Remarkably, the same influence of the Pt precursor than with the monometallic samples is observed in the micrographs (Figures 3.19 to 3.22). The NPs are indeed mostly present at the boundaries of the  $\text{TiO}_2$  P25 support with  $\text{H}_2\text{PtCl}_6 \cdot 6\text{H}_2\text{O}$  (~ 2.3 nm), instead of more agglomerated with about a double average mean size (~ 4 nm) and deposited on the entire surface with  $\text{K}_2\text{PtCl}_6$  (Kanda et al. 2009). The metal NPs are preferentially deposited on the anatase phase of P25 instead of on the rutile phase (Sclafani et al. 1997, 1998). Moreover, the increase of the Pt load does not influence the NPs location, only a larger quantity is noticed (Particles Number, Table 3.9). The impregnation order Ag-Pt (Figures 3.19 and 3.20) and Pt-Ag (Figures 3.21 and 3.22) affects neither the location of the particles nor their average sizes.

Therefore, the factor that influences the morphology of the catalysts is the type of platinum precursor used in the synthesis, with a larger mean nanoparticle sizes of ca. 2 nm when using  $\text{K}_2\text{PtCl}_6$  – independently of Pt load and impregnation order - due to a better dispersion onto the support with the  $\text{H}_2\text{PtCl}_6 \cdot 6\text{H}_2\text{O}$ . Such feature would give differences in the catalyst performances.

The images of the Ag-Pt based bimetallic catalysts are displayed in the following figures, depending on the Pt precursor used: Figure 3.19 ( $\text{H}_2\text{PtCl}_6 \cdot 6\text{H}_2\text{O}$ ) and Figure 3.20 ( $\text{K}_2\text{PtCl}_6$ ).

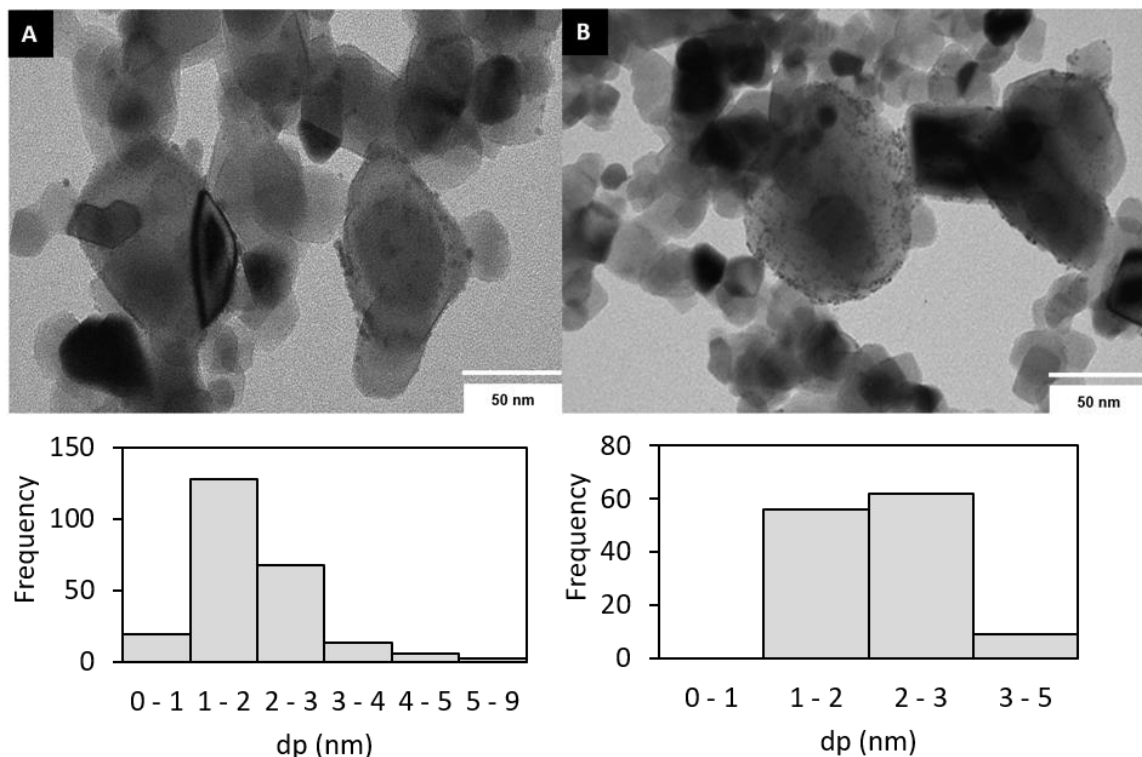


Figure 3.19. TEM images and histograms: A)  $\text{Ag}(2)\text{-Pt}(2)/\text{P25(H)}$  and B)  $\text{Ag}(2)\text{-Pt}(4)/\text{P25(H)}$

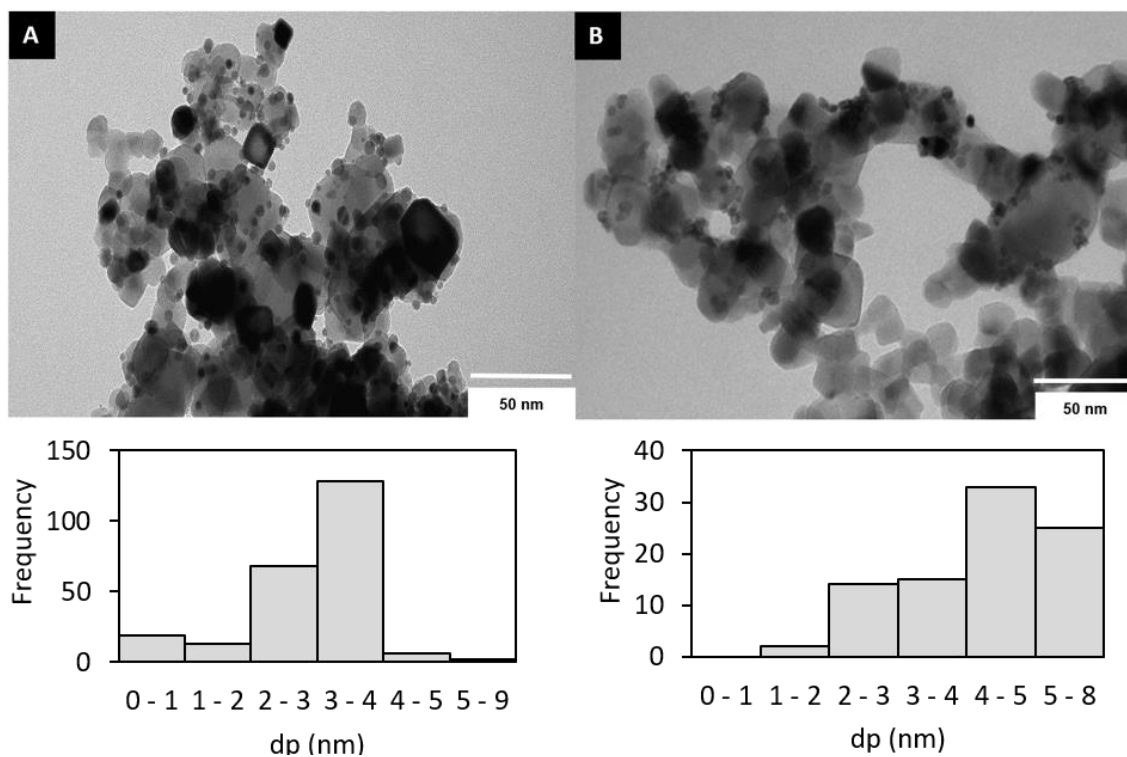


Figure 3.20. TEM images and histograms: A)  $\text{Ag}(2)\text{-Pt}(2)/\text{P25(K)}$  and B)  $\text{Ag}(2)\text{-Pt}(4)/\text{P25(K)}$

The images of the Pt-Ag based bimetallics are shown in the figures Figure 3.19 ( $\text{H}_2\text{PtCl}_6 \cdot 6\text{H}_2\text{O}$ ) and Figure 3.20 ( $\text{K}_2\text{PtCl}_6$ ).

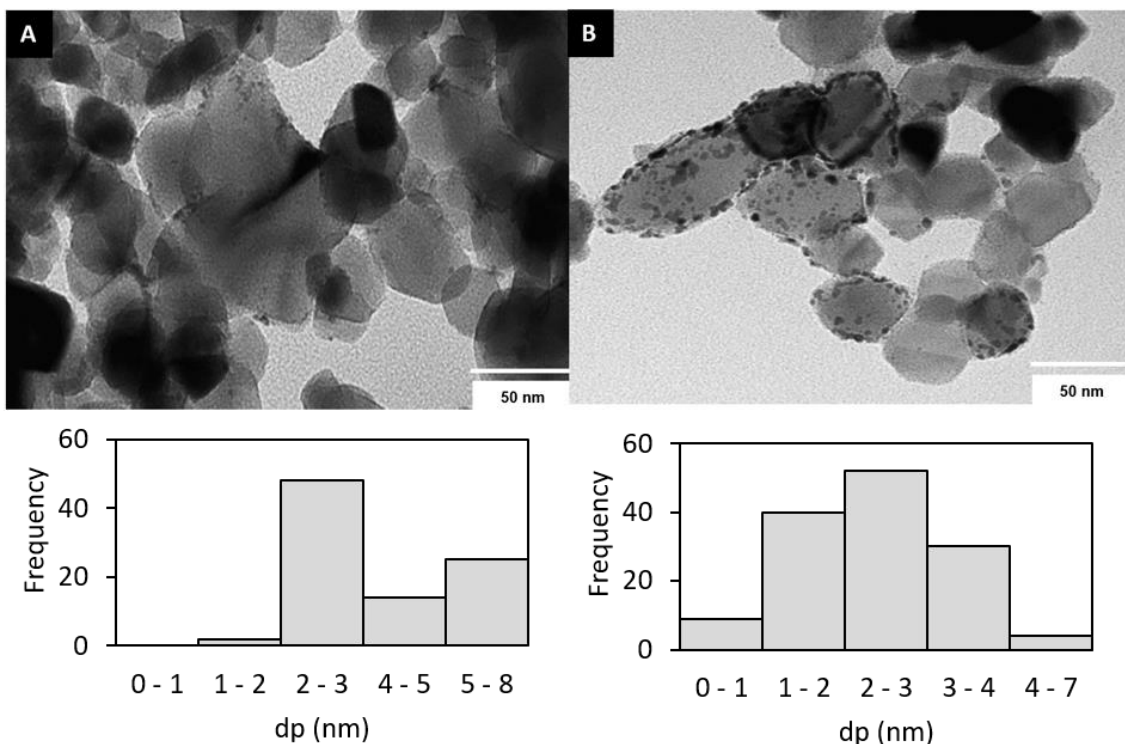


Figure 3.21. TEM images and histograms: A) Pt(2)-Ag(2)/P25(H) and B) Pt(4)-Ag(2)/P25(H)

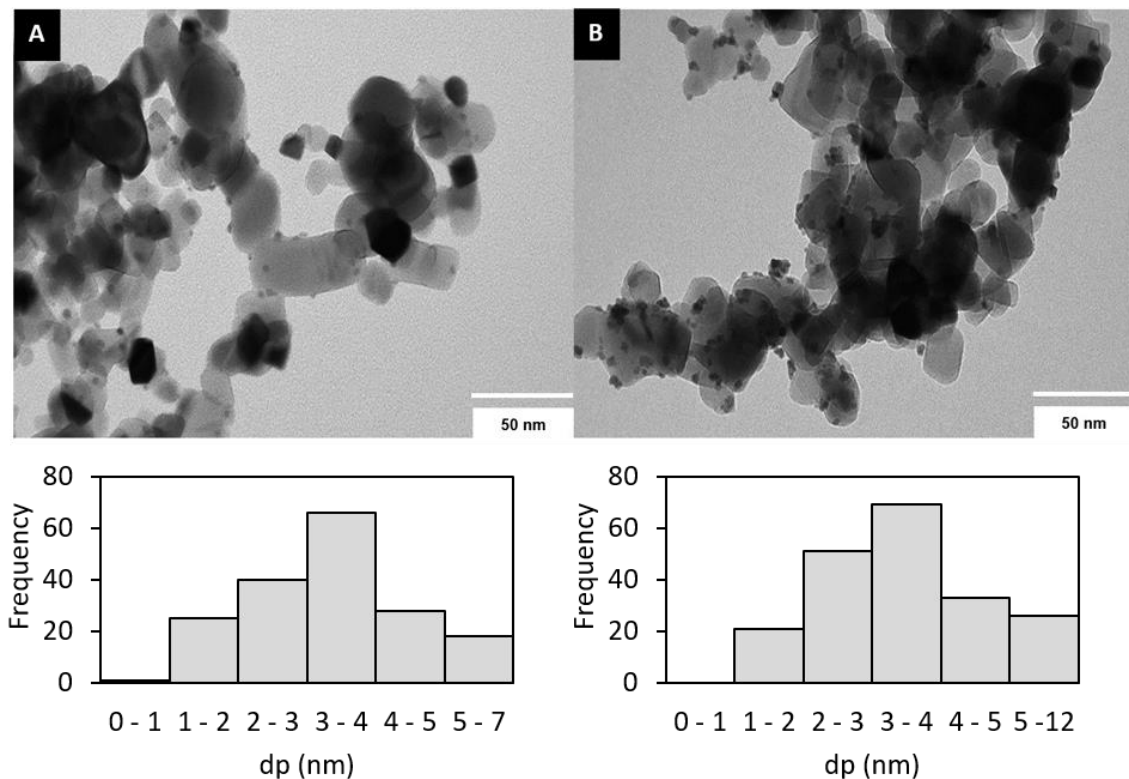


Figure 3.22. TEM images and histograms: A) Pt(2)-Ag(2)/P25(K), and B) Pt(4)-Ag(2)/P25(K)

Table 3.9 presents the mean nanoparticles size and their standard deviation, as well as the number of particles measured for its calculation of the bimetallic catalysts.

Table 3.9. Mean nanoparticles size and number of particles measured in the bimetallic catalysts

Catalyst	Mean dp (nm)	Std deviation (nm)	Particles number
Ag(2)-Pt(2)/P25(H)	1.9	± 0.9	236
Ag(2)-Pt(2)/P25(K)	3.7	± 2.4	233
Ag(2)-Pt(4)/P25(H)	2.1	± 0.6	127
Ag(2)-Pt(4)/P25(K)	4.4	± 1.3	89
Pt(2)-Ag(2)/P25(H)	2.3	± 0.7	85
Pt(2)-Ag(2)/P25(K)	3.4	± 1.2	178
Pt(4)-Ag(2)/P25(H)	2.5	± 1.1	135
Pt(4)-Ag(2)/P25(K)	3.5	± 1.5	200

### 3.2.2.4 Diffuse Reflectance UV-Vis spectroscopy (DRUV-Vis)

The absorption bands of the fresh bimetallic catalysts were determined by DRUV-Visible light in the spectral range of 250 - 800 nm. As explained for the monometallic catalysts, the reflectance spectra were converted to the absorbance spectra using the Kubelka-Munk (K-M) function to calculate the DRUV-Vis spectrums (Wodka et al. 2010; Doudrick et al. 2013). The K-M function and the results regarding bare P25, P25 calcined at 400 °C and the monometallic catalysts are, for comparison, described in the section 3.1.2.4 of this chapter.

The Ag loading was fixed at 2 %, thus the influence of the Pt loading, the platinum precursor salts and the impregnation order (Ag-Pt, Pt-Ag) were likely studied. The DRUV-Vis spectra of the P25 calcined at 400 °C and the Ag(2)-Pt(x)/P25 catalysts are displayed in the Figure 3.23.

The optical absorptions below ~ 400 nm are assigned to the transition band of the titania calcined at 400 °C. Like the monometallic catalysts, the Ag-Pt based catalysts reveal enhanced light absorption capability in the wavelength range of ~ 400 - 800 nm, with a maximum at around 530 nm, probably due to a moderate localized surface plasmon resonance (LSPR) (Pulido Melián et al. 2012), as previously seen in the Ag(x)/P25 catalysts (3.1.2.4). In the monometallic catalysts, the Pt NPs absorption range is between 300 to 700 nm with a maximum centered at around 550 nm (Figure 3.13) (Li et al. 2002). It suggests that in the bimetallic catalysts an overlap of the absorption peaks from Ag<sup>0</sup> and Pt (Pt<sup>0</sup> and Pt<sup>2+</sup>) particles occurs.

The light absorption is more intense and the bands are broadened when preparing the catalysts with the  $\text{H}_2\text{PtCl}_6 \cdot 6\text{H}_2\text{O}$  precursor (A and B) than with  $\text{K}_2\text{PtCl}_6$  (C and D). The intensity is also higher when increasing the Pt loading from 2 to 4 % in the case of the  $\text{H}_2\text{PtCl}_6 \cdot 6\text{H}_2\text{O}$ . On the other hand, no significant change in the absorption is recorded with the catalysts prepared using the  $\text{K}_2\text{PtCl}_6$  precursor.

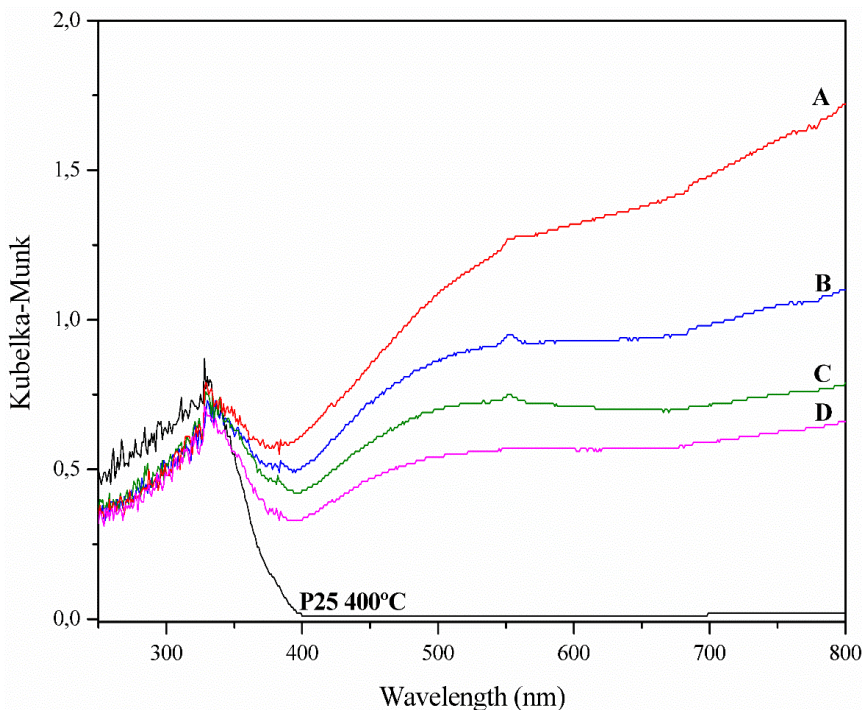


Figure 3.23. DRUV-Vis spectra of P25 calcined at 400°C and of: A) Ag(2)-Pt(4)/P25(H), B) Ag(2)-Pt(2)/P25(H), C) Ag(2)-Pt(2)/P25(K), and D) Ag(2)-Pt(4)/P25(K)

The DRUV-Vis spectra of the P25 400 °C and the Pt(x)-Ag(2)/P25 catalysts varying the same parameters as the previously described for Ag-Pt bimetallic catalysts (the Pt loading and the Pt precursor) are depicted in Figure 3.24. The absorption band appears in the wavelength domain ranging from 400 to 800 nm with a maximum at 530 nm, as commented for the Ag-Pt addition order. Then, it could be also suggested an overlap of the peaks coming from silver and platinum nanoparticles. Moreover, the influence of the Pt precursor and loading appears similar, as well as the K-M intensities obtained (from 0.5 to 0.8), with the noticeable exception of Pt(4)-Ag(2)/P25(H) (graph A, Figure 3.24) like Ag(2)-Pt(4)/P25(H) (graph A, Figure 3.23). The Pt-Ag order gives almost a two-fold higher intensity.

The broadening of the absorption bands can be attributed to the different size of the particles (Zaleska-Medynska et al. 2016), which are indeed strongly enhanced in Pt(4)-Ag(2)/P25(H) like Ag(2)-Pt(4)/P25(H) as described before, which are exhibiting the smaller mean particle size of 2.5 and 2.1 nm, respectively.

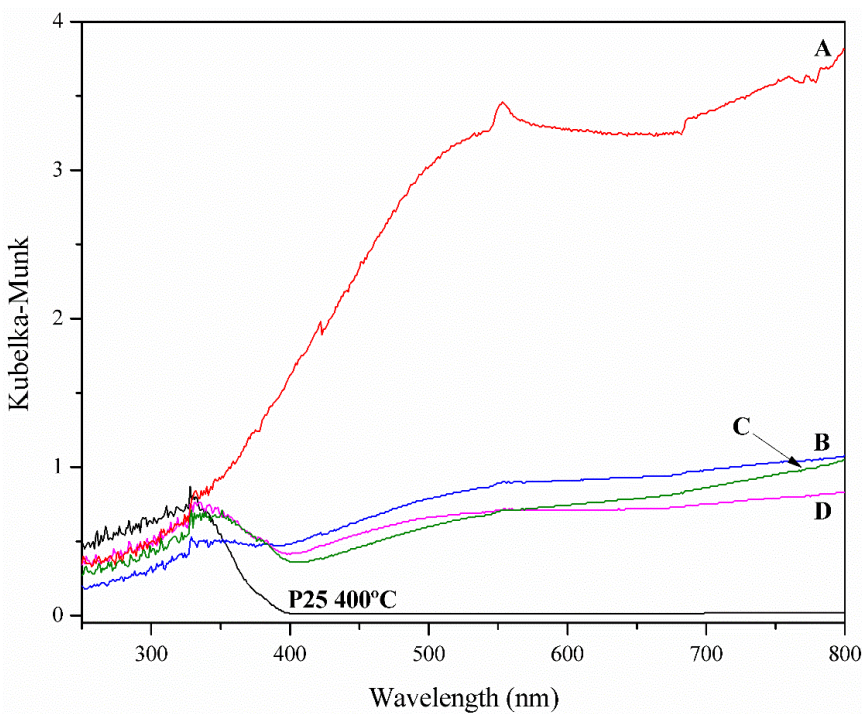


Figure 3.24. DRUV-Vis spectra of P25 calcined at 400°C and of: A) Pt(4)-Ag(2)/P25(H), B) Pt(2)-Ag(2)/P25(H), C) Pt(4)-Ag(2)/P25(K), and D) Pt(2)-Ag(2)/P25(K)

### 3.2.2.5 X-Ray Photoelectron Spectroscopy (XPS)

The surface of the reduced monometallic Ag(2)/P25 and selected bimetallic catalysts (Ag(2)-Pt(4)/P25(K), Pt(2)-Ag(2)/P25(H), Pt(2)-Ag(2)/P25(K) and Pt(4)-Ag(2)/P25(K)) was analyzed by XPS to determine the valence state and the chemical environment of the active noble metals. The monometallic catalyst is introduced in this section for the sake of comparison. Furthermore, these catalysts were selected because they exhibit the most interesting catalytic activities as will be shown in *Chapter 4*, and also because they allow to examine the influences of: the impregnation order, the Pt loading - from 2 to 4 wt. % - and the Pt precursor. A survey of the spectra of the selected samples recorded by XPS are shown in the Figure 3.25, which clearly accounts for the presence of C, Ti, O, Ag and Pt elements in the samples. The Oxygen and Titanium species are provided by the support Aeroxide Titania P25, and the Silver and Platinum species by the noble metals impregnated over P25. The peaks of O1s, Ti2p, Ag3d and Pt4f spectra were deconvoluted in order to focus on the different species present in each catalyst.

The binding energies (BE) are referenced to the carbon 1s ( $C_{1s}$ ) signal at 284.8 eV (Chapter 2, section 2.1.5).

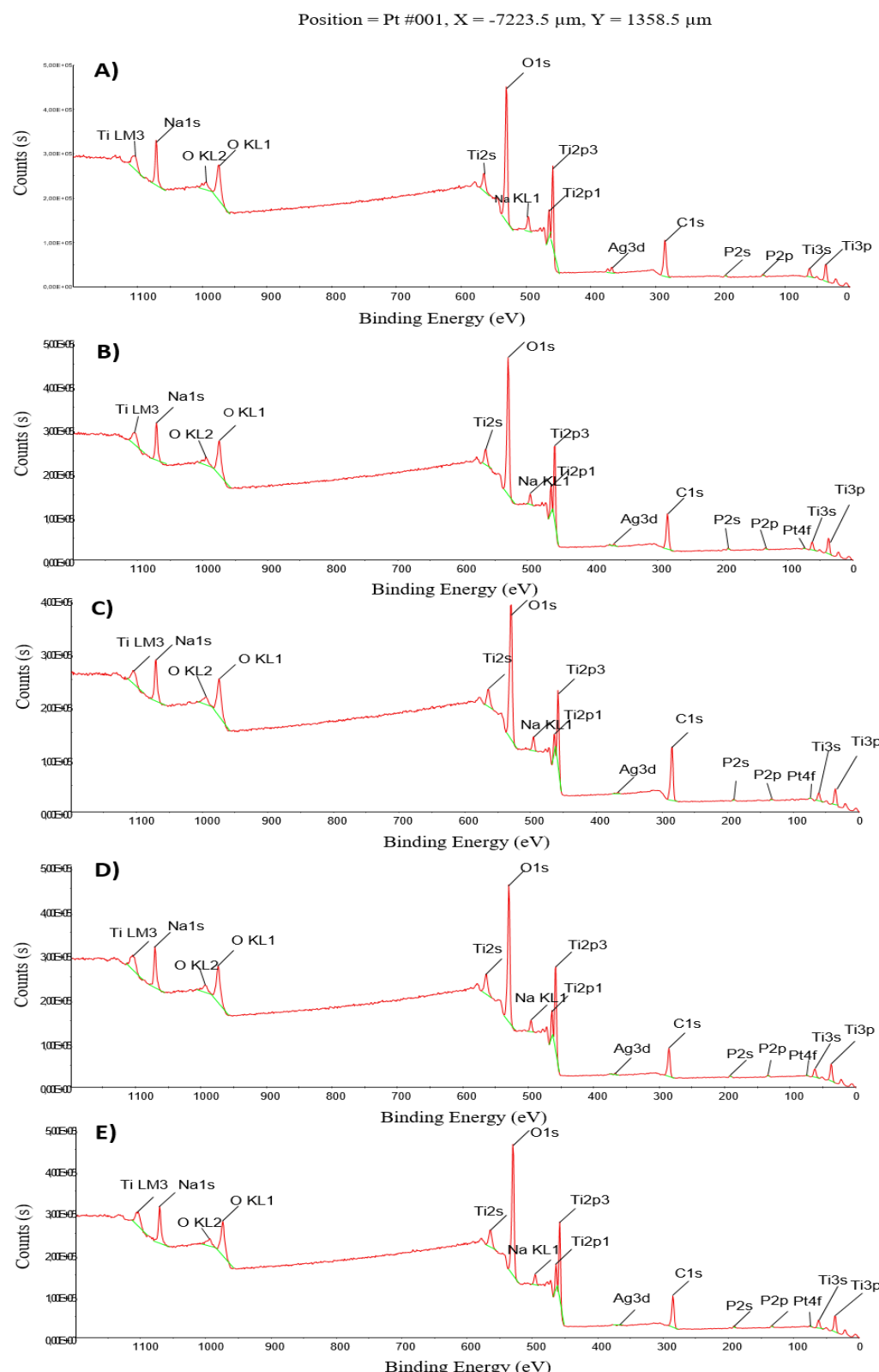


Figure 3.25. Survey of the spectra of the selected catalysts: A) Ag(2)/P25, B) Ag(2)-Pt(4)/P25(K), C) Pt(2)-Ag(2)/P25(H), D) Pt(2)-Ag(2)/P25(K), and E) Pt(4)-Ag(2)/P25(K)

The Oxygen O1s and Titanium Ti2p species of the support P25 from the catalyst Ag(2)/P25 are depicted in Figure 3.26, which are representative of the typical scan obtained for each catalyst studied. The peaks are identified by a letter for recognition and their BE values are reported in the Table 3.10.

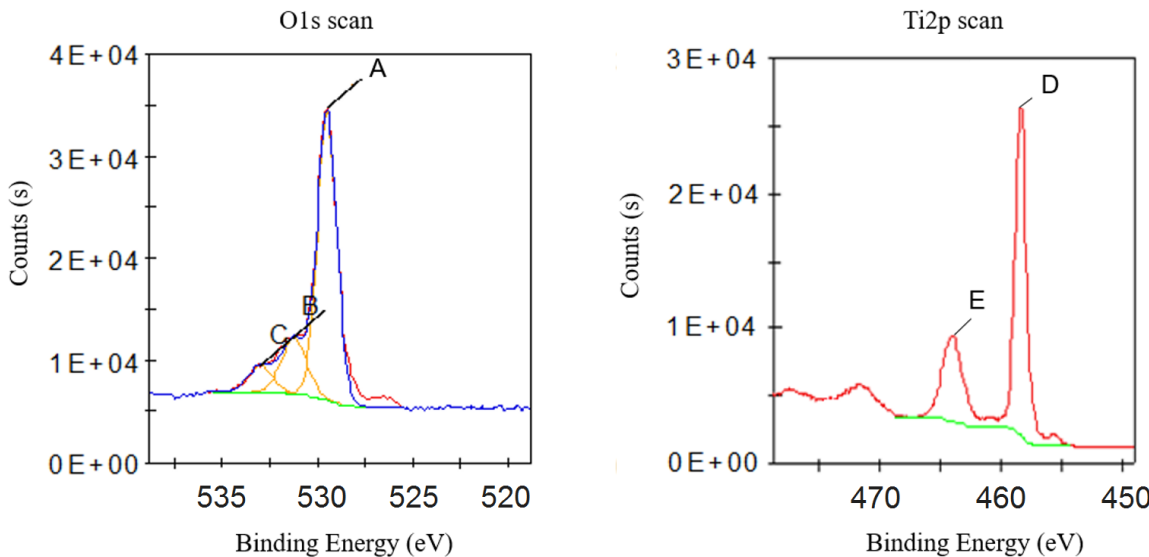


Figure 3.26. O1s and Ti2p scan of Ag(2)/P25

The values of BE of O1s and Ti2p in the spectra of the different catalysts are very similar and reported in the following Table 3.10.

Table 3.10. BE of Oxygen and Titanium species recorded by XPS

<b>Catalyst</b>	<b>BE (eV)</b>				
	<b>A</b> <b>O1s</b>	<b>B</b> <b>O1s</b>	<b>C</b> <b>O1s</b>	<b>D</b> <b>Ti<sup>4+</sup> 2p<sub>1/2</sub></b>	<b>E</b> <b>Ti<sup>4+</sup> 2p<sub>3/2</sub></b>
Ag(2)/P25	529.5	531.2	533	458.3	464.2
Ag(2)-Pt(4)/P25(K)	529.6	531.3	533	458.4	464.2
Pt(2)-Ag(2)/P25(H)	529.6	531.4	533	458.5	464.3
Pt(2)-Ag(2)/P25(K)	529.5	531.2	532.9	458.3	464.1
Pt(4)-Ag(2)/P25(K)	529.5	531.1	532.8	458.3	464.2

The peaks of O1s were deconvoluted in three species (A, B and C). The BE of the main species noted A at around 529.5 eV is assigned to the oxygen involved in Ti-O bonds. The BE of ~ 531.3 eV, corresponding to species noted B, is generally associated to the presence of oxygen vacancies in the TiO<sub>2</sub> lattice, and that at ~ 532.9 eV, corresponding to species noted C, is usually attributed to chemisorbed or dissociated oxygen on the surface (Sowmya et al. 2014).

The BE of  $\text{Ti}^{4+}$   $2\text{p}_{1/2}$  and  $\text{Ti}^{4+}$   $2\text{p}_{3/2}$  peaks of the Ti2p scan are centered at  $\sim 458.3$  eV (peak D) and  $\sim 464.2$  eV (peak E), respectively. These species well correspond to the standard values reported in literature ( $458.3 - 458.6$  eV and  $464 - 464.4$  eV) (Sowmya et al. 2014; Talat-Mehrabad et al. 2015).

The spectra Ag3d and Pt4f are deconvoluted and depicted in Figure 3.27. Their BE are reported in the Table 3.11.

The Silver species (Ag3d scan Figure 3.27) for all catalysts show two main peaks owing to high ( $\text{Ag } 3\text{d}_{5/2}$ ) and low ( $\text{Ag } 3\text{d}_{3/2}$ ) transition energies. They correspond to metallic  $\text{Ag}^0$  particles with different size. The BE of  $\text{Ag } 3\text{d}_{5/2}$  and  $\text{Ag } 3\text{d}_{3/2}$  are recorded at ca.  $367.1$  (peak A) and  $373.2$  eV (peak C), respectively. They are shifted to lower values in comparison to those reported in the literature at ca.  $369.1$  and  $375.1$  eV, respectively (Rodríguez-González et al. 2010; Sowmya et al. 2014), accounting for several concurrent features such as: strong interaction between  $\text{TiO}_2$  and  $\text{Ag}^0$ , due to a sufficient excited electron transfer from titania to  $\text{Ag}^0$  (Lee et al. 2014); the presence of an environment of chlorine provided by  $\text{K}_2\text{PtCl}_6$  (Aristizábal et al. 2014); and finally an electron transfer from Ag to Pt might occur.

Besides, the  $\text{Ag } 3\text{d}_{5/2}$  peak in the catalysts  $\text{Ag}(2)/\text{P25}$  and  $\text{Pt}(4)\text{-Ag}(2)/\text{P25(K)}$  show a slight asymmetry giving two peaks after their deconvolution (peaks A and B). The  $\text{Ag}(2)/\text{P25}$  presents a component with a BE of  $368$  eV (peak B), showing that part of Ag forms nanoparticles in different interaction with  $\text{TiO}_2$  (Wodka et al. 2010). It is more remarkable for the catalyst  $\text{Pt}(4)\text{-Ag}(2)/\text{P25(K)}$ , where the asymmetry of the peak is the highest among all catalysts, being shifted to  $366.9$  eV (peak A). This can be assigned, like for Pt-Ag particles supported on activated carbon (Pt-Ag/AC), to a larger electron transfer from Ag to Pt due to formation of Pt-Ag solid solution (Aristizábal et al. 2014). It will be likely formed when Ag is secondly impregnated and then deposited with strong interaction on Pt. Han et al. reported also impregnated Pt-Ag/ $\text{TiO}_2$  catalysts (Pt  $\sim 1$  wt. %; Ag:  $0.25\text{-}1$  wt. %) with formation of Pt-Ag solution ensemble of well mixed Pt and Ag atoms (Han et al. 2012). Moreover, this shift is larger when  $\text{K}_2\text{PtCl}_6$  is used as platinum precursor ( $366.9 - 367.1$  eV) instead of  $\text{H}_2\text{PtCl}_6 \cdot 6\text{H}_2\text{O}$  ( $367.2$  eV). As commented before, the  $\text{Ag } 3\text{d}_{5/2}$  peak in  $\text{Pt}(4)\text{-Ag}(2)/\text{P25(K)}$  reveals a weak component at  $367.9$  eV (peak B) in agreement with the large size distribution of the nanoparticles observed for these mono- and bimetallic samples by TEM (3.2.2.3). Such nanoparticles are not observed in the case of the Ag-Pt impregnation order over P25.

The XPS Platinum spectra (Pt4f scan Figure 3.27) are deconvoluted into three sets of peaks. The two Pt 4f<sub>7/2</sub> and Pt 4f<sub>5/2</sub> peaks with binding energies of ~ 70 eV (peak D) and ~ 74.4 eV (peak E) correspond to metallic state Pt<sup>0</sup> particles. These BE are close to the literature data for Pt<sup>0</sup> in Pt/TiO<sub>2</sub> catalyst at 70.5 and 73.9 eV (Ohtani et al. 1997), and bimetallic Pt-Ag/AC at ca. 71.1 and 74.4 eV (Aristizábal et al. 2014). It is noteworthy that the BE of Pt<sup>0</sup> are more slightly shifted toward lower energy values at 69.9 eV and 74.3 eV in Pt(2)-Ag(2)/P25(K) and Pt(4)-Ag(2)/P25(K) in agreement with the behavior also observed for Ag<sup>0</sup> and assigned to the main formation of a solid solution between Pt and Ag. These negative shifts are related to an enhancement of the electron transfer from TiO<sub>2</sub> to Pt due to a stronger metal-support interaction (Nie et al. 2013). Furthermore, a shoulder appears at BE of ~72.5 eV (peak F), suggesting the presence of a positively charged form of Pt (Ohtani et al. 1997).

Different Pt/Ag surface atomic ratios calculated by XPS that could be related to the catalyst preparation are observed (Table 3.12). These ratios are always lower than the theoretical values, except in the case of Pt(2)-Ag(2)/P25(H) where it is twofold higher than expected corresponding to a high Pt enrichment on the surface. The decrease of the Pt/Ag atomic ratio occurs when catalysts are prepared with K<sub>2</sub>PtCl<sub>6</sub> and particularly when Ag is impregnated first in Ag(2)-Pt(4)/P25(K). Increasing the Pt loading from 2 to 4 wt. % in the Pt-Ag based catalysts increases the Pt/Ag ratio from 0.8 to 1.4, which represents 80 and 60 % of the expected values, respectively. This reveals a lower enrichment in Pt of the surface at higher Pt loading. Thereupon, Pt/Ag atomic ratio is decreased by: Ag-Pt precursor impregnation addition instead of Pt-Ag; K<sub>2</sub>PtCl<sub>6</sub> as Pt precursor; and higher Pt load.

Summarizing, Ag is almost totally reduced, as in addition to Pt<sup>0</sup>, only slight amount of non-reduced platinum is present in the bimetallic samples following the NaBH<sub>4</sub> treatment. Ag and Pt appear mainly involved in a solid solution when Pt is firstly impregnated, with also the presence of silver nanoparticles similar to those observed in Ag(2)/P25. Ag impregnated first is probably decorated by Pt. In this case the electronic properties of Ag<sup>0</sup> in the bimetallic Ag(2)-Pt(4)/P25(K) sample are close to those observed in Ag(2)/P25. When the Pt is impregnated first, the surface is more enriched by Ag if the Pt loading is decreased. K<sub>2</sub>PtCl<sub>6</sub> precursor and the Ag-Pt impregnation order decrease the surface Pt/Ag atomic ratios.

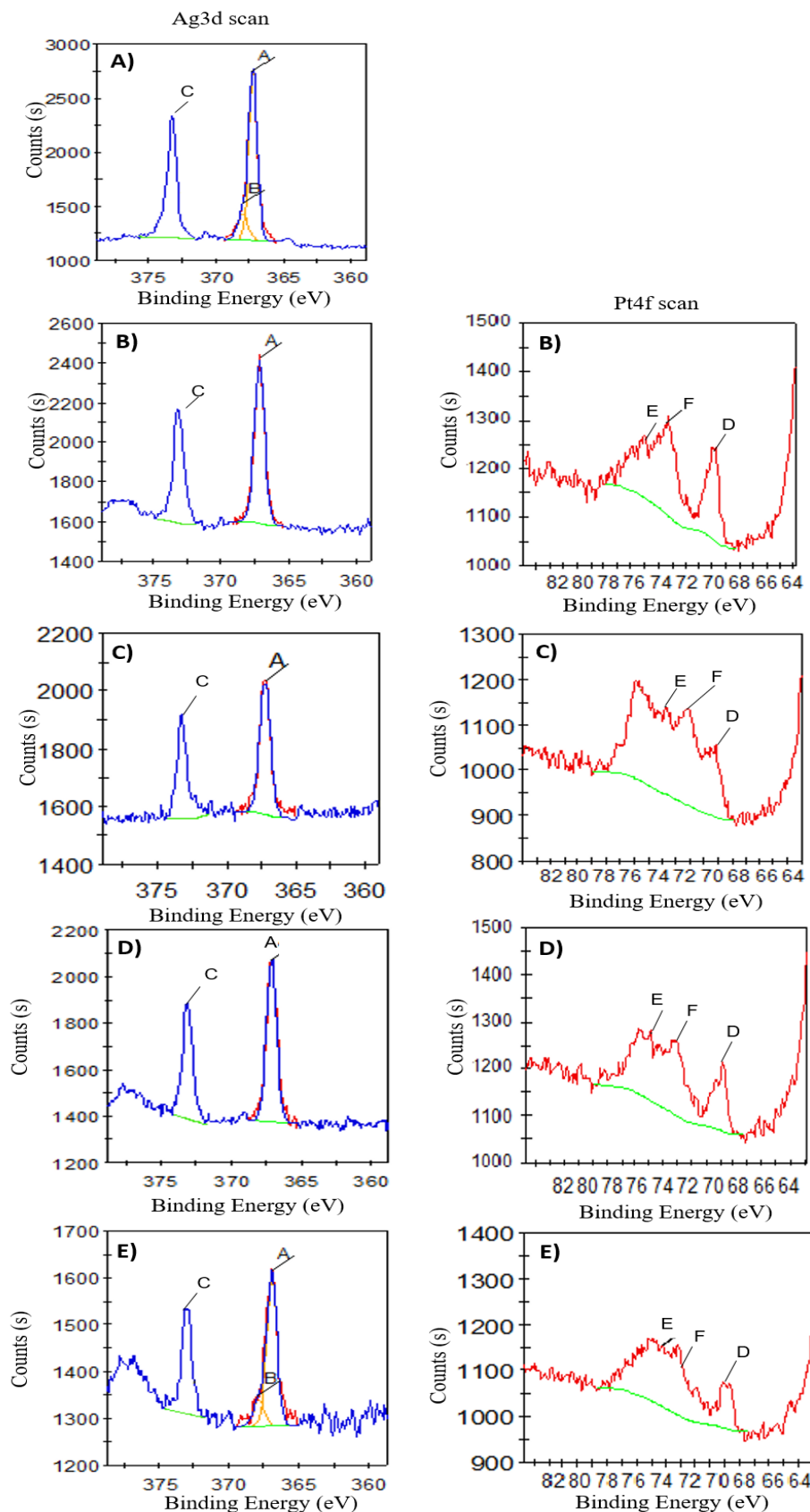


Figure 3.27. Ag3d and Pt4f scans of selected catalysts: A)  $\text{Ag}(2)/\text{P}25$ , B)  $\text{Ag}(2)\text{-Pt}(4)/\text{P}25(\text{K})$ , C)  $\text{Pt}(2)\text{-Ag}(2)/\text{P}25(\text{H})$ , D)  $\text{Pt}(2)\text{-Ag}(2)/\text{P}25(\text{K})$ , and E)  $\text{Pt}(4)\text{-Ag}(2)/\text{P}25(\text{K})$

The following Table 3.11 shows the BE extracted from the Ag3d and Pt4f spectra for the selected catalysts.

Table 3.11. BE of silver and platinum species recorded by XPS

Catalyst	BE (eV)					
	A $\text{Ag}^0\text{3d}_{5/2}$	B $\text{Ag}^0\text{3d}_{5/2}$	C $\text{Ag}^0\text{3d}_{3/2}$	D $\text{Pt}^0\text{4f}_{7/2}$	E $\text{Pt}^0\text{4f}_{5/2}$	F $\text{Pt(II)}\text{4f}_{7/2}$
Ag(2)/P25	367.2	368	373.2	-	-	-
Ag(2)-Pt(4)/P25(K)	367.1	-	373.2	70	74.5	72.8
Pt(2)-Ag(2)/P25(H)	367.2	-	373.2	70.3	74.4	72.2
Pt(2)-Ag(2)/P25(K)	367	-	373.1	69.9	74.3	72.8
Pt(4)-Ag(2)/P25(K)	366.9	367.9	373.2	69.9	74.3	72.1

The theoretical Pt/Ag atomic ratios and the ones calculated by XPS are shown in the following Table 3.12.

Table 3.12. Pt/Ag atomic ratios of select bimetallics by XPS.

Catalyst	Pt/Ag (% at.)	
	Theoretical	XPS
Ag(2)-Pt(4)/P25(K)	2	0.9
Pt(2)-Ag(2)/P25(H)	1	2
Pt(2)-Ag(2)/P25(K)	1	0.8
Pt(4)-Ag(2)/P25(K)	2	1.4

### 3.2.2.6 Temperature-Programmed Reduction by hydrogen (H<sub>2</sub>-TPR)

The reducibility of all the bimetallic catalysts, was studied by H<sub>2</sub>-TPR as previously described for the monometallic catalysts (3.1.2.5). The Figures 3.28 (monometallics and Ag-Pt bimetallics) and 3.29 (Pt-Ag bimetallics) at the end of the section display the TPR profiles of the bimetallic catalysts analyzed in the temperature range from -50 °C to 400 °C. For the sake of comparison, the TPR profiles of the monometallic catalysts are also reported in Figure 3.28. The reduction of bulk oxygen of TiO<sub>2</sub> takes place at T > 600 °C (Zhang et al. 2012).

At first glance the TPR profiles of the bimetallic samples have the same shape than those of the monometallic ones with the corresponding Pt precursor and loading with the same assignment of the reduction peaks. It can be assumed that Ag is reduced to metallic state Ag<sup>0</sup> during impregnation because any shoulder at T ~ 100 °C related to silver oxide species or AgNO<sub>3</sub> reduction is registered in the bimetallic catalysts (Nanba et al. 2012; Aristizábal et al. 2014).

The decrease of the 56.2 % of the H<sub>2</sub> consumption in comparison to the corresponding Pt-monometallic samples is due to the large increase of the mean particle sizes and this confirms that there is probably no contribution of Ag reduction (Table 3.13).

The peak of high intensity at T ~ 25 °C when H<sub>2</sub>PtCl<sub>6</sub>·6H<sub>2</sub>O was used as precursor is attributed to highly dispersed Pt<sup>0</sup> particles as observed by TEM in the reduced samples (3.1.2.3). The TPR profiles of all the bimetallic catalysts reveal a reduction in different stages, obtaining the majority of Pt<sup>0</sup> particles at approximately room temperature (Ou et al. 2007). An exception among all catalysts is the Pt(4)-Ag(2)/P25(H) catalyst (Figure 3.29), which chemisorbs hydrogen below 0 °C (-34 and -3 °C) (Wagstaff et al. 1979), showing that the metal particles might be highly dispersed and interact weakly with the support when located at the boundaries of the anatase particles. These Pt reduction differences are reflected in the catalytic activity behavior (*Chapter 4*).

Generally, indifferently of the platinum precursor used and the impregnation order in the catalyst preparation, the catalysts loaded with 4 % of Pt showed a higher hydrogen consumption (0.20 - 0.73 mmol g<sup>-1</sup>) than the ones with 2 % (0.18 - 0.33 mmol g<sup>-1</sup>). These increases are dramatically observed with the H<sub>2</sub>PtCl<sub>6</sub>·6H<sub>2</sub>O precursor, especially when the addition order was Ag-Pt (170.4 %) rather than Pt-Ag (similar %).

A quite different feature is observed when Ag was secondly impregnated (Pt-Ag), suggesting that decoration of Pt particles by Ag occurs, as confirmed by XPS (3.2.2.5), thus hindering Pt reduction.

The bimetallic catalysts impregnated with the K<sub>2</sub>PtCl<sub>6</sub> precursor exhibit very weak peaks of Pt reduction at around 11, 25 and 232 °C, and lower amounts of H<sub>2</sub> consumed due to the large mean particle sizes (~ 2 nm) (3.2.2.3), the presence of residual K<sub>2</sub>PtCl<sub>6</sub> detected by XRD (3.2.2.1); and the strong Ag-Pt interaction revealed by XPS (3.2.2.5). These characteristics were remarkably recorded by the catalyst Pt(4)-Ag(2)/P25(K).

The Figure 3.28 reports the TPR profiles of the monometallic and bimetallic Ag-Pt catalysts.

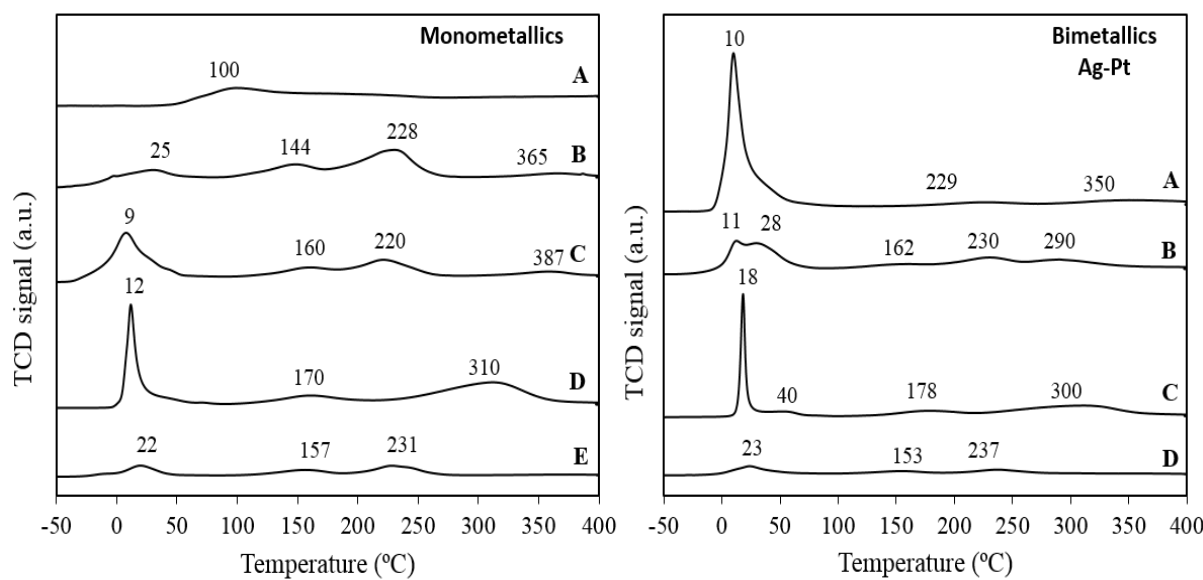


Figure 3.28. H<sub>2</sub>-TPR profiles of monometallic catalysts: A) Ag(2)/P25, B) Pt(2)/P25(H), C) Pt(2)/P25(K), D) Pt(4)/P25(H), and E) Pt(4)/P25(K); and Ag-Pt bimetallic catalysts: A) Ag(2)-Pt(2)/P25(H), B) Ag(2)-Pt(2)/P25(K), C) Ag(2)-Pt(4)/P25(H), and D) Ag(2)-Pt(4)/P25(K)

Fig. 3.29 displays the TPR profiles of the Pt-Ag bimetallic catalysts.

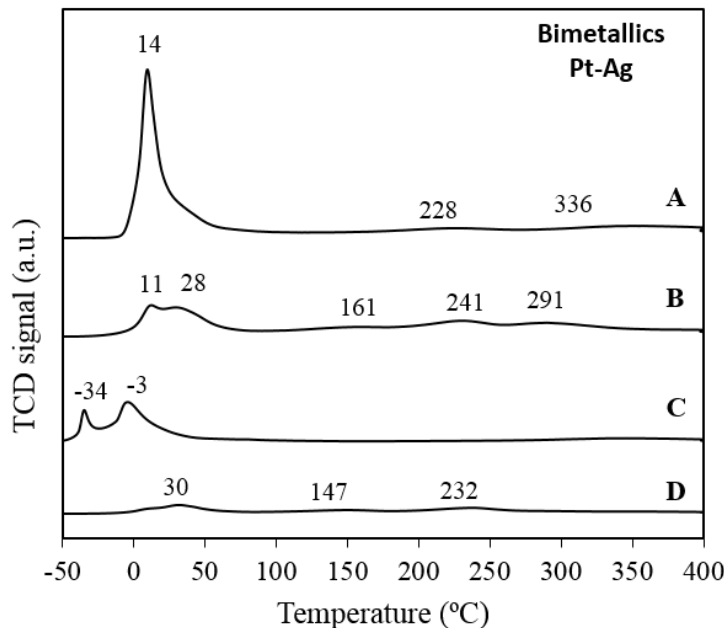


Figure 3.29. H<sub>2</sub>-TPR profiles of Pt-Ag bimetallic catalysts: A) Pt(2)-Ag(2)/P25(H), B) Pt(2)-Ag(2)/P25(K), C) Pt(4)-Ag(2)/P25(H), and D) Pt(4)-Ag(2)/P25(K)

The Table 3.13 reports the H<sub>2</sub> consumed for all bimetallic catalysts.

Table 3.13. Hydrogen consumption of bimetallic catalysts

Catalyst	H <sub>2</sub> TPR (mmol/g)
Ag(2)-Pt(2)/P25(H)	0.27
Ag(2)-Pt(2)/P25(K)	0.22
Ag(2)-Pt(4)/P25(H)	0.73
Ag(2)-Pt(4)/P25(K)	0.33
Pt(2)-Ag(2)/P25(H)	0.32
Pt(2)-Ag(2)/P25(K)	0.18
Pt(4)-Ag(2)/P25(H)	0.29
Pt(4)-Ag(2)/P25(K)	0.20

### 3.3 References

- Antos G.J., A.M. Aitani, J. M. Parera. Catalytic Naphtha Reforming, Marcel Dekker, New York, 2004.
- Aristizábal, A., S. Contreras, N. J. Divins, J. Llorca, and F. Medina. 2014. “Effect of Impregnation Protocol in the Metallic Sites of Pt-Ag/activated Carbon Catalysts for Water Denitration.” *Applied Surface Science* 298:75–89.
- Calderón-Magdaleno, M. A., J. A. Mendoza-Nieto, and T. E. Klimova. 2014. “Effect of the Amount of Citric Acid Used in the Preparation of NiMo/SBA-15 Catalysts on Their Performance in HDS of Dibenzothiophene-Type Compounds.” *Catalysis Today* 220-222:78–88.
- Coutanceau, C., S. Baranton, and T. W. Napporn. 2012. “Platinum Fuel Cell Nanoparticle Syntheses: Effect on Morphology , Structure and Electrocatalytic Behavior.” *The Delivery of Nanoparticles* 403–30.
- Doudrick, K., T. Yang, K. Hristovski, and P. Westerhoff. 2013. “Photocatalytic Nitrate Reduction in Water: Managing the Hole Scavenger and Reaction by-Product Selectivity.” *Applied Catalysis B: Environmental* 136-137:40–47.
- Ghosh Chaudhuri, R., and Sa. Paria. 2012. “Core/shell Nanoparticles: Classes, Properties, Synthesis Mechanisms, Characterization, and Applications.” *Chemical Reviews* 112(4):2373–2433.
- Gomathi Devi, L., and K. Mohan Reddy. 2010. “Enhanced Photocatalytic Activity of Silver Metallized TiO<sub>2</sub> Particles in the Degradation of an Azo Dye Methyl Orange: Characterization and Activity at Different pH Values.” *Applied Surface Science* 256(10):3116–21.
- Han, Y., J. Zhou, W. wang, H. Wan, Z. Xu, S. Zheng, and D. Zhu. 2012. “Enhanced Selective Hydrodechlorination of 1,2-Dichloroethane to Ethylene on Pt-Ag/TiO<sub>2</sub> Catalysts Prepared by Sequential Photodeposition.” *Applied Catalysis B: Environmental* 125:172–79.
- Iliev, V., D. Tomova, L. Bilyarska, A. Eliyas, and L. Petrov. 2006. “Photocatalytic Properties of TiO<sub>2</sub> Modified with Platinum and Silver Nanoparticles in the Degradation of Oxalic Acid in Aqueous Solution.” *Applied Catalysis B: Environmental* 63:266–71.
- Kanda, Y., A. Seino, T. Kobayashi, Y. Uemichi, and M. Sugioka. 2009. “Catalytic Performance of Noble Metals Supported on Mesoporous Silica MCM-41 for Hydrodesulfurization of Benzothiophene.” *Journal of the Japan Petroleum Institute* 52(2):42–50.

- Krejcikova, S., L. Matejova, K. Koci, L. Obalova, Z. Matej, L. Capek, and O. Solcova. 2012. “Preparation and Characterization of Ag-Doped Crystalline Titania for Photocatalysis Applications.” *Applied Catalysis B: Environmental* 111-112:119–25.
- Lee, D. S., and Y. W. Chen. 2014. “Nano Ag/TiO<sub>2</sub> Catalyst Prepared by Chemical Deposition and Its Photocatalytic Activity.” *Journal of the Taiwan Institute of Chemical Engineers* 45:705–12.
- Li, F. B., F. B. Li, X. Z. Li, and X. Z. Li. 2002. “The Enhancement of Photodegradation Efficiency Using Pt-TiO<sub>2</sub> Catalyst.” *Chemosphere* 48:1103–11.
- Li, S. S., J. N. Zheng, A. J. Wang, G. L. Tao, J. j. Feng, J. R. Chen, and H. Yu. 2014. “Branched Platinum-on-Palladium Bimetallic Heteronanostructures Supported on Reduced Graphene Oxide for Highly Efficient Oxygen Reduction Reaction.” *Journal of Power Sources* 272:1078–85.
- Matos, J., T. Marino, R. Molinari, and H. García. 2012. “Hydrogen Photoproduction under Visible Irradiation of Au-TiO<sub>2</sub>/activated Carbon.” *Applied Catalysis A: General* 417-418:263–72.
- Mulfinger, L., S. D. Solomon, M. Bahadory, A. V. Jeyajasingam, S. A. Rutkowsk, and C. Boritz. 2007. “Synthesis and Study of Silver Nanoparticles.” *Journal of Chemical Education* 84(2):322–25.
- Nanba, T., S. Masukawa, J. Uchisawa, and A. Obuchi. 2012. “Influence of TiO<sub>2</sub> Crystal Structure on Acrylonitrile Decomposition over Ag/TiO<sub>2</sub>.” *Applied Catalysis A: General* 419-420:49–52.
- Nie, L., J. Yu, X. Li, B. Cheng, G. Liu, and M. Jaroniec. 2013. “Enhanced Performance of NaOH-Modified Pt/TiO<sub>2</sub> toward Room Temperature Selective Oxidation of Formaldehyde.”
- Ohtani, B., K. Iwai, S. I. Nishimoto, and S. Sato. 1997. “Role of Platinum Deposits on Titanium (IV) Oxide Particles : Structural and Kinetic Analyses of Photocatalytic Reaction in Aqueous Alcohol and Amino Acid Solutions.” *Society* 101(Iv):3349–59.
- Ou, H. H., and S. Lien Lo. 2007. “Effect of Pt/Pd-Doped TiO<sub>2</sub> on the Photocatalytic Degradation of Trichloroethylene.” *Journal of Molecular Catalysis A: Chemical* 275(1-2):200–205.
- Panagiotopoulou, P., A. Christodoulakis, D. I. Kondarides, and S. Boghosian. 2006. “Particle Size Effects on the Reducibility of Titanium Dioxide and Its Relation to the Water-Gas Shift Activity of Pt/TiO<sub>2</sub> Catalysts.” *Journal of Catalysis* 240(2):114–25.
- Pulido Melián, E., O. González Díaz, J. M. Doña Rodríguez, G. Colón, J. A. Navío, M. Macías, and J. Pérez Peña. 2012. “Effect of Deposition of Silver on Structural Characteristics and Photoactivity of TiO<sub>2</sub>-Based Photocatalysts.” *Applied Catalysis B: Environmental* 127:112–20.

- Qiu, S., and S. J. Kalita. 2006. "Synthesis, Processing and Characterization of Nanocrystalline Titanium Dioxide." *Materials Science and Engineering A* 435-436:327–32.
- Rashid, M. U., K. H. Bhuiyan, and M. E. Quayum. 2013. "Synthesis of Silver Nano Particles (Ag-NPs) and Their Uses for Quantitative Analysis of Vitamin C Tablets." *J. Pharm., Sci.* 12(1):29–35.
- Rodríguez-González, V., S. Obregón Alfaro, L. M. Torres-Martínez, S. H. Cho, and S. Wohn Lee. 2010. "Silver-TiO<sub>2</sub> Nanocomposites: Synthesis and Harmful Algae Bloom UV-Photoelimination." *Applied Catalysis B: Environmental* 98(3-4):229–34.
- Rupa, A. Valentine, D. Divakar, and T. Sivakumar. 2009. "Titania and Noble Metals Deposited Titania Catalysts in the Photodegradation of Tartazine." *Catalysis Letters* 132(1-2):259–67.
- S.I-No.106. 2007. "European Communities Drinking Water Regulations."
- Sakthivel, S., M. V. Shankar, M. Palanichamy, B. Arabindoo, D. W. Bahnemann, and V. Murugesan. 2004. "Enhancement of Photocatalytic Activity by Metal Deposition: Characterisation and Photonic Efficiency of Pt, Au and Pd Deposited on TiO<sub>2</sub> Catalyst." *Water Research* 38(13):3001–8.
- Sclafani, A., M.N. Mozzanegra, and J. M. Herrmann. 1997. "Influence of Silver Deposits on the Photocatalytic Activity of Titania." *Journal of Catalysis* 120:117–20.
- Sclafani, A., and J. M. Herrmann. 1998. "Influence of Metallic Silver and of Platinum-Silver Bimetallic Deposits on the Photocatalytic Activity of Titania (Anatase and Rutile) in Organic and Aqueous Media." *Journal of Photochemistry and Photobiology A: Chemistry* 113:181–88.
- Sing, K. S. W. 1985. "Reporting Physisorption Data for Gas/solid Systems with Special Reference to the Determination of Surface Area and Porosity (Recommendations 1984)." *Pure and Applied Chemistry* 57(4):603–19.
- Sobana, N., M. M., and M. Swaminathan. 2006. "Nano-Ag Particles Doped TiO<sub>2</sub> for Efficient Photodegradation of Direct Azo Dyes." *Journal of Molecular Catalysis A: Chemical* 258(1-2):124–32.
- Sowmya, A., and S. Meenakshi. 2014. "Photocatalytic Reduction of Nitrate over Ag-TiO<sub>2</sub> in the Presence of Oxalic Acid." *Journal of Water Process Engineering* 4–11.
- Sridharan, K., T. Endo, S. G. Cho, J. Kim, T. J. Park, and R. Philip. 2013. "Single Step Synthesis and Optical Limiting Properties of Ni–Ag and Fe–Ag Bimetallic Nanoparticles." *Optical Materials* 35(5):860–67.
- Suttiponparnit, Komkrit, J. Jiang, m. Sahu, S. Suvachittanont, T. Charinpanitkul, and P. Biswas. 2011. "Role of Surface Area, Primary Particle Size, and Crystal Phase on Titanium Dioxide Nanoparticle Dispersion Properties." *Nanoscale Research Letters* 6(1):1–8.

- Talat-Mehrabad, J., M. Khosravi, N. Modirshahla, and M. A. Behnajady. 2015. "Synthesis, Characterization, and Photocatalytic Activity of Co-Doped Ag-, Mg-TiO<sub>2</sub>-P25 by Photodeposition and Impregnation Methods." Desalination and Water Treatment 1–11).
- Tang, X., B. Zhang, Y. Li, Y. Xu, q. Xin, and W. Shen. 2004. "Structural Features and Catalytic Properties of Pt/CeO<sub>2</sub> Catalysts Prepared by Modified Reduction-Deposition Techniques." *Catalysis Letters* 97(3-4):163–69.
- Tsai, C. C., and H. Teng. 2004. "Regulation of the Physical Characteristics of Titania Nanotube Aggregates Synthesized from Hydrothermal Treatment." *Chemistry of Materials* 16(22):4352–58.
- Viswanathan, B., and K. J. Antony Raj. 2009. "Effect of Surface Area, Pore Volume and Particle Size of P25 Titania on the Phase Transformation of Anatase to Rutile." *Indian Journal of Chemistry - Section A Inorganic, Physical, Theoretical and Analytical Chemistry* 48(October):1378–82.
- Wagstaff, N., and R. Prins. 1979. "Alloy Formation and Metal Oxide Segregation in PtRe/γ-AlO Catalysts as Investigated by Temperature-Programmed Reduction." *Journal of Catalysis* 59(3):434–45.
- Wang, G., L. Xu, J. Zhang, T. Yin, and D. Han. 2012. "Enhanced Photocatalytic Activity of TiO<sub>2</sub> Powders (P25) via Calcination Treatment." *International Journal of Photoenergy* 2012.
- Wodka, D., E. Bielanska, R. P. Socha, M. Elzbieciak-Wodka, J. Gurgul, P. Nowak, P. Warszynski, and I. Kumariki. 2010. "Photocatalytic Activity of Titanium Dioxide Modified by Silver Nanoparticles." *ACS Applied Materials and Interfaces* 2(7):1945–53.
- Xu, Z., J. Yu, and M. Jaroniec. 2015. "Efficient Catalytic Removal of Formaldehyde at Room Temperature Using AlOOH Nanoflakes with Deposited Pt." *Applied Catalysis B: Environmental* 163:306–12.
- Yu, J., and J. Ran. 2011. "Facile Preparation and Enhanced Photocatalytic H<sub>2</sub>-Production Activity of Cu(OH)<sub>2</sub> Cluster Modified TiO<sub>2</sub>." *Energy & Environmental Science* 4:1364.
- Yu, J., M. Zhou, B. Cheng, and X. Zhao. 2006. "Preparation, Characterization and Photocatalytic Activity of in Situ N,S-Codoped TiO<sub>2</sub> Powders." *Journal of Molecular Catalysis A: Chemical* 246(1-2):176–84.
- Zaleska-Medynska, A., M. Marchelek, M. Diak, and E. Grabowska. 2016. "Noble Metal-Based Bimetallic Nanoparticles: The Effect of the Structure on the Optical, Catalytic and Photocatalytic Properties." *Advances in Colloid and Interface Science* 229:80–107
- Zhang, L., H. H. Mohamed, R. Dillert, and D. Bahnemann. 2012. "Kinetics and Mechanisms of Charge Transfer Processes in Photocatalytic Systems: A Review." *Journal of Photochemistry and Photobiology C: Photochemistry Reviews* 13(4):263–76.

## CHAPTER 4:

# Catalytic and Photocatalytic nitrate abatement using Ag and Pt/P25 catalysts

#### 4. Catalytic and Photocatalytic nitrate abatement using Ag and Pt/P25 catalysts

In this chapter, the heterogeneous catalytic process (non-photocatalytic) and the photocatalytic processes (UV-A and UV-C) of nitrate reduction with various nanocatalysts based on silver and/or platinum (Ag, Pt, Ag-Pt, Pt-Ag) supported on Aerioxide Titania P25 are studied in order to reach the European Normative regarding nitrate, nitrite and ammonium ions concentration in drinking water (S.I-No.106 2007). Several parameters related to the preparation and composition of the catalysts and to the catalytic and photocatalytic reactions have been varied in order to determine their influence on the nitrate conversion and reduction rate, the selectivity and the yield of products. The performances of the catalysts are related to their physicochemical properties, which are extensively detailed in the previous *Chapter 3*.

The first section (4.1) describes the experimental conditions of the different denitration experiments. The studies were carried out in a PTFE batch reactor under standard operational conditions in absence/presence of pure hydrogen stream, which is used as reducing agent. In the photocatalytic process, two types of ultraviolet irradiations were used at  $\lambda = 254$  nm (UV-C) and 365 nm (UV-A) in absence/presence of hydrogen flow.

The second section (4.2) shows the aqueous denitration tests carried out only with the support Aerioxide Titania P25, named as Blank experiments.

The sections 4.3 and 4.4 largely detail the catalytic and photocatalytic performances obtained with the monometallic and bimetallic catalysts, respectively. The specific role of each noble metal (silver and platinum) is determined.

In the section 4.3 the effect of different parameters in the monometallic catalysts (Ag/P25, Pt/P25) have been studied: the noble metals loading (Ag: from 0.5 to 4 wt. %.; Pt: 2 and 4 wt. %); and the nature of the platinum precursors ( $H_2PtCl_6 \cdot 6H_2O$  and  $K_2PtCl_6$ ). The influence of the reagent used as nitrate source for the nitrate solution has been studied as well ( $NaNO_3$  and  $HNO_3$ ).

The last section of this chapter (4.4) describes the effect of various parameters in the bimetallic catalysts (Ag-Pt/P25, Pt-Ag/P25): the platinum loading (2 and 4 wt. %); the platinum precursors ( $H_2PtCl_6 \cdot 6H_2O$  and  $K_2PtCl_6$ ); and the impregnation order of both metals (Ag-Pt and Pt-Ag).

## 4.1 Experimental conditions and calculations

Denitration experiments were performed under inert standard operational conditions during 6 h of reaction (*Chapter 2, section 2.3*). Sodium nitrate ( $\text{NaNO}_3$ ) was used as the nitrate source ( $\text{pH} \approx 5.5$ ), except in the photocatalytic nitrate reduction with the monometallic catalyst  $\text{Ag}(2)/\text{P25}$ , where for the sake of comparison of nitrate sources, nitric acid ( $\text{HNO}_3$ ) with an initial  $\text{pH} \approx 2.5$  was used (4.4.1.2). An experiment of photocatalytic nitrite reduction was also performed (4.4.1.2), where 50 mg/L of  $\text{NO}_2^-$  ( $\text{pH} \approx 6.2$ ) was introduced -  $\text{NaNO}_2$  as nitrite source - to determine the role of platinum in the reaction.

Several studies were made in presence or absence of hydrogen, without UV irradiations (4.1.1) and with two different types of UV irradiations (4.1.2). Photocatalytic nitrate removal using solar irradiation and heterogeneous catalysts has raised as a very promising and ecofriendly technique (Ibhodon et al. 2013). The catalytic and photocatalytic experimental conditions are commented in points 4.1.1 and 4.1.2, and their notation (CAT, P(2), P(3), P(2)+ $\text{H}_2$  and P(3)+ $\text{H}_2$ ) will be explained (Table 4.1).

The experimental conditions (Cond) are described below and summarized in the Table 4.1.

### 4.1.1 Catalytic conditions

Catalytic, or non-photocatalytic, studies were carried out in the presence of a continuous and constant pure  $\text{H}_2$  stream of 150 mL/min ( $Q_{\text{H}_2}$ ) (CAT). For comparison, experiments without  $\text{H}_2$  were also performed. Ultraviolet irradiations were not applied (dark conditions).

### 4.1.2 Photocatalytic conditions

Photocatalytic experiments have been tested under 4W medium mercury maximum ultraviolet irradiations ( $\lambda = 254 \text{ nm}$  (UV-C) and  $\lambda = 365 \text{ nm}$  (UV-A)), in absence of  $\text{H}_2$  flow, noted as P(2) and P(3), respectively, and in presence of  $Q_{\text{H}_2} = 150 \text{ mL/min}$  (P(2)+ $\text{H}_2$  and P(3)+ $\text{H}_2$ ) for the sake of comparison. Their light intensity is  $7 \text{ mWcm}^{-2}$ . The two UV lamps are located on the top of the PTFE reactor.

No direct photolysis attributed to nitrate or nitrite should exist, and results should be entirely photocatalytic results, due to titania P25 in suspension absorbs most of the light below than  $\sim 400 \text{ nm}$ .  $\text{NO}_3^-$  absorbs at wavelengths primarily below  $\sim 250 \text{ nm}$  with a small absorption peak at  $\sim 305 \text{ nm}$ , which is lower than 1% of the total, and  $\text{NO}_2^-$  also presents a small peak at  $\sim 354$

nm. Thereupon, TiO<sub>2</sub> blocks the light absorption that could be absorbed by the NO<sub>3</sub><sup>-</sup> and NO<sub>2</sub><sup>-</sup> (Doudrick et al. 2012). Furthermore, the quartz glass blocks most of the NO<sub>3</sub><sup>-</sup> absorption wavelengths.

Catalytic and photocatalytic experimental conditions and notation applied are reported in the following Table 4.1.

Table 4.1. Notation of the experimental conditions

Process	Conditions		Nomenclature
	H <sub>2</sub>	λ (nm)	
Catalytic	Yes	No	CAT
Photocatalytic without H <sub>2</sub> flow	No	254	P(2)
		365	P(3)
Photocatalytic with H <sub>2</sub> flow	Yes	254	P(2)+H <sub>2</sub>
		365	P(3)+H <sub>2</sub>

The calculation data for the catalytic and photocatalytic results obtained with the monometallic and bimetallic catalysts are: nitrate conversion (Conv); nitrite, ammonium and nitrogen selectivities (Sel) and yields (Yield); and nitrate reduction rates (*k*). Nitrite conversion, selectivity and yields to nitrate, ammonium and nitrogen are only calculated for the photocatalytic nitrite reduction tests (4.3.2.2) to study the role of platinum in the catalytic/photocatalytic nitrate reduction. All information to calculate data can be observed in the section 2.4 of Chapter 2.

## 4.2 Aeroxide Titania P25

Titania (TiO<sub>2</sub>) is extensively applied for widespread environmental applications among several oxide semiconductor photocatalysts, due to its low-cost, strong oxidizing power, its biological and chemical inertness (non-toxic), long-term stability and redox efficiency (Chapter 1, 1.3.2.2).

First of all, nitrate and nitrite *adsorption* tests in ultrapure water have been done at dark conditions (no UV light) with the support Aeroxide Titania P25 (P25) in continuously suspension. No adsorption of both reagents onto the surface of titania has been obtained (Soares et al. 2014), therefore the results are purely catalytic and photocatalytic.

Blank experiments – dispersing only bare P25 – have been carried out under each catalytic and photocatalytic condition (shown in Table 4.2) – absence/presence of H<sub>2</sub> and UV irradiations (UV-C and UV-A). It could be considered that no NO<sub>3</sub><sup>-</sup> reduction occurs (~ 1 %). The blank experiment at dark conditions in absence of H<sub>2</sub> gives 0 % of nitrate conversion, thus this experiment has been only performed for the support (not shown).

Table 4.2. Catalytic and photocatalytic activities of Titania P25

<b>Catalyst</b>	<b>Cond</b>	<b>Conv (%)</b>	<b>Sel (%)</b>		
			<b>NO<sub>2</sub></b>	<b>NH<sub>4</sub><sup>+</sup></b>	<b>N<sub>2</sub></b>
P25	CAT	1	0	0	100
	P(2)	0.9	3.4	6.3	90.3
	P(3)	1	7	7	86
	P(2)+H <sub>2</sub>	0.8	10.4	2.1	87.5
	P(3)+H <sub>2</sub>	1	13.5	2	84.5

Titania has a limited band gap (anatase ca. 3.2 eV, rutile ca. 3 eV), then a high recombination rate between photogenerated electrons and holes exists, limiting the photocatalytic efficiency. Considering our results, the photocatalytic activity of titania has to be enhanced. Thus, TiO<sub>2</sub> is generally doped with noble metals improving the electron-hole separation and shifting the light absorption into the visible-light range (Asahi et al. 2001; Gomathi et al. 2010; Wang et al. 2012) (*Chapter 1, 1.3.2.3*). The light absorption band of titania P25 is shown in the *Chapter 3*, section *3.1.2.4*. In our research, silver and platinum are used to dope Titania P25.

The nitrate removal by heterogeneous non-photocatalytic and photocatalytic hydrogenation with the Ag- or Pt-monometallic (4.3) and Ag-Pt(Pt-Ag)-bimetallic catalysts (4.4) are extensively described in the following sections.

## 4.3 Monometallic catalysts

The influence of two parameters on the catalytic performances of the silver and platinum based monometallic catalysts has been studied: the noble metal loading (Ag: from 0.5 to 4 wt. %; Pt: 2 and 4 wt. %) and the platinum precursors ( $\text{H}_2\text{PtCl}_6 \cdot 6 \text{ H}_2\text{O}$  and  $\text{K}_2\text{PtCl}_6$ ). The nitrate source in the solution ( $\text{NaNO}_3$  and  $\text{HNO}_3$ ) is also varied using the monometallic 2 wt. % Ag/P25 catalyst.

### 4.3.1 Silver based monometallic catalysts

Silver is among the most largely used dopant of the photocatalytic activity of  $\text{TiO}_2$  (Zhang et al. 2007; Behnajady et al. 2008; Doudrick et al. 2013; Sowmya et al. 2014). The Ag particles can act as electron-hole separation centers. The photogenerated electrons are transferred from the P25 conduction band to metallic Ag NPs impregnated on P25, because the Fermi level of titania is higher than that of silver particles, which retards the recombination of the photogenerated electrons and holes (Kočí et al. 2012, Lee et al. 2014) (*Chapter 1, 1.3.1.1 and 1.3.2.3*).

The effect of the silver loading from 0.5 to 4 wt. % (4.3.1.1) and of the nitrate source (4.3.1.2) are detailed in the sections below.

#### 4.3.1.1 Effect of silver loading

The non-photocatalytic and photocatalytic behaviors of the Ag-monometallic catalysts with 0.5 - 4 wt. % Ag onto P25 are reported in Table 4.3 and Figures 4.1 to 4.4.

The catalysts are poorly active for the non-photocatalytic (entries 1 - 3) and photocatalytic reduction in absence of  $\text{H}_2$  (entries 4 - 9). In contrast, there is an increase of  $\text{NO}_3^-$  conversion and  $\text{N}_2$  selectivity and yield for the photocatalytic reduction in presence of  $\text{H}_2$  (entries 10 – 19) in comparison to the  $\text{H}_2$ -free condition (entries 4 - 9). Therefore, there is a clear influence of the presence of hydrogen on the photocatalytic nitrate reduction as reported by Hirayama et al (Hirayama et al. 2012). Also, they demonstrated that UV irradiation increased the nitrate conversion (27 - 40 %), selectivity and yield to  $\text{N}_2$  (5 - 20 % and 12 – 26 %, respectively), attributed to a synergistic effect induced by light between photo-generated electrons and  $\text{H}_2$ , as also reported by Soares et al. (Soares et al. 2014). Interestingly, high photocatalytic activities have been obtained at a closer wavelength to visible light irradiation ( $\lambda = 365 \text{ nm}$ ) and with  $\text{H}_2$  ( $\text{P(3)} + \text{H}_2$ ). This feature could lead to valuable practical applications. The enhancement of the

photocatalytic activity of the TiO<sub>2</sub> P25 support doped with Ag is consistent with the higher absorbance capability observed in the DRUV-Vis silver spectra (*Chapter 3, 3.1.2.4*).

Table 4.3. Catalytic and photocatalytic activities of 0.5 - 4 wt. % Ag/P25 samples under different experimental conditions

Entry	Catalyst	Cond	Conv (%)	Sel (%)			Yield (%)			Final pH
				NO <sub>2</sub> <sup>-</sup>	NH <sub>4</sub> <sup>+</sup>	N <sub>2</sub>	NO <sub>2</sub> <sup>-</sup>	NH <sub>4</sub> <sup>+</sup>	N <sub>2</sub>	
1	Ag(0.5)/P25		1.5	0	0	100	0	0	1.5	9.8
2	Ag(1)/P25	CAT	0	0	0	0	0	0	0	9.6
3	Ag(2)/P25		3	3.7	0	96.3	0.1	0	2.9	7.3
4	Ag(0.5)/P25		2.7	95.4	3.4	1.2	2.6	0.1	0	6.6
5	Ag(1)/P25	P(2)	2.4	54.3	9.8	35.9	1.3	0.2	0.9	5.5
6	Ag(2)/P25		6	83.5	0	16.5	5	0	1	4.8
7	Ag(0.5)/P25		2.3	96.5	3.1	0.4	2.2	0.1	0	6.7
8	Ag(1)/P25	P(3)	3.8	66.1	4.6	29.3	2.5	0.2	1.1	6.2
9	Ag(2)/P25		10	89.3	7.9	2.8	8.9	0.8	0.3	6.6
10	Ag(0.5)/P25		30.5	77.4	0.2	22.4	23.6	0.1	6.8	8
11	Ag(1)/P25	P(2)+H <sub>2</sub>	30.4	60.9	0.1	39	18.5	0.0	11.9	6.5
12	Ag(1.5)/P25		50.3	61.5	0.2	38.3	30.9	0.1	19.3	7.4
13	Ag(2)/P25		52	55.8	0	44.2	29.0	0	23	7.3
14	Ag(0.5)/P25		17.5	70.6	0.1	29.3	12.4	0	5.1	9
15	Ag(1)/P25		33	53.7	0	46.3	17.7	0	15.3	8.1
16	Ag(1.5)/P25	P(3)+H <sub>2</sub>	43.6	61.8	1.2	37	26.9	0.5	16.1	9.7
17	Ag(2)/P25		57	56.7	0	43.3	32.3	0	24.7	7.5
18	Ag(3)/P25		48.1	56.6	0.7	42.7	27.2	0.3	20.5	6.4
19	Ag(4)/P25		52.7	60.4	1	38.6	31.8	0.5	20.3	7.3

Until Ag loading of 2 wt. % the highest NO<sub>3</sub><sup>-</sup> conversion and yield to N<sub>2</sub> were observed working under P(3)+H<sub>2</sub> (entry 17; Figures 4.2 and 4.3) rather than P(2)+H<sub>2</sub> condition (entry 13; Figure 4.1). So, under P(3)+H<sub>2</sub> condition the influence of higher Ag loading, i.e. 3 and 4 wt. %, was investigated in order to determine the optimum value. It is obtained for 2 wt. % Ag(2)/P25 catalyst indeed leading to the highest nitrate conversion, and yield to nitrogen (Figures 4.1 and 4.2). At higher Ag loading, the nitrate conversion remains almost similar (48 - 53 %) but the N<sub>2</sub> yield slightly decreases (~ 20.5 %). Above 2 wt. % the increase of the silver particle size lowers its ability to store electrons (Takai et al. 2011). This has a slight influence on the N<sub>2</sub> yield. An important point is that ammonium is practically never formed (the worst case ca. 0.6 mg/L, Figure 4.4).

It is also noteworthy that, for a same catalyst, the final pH in P(2)+H<sub>2</sub> and P(3)+H<sub>2</sub> conditions is always higher than in P(2) and P(3) conditions. Moreover, the pH in presence of H<sub>2</sub> is above 6.3.

The photocatalytic nitrate conversion and yields to nitrogen and nitrite for all silver based monometallics are depicted in the following figures, applying the P(2)+H<sub>2</sub> (Figure 4.1) and P(3)+H<sub>2</sub> (Figure 4.2) experimental conditions. Figure 4.3 displays the conversion and selectivity to products under the most interesting experimental condition (P(3)+H<sub>2</sub>).

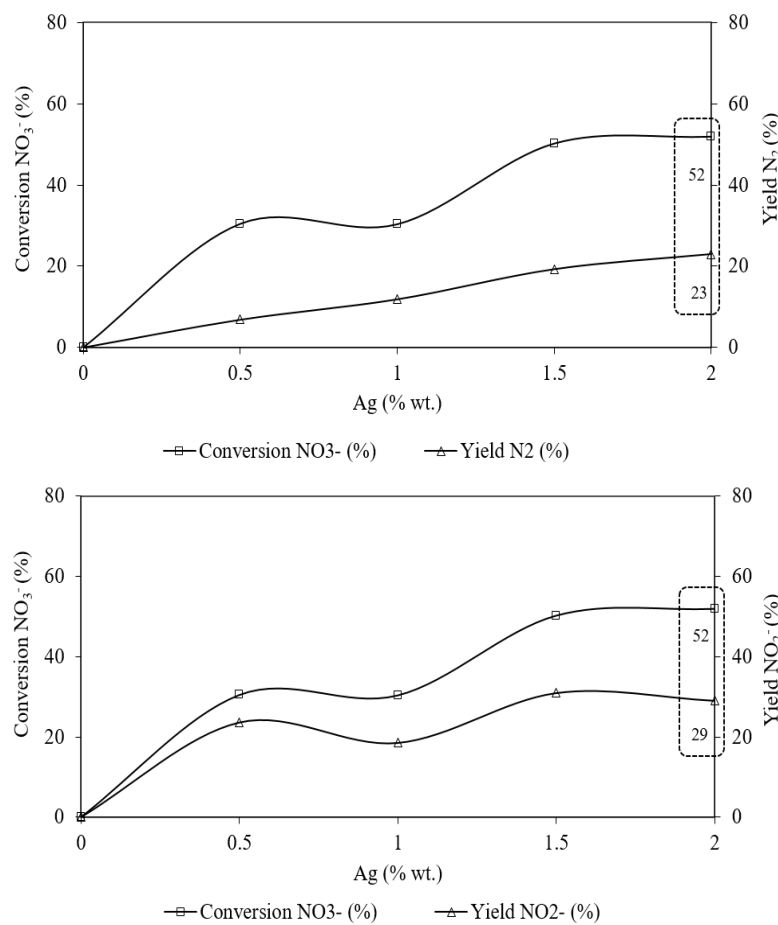


Figure 4.1. NO<sub>3</sub><sup>-</sup> conversion and yields (%) toward NO<sub>2</sub><sup>-</sup> and N<sub>2</sub>, varying the Ag loading (0.5 - 2 wt. %) under P(2)+H<sub>2</sub> condition after 6 h reaction

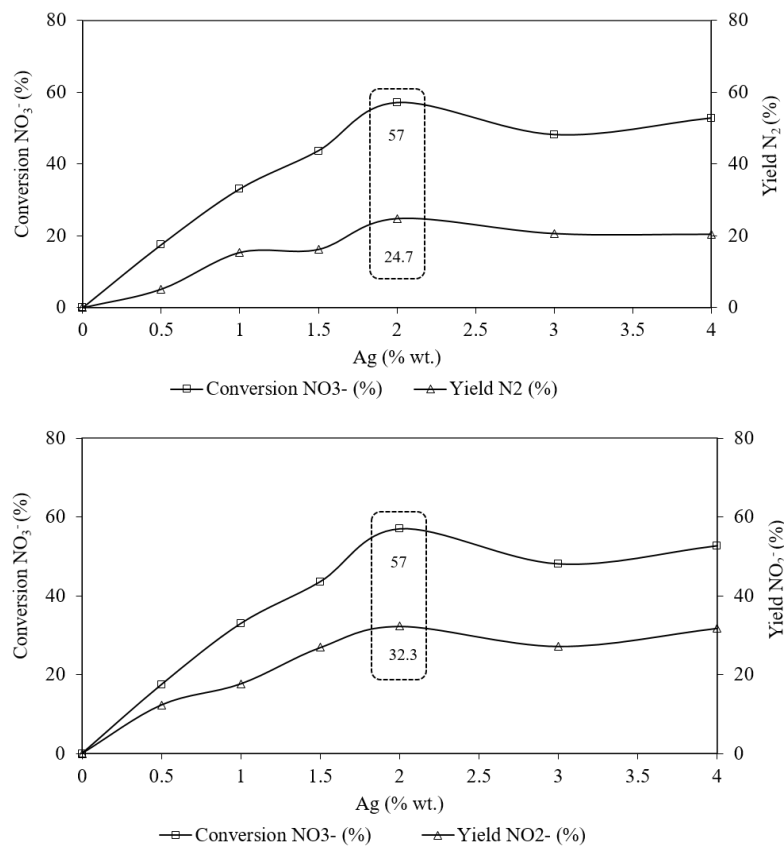


Figure 4.2. NO<sub>3</sub><sup>-</sup> conversion and yields (%) toward NO<sub>2</sub><sup>-</sup> and N<sub>2</sub>, varying the silver loading (0.5 - 4 wt. %) under P(3)+H<sub>2</sub> after 6 h reaction

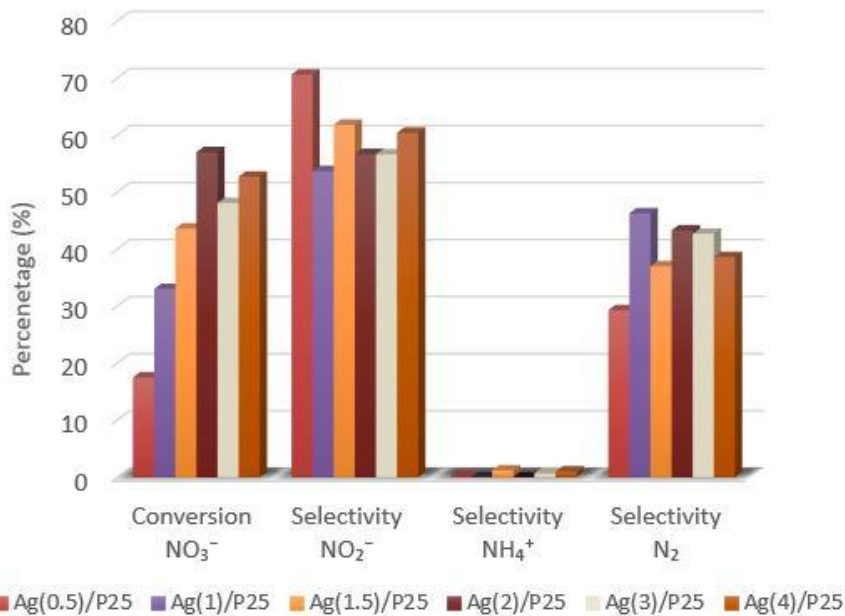


Figure 4.3. NO<sub>3</sub><sup>-</sup> conversion and selectivity to products (%) measured from Ag(x)/P25 catalysts under P(3)+H<sub>2</sub> condition after 6h reaction

The  $\text{NO}_3^-$ ,  $\text{NO}_2^-$  and  $\text{NH}_4^+$  concentrations ( $C_{\text{NO}_3^-}$ ,  $C_{\text{NO}_2^-}$ ,  $C_{\text{NH}_4^+}$ ) in function of the reaction time (h) registered for the Ag-based monometallic catalysts under  $\text{P}(2)+\text{H}_2$  and  $\text{P}(3)+\text{H}_2$  conditions are shown in the following Figure 4.4.

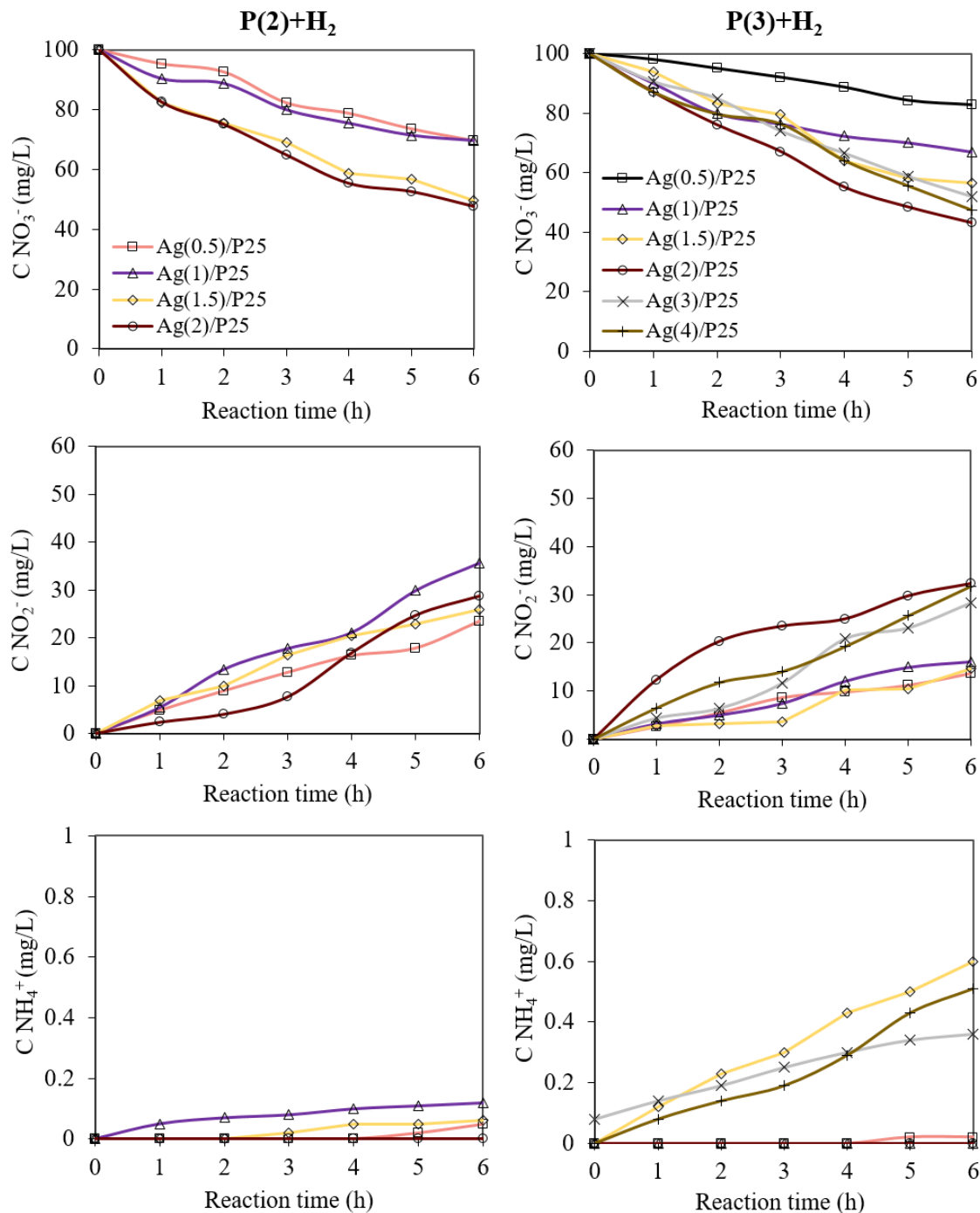


Figure 4.4.  $\text{NO}_3^-$ ,  $\text{NO}_2^-$  and  $\text{NH}_4^+$  concentrations (mg/L) in function of reaction time (h) recorded by the  $\text{Ag}(x)/\text{P}25$  catalysts under  $\text{P}(2)+\text{H}_2$  and  $\text{P}(3)+\text{H}_2$  conditions

Furthermore, the photocatalytic  $\text{NO}_3^-$  rate consumption ( $k$ ) (Chapter 2, 2.4.4) under  $\text{P}(2)+\text{H}_2$  and  $\text{P}(3)+\text{H}_2$  for each Ag-monometallic catalyst were calculated (Table 4.4 and 4.5). Ag(2)/P25 presented the highest nitrate reduction rate under both experimental conditions ( $0.113 \pm 0.040$  and  $0.165 \pm 0.065 \text{ h}^{-1}$ ), being higher obtained under UV-A irradiation. The improvement in the reaction rate as Ag loading increases up to 2 wt. % might be assigned to the ability of silver to build up excess electrons (Doudrick et al. 2012). Then at higher Ag loading the reaction rate decreases probably due to the increase of the particle size (Table 4.5).

Table 4.4. Pseudo-1<sup>st</sup> order nitrate reaction rates and correlation coefficients of Ag based monometallic catalysts at  $\text{P}(2)+\text{H}_2$  condition after 6 h reaction

Catalyst	$k$ ( $\text{h}^{-1}$ )	$R^2$
Ag(0.5)/P25	$0.066 \pm 0.019$	0.980
Ag(1)/P25	$0.057 \pm 0.024$	0.975
Ag(1.5)/P25	$0.101 \pm 0.037$	0.985
Ag(2)/P25	$0.113 \pm 0.040$	0.982

Table 4.5. Pseudo-1<sup>st</sup> order nitrate reaction rates and correlation coefficients of Ag based monometallic catalysts at  $\text{P}(3)+\text{H}_2$  condition after 6 h reaction

Catalyst	$k$ ( $\text{h}^{-1}$ )	$R^2$
Ag(0.5)/P25	$0.038 \pm 0.010$	0.998
Ag(1)/P25	$0.074 \pm 0.019$	0.991
Ag(1.5)/P25	$0.069 \pm 0.017$	0.990
Ag(2)/P25	$0.165 \pm 0.065$	0.987
Ag(3)/P25	$0.091 \pm 0.038$	0.962
Ag(4)/P25	$0.097 \pm 0.060$	0.983

The amount of 2 wt. % Ag was further chosen for the bimetallic catalysts, because it led to the best photocatalytic activity (Figures 4.1 to 4.4.) and the highest nitrate rate (Table 4.5) under UV-A irradiation in the monometallic catalysts. Nevertheless, the nitrite amount exceeds the European limits for drinking water (0.5 mg/L  $\text{NO}_2^-$ , Figure 4.4) (S.I-No.106 2007). This proves that Ag does not allow the reduction step from nitrite intermediate compound towards nitrogen gas and water.

The photocatalytic activity exhibited by the Ag(x)/P25 catalysts of this study in presence of H<sub>2</sub> is in agreement with that reported using Ag/TiO<sub>2</sub> catalysts prepared by photodeposition in presence of oxalic acid (Sowmya et al. 2014) or sodium oxalate (Gekko et al. 2012) as hole scavengers. In contrast, it disagrees with the results reported using on the one hand formic acid as hole scavenger, where complete NO<sub>3</sub><sup>-</sup> removal and residual NO<sub>2</sub><sup>-</sup> and NH<sub>4</sub><sup>+</sup> amounts were obtained with no significant improvement compared to bare TiO<sub>2</sub> P25 (Sá et al. 2009); and on the other hand, with the Ag-TiO<sub>2</sub> thin films leading to NO<sub>3</sub><sup>-</sup> removal of 70 % with complete selectivity toward N<sub>2</sub> (Kobwittaya et al. 2014). These differences emphasize the role of the reaction conditions and the preparation method of the photocatalyst. Our results, particularly the high NO<sub>2</sub><sup>-</sup> yields, are consistent with the low photoreduction ability to reduce NO<sub>2</sub><sup>-</sup> on Ag/TiO<sub>2</sub> with only a slight enhancement compared to bare TiO<sub>2</sub> (Zhang et al. 2007). However, with these Ag(x)/P25 catalysts, nitrite yields have to be greatly diminished to reach the limit of 0.5 mg/L NO<sub>2</sub><sup>-</sup> to fulfill the European nitrate, and in few cases also the ammonium, limits in drinking water (S.I-No.106 2007). No pH adjustment was done in all the experiments, then the pH increased from initial pH ≈ 5.5 to a value higher than 6.3 at the end of the reaction (Table 4.3). However, it is well-known that the pH is an important parameter of the reaction as increasing the pH decreases the number of protons available in the photocatalytic nitrate reduction reactions and increases the net negative surface charge of P25. These features induce a decrease of the nitrate removal and a great increase of the nitrite selectivity, which is the only product at pH > 5 (Doudrick et al. 2013). Therefore, in order to decrease the initial pH, we carried out denitration tests using nitric acid as nitrate source (pH ≈ 2.5) for sake of comparison with the ones performed with sodium nitrate (pH ≈ 5.5) using the Ag(2)/P25 catalyst.

#### 4.3.1.2 Effect of pH

The results of the catalytic and photocatalytic denitration tests in aqueous solution using Ag(2)/P25 catalyst and NaNO<sub>3</sub> (Riser S.A.) (pH ≈ 5.5) or HNO<sub>3</sub> (Aldrich) (pH ≈ 2.5) as nitrate sources are reported in Table 4.6. Acidic conditions have been reported to enhance the nitrate removal because the positive surface charge of the catalyst surface obtained as the pH decreases promotes the nitrate adsorption (Doudrick et al. 2013). But this is controversial in the literature as reverse behavior has been reported by Sá et al. and Soares et al. at too low pH, probably due to strong NO<sub>3</sub><sup>-</sup> adsorption (Sá et al. 2009; Soares et al. 2014).

Table 4.6. Catalytic and photocatalytic nitrate reductions varying the nitrate source, using Ag(2)/P25 catalyst.

Catalyst	Cond	NO <sub>3</sub> <sup>-</sup> source		Conv (%)	Sel (%)		Final pH	
		NaNO <sub>3</sub>	HNO <sub>3</sub>		NO <sub>2</sub> <sup>-</sup>	NH <sub>4</sub> <sup>+</sup>		
Ag(2)/P25	CAT	X		3	3.7	0	96.3	7.3
			X	1.2	0.1	0	99.9	2.4
	P(2)	X		6	83.5	0	16.5	4.8
			X	3.5	0	0	100	2.6
	P(3)	X		10	89.3	7.8	2.9	6.6
			X	9	0	0	100	2.6
	P(2)+H <sub>2</sub>	X		52	55.8	0	44.2	7.3
			X	6.8	0.2	0	99.8	2.6
	P(3)+H <sub>2</sub>	X		57	56.7	0	43.3	7.5
			X	16	20.4	0	79.6	2.7

In our research, the selectivity to nitrogen slightly increases using HNO<sub>3</sub> but with concurrent decrease of the nitrate conversion, even under the best photocatalytic conditions (P(3)+H<sub>2</sub>). This is in contradiction with the results reported by Doudrick et al. (Doudrick et al. 2013) but in agreement with the behavior reported by Sá and Soares (Sá et al. 2009; Soares et al. 2014). It can be noted that the experiments were performed in presence of formic acid in the case of Doudrick and Sá, but in presence of H<sub>2</sub> in the case of Soares. Both, these results of the literature and the behavior observed in our work, emphasize on the role of the other operating parameters than the pH in the activity.

Regarding the photocatalytic activity of the best monometallic catalyst (Ag(2)/P25), it becomes compulsory to add a second co-catalyst to improve the nitrate conversion and selectivity towards nitrogen while decreasing that towards nitrite. Therefore, it is a major target to perform the reaction using a bimetallic catalyst.

#### 4.3.2 Platinum based monometallic catalysts

Platinum has been chosen as second metal noble in the bimetallic catalysts because it is known as an electron sink for the semiconductor TiO<sub>2</sub>, then reducing the rate of electron-hole pair recombination rate (Kozlova et al. 2007). Besides, it possess the ability to dissociate easily H<sub>2</sub> and reduce NO<sub>2</sub><sup>-</sup> (Prüssee et al. 2000) (*Chapter 1, 1.3.1.1 and 1.3.2.3*). Due to the importance of metal loading, we have made denitration tests with 2 and 4 wt. % Pt, which is a similar approach than with monometallics Ag-containing samples. Another main parameter to take into

account is the nature of the Pt precursor, as it directly influences the surface metal chemistry and dispersion over the support. We have used  $\text{H}_2\text{PtCl}_6 \cdot 6\text{H}_2\text{O}$  and  $\text{K}_2\text{PtCl}_6$  as Pt precursors (Aristizábal et al. 2014)

To establish the catalytic and the photocatalytic contributions in the reduction of  $\text{NO}_3^-$ , experiments were done without UV irradiation in presence of  $\text{H}_2$  (CAT); under irradiation (254 and 365 nm) in  $\text{H}_2$ -free condition (P(2) and P(3)); and lastly under UV irradiation and in presence of  $\text{H}_2$  (P(2)+ $\text{H}_2$  and P(3)+ $\text{H}_2$ ).

#### 4.3.2.1 Effect of platinum loading and Pt precursor

Firstly, to study the influence of the experimental conditions on the performance of the catalyst we chose a Pt load of 4 wt. % and  $\text{H}_2\text{PtCl}_6 \cdot 6\text{H}_2\text{O}$  as precursor (Pt(4)/P25(H) sample). The catalytic results are reported in Table 4.7 (entries 1 - 5 and 7), and conversion and selectivity towards products in Figure 4.5.

Similarly to the Ag-based monometallic catalysts, higher nitrate conversions were obtained under photocatalytic conditions in presence of hydrogen flow, being better at the wavelength of 365 nm closer to solar light (P(3)+ $\text{H}_2$ ). However, the nitrate conversion (< 3 %) and the  $\text{N}_2$  yield (< 2 %) are very low (entry 7).

Secondly, denitration experiments were performed under P(3)+ $\text{H}_2$  condition, varying the Pt load (2 and 4 wt. %) and the Pt precursor:  $\text{H}_2\text{PtCl}_6 \cdot 6\text{H}_2\text{O}$  (entries 5 and 7) and  $\text{K}_2\text{PtCl}_6$  (entries 6 and 8).

Higher  $\text{NO}_3^-$  removal has been achieved when the Pt loading was increased from 2 to 4 wt. %, which is in agreement with the higher absorption observed in the DRUV-Vis spectrum of the Pt(4)/P25(H) sample (*Chapter 3, 3.1.2.4*). Impregnation with  $\text{K}_2\text{PtCl}_6$  precursor enhances the nitrate conversion at about 7 % and increases 10 times the nitrate reduction rate (Table 4.8) in comparison to the impregnation with  $\text{H}_2\text{PtCl}_6 \cdot 6\text{H}_2\text{O}$ . However, such variations observed in a low conversion range from 2.5 to 10 % can hardly be discussed. The maximum nitrate conversion was reached after 1 hour of reaction for the Pt(2)/P25 samples and 2 hours of reaction for the Pt(4)/P25 ones, and afterwards remain stable until the 6 hours of reaction. The final pH obtained for all of them was at ca. 5.5.

Table 4.7. Catalytic and photocatalytic activities of Pt based monometallic catalysts varying the Pt loading and precursor ( $\text{H}_2\text{PtCl}_6 \cdot 6\text{H}_2\text{O}$ / $\text{K}_2\text{PtCl}_6$ )

Entry	Catalyst	Cond	Conv (%)	Sel (%)			Yield (%)			Final pH
				$\text{NO}_2^-$	$\text{NH}_4^+$	$\text{N}_2$	$\text{NO}_2^-$	$\text{NH}_4^+$	$\text{N}_2$	
1	Pt(4)/P25(H)	CAT	0.8	0	3.2	96.8	0	0	0.8	5.5
2	Pt(4)/P25(H)	P(2)	1	4.5	2.8	92.7	0	0	0.9	5.5
3	Pt(4)/P25(H)	P(3)	1	7.6	2.1	90.3	0.1	0	0.9	5.2
4	Pt(4)/P25(H)	P(2)+ $\text{H}_2$	0.9	8	0.2	91.8	0.1	0	0.8	5.1
5	Pt(2)/P25(H)		1.4	1.6	34	64.4	0	0.5	0.9	5.4
6	Pt(2)/P25(K)		7.2	1.1	12.2	86.7	0.1	0.9	6.2	5.3
7	Pt(4)/P25(H)	P(3)+ $\text{H}_2$	2.6	0.1	32.9	67	0	0.9	1.7	5.3
8	Pt(4)/P25(K)		10.3	0.2	2.9	96.9	0	0.3	10	5.7

The most efficient catalyst is the Pt(4)/P25(K) (Table 4.7, entry 8), which gives the highest values of nitrate conversion (10.3 %), nitrate reduction rate ( $0.013 \pm 0.003 \text{ h}^{-1}$ ) (Table 4.8), selectivity and yield to  $\text{N}_2$  (96.9 and 10 %).

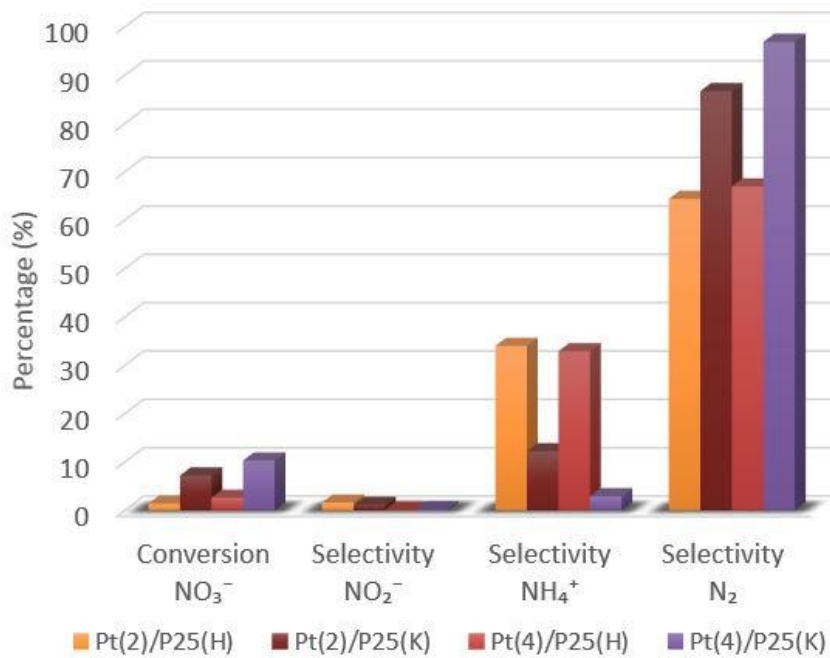


Figure 4.5.  $\text{NO}_3^-$  conversion and selectivity (%) to products measured from  $\text{Ag}(x)/\text{P25}$  catalysts under  $\text{P}(3)+\text{H}_2$  condition after 6h reaction

Table 4.8. Pseudo-1<sup>st</sup> order nitrate reaction rates and correlation coefficients of Pt(x)/P25(H/K) catalysts at P(3)+H<sub>2</sub> condition after 6 h reaction

Catalyst	k (h <sup>-1</sup> )	R <sup>2</sup>
Pt(2)/P25(H)	0.003 ± 0.003	0.987
Pt(2)/P25(K)	0.011 ± 0.006	0.966
Pt(4)/P25(H)	0.005 ± 0.001	0.987
Pt(4)/P25(K)	0.013 ± 0.003	0.976

Although nitrate conversions are very low (< 11 %), it must be emphasized that selectivities are totally different than those observed with the monometallic Ag-containing catalysts. Nitrite is indeed not formed and ammonium is the main by-product. The ammonium amount exceeds the European legal limits (0.3 mg/L NH<sub>4</sub><sup>+</sup>) (S.I-No.106 2007).

In order to check the influence in the catalytic activity of the potassium provided by the K<sub>2</sub>PtCl<sub>6</sub> precursor, two samples - K(2)/P25 and K(4)/P25 - prepared by impregnation of P25 with 2 and 4 wt. % K were tested under P(3)+H<sub>2</sub> condition. The results are reported in Table 4.9. They show on the one hand that the presence of K enhances the activity of the P25 support totally inactive in this condition. On the other hand, these samples exhibit a very different behavior than their Pt-containing Pt(2)/P25(K) and Pt(4)/P25(K) counterparts (Table 4.7 entries 6 and 8). Conversions are indeed in the same range but, as expected, higher selectivity toward NO<sub>2</sub><sup>-</sup> is observed in agreement with the high ability of Pt to reduce this compound. The final pH greatly enhances due to the basicity induced by the presence of potassium. It can be pointed out that the presence of K weakly contributes to the N<sub>2</sub> yield.

Table 4.9. Comparison performances varying the amount of K loaded at P(3)+H<sub>2</sub> condition after 6 h reaction

Catalyst	Cond	Conv (%)	Sel (%)			Yield (%)			Final pH
			NO <sub>2</sub> <sup>-</sup>	NH <sub>4</sub> <sup>+</sup>	N <sub>2</sub>	NO <sub>2</sub> <sup>-</sup>	NH <sub>4</sub> <sup>+</sup>	N <sub>2</sub>	
K(2)/P25	P(3)+H <sub>2</sub>	8.3	39.6	23.1	37.3	3.3	1.9	3.1	8.3
K(4)/P25		19.3	34.8	15.3	49.9	6.7	3	9.6	9.7

Pt probably allows reduction from nitrite to nitrogen. This was checked performing the photocatalytic NO<sub>2</sub><sup>-</sup> reduction tests under P(3)+H<sub>2</sub> condition varying the Pt load and precursor.

### 4.3.2.2 Photocatalytic nitrite reduction

The results obtained in the nitrite reduction tests with all Pt monometallic catalysts synthesized, under  $\lambda = 365$  nm UV irradiation and hydrogen stream (P(3)+H<sub>2</sub> condition) are displayed in Table 4.10. The concentration of the initial nitrite solution was fixed at 50 mg/L using NaNO<sub>2</sub> (Riser S.A.) as source because it was the highest concentration obtained over all nitrate reduction tests.

Table 4.10. Results of photocatalytic nitrite reduction tests varying the Pt loading and the precursor at P(3)+H<sub>2</sub> condition after 6 h reaction

<b>Catalyst</b>	<b>Cond</b>	<b>Conv (%)</b>	<b>Sel (%)</b>			<b>Yield (%)</b>			<b>Final pH</b>
			NO <sub>3</sub> <sup>-</sup>	NH <sub>4</sub> <sup>+</sup>	N <sub>2</sub>	NO <sub>3</sub> <sup>-</sup>	NH <sub>4</sub> <sup>+</sup>	N <sub>2</sub>	
Pt(2)/P25(H)	P(3)+H <sub>2</sub>	10	12.9	64.1	23	1.3	6.4	2.3	8.9
Pt(2)/P25(K)		17.1	7.4	33	59.6	1.3	5.6	10.2	9.4
Pt(4)/P25(H)		19.4	20	28.1	51.9	3.9	5.5	10.1	10
Pt(4)/P25(K)		34.5	11.6	42.6	45.8	4.0	14.7	15.8	8.9

Nitrite conversions increase when increasing the amount of Pt from 2 to 4 wt.%, specially using K<sub>2</sub>PtCl<sub>6</sub> instead of H<sub>2</sub>PtCl<sub>6</sub>·6H<sub>2</sub>O. Comparison with results reported in Table 4.6 shows that Pt is by far more active for reduction of nitrite than nitrate, although high selectivity to NH<sub>4</sub><sup>+</sup> is observed. Formation of NO<sub>3</sub><sup>-</sup> is obtained, as previously reported by Gekko et al. and assigned to oxidation by holes (Gekko et al. 2012).

### 4.3.3 Conclusions

The monometallic catalysts have been prepared with different amounts of Ag (0.5, 1, 1.5, 2, 3 and 4 wt. %); Pt (2 and 4 wt. %) and Pt precursor (H<sub>2</sub>PtCl<sub>6</sub>·6H<sub>2</sub>O(H)/K<sub>2</sub>PtCl<sub>6</sub>(K)). Their activities were studied under catalytic and photocatalytic conditions in absence/presence of pure hydrogen.

Monometallic catalysts are practically inactive under catalytic conditions (maximum conversion of 3 %). Ag(2)/P25 and Pt(4)/P25(K) catalysts exhibit the best photocatalytic activity for the removal of NO<sub>3</sub><sup>-</sup> from water, especially at wavelength of 365 nm UV irradiation and in presence of hydrogen. Conversion is improved in presence of H<sub>2</sub> due to a synergetic effect induced by light between photo-generated electrons and H<sub>2</sub>. Sodium nitrate is used as nitrate source. Ag(2)/P25 is the most efficient photocatalyst – most active - but NO<sub>2</sub><sup>-</sup> selectivity

is too high. Pt-catalysts enhance the selectivity to N<sub>2</sub> but the NH<sub>4</sub><sup>+</sup> amount is also high. Therefore, bimetallic catalyst studies with Ag (2 wt. %) and Pt (2 and 4 wt. %) varying the same Pt precursor were also performed.

#### **4.4 Bimetallic catalysts**

Several studies have shown that bimetallic pairs improve the catalytic properties in comparison to their monometallic counterparts. An appropriate composition made of Pt with additional metal enhances the activity, increasing the electronic vacancy in the d-band induced by the bimetallic structures (Yamamoto et al. 2010, Zaleska-Medynska et al. 2016). Thereupon, the bimetallic pair Ag-Pt could be able to enhance the catalytic activity, combining the property of silver acting as electron-hole separation centers and the ability of Pt to dissociate easily H<sub>2</sub> and reduce NO<sub>2</sub><sup>-</sup>. To the best of our knowledge, there is no study dealing with the photocatalytic reduction of NO<sub>3</sub><sup>-</sup> with this type of catalyst. Nevertheless, it is noteworthy that Ag-Pt pair supported on active carbon and Al<sub>2</sub>O<sub>3</sub> has been already tested for nitrate removal under non-photocatalytic conditions and H<sub>2</sub> stream (Aristizábal et al. 2012) (*Chapter 1, 1.3.1.1 and 1.3.2.3*).

In our research, the necessity of using the bimetallic pair Ag-Pt supported on titania P25 is a major pursue, because the monometallic catalysts based on silver (4.3.1) or platinum (4.3.2) supported on P25 exceed the nitrite or ammonium amounts to accomplish the European limits (0.5 mg/L NO<sub>2</sub><sup>-</sup> and 0.3 mg/L NH<sub>4</sub><sup>+</sup>).

To study the catalytic and photocatalytic nitrate removal in water with Ag-Pt impregnated onto P25 (*Chapter 3*), the metal loading of Ag was fixed to 2 wt. % giving the best activity in the monometallic sample. The impregnation order of both noble metals has been varied (Ag-Pt and Pt-Ag) and catalyst formulation to establish if there is an effect on the activity (4.4.1). The noble metal loading of Pt (2 and 4 wt. %) and the platinum precursors (H<sub>2</sub>PtCl<sub>6</sub>·6H<sub>2</sub>O and K<sub>2</sub>PtCl<sub>6</sub>) have been also varied like in the monometallic Pt catalyst (4.4.2). The catalytic and photocatalytic denitration experiments using the bimetallic catalysts were performed in the same conditions than for the monometallic catalysts: without UV irradiation in presence of H<sub>2</sub> (catalytic process), and under UV irradiations (UV-C, UV-A) in absence/presence of H<sub>2</sub> (photocatalytic process). Even though, the monometallic catalysts were practically inactive

under non-photocatalytic condition we wanted to evaluate this condition in the bimetallic catalysts as well.

#### 4.4.1 Effect of Ag-Pt/Pt-Ag impregnation order and catalyst formulation

To study the effect of the impregnation order of the Ag and Pt precursors onto P25 support, the metal loading of Pt was fixed at 4 wt. % and  $\text{H}_2\text{PtCl}_6 \cdot 6\text{H}_2\text{O}$  was chosen as Pt precursor (Pt(4)/P25(H)). As explained before, the Ag amount used in the bimetallic samples was 2 wt.% (Ag(2)). In order to compare the catalyst formulation as well, we have carried out denitration tests (under irradiation at  $\lambda = 365$  nm) with a physical mixture of Ag(2)/P25 and Pt(4)/P25(H) monometallic catalysts (50/50 : wt/wt). The nitrate conversions and selectivities to products are reported in Table 4.11. The yields are shown in Table 4.12. Both tables present the same notation regarding the entries related to the denitration tests performed in the same conditions.

Table 4.11. Comparison studies of physical mixture of Ag(2)/P25 + Pt(4)/P25(H), and bimetallic Ag(2)-Pt(4)/P25 and Pt(4)-Ag(2)/P25 catalysts, under catalytic and photocatalytic conditions, using  $\text{H}_2\text{PtCl}_6 \cdot 6\text{H}_2\text{O}$  as Pt precursor

Entry	Catalyst	Cond	Conv (%)	Sel (%)			Final pH
				$\text{NO}_2^-$	$\text{NH}_4^+$	$\text{N}_2$	
1	Ag(2)-Pt(4)/P25(H)		44.2	15.9	1.5	82.6	9
2	Pt(4)-Ag(2)/P25(H)	CAT	57.6	81	2.3	16.7	9.4
3	Ag(2)/P25 + Pt(4)/P25(H)		55.7	22.7	1.3	76	9.6
4	Ag(2)-Pt(4)/P25(H)	P(2)	6.9	1.1	0	98.9	4.6
5	Pt(4)-Ag(2)/P25(H)		1	8	0	92	5.4
6	Ag(2)-Pt(4)/P25(H)		9.1	1.8	0	98.2	4.7
7	Pt(4)-Ag(2)/P25(H)	P(3)	7	2	0	98	5.6
8	Ag(2)/P25 + Pt(4)/P25(H)		2.7	0	0	100	6.3
9	Ag(2)-Pt(4)/P25(H)	P(2)+H <sub>2</sub>	22.1	24.2	3.6	72.2	7.4
10	Pt(4)-Ag(2)/P25(H)		56	83.7	1.7	14.6	9.4
11	Ag(2)-Pt(4)/P25(H)		37.9	32.5	2.6	64.9	9.3
12	Pt(4)-Ag(2)/P25(H)	P(3)+H <sub>2</sub>	46.3	88.4	2.2	9.4	9.6
13	Ag(2)/P25 + Pt(4)/P25(H)		19.8	60	2.9	37.1	9.3

Table 4.12. Yields to products of the physical mixture of Ag(2)/P25 + Pt(4)/P25, and bimetallic Ag(2)-Pt(4)/P25 and Pt(4)-Ag(2)/P25 catalysts, under catalytic and photocatalytic conditions, using  $\text{H}_2\text{PtCl}_6 \cdot 6\text{H}_2\text{O}$  as Pt precursor

Entry	Catalyst	Cond	Yield (%)		
			$\text{NO}_2^-$	$\text{NH}_4^+$	$\text{N}_2$
1	Ag(2)-Pt(4)/P25(H)		7	0.7	36.5
2	Pt(4)-Ag(2)/P25(H)	CAT	46.7	1.3	9.6
3	Ag(2)/P25 + Pt(4)/P25(H)		12.6	0.7	42.3
4	Ag(2)-Pt(4)/P25(H)	P(2)	0.1	0	6.8
5	Pt(4)-Ag(2)/P25(H)		0.1	0	0.9
6	Ag(2)-Pt(4)/P25(H)		0.2	0	8.9
7	Pt(4)-Ag(2)/P25(H)	P(3)	0.1	0	6.9
8	Ag(2)/P25 + Pt(4)/P25(H)		0	0	2.7
9	Ag(2)-Pt(4)/P25(H)	P(2)+ $\text{H}_2$	5.3	0.8	16
10	Pt(4)-Ag(2)/P25(H)		46.9	1	8.2
11	Ag(2)-Pt(4)/P25(H)		12.3	1	24.6
12	Pt(4)-Ag(2)/P25(H)	P(3)+ $\text{H}_2$	40.9	1	4.4
13	Ag(2)/P25 + Pt(4)/P25(H)		11.9	0.6	7.3

A first fruitful comparison can be done between the non-photocatalytic reactions (entries 1–3) and the photocatalytic reactions with  $\text{H}_2$  (entries 9 - 13).

When the reaction was carried out with the Ag(2)/P25+ Pt(4)/P25(H) mixture, better non-photocatalytic activity (entry 3) than with each monometallic catalyst (4.4.1, 4.4.2) was obtained. The  $\text{NO}_3^-$  conversion and  $\text{N}_2$  yield reached 55.7 % and 42.3 %, respectively. Note that the  $\text{NO}_2^-$  yield of ca. 13 % does not satisfy the requirements for drinking water (S.I-No.106 2007).

These results show, if one consider the redox mechanism for  $\text{NO}_3^-$  reduction into  $\text{NO}_2^-$  including oxidation of the Ag promoter then reduced by  $\text{H}_2$  adsorbed and dissociated on Pt, that this latter step and the migration of  $\text{H}_2$  is efficient in the catalysts mixture, improving the  $\text{NO}_3^-$  conversion. Pt allows  $\text{NO}_2^-$  reduction, but this is not observed using Ag(2)/P25 + Pt(4)/P25(H), suggesting that migration of  $\text{NO}_2^-$  to the Pt sites is not effectively achieved.

The photocatalytic activity of the Ag(2)/P25 + Pt(4)/P25(H) mixture in  $\text{H}_2$ -free condition (entry 8) is very low (2.7 %) and lower than that of Ag(2)/P25 (10 %, 4.4.1), mainly accounting for the decrease in the number of  $\text{Ag}^0$  accessible sites. Although conversion is low, it is noted that  $\text{NO}_2^-$  and  $\text{NH}_4^+$  are not formed, because the reduction of nitrate and nitrite is only due to the

photo-excited electrons transferred from TiO<sub>2</sub> P25 to the metal particles trapped on them. This shows that it is limited without H<sub>2</sub> (Soares et al. 2014).

It is remarkable that the photocatalytic activity of Ag(2)/P25 + Pt(4)/P25(H) in presence of H<sub>2</sub> (entry 13) is lower than the non-photocatalytic activity (entry 3) with a concurrent increase of NO<sub>2</sub><sup>-</sup> selectivity at the expense of N<sub>2</sub>. This fact suggests that the higher H<sub>2</sub> coverage on Pt(x)/P25 catalysts due to additional H<sub>2</sub> evolved by photooxidation of water inhibits the reaction (Hirayama et al. 2012).

To conclude on the behavior of the mixture Ag(2)/P25 + Pt(4)/P25(H), it is more efficient for the non-photocatalytic (conversion of 55.7 %) than for the photocatalytic reaction (conversion of 19.8 %), although leading to NO<sub>2</sub><sup>-</sup> intermediate, then not satisfying the requirements of drinking water (> 0.5 mg/L NO<sub>2</sub><sup>-</sup>, Figure 4.6). If Ag and Pt are mainly isolated, the nitrate conversion is likely sustained by the H<sub>2</sub> spillover, which is not the best formulation to maximize the conversion and selectivity to N<sub>2</sub> (Aristizábal et al. 2011).

We will now examine the behavior of the Ag(2)-Pt(4)/P25(H) and Pt(4)-Ag(2)/P25(H) bimetallic samples. Firstly, like the mixture Ag(2)/P25 + Pt(4)/P25(H), they are poorly active in the H<sub>2</sub>-free photocatalytic reduction (P(2) and P(3)) (entries 4 - 7). The final solution pH is ~ 5, being the reaction performed in non-buffered media. At pH values lower than the pH<sub>PZC</sub> of the support (~ 6.2), the positively charged surface weakly adsorbed NO<sub>3</sub><sup>-</sup>. This normally favors conversion. However, it has been observed that NO<sub>3</sub><sup>-</sup> reduction does not occur if pH is too low, although this is controversial in literature (Sá et al. 2009; Soares et al. 2014). This last behavior likely occurs in our case.

Secondly, in the catalytic (CAT) and the photocatalytic reduction in presence of H<sub>2</sub> (P(2)+H<sub>2</sub>; P(3)+H<sub>2</sub>) conditions can be observed a dramatic influence of the impregnation order on the conversion, and particularly on the selectivity and yield towards N<sub>2</sub>. Figure 4.6 displays the nitrate, nitrite and ammonium concentrations in function of the reaction time obtained with these catalysts under CAT and P(3)+H<sub>2</sub> experimental conditions.

When Pt is first impregnated, Pt(4)-Ag(2)/P25(H) (entries 2 and 12), NO<sub>3</sub><sup>-</sup> conversion is slightly higher and NO<sub>2</sub><sup>-</sup> yield is enhanced at the expense of N<sub>2</sub> in comparison to the reverse impregnation order, Ag(2)-Pt(4)/P25(H) (entries 1 and 11).

One can thus explain this behavior. When Pt is impregnated in a second time (Ag-Pt), it is probably involved both in individual particles and deposited on the Ag particles. This last

feature decreases the number of Ag active sites available for  $\text{NO}_3^-$  reduction. Nevertheless,  $\text{NO}_2^-$  reduction towards  $\text{N}_2$  gas is improved benefiting from the high ability of the accessible Pt particularly when forming individual particles. This more likely occurs in non-photocatalytic reduction (entry 1).  $\text{NO}_2^-$  reduction is inhibited in all operating conditions because Pt decorates Ag particles as suggested from the XPS and TPR characterizations (entries 1 and 11) (*Chapter 3*).

Besides, Pt(4)-Ag(2)/P25(H) (entry 2) and the Ag(2)/P25 + Pt(4)/P25(H) mixture (entry 3) exhibit closer  $\text{NO}_3^-$  conversion under catalytic condition, but  $\text{NO}_2^-$  conversion to  $\text{N}_2$  is not favored with the former sample accounting for its lower accessibility to Pt decorated with Ag.

In the photocatalytic reductions with  $\text{H}_2$ , the two bimetallic samples (entries 11 and 12) are more active than the Ag(2)/P25 + Pt(4)/P25(H) mixture (entry 13), suggesting a higher synergetic effect by light similar to that previously reported for Ag(2)/P25 catalyst. Probably there is a high availability of electrons at the metal particles (photo-excitation of titania) which possibly are involved in the reduction of the nitrate adsorbed on Ag sites and reducing the metal oxide in the catalytic cycle. For the two bimetallic samples, the best photocatalytic activity was obtained, as in the monometallic samples, under the wavelength of 365 nm and pure  $\text{H}_2$  flow (P(3)+ $\text{H}_2$ ).

The photocatalytic nitrate reduction rates (pseudo-1<sup>st</sup> order) under P(3)+ $\text{H}_2$  condition for the catalysts were calculated and reported in the Table 4.13. The bimetallic samples reported higher reduction rate than the physical mixture of monometallic samples. The highest rate is indeed recorded for the Pt(4)-Ag(2)/P25(H) catalyst ( $0.065 \pm 0.020 \text{ h}^{-1}$ ), related to the highest nitrate conversion obtained with this Pt-Ag (ca. 46 %) impregnation order rather than Ag-Pt one (ca. 38 %).

Table 4.13. Pseudo-1<sup>st</sup> order nitrate reaction rates and correlation coefficients of the physical mixture of Ag(2)/P25 + Pt(4)/P25(H), and bimetallic Ag(2)-Pt(4)/P25 and Pt(4)-Ag(2)/P25 samples at P(3)+ $\text{H}_2$  condition after 6 h reaction using  $\text{H}_2\text{PtCl}_6 \cdot 6\text{H}_2\text{O}$  as Pt precursor

Catalyst	$k$ ( $\text{h}^{-1}$ )	$R^2$
Ag(2)-Pt(4)/P25(H)	$0.055 \pm 0.004$	0.999
Pt(4)-Ag(2)/P25(H)	$0.065 \pm 0.020$	0.988
Ag(2)/P25 + Pt(4)/P25(H)	$0.029 \pm 0.011$	0.983

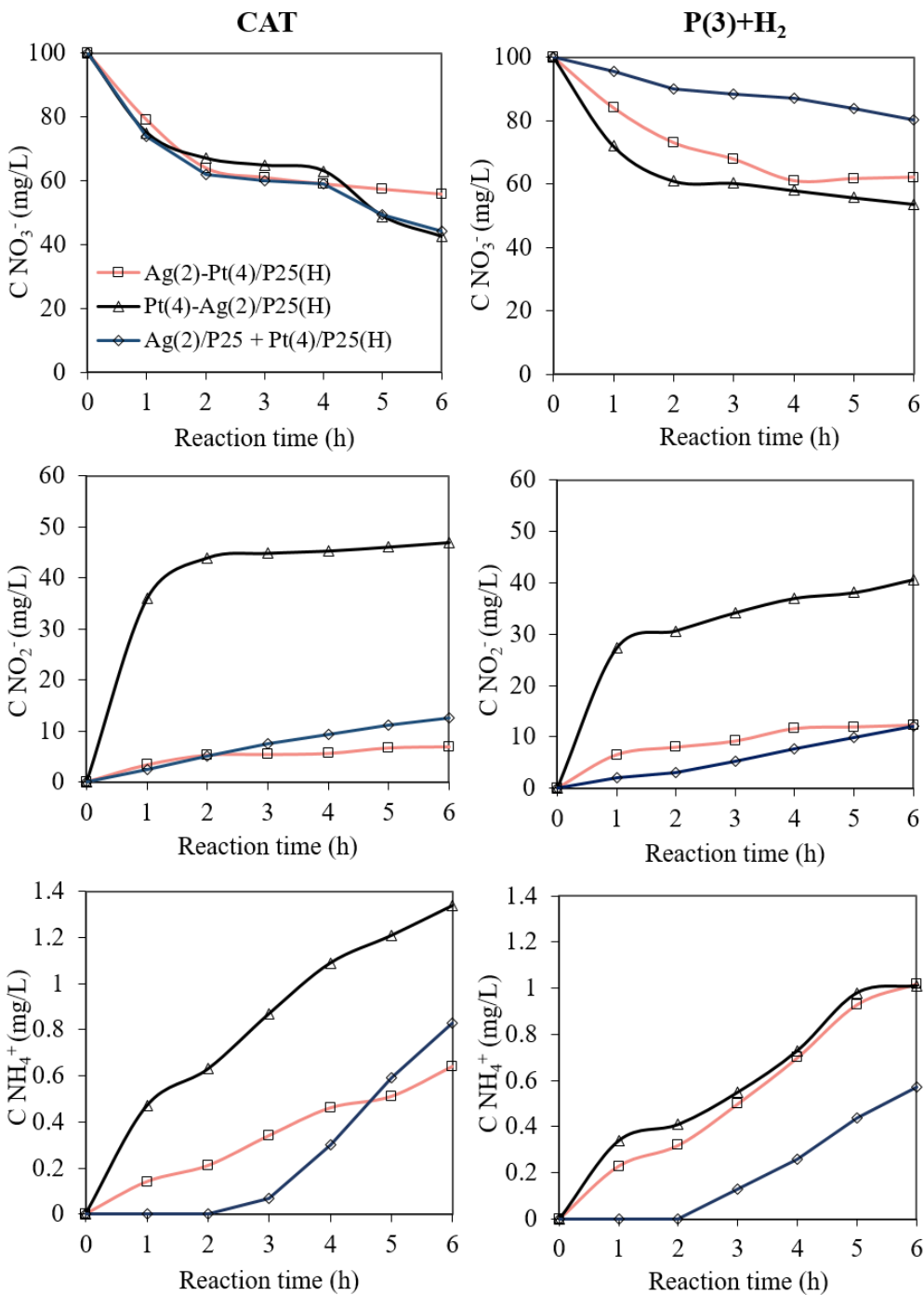


Figure 4.6.  $\text{NO}_3^-$ ,  $\text{NO}_2^-$  and  $\text{NH}_4^+$  concentrations (mg/L) in function of reaction time (h) recorded by Ag(2)-Pt(4)/P25(H), Pt(4)-Ag(2)/P25(H) and physical mixture Ag(2)/P25 + Pt(4)/P25(H) under CAT and P(3)+H<sub>2</sub> conditions

#### 4.4.2 Effect of Pt loading and Pt precursor

As observed in the previous point, Pt-Ag impregnation order favors the nitrate conversion using  $\text{H}_2\text{PtCl}_6 \cdot 6 \text{ H}_2\text{O}$  as Pt precursor at a platinum loading of 4 wt. % in the non-photocatalytic (CAT) and photocatalytic with  $\text{H}_2$  ( $\text{P}(2)+\text{H}_2$ ;  $\text{P}(3)+\text{H}_2$ ) reductions. However, the nitrite contents have to be strongly diminished, so the influence of varying the Pt loading (Pt(2) and Pt(4)) and its precursor ( $\text{H}_2\text{PtCl}_6 \cdot 6 \text{ H}_2\text{O}$  and  $\text{K}_2\text{PtCl}_6$ ) have been studied in this last part of the chapter.

All set of bimetallic catalysts synthesized (*Chapter 3*) were compared under the photocatalytic condition ( $\text{P}(3)+\text{H}_2$ ) giving rise to the best results and to the most interesting scenario because the use of solar natural light. The values corresponding to  $\text{NO}_3^-$  removal and selectivity towards  $\text{NO}_2^-$ ,  $\text{NH}_4^+$  and  $\text{N}_2$  are detailed in Table 4.14 and Figures 4.7 and 4.8, and the yields in Table 4.15. Both tables have the same notation of entries. Their photocatalytic nitrate reduction rates are depicted in Table 4.16. It is observed that the metal amount and Pt precursor highly affects the results. Furthermore, as studied in the previous section 4.4.1, the impregnation order influences as well.

Table 4.14. Comparison studies of the bimetallic catalysts under photocatalytic conditions at  $\text{P}(3)+\text{H}_2$  condition after 6 h reaction

Entry	Catalyst	Cond	Conv (%)	Sel (%)			Final pH
				$\text{NO}_2^-$	$\text{NH}_4^+$	$\text{N}_2$	
1	Ag(2)-Pt(2)/P25(H)		48.3	46.5	5.7	47.8	9.5
2	Ag(2)-Pt(2)/P25(K)		43.3	45.8	11.7	42.5	8.8
3	Ag(2)-Pt(4)/P25(H)		37.9	32.5	2.7	64.8	9.3
4	Ag(2)-Pt(4)/P25(K)		17.4	31.3	15.8	52.9	8.9
5	Pt(2)-Ag(2)/P25(H)	$\text{P}(3)+\text{H}_2$	70.4	24.7	10.7	64.6	10.5
6	Pt(2)-Ag(2)/P25(K)		42.1	6.5	23.2	70.3	10.1
7	Pt(4)-Ag(2)/P25(H)		46.3	88.4	2.2	9.4	9.6
8	Pt(4)-Ag(2)/P25(K)		45	6	14	80	10.1

Table 4.15. Yields to products of the bimetallic catalysts under photocatalytic conditions at P(3)+H<sub>2</sub> condition after 6 h reaction

Entry	Catalyst	Cond	Yield (%)		
			NO <sub>2</sub> <sup>-</sup>	NH <sub>4</sub> <sup>+</sup>	N <sub>2</sub>
1	Ag(2)-Pt(2)/P25(H)	P(3)+H <sub>2</sub>	22.5	2.8	23.1
2	Ag(2)-Pt(2)/P25(K)		19.8	5.1	18.4
3	Ag(2)-Pt(4)/P25(H)		12.3	1.0	24.6
4	Ag(2)-Pt(4)/P25(K)		5.4	2.7	9.2
5	Pt(2)-Ag(2)/P25(H)		17.4	7.5	45.5
6	Pt(2)-Ag(2)/P25(K)		2.7	9.8	29.6
7	Pt(4)-Ag(2)/P25(H)		40.9	1.0	4.4
8	Pt(4)-Ag(2)/P25(K)		2.7	6.3	36

Nitrate conversion and selectivity to products (%) of bimetallic catalysts synthesized under the best photocatalytic conditions are depicted in Figures 4.7 (Ag-Pt/P25) and 4.8 (Pt-Ag/P25) varying the impregnation order of both metals, and in Figure 4.9 varying the Pt precursor.

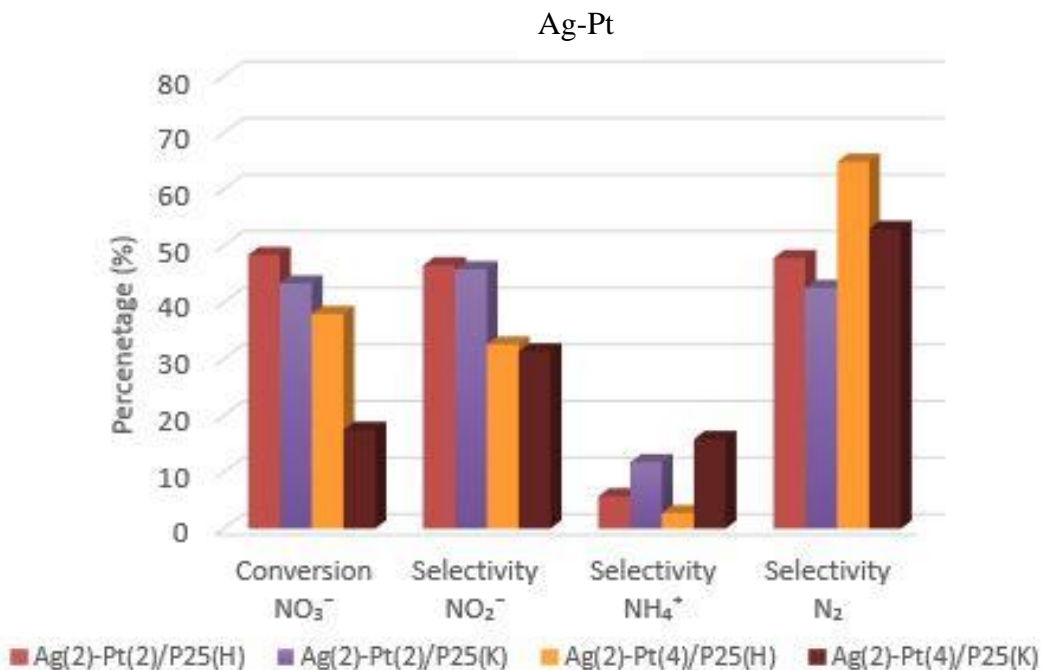


Figure 4.7. NO<sub>3</sub><sup>-</sup> conversion and selectivity (%) toward products measured from Ag-Pt/P25 catalysts under P(3)+H<sub>2</sub> condition after 6 h reaction

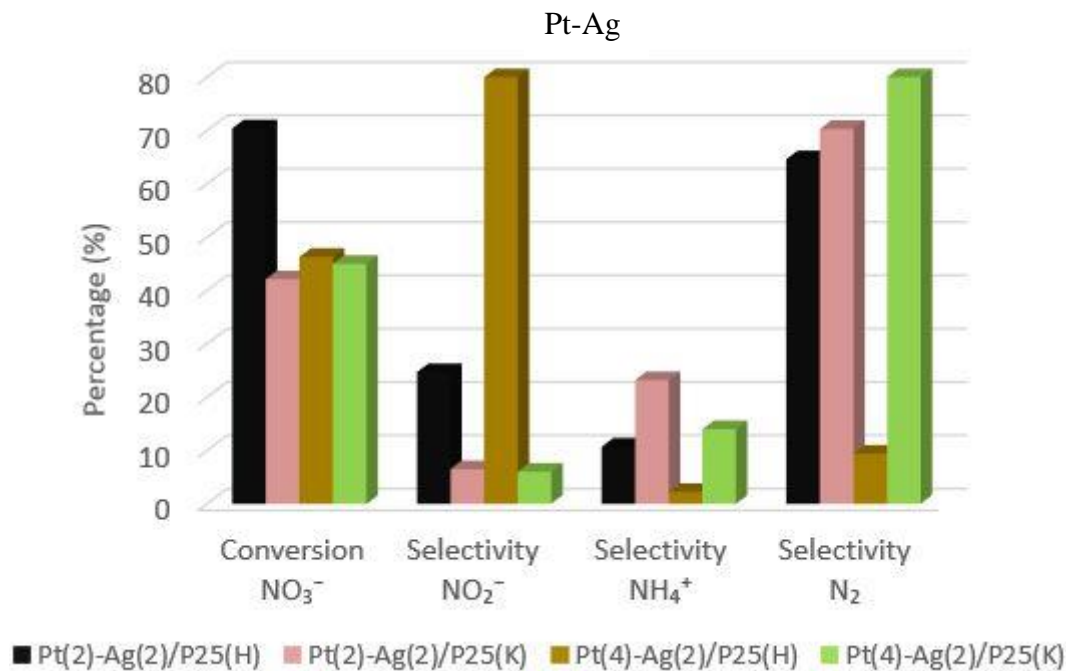


Figure 4.8.  $\text{NO}_3^-$  conversion and selectivity (%) toward products measured from Pt-Ag/P25 catalysts under  $\text{P}(3)+\text{H}_2$  after 6 h reaction

There is a general tendency toward an enhancement of nitrate conversion and yield to the desirable  $\text{N}_2$  non-toxic gas when Pt (Pt-Ag) rather than Ag (Ag-Pt) was firstly added.

The influence of the Pt precursor already reported for other types of precursors like  $\text{H}_2\text{PtCl}_6$  and  $\text{Pt}(\text{NH}_3)_4(\text{NO}_2)_2$  (Aristizábal et al. 2012, 2014), is also observed in our bimetallic catalysts, because a higher  $\text{NO}_3^-$  conversion is achieved with the Ag(2)-Pt(x)/P25(H) than the Ag(2)-Pt(x)/P25(K) series of catalysts due to the smaller mean particle size of the former observed by TEM (2.1 nm versus 4.4 nm, *Chapter 3*), and then to the higher number of accessible active sites. The larger particles also favor  $\text{NH}_4^+$  selectivity with Ag(2)-Pt(x)/P25(K) (entries 2 and 4).

The dramatic influence of the Pt precursor on the selectivity observed with Pt(4)-Ag(2)/P25(H/K) samples deserves comment as they exhibit similar conversion showing that it is probably not related to their different mean particle size. The higher  $\text{N}_2$  selectivity of Pt(4)-Ag/P25(K) (45 %, entry 8) and its reaction rate ( $0.104 \pm 0.022 \text{ h}^{-1}$ ) (Table 4.16), two times higher than in the other bimetallic catalysts, must be related to the large extent of Pt and Ag strongly interacting in solid solution as shown by XPS (*Chapter 3*). These species enhance  $\text{NO}_2^-$  reduction, although  $\text{NH}_4^+$  over-hydrogenation is still occurring in too large amount ( $> 0.3 \text{ mg/L}$

$\text{NH}_4^+$ , Figure 4.10). A  $\text{N}_2$  yield of 36 % is thus obtained in the photocatalytic process which compares well with those reached with  $\text{Ag}(2)\text{-Pt}(4)/\text{P25}(\text{H})$  and the mixture  $\text{Ag}(2)/\text{P25} + \text{Pt}(4)/\text{P25}(\text{H})$ , ranging from 36 to 42 % in the catalytic process (4.4.1).

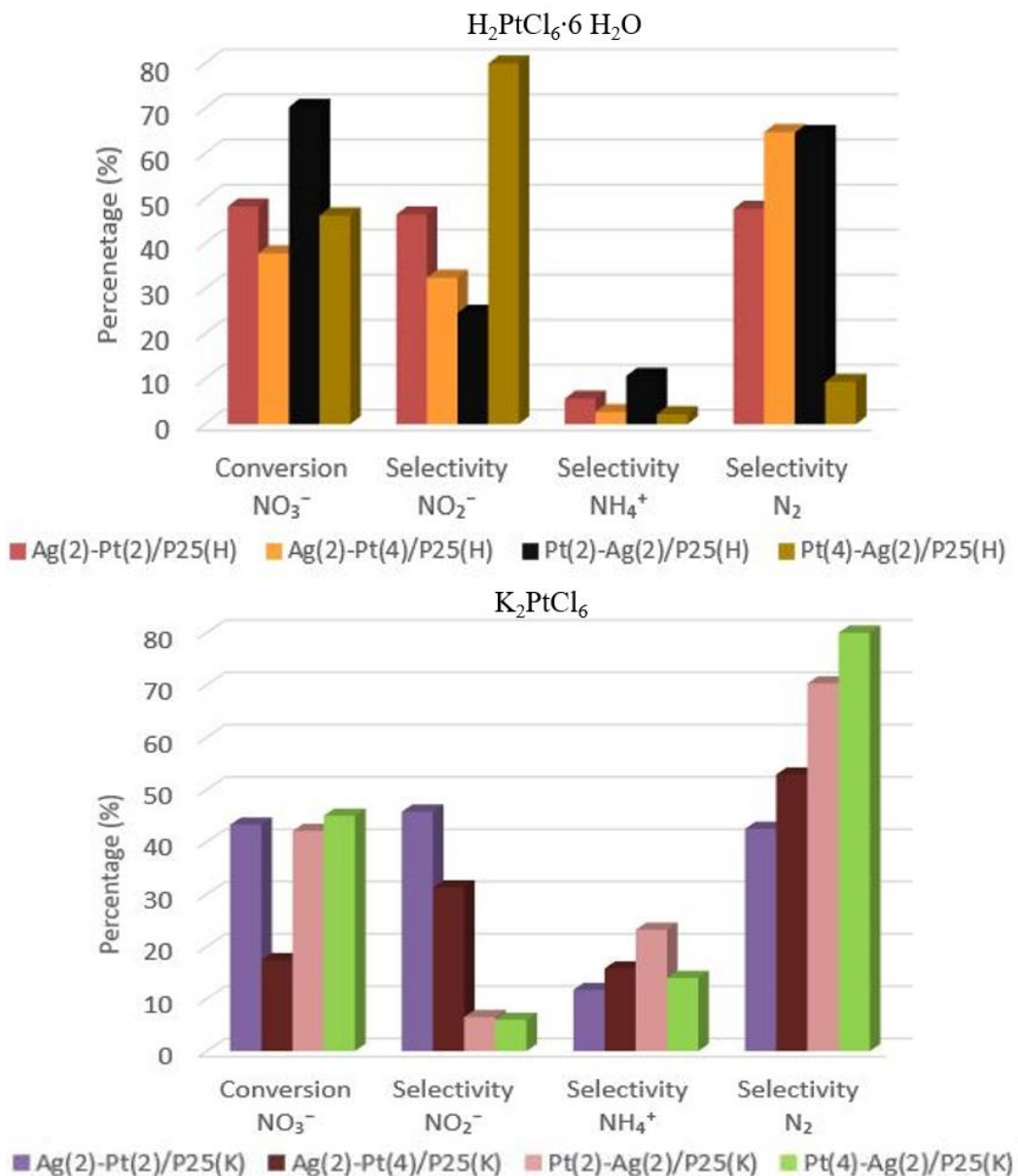


Figure 4.9.  $\text{NO}_3^-$  conversion and selectivity (%) toward products measured from Ag and Pt-based bimetallic catalysts depending on Pt loading and precursor

When increasing the metal loading from 2 to 4 wt. %, a tendency of obtaining higher selectivity and yield towards  $\text{N}_2$  instead of  $\text{NO}_2^-$  intermediate is also observed, particularly when using  $\text{K}_2\text{PtCl}_6$  as Pt precursor.

To sum up, the best photocatalytic performance among the bimetallic catalysts was observed with the Pt(4)-Ag(2)/P25(K) catalyst. Using this catalyst, it is significantly decreased the nitrite amount and few amount of ammonium is also obtained, although these limits are still surpassing the european limits in drinking water.

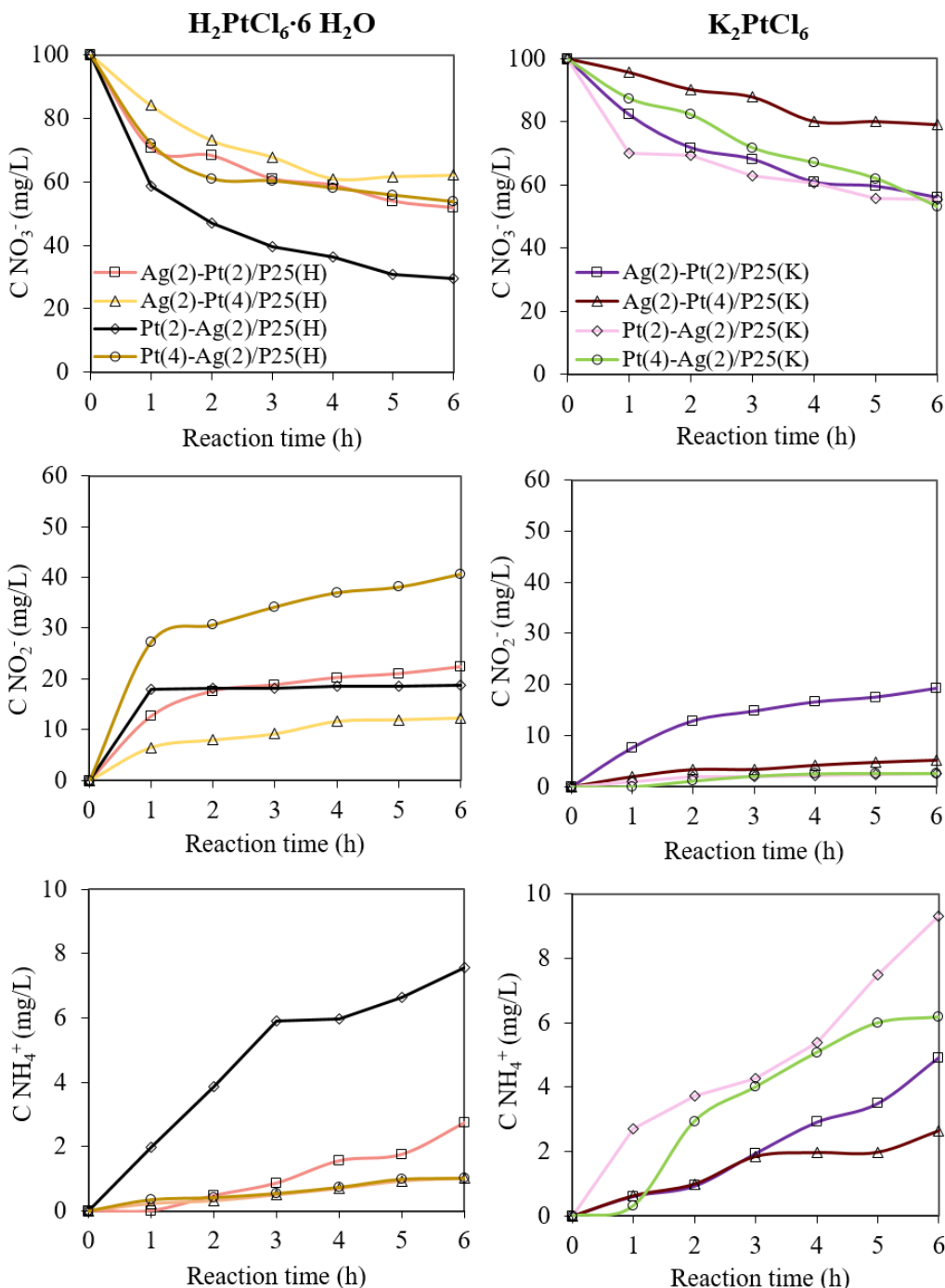


Figure 4.10.  $\text{NO}_3^-$ ,  $\text{NO}_2^-$  and  $\text{NH}_4^+$  concentrations ( $\text{mg/L}$ ) in function of reaction time (h) obtained with bimetallic catalysts

Table 4.16. Pseudo-1<sup>st</sup> order nitrate reaction rates and correlation coefficients of bimetallic catalysts under photocatalytic conditions at P(3)+H<sub>2</sub> condition after 6 h reaction

Catalyst	k (h <sup>-1</sup> )	R <sup>2</sup>
Ag(2)-Pt(2)/P25(H)	0.076 ± 0.018	0.988
Ag(2)-Pt(2)/P25(K)	0.079 ± 0.013	0.994
Ag(2)-Pt(4)/P25(H)	0.055 ± 0.004	0.999
Ag(2)-Pt(4)/P25(K)	0.073 ± 0.018	0.991
Pt(2)-Ag(2)/P25(H)	0.145 ± 0.034	0.988
Pt(2)-Ag(2)/P25(K)	0.061 ± 0.013	0.999
Pt(4)-Ag(2)/P25(H)	0.065 ± 0.020	0.988
Pt(4)-Ag(2)/P25(K)	0.104 ± 0.022	0.999

#### 4.4.3 Conclusions

Ag (2 wt. %) and Pt (2 and 4 wt. %.) supported on TiO<sub>2</sub> P25 materials synthesized by drop-wise wetness impregnation either as mixture of monometallic catalysts or as co-impregnated catalysts promoted both the catalytic and the photocatalytic ( $\lambda = 365$  nm) removal of NO<sub>3</sub><sup>-</sup> in water. In comparison to H<sub>2</sub>-free condition, the photocatalytic activity was highly enhanced in presence of H<sub>2</sub>.

The impregnated bimetallic samples are highly versatile. They are indeed active both in the catalytic and the photocatalytic processes with a clear influence of the impregnation order and the Pt precursor. Pt impregnated first leads to higher conversion due to improved accessibility of NO<sub>3</sub><sup>-</sup> to Ag<sup>0</sup> sites partially covering Pt, and high NO<sub>2</sub><sup>-</sup> selectivity at the expense of N<sub>2</sub> due to low Pt accessibility. Higher synergetic effect by light probably occurs in the most active bimetallic impregnated photocatalysts than in the Ag(2)/P25 + Pt(4)/P25(H) mixture of monometallic catalysts.

Using K<sub>2</sub>PtCl<sub>6</sub> instead of H<sub>2</sub>PtCl<sub>6</sub>·6H<sub>2</sub>O as Pt precursor increases the mean particle size accounting for the decrease of photocatalytic NO<sub>3</sub><sup>-</sup> conversion when Ag is first impregnated (Ag-Pt). When Pt is first impregnated (Pt-Ag) the closer interaction between the metals observed by XPS using K<sub>2</sub>PtCl<sub>6</sub> (Pt-Ag/P25(K)) leads to a great improvement of N<sub>2</sub> yield reaching 36 %. It is equivalent to that obtained in the catalytic reaction with Ag(2)-Pt(4)/P25(H), which exhibits higher NO<sub>2</sub><sup>-</sup> selectivity (16 %).

The Ag(2)/P25 + Pt(4)/P25(H) mixture is more efficient in the catalytic process with N<sub>2</sub> yield of 42.3 % than in the photocatalytic process (Yield<sub>N2</sub> = 7.3 %), probably due in this latter case to inhibition by H<sub>2</sub> produced by photooxidation of H<sub>2</sub>O. This suggests that when Pt is secondly added, it covers the Ag particles, which are the most active in this reaction. It could be concluded that Ag allows the nitrate reduction step to nitrite, and Pt the nitrite reduction step toward the desirable N<sub>2</sub> gas. If Ag and Pt are mainly isolated, the nitrate conversion is likely sustained by the H<sub>2</sub> spillover, which is not the best formulation to maximize the conversion and selectivity to N<sub>2</sub>.

Since the reactions occurs in non-buffered media the final pH solution tends to increase to values higher than the pH<sub>pzc</sub> of Titania P25 (> 6.2). Further studies must be done to improve the nitrate conversions and selectivity towards nitrogen to reach the European legal limits (*Chapter 6*).

## 4.5 References

- Aristizábal, A., S. Contreras, N. Barrabés, J. Llorca, D. Tichit, and F. Medina. 2011. "Catalytic reduction of nitrates in water on Pt promoted Cu hydrotalcite-derived catalysts: Effect of the Pt-Cu alloy formation". *Applied Catalysis B: Environmental*, 110, 58–70.
- Aristizábal, A., S. Contreras, N. J. Divins, N. J. Llorca, and F. Medina. 2012. "Pt-Ag/activated carbon catalysts for water denitration in a continuous reactor: Incidence of the metal loading, Pt/Ag atomic ratio and Pt metal precursor". *Applied Catalysis B: Environmental*, 127, 351–362.
- Aristizábal, A., S. Contreras, Divins, N. J., Llorca, J., and F. Medina. 2014. "Effect of impregnation protocol in the metallic sites of Pt-Ag/activated carbon catalysts for water denitration". *Applied Surface Science*, 298, 75–89.
- Asahi, R., T. Mikawa, T. Ohwaki, K. Aoki, and Y. Taga 2001. "Visible Light Photocatalysis in Nitrogen-Doped Titanium Oxides". *Science*, 293(July), 269–271.
- Behnajady M.A., N. Modirshahla, M. Shokri, and B. Rad. 2008. "Enhancement of photocatalytic activity of TiO<sub>2</sub> nanoparticles by Silver doping: Photodeposition versus liquid impregnation methods". *Global Nest Journal*, 10(1), 1–7.
- Chen, L., W. Zhao, Y. Jiao, X. He, J. Wang, and Y. Zhang. 2007. "Characterization of Ag/Pt core-shell nanoparticles by UV-vis absorption, resonance light-scattering techniques". *Spectrochimica Acta - Part A: Molecular and Biomolecular Spectroscopy*, 68(3), 484–490.
- Doudrick, K., M. Asce, O. Monzón, A. Mangonon, K. Hristovski, and P. Westerhoff. 2012. "Nitrate Reduction in Water Using Commercial Titanium dioxide photocatalysts (P25, P90, and Hombkat UV100)", (August), 852–861.
- Doudrick, K., T. Yang, K. Hristovski, and P. Westerhoff. 2013. "Photocatalytic nitrate reduction in water: Managing the hole scavenger and reaction by-product selectivity". *Applied Catalysis B: Environmental*, 136–137, 40–47.
- Gekko, H., K. Hashimoto, and H. Kominami. 2012. "Photocatalytic reduction of nitrite to dinitrogen in aqueous suspensions of metal-loaded titanium(iv) oxide in the presence of a hole scavenger: an ensemble effect of silver and palladium co-catalysts". *Physical Chemistry Chemical Physics*, 14(22), 7965.
- Gomathi Devi, L., and K. Mohan Reddy. 2010. "Enhanced photocatalytic activity of silver metallized TiO<sub>2</sub> particles in the degradation of an azo dye methyl orange: Characterization and activity at different pH values". *Applied Surface Science*, 256(10), 3116–3121.
- Hirayama, J., H. Kondo, Y. K. Miura, R. Abe, and Y. Kamiya. 2012. "Highly effective photocatalytic system comprising semiconductor photocatalyst and supported bimetallic non-photocatalyst for selective reduction of nitrate to nitrogen in water". *Catalysis Communications*, 20(3), 99–102.

- Hörold, S., K. D. Vorlop, T. Tacke, and M. Sell. 1993. "Development of catalysts for a selective nitrate and nitrite removal from drinking water". *Catalysis Today*, 17, 21–30.
- Ibhadon, A., and P. Fitzpatrick. 2013. "Heterogeneous Photocatalysis: Recent Advances and Applications". *Catalysts*, 3(1), 189–218.
- Kobwittaya, K., and S. Sirivithayapakorn. 2014. "Photocatalytic reduction of nitrate over TiO<sub>2</sub> and Ag-modified TiO<sub>2</sub>". *Journal of Saudi Chemical Society*, 18, 291–298.
- Kočí, K., S. Krejčíková, O. Šolcová, and L. Obalová. 2012. "Photocatalytic decomposition of N<sub>2</sub>O on Ag-TiO<sub>2</sub>". *Catalysis Today*, 191(1), 134–137.
- Kozlova, E. A., and A. V. Vorontsov. 2007. "Influence of mesoporous and platinum-modified titanium dioxide preparation methods on photocatalytic activity in liquid and gas phase". *Applied Catalysis B: Environmental*, 77(1–2), 35–45.
- Lee, D. S., and Y. W Chen. 2014. "Nano Ag/TiO<sub>2</sub> catalyst prepared by chemical deposition and its photocatalytic activity". *Journal of the Taiwan Institute of Chemical Engineers*, 45, 705–712.
- Prüsse, U., M. Hähnlein, J. Daum, and K. D. Vorlop. 2000. "Improving the catalytic nitrate reduction". *Catalysis Today*, 55(2), 79–90.
- S.I-No.106. (2007). European Communities Drinking Water Regulations.
- Sá, J., C. A. Agüera, S. Gross, and J. A. Anderson. 2009. "Photocatalytic nitrate reduction over metal modified TiO<sub>2</sub>". *Applied Catalysis B: Environmental*, 85(3–4), 192–200.
- Soares, O. S. G. P., M. F. R. Pereira, J. J. M. Órfão, J. L. Faria, and C. G. Silva. 2014. "Photocatalytic nitrate reduction over Pd–Cu/TiO<sub>2</sub>". *Chemical Engineering Journal*, 251, 123–130.
- Sowmya, A., and S. Meenakshi. 2014. "Photocatalytic reduction of nitrate over Ag–TiO<sub>2</sub> in the presence of oxalic acid". *Journal of Water Process Engineering*, 4–11.
- Takai, A., and P. V. Kamat. 2011. "Capture, store, and discharge. Shuttling photogenerated electrons across TiO<sub>2</sub>-silver interface". *ACS Nano*, 5(9), 7369–7376.
- Wang, G., L. Xu, J. Zhang, T. Yin, and D. Han. 2012. "Enhanced photocatalytic activity of TiO<sub>2</sub> powders (P25) via calcination treatment". *International Journal of Photoenergy*, 2012.
- Yamamoto, T. A., T. Nakagawa, S. Seino, and H. Nitani. 2010. "Bimetallic nanoparticles of PtM (M = Au, Cu, Ni) supported on iron oxide: Radiolytic synthesis and CO oxidation catalysis". *Applied Catalysis A: General*, 387(1–2), 195–202.
- Zaleska-Medynska, A., M. Marchelek, M. Diak, and E. Grabowska. 2016. "Noble metal-based bimetallic nanoparticles: The effect of the structure on the optical, catalytic and photocatalytic properties". *Advances in Colloid and Interface Science*, 229, 80–107.

Zhang, F., Y. Pi, J. Cui, Y. Yang, X. Zhang, and N. Guan. 2007."Unexpected selective photocatalytic reduction of nitrite to nitrogen on silver-doped titanium dioxide". Journal of Physical Chemistry C, 111(9), 3756–3761.

## **CHAPTER 5:**

# **Pd<sub>2</sub>Sn-based catalysts and their water denitration properties**

Article published: DOI: 10.1021/la504906q, Langmuir 2015, 31, 3952 – 3957

Title: Size and aspect ratio control of Pd<sub>2</sub>Sn Nanorods and their water denitration properties.

Authors: ZhiShan Luo, Maria Ibáñez, Ana M. Antolín, Aziz Genç, Alexey Shavel, Sandra Contreras, Francesc Medina, Jordi Arbiol, and Andreu Cabot.

## **5. Pd<sub>2</sub>Sn-based catalysts and their water denitration properties**

This chapter belongs to the article already published in collaboration with various research groups: the Catalonia Institute for Energy Research (IREC, Barcelona), Institut de Ciència de Materials de Barcelona (ICMAB, Barcelona), Institut Català de Nanociència i Nanotecnologia (ICN2, Barcelona) and Institució Catalana de Recerca i Estudis Avançats (ICREA, Barcelona)

In the section 5.1 the introduction about these type of catalysts is shown.

The section 5.2 describes all the chemicals used, the preparation of the particles synthesized by the IREC group and the description of the denitration experiments carried out in our group.

In the point 5.3, the discussion and results related to the different Pd<sub>2</sub>Sn (spherical NPs and NRs) supported on Titania P25 and the water denitration tests are detailed.

The general conclusions of the research performed for all collaborators are described in section 5.4.

The last section 5.5 of this chapter shows the supplementary information (SI) concerned to the research published in the article and carried out by the collaborators, such as the characterization techniques (TEM, XRD) and the other reduction reaction in which this type of catalysts were tested (*p*-Nitrophenol reaction).

## **5.1 Introduction**

The development of alternative Pt-free catalysts with comparable or improved activities, selectivities, and stabilities is critical to reduce the cost of catalytic materials and processes. In this direction, bimetallic catalysts, including abundant elements, are one first step toward cost reduction (Flox et al. 2012; Porter et al. 2013; Herranz et al. 2014). In particular, Pd-based bimetallic particles with tuned chemical composition, electronic states, and synergy between the two metals have allowed for not only the reduction of material costs but also the improvement of performance and stability with respect to Pt-based and pure Pd catalysts (Shao et al. 2006, 2007; Yang et al. 2011). As an example, Pd and Pd-based bimetallic catalysts are particularly suitable for hydrogenation and dehydrogenation reactions, carbon–carbon bond-forming reactions, such as Heck or Suzuki, and electrooxidation of primary alcohols (Kim et al. 2002; Son et al. 2006; Yin et al. 2006; Xia et al. 2009; Kariuki et al. 2010). Pd alloys with metals that bind strongly to oxygen also provide greater resistance to CO, C, and S poisoning (Tang et al. 2011; Zhang et al. 2012; Jin et al. 2012; Mazumder et al. 2012; Gao et al. 2013; Hokenek et al. 2013). Besides composition, the shape of catalytic nanoparticles (NPs), which dictates surface facets and active reaction sites, is the other key parameter determining a catalyst performance (Narayanan et al. 2005; Rupprechter et al. 2007; Long et al. 2013). However, because of the limitations of conventional impregnation methods to control NP geometry, this parameter is generally neglected during catalyst optimization. Colloidal synthesis methods allow for adjusting catalytic NP properties beyond conventional impregnation methods, offering the opportunity to design and engineer well-controlled model systems. In this direction, the development of synthetic routes to produce Pd-based bimetallic NPs with tuned size and shape has attracted significant effort in the past decade (Heeimer et al. 2002; Yang et al. 2011; Tang et al. 2011; Zhang et al. 2012a; Jin et al. 2012; Mazumder et al. 2012; Gao et al. 2013; Hokenek et al. 2013). Among the various bimetallic NPs, Pd–Sn is a particularly interesting candidate for the ethanol oxidation reaction (Du et al. 2012; Jou et al. 2013) and water denitration (Garron et al. 2005; Barbosa et al. 2013). However, despite its interest, the synthesis of Pd–Sn NPs with controlled morphology still remains a major challenge.

A synthetic route fully done by the IREC research group is described to produce highly monodisperse Pd<sub>2</sub>Sn NPs with tuned size and morphology. Besides, results from the functional characterization of the new materials produced are shown. The catalytic properties of Pd<sub>2</sub>Sn

NPs using the reduction of *p*-nitrophenol by NaBH<sub>4</sub> as a model reaction (Hayakama et al. 2003) were tested by the collaborators and all data related with this reaction is shown in *section 5.6.8 (SI)*. In our group, we have evaluated the performance of TiO<sub>2</sub>-supported Pd<sub>2</sub>Sn nanorods (NRs) and nanospheres (spherical NPs) in water denitration.

## 5.2 Experimental section

### 5.2.1 Chemicals

Palladium(II) acetylacetone [Pd(acac)<sub>2</sub>, 99%], tin(II) acetylacetone [Sn(acac)<sub>2</sub>, 99.9%], oleylamine (OLA, >70%), 3- mercaptopropionic acid (MPA, ≥99%), oleic acid (OA, 90%), hexadecylamine (HDA, 90%), cyclohexanone (C<sub>6</sub>H<sub>10</sub>O, 99.8%), sodium hydroxide pellets (NaOH, ≥97%), and hydrochloric acid (37% in water) were purchased from Sigma-Aldrich. Tri-noctylphosphine (TOP, 97%) was purchased from Strem. Sodium nitrate (NaNO<sub>3</sub>, 99%) was purchased Riser S.A. Aeroxide P25 (TiO<sub>2</sub>) was purchased from Acros Organics. Hexane, chloroform, and ethanol were of analytical grade and obtained from various sources. Milli-Q water was supplied by the PURELAB flex from ELGA. All chemicals were used as received without further purification, except OLA, which was purified by distillation. All syntheses were carried out using standard airless techniques: a vacuum/dry argon gas Schlenk line was used for the syntheses, and an argon glovebox was used for storing and handling air and moisture-sensitive chemicals.

### 5.2.2 Synthesis of Pd<sub>2</sub>Sn Nanorods

In a typical synthesis, 5 mL of OLA, 0.2 mmol of HDA·HCl, and 0.075 mmol of Pd(acac)<sub>2</sub> were placed in a 25 mL four-neck flask and purged under argon flow for 30 min at 60 °C. Next, 0.25 mL of 0.1 M Sn(acac)<sub>2</sub> in TOP was injected. Upon injection, the solution color changed to dark yellow. The solution was heated to 200 °C at 12 °C/min and maintained at this temperature for 30 min. Afterward, the temperature was further increased to 300 °C at 2.5 °C/min and kept for an additional 30 min. During heating, the color changed gradually to black. Then, the solution was cooled to room temperature. While cooling, when the temperature reached approximately 70 °C, 1 mL of OA was added to improve nanoparticle (NP) solubility. Pd<sub>2</sub>Sn NPs were separated from the reaction mixture by adding 20 mL of ethanol and centrifuging at

3000 rpm for 5 min. NPs were washed with chloroform as the solvent and ethanol as the non-solvent by multiple precipitation/redispersion steps.

#### 5.2.2.1 Preparation of Hexadecylammonium Chloride (HDA·HCl)

HDA·HCl was prepared by the direct reaction of HDA with an aqueous solution of hydrochloric acid. A total of 20 mmol (4.83 g) of HDA was dissolved in 50 mL of acetone, and 30 mmol (2.96 g) of HCl (37% in water) was added dropwise to the solution. The white precipitate was kept stirring in solution overnight. The HDA·HCl precipitate was filtered out, thoroughly washed with Milli-Q water, and dried under vacuum.

#### 5.2.3 Synthesis of Pd<sub>2</sub>Sn Spherical NPs for Catalytic Performance Evaluation

Pd<sub>2</sub>Sn spherical NPs were obtained following the same procedure used to produce Pd<sub>2</sub>Sn NRs but without introducing HDA·HCl.

#### 5.2.4 Water Denitration

For the nitrate heterogeneous catalytic reduction reaction, 5 wt.% Pd<sub>2</sub>Sn spherical NPs and NRs were supported on Aerioxide TiO<sub>2</sub> P25 (P25) powder form. A constant hydrogen flow (150 mL/min) was used as a reducing agent to transform nitrate into nitrogen gas as the desirable product.

Denitration experiments were performed in a 350 mL polytetrafluoroethylene (PTFE) batch reactor under standard operational conditions (atmospheric pressure and room temperature). Sodium nitrate (NaNO<sub>3</sub>) was used as the nitrate source in ultrapure water. The amount of 0.2 g of catalyst was introduced in the 100 mg/L nitrate (NO<sub>3</sub><sup>-</sup>) solution and remained in suspension by continuously stirring at 500 rpm. Samples were periodically withdrawn to analyze NO<sub>3</sub><sup>-</sup> and reaction byproducts, such as nitrite (NO<sub>2</sub><sup>-</sup>) and ammonia (NH<sub>4</sub><sup>+</sup>) ions, which were quantified by Photometry (PC MultiDirect Lovibond) (*Chapter 2*, 2.2.2 and *Annex C*). The experimental set-up is shown in the *section 2.1* of the *Chapter 2*.

### 5.3 Results and discussion

#### 5.3.1 Pd–Sn spherical NPs and NRs

Figure 5.1 displays representative transmission electron microscopy (TEM) and high-resolution transmission electron microscopy (HRTEM) micrographs of Pd–Sn NPs obtained by the procedure described above. Pd–Sn NPs were characterized by very narrow size distributions and rod-like geometry.

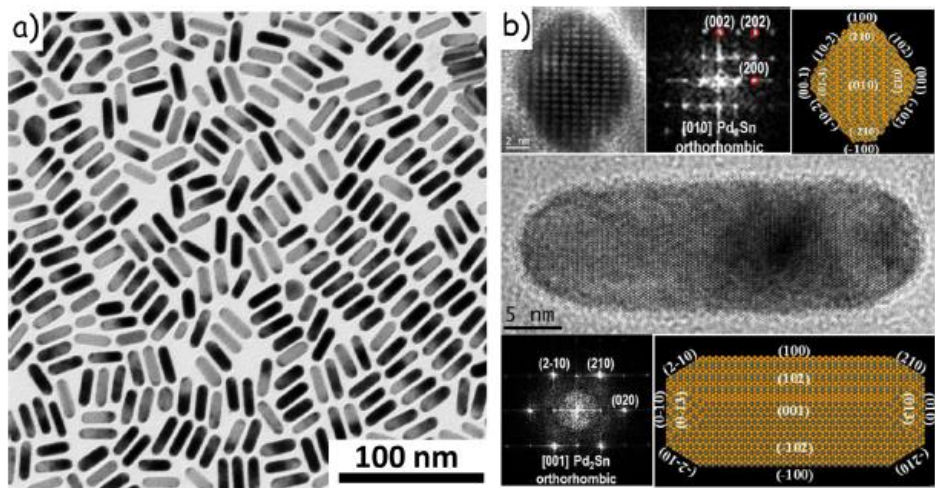


Figure 5.1. a) TEM micrograph of 27 nm long and 9 nm wide Pd<sub>2</sub>Sn NRs, b) HRTEM micrographs, power spectra, and 3D atomic models of vertically and horizontally aligned Pd<sub>2</sub>Sn NRs

Power spectrum analysis revealed Pd–Sn NRs to have an orthorhombic Pd<sub>2</sub>Sn phase (space group Pnma) with lattice parameters  $a = 0.5635$  nm,  $b = 0.4283$  nm, and  $c = 0.8091$  nm. The NR growth direction was identified as [010]. HRTEM micrographs taken from vertically (along the growth axis) and horizontally (lateral view) aligned NRs showed them to have eight facets, {100} and {102}, forming a rhombitruncated hexahedron (Barnard et al. 2014). Pd<sub>2</sub>Sn NR tips were also faceted, as shown in Figure 5.1b, and three-dimensional (3D) models were obtained using Rhodius software (Bernal et al. 1998) (see animated 3D models in [www.gaencat/research/240](http://www.gaencat/research/240)). The Pd/Sn ratio within Pd–Sn NPs was 2:1, as determined by energy-dispersive X-ray spectroscopy within scanning electron microscopy and confirmed by

inductively coupled plasma spectrometry. X-ray diffraction analysis further confirmed Pd–Sn NRs to have a Pd<sub>2</sub>Sn orthorhombic crystal structure [Joint Committee on Powder Diffraction Standards (JCPDS) number 00-026-1297; see Figure 5.9 of SI].

With adjustment of the synthetic conditions (details in section 5.6.5), the average NR length could be tuned in the range from 20 to 600 nm and its diameter could be tuned in the range between 6 and 40 nm (Figure 5.2).

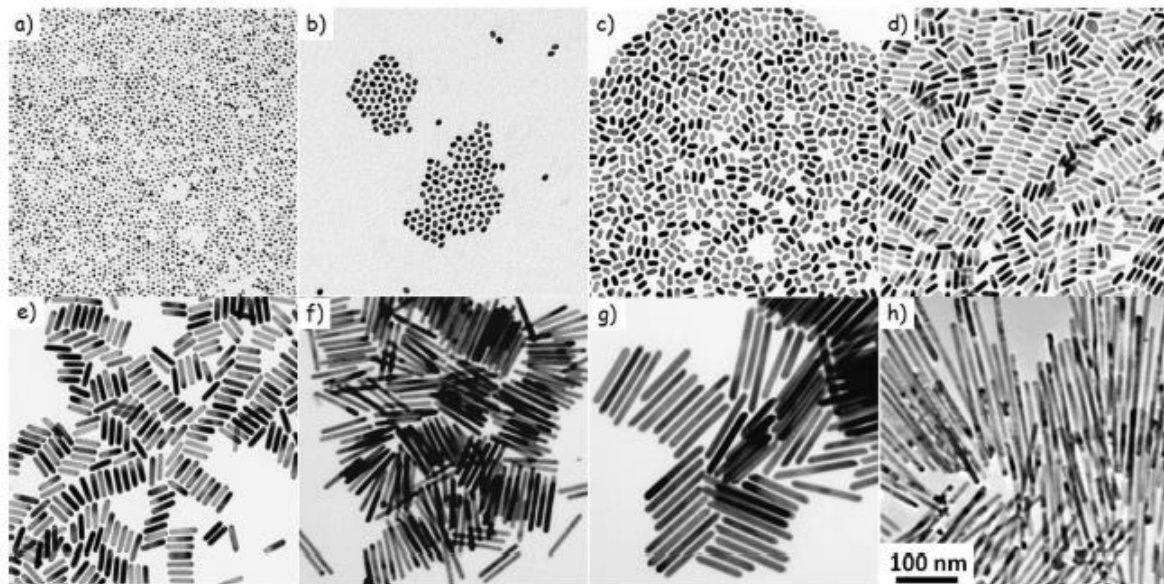


Figure 5.2. Tem micrographs of Pd<sub>2</sub>Sn spherical NPs and NRs with different aspect ratios (AR) : a)  $4.3 \pm 0.2$  nm, AR = 1; b)  $9 \pm 1$  nm x  $6.8 \pm 0.6$  nm, AR = 1.3; c)  $15 \pm 1$  nm x  $7 \pm 1$  nm, AR = 2.1; d)  $24 \pm 2$  nm x  $7 \pm 1$  nm, AR = 3.4; e)  $44 \pm 4$  nm x  $10 \pm 2$  nm, AR = 4.4; f)  $98 \pm 8$  nm x  $9 \pm 1$  nm, AR = 10.8; g)  $130 \pm 10$  nm x  $24 \pm 4$  nm, AR = 5.4; and h)  $290 \pm 20$  nm x  $12 \pm 3$  nm, AR = 24.2

The presence of both chloride ions and TOP was critical to produce rod-shaped Pd<sub>2</sub>Sn NPs. Moreover, the chlorine and TOP concentrations determined NR size and aspect ratio. Experimental results pointed out that the NR thickness was mainly influenced by the TOP concentration, while the length mainly depended upon the amount of chloride ions (Figure 5.3).

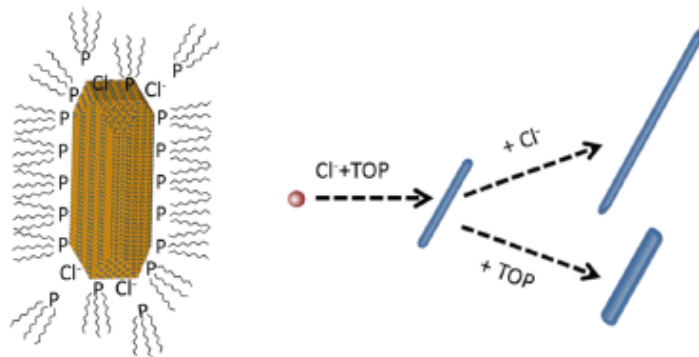


Figure 5.3. Schematic illustration of the influence of TOP and chloride ions on the shape and size of the Pd<sub>2</sub>Sn NRs

Several theories have been proposed to explain the influence of halide ions on the shape control of Pd (Zhang et al. 2012b), Ag (Wiley et al. 2004; Cathcart et al. 2004), Au (Millstone et al. 2008; DuChene et al. 2012; Gómez-Graña et al. 2013), and CdSe (Meyns et al. 2010; Lim et al. 2011; Iacono et al. 2013; Palencia et al. 2014) NPs. Halides may modify the reduction potential of the metal ions, passivate specific NP surfaces, or control surface passivation by modulating the concentration of surface ligands (Wiley et al. 2004; Cathcart et al. 2004; Millstone et al. 2008; DuChene et al. 2012; Kim et al. 2012; Lohse et al. 2013). In our system, while OLA played an essential role as coordinating solvent in controlling NP size, TOP and chlorine ions were the key compounds directing Pd<sub>2</sub>Sn NP asymmetric growth and determining its aspect ratio. Experimental results evidenced that both TOP and chlorine ions were necessary to produce Pd<sub>2</sub>Sn NRs and that they both competed for the passivation of the NR tips (5.6.5). We believe that a preferential organic ligand desorption from Pd<sub>2</sub>Sn NP tip facets directs the growth of asymmetric Pd<sub>2</sub>Sn NPs. We hypothesize that, while TOP bonded across the whole NP surface, chlorine ions (harder base than phosphine) induced TOP desorption at the NP tip facets, where a larger density of Sn ions (harder acid than Pd ions) was probably found. From another point of view, rods were formed in the presence of Cl<sup>-</sup> because the surface energy differences among the various facets allowed Cl<sup>-</sup> to selectively desorb TOP from the (010) facets. These hypotheses are consistent with the larger amounts of TOP providing a more efficient protection

of the NR tips, thus resulting in thicker NRs. At the same time, larger amounts of Cl<sup>-</sup> displace TOP from the NR tips more efficiently, resulting in longer Pd<sub>2</sub>Sn NRs.

### 5.3.2 Catalytic nitrate reduction

In our group, we have compared the activity and selectivity of Pd<sub>2</sub>Sn NRs (AR = 1.9) and Pd<sub>2</sub>Sn spherical NPs toward water denitration. The removal of nitrate is becoming a major social and environmental challenge because nitrate is growing to be one main pollutant of natural aquifers and drinking water produced from groundwater. The catalytic hydrogenation of nitrate to nitrogen is a potential cost-effective and ecological alternative to biological and physicochemical processes of denitrification (Prüsse et al. 2000; Aristizábal 2012, 2014). However, an efficient and selective nitrate hydrogenation requires the synergy between different metals, complicating the catalyst optimization by conventional impregnation methods. Among the different materials tested, Pd-based bimetallic catalysts have shown some of the best conversion rates and selectivities (Lemaignen et al. 2002; Garron et al. 2005; Dodouche et al. 2009). A general mechanism for nitrate reduction in aqueous solution (Hörold et al. 1993) is shown in Figure 5.4. In the pathway of nitrate reduction into nitrogen by hydrogenation, it is accepted that nitrite is obtained as an intermediate and ammonia as a by-product if the reaction is over-hydrogenated.

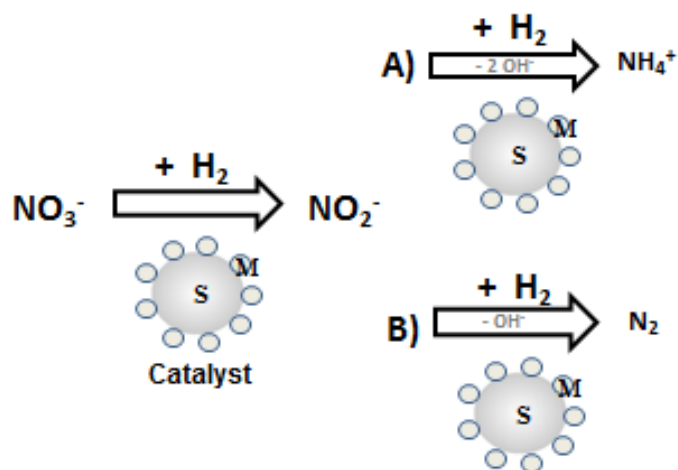


Figure 5.4. Mechanism of nitrate reduction by catalyzed hydrogenation to final product A) Ammonia and/or B) Nitrogen. The letter S represents the support of the catalyst, and the M, its metal phase

To evaluate Pd<sub>2</sub>Sn NP activity toward water denitration, water-soluble spherical Pd<sub>2</sub>Sn NPs and Pd<sub>2</sub>Sn NRs were supported on TiO<sub>2</sub> P25 with a 5 wt. %. Panels a and b of Figure 5.5 show TEM images of  $4.3 \pm 0.2$  nm Pd<sub>2</sub>Sn spherical NPs and  $27 \pm 2$  nm long and  $9 \pm 1$  nm Pd<sub>2</sub>Sn NRs, respectively, supported on TiO<sub>2</sub>. A constant hydrogen gas flow (150 mL/min) was used as a reducing agent to transform nitrate into nitrogen gas.

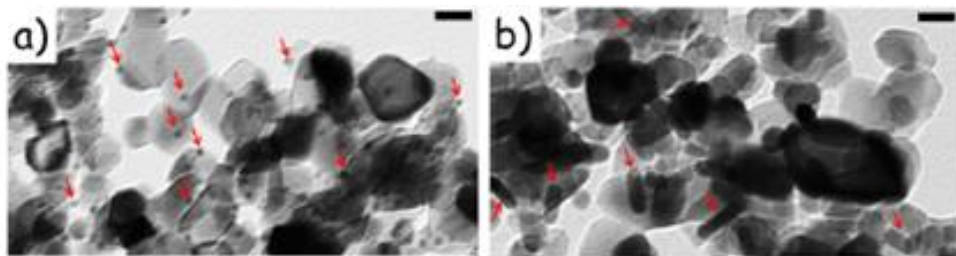


Figure 5.5. TEM images of Pd<sub>2</sub>Sn/P25: a) spherical NPs and b) NRs, supported on TiO<sub>2</sub> P25.  
Scale bars correspond to 20 nm

Figure 5.6 shows the percentage of nitrate conversion and the selectivity to N<sub>2</sub>, NO<sub>2</sub><sup>-</sup> and NH<sub>4</sub><sup>+</sup> obtained after 24 hours of reaction. The catalyst containing 5 wt. % Pd<sub>2</sub>Sn NRs showed much higher catalytic activity than the spherical NPs; around 3 times higher nitrate conversion was observed with the NRs. The initial reaction rate for nitrate removal was  $21.7 \text{ mg h}^{-1} \text{ g}^{-1}$  ( $0.5 \text{ mg h}^{-1} \text{ m}^{-2}$ ) of metal and  $7.4 \text{ mg h}^{-1} \text{ g}^{-1}$  ( $0.06 \text{ mg h}^{-1} \text{ m}^{-2}$ ) of metal for NRs and spherical NPs, respectively. The selectivity to nitrogen for NRs was higher (51 %) than that for spherical NPs (32 %). Furthermore, the NH<sub>4</sub><sup>+</sup> formation (5 % of selectivity) was lower than other reported Pd–Sn catalysts, e.g., the catalyst reported by Palomares et al. (Palomares et al. 2011) (around 40 % of selectivity to NH<sub>4</sub><sup>+</sup>).

To determine the palladium dispersion (%) and metallic surface area (m<sup>2</sup>/g) in each catalyst, hydrogen chemisorption studies were carried out with a Micromeritics ASAP 2010 equipment (*Chapter 2, 2.1.7*). Table 5.1 shows the hydrogen chemisorption results, which are so far under the expected values. The 5% Pd<sub>2</sub>Sn NRs exhibited a dispersion of 0.37%, while the 5% Pd<sub>2</sub>Sn spherical NPs showed a lower dispersion (0.16%). These very low values of metal dispersion indicate that the formation of the PdSn alloy inhibits the hydrogen chemisorption, as reported by other authors (Rochefort et al. 1990; Tanielyan et al. 1994). Consequently, the alloy

formation could be responsible for the lower selectivity to NH<sub>4</sub><sup>+</sup>, reducing the over-hydrogenation reaction.

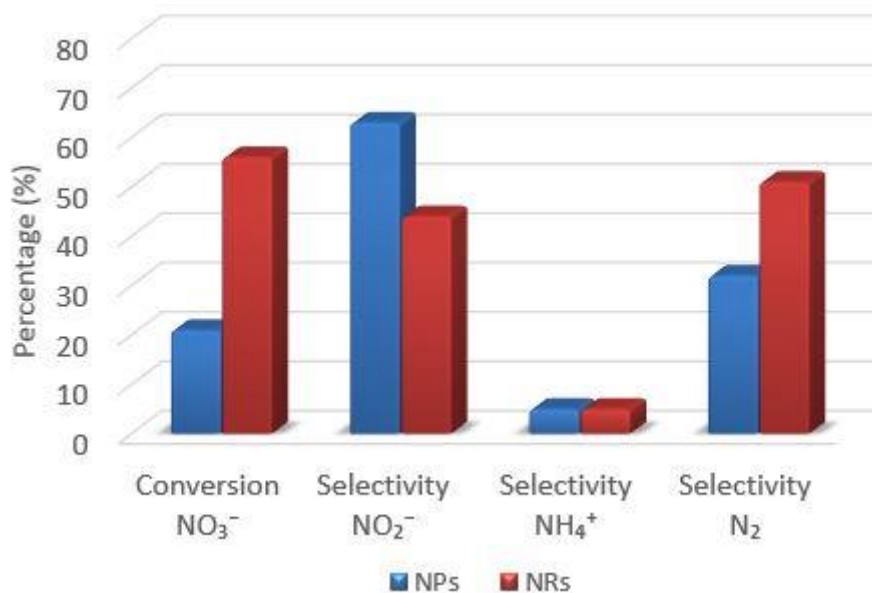


Figure 5.6. NO<sub>3</sub><sup>-</sup> conversion and selectivity (%) toward products measured from Pd<sub>2</sub>Sn/P25 spherical NPs and Pd<sub>2</sub>Sn/P25 NRs after 24 h reaction

Although the amount of nitrate obtained is under the legal limit (50 mg/L), the European limits of drinking water for nitrite and ammonia are not reached (0.5 mg/L and 0.3 mg/L, respectively) (Figure 5.7) (S.I-No.106, 2007). Further optimization has to be done.

Table 5.1. Hydrogen chemisorption results for 5 % Pd<sub>2</sub>Sn spherical NPs and 5 % Pd<sub>2</sub>Sn NRs.

Catalyst	Metal (%)		Metal Dispersion (%)	Metallic Surface Area (m <sup>2</sup> /g)		Volume of H <sub>2</sub> adsorbed (cm <sup>3</sup> /g catalyst STP)
	Pd	Sn		Sample (m <sup>2</sup> /g sample)	Metal (m <sup>2</sup> /g Metal)	
NPs	3	2	0.1604	0.0214	0.7148	0.010140 ± 0.004332
NRs	3	2	0.3731	0.0499	1.6622	0.000280 ± 0.000039

Figure 5.7 shows the nitrate, nitrite and ammonium concentrations (mg/L) in function of reaction time (h) for both catalysts.

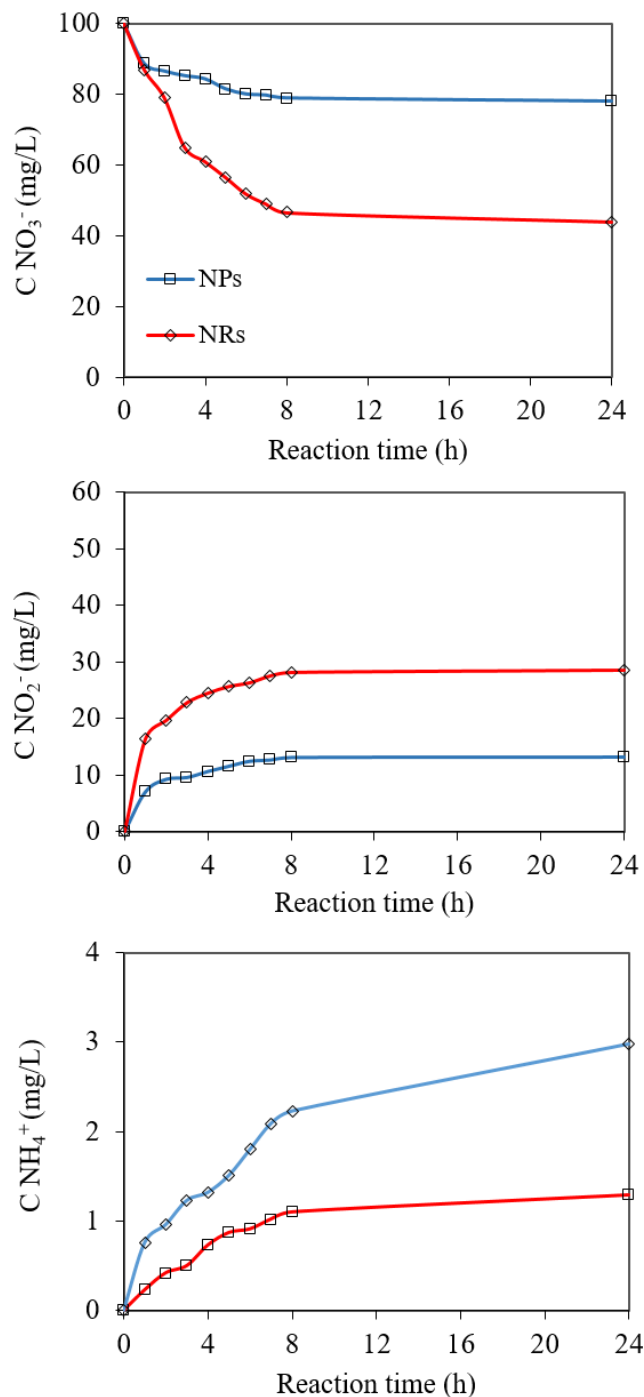


Figure 5.7.  $\text{NO}_3^-$ ,  $\text{NO}_2^-$  and  $\text{NH}_4^+$  concentrations (mg/L) in function of reaction time (h) obtained with 5%Pd<sub>2</sub>Sn/P25 spherical NPs and NRs

Figure 5.8 displays the nitrate conversion and selectivity to products after 6h of reaction for the sake of comparison with the AgPt/P25 catalysts tested in previous chapter (*Chapter 4*) under non-photocatalytic conditions (CAT). The physical mixture Ag(2)/P25 + Pt(4)/P25(H) (best case scenario under catalytic conditions) presents higher nitrate conversion (ca. 56 %) and higher selectivity to desired N<sub>2</sub>(ca. 76 %) than 5 % Pd<sub>2</sub>Sn/P25. Nevertheless, this configuration is not the best to maximize the conversion and selectivity because the conversion is mainly probably maintained by H<sub>2</sub> spillover due to Pt and Ag particles are isolated. Moreover, in the physical mixture Ag(2)/P25+Pt(4)/P25(H) seems that the migration of NO<sub>2</sub><sup>-</sup> to the Pt sites is not effectively achieved. Ag(2)-Pt(4)/P25(H) and Pt(4)-Ag(2)/P25(H) catalysts also showed similar conversions than physical mixture and 5 % Pd<sub>2</sub>Sn/P25 NRs (*Chapter 4*). In addition, the Ag-Pt bimetallics are versatile under both catalytic and photocatalytic nitrate reduction what makes them more interesting catalysts. Moreover, the selectivity to nitrite with Pd-Sn/P25 catalysts is really high indifferently of their morphology.

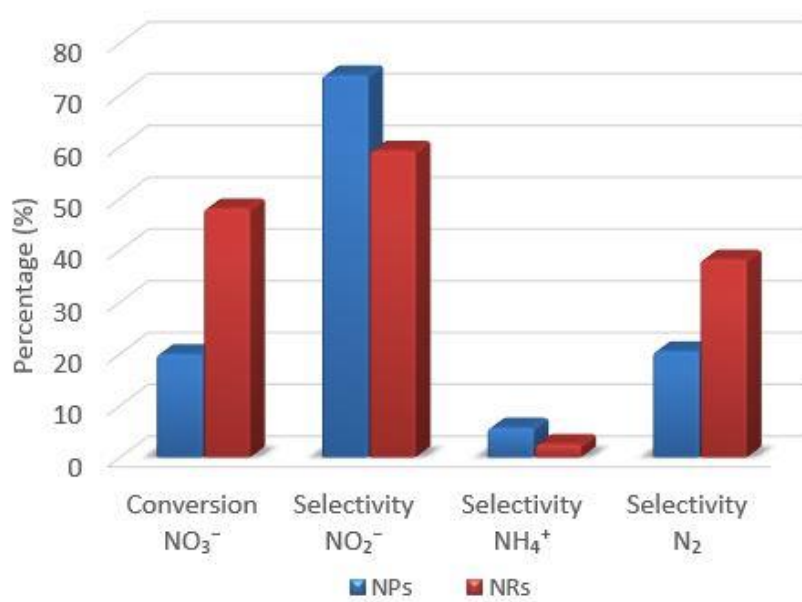


Figure 5.8. NO<sub>3</sub><sup>-</sup> conversion and selectivity (%) toward products measured from Pd<sub>2</sub>Sn/P25 spherical NPs and Pd<sub>2</sub>Sn/P25 NRs after 6 h reaction

## 5.4 Conclusions

In summary, we detailed a procedure to produce Pd<sub>2</sub>Sn NRs with controlled size and aspect ratio. The growth mechanism was based on the selective desorption of TOP by chlorine ions. Pd<sub>2</sub>Sn NRs showed higher catalytic performance than smaller spherical NPs in the catalytic nitrate reduction towards nitrogen in drinking water. Furthermore, the NRs presented better catalytic behavior than NPs in the reduction of *p*-nitrophenol by sodium borohydride (5.6.8, SI). Enhanced catalytic properties must be associated with the more active surface facets of Pd<sub>2</sub>Sn NRs. A systematic optimization of the catalyst, which should probably involve the decrease of the NR dimensions, is now required to maximize its catalytic activity and selectivity in several potential applications of this material.

## 5.5 Supplementary Information (SI)

### 5.5.1 Synthesis of Pd Spherical NPs for Catalytic Performance Evaluation.

Pd spherical NPs were prepared following the same procedure used to produce Pd<sub>2</sub>Sn NRs but without introducing HDA·HCl and Sn(acac)<sub>2</sub> and setting the growth temperature to 200 °C and growth time to 30 min.

### 5.5.2 Characterization techniques

#### 5.5.2.1 Transmission electron microscopy (TEM) studies

Size and shape of initial nanoparticles were examined by transmission electron microscopy (TEM) using a ZEISS LIBRA 120, operating at 120 kV. Structural and compositional characterization of the nanocomposites were also examined under TEM. High resolution TEM (HRTEM) studies are conducted by using a field emission gun FEIT<sup>TM</sup> Tecnai F20 microscope at 200 kV with a point-to-point resolution of 0.19 nm.

#### 5.5.2.2 X-ray power diffraction (XRD)

XRD analyses were collected directly from the as-synthesized NPs dropped on Si(501) substrate on a Bruker AXS D8 Advance X-ray diffractometer with Ni-filtered (2 μm thickness) Cu K radiation ( $\lambda = 1.5406 \text{ \AA}$ ) operating at 40kV and 40mA. A LynxEye linear position-sensitive detector was used in reflection geometry.

### 5.5.3 TEM micrograph spherical Pd NPs



Figure 5.9. TEM micrograph of spherical Pd NPs

### 5.5.4 Geometric and crystal structure characterization

As shown in Figures 5.9 and 5.10, X-ray diffraction confirmed the Pd<sub>2</sub>Sn spherical NPs and NRs to have the orthorhombic Pd<sub>2</sub>Sn phase (space group Pnma, JCPDS no. 00-026-1297). Which was further verified by HRTEM studies performed either in the Pd<sub>2</sub>Sn nanorods and Pd<sub>2</sub>Sn spherical nanoparticles.

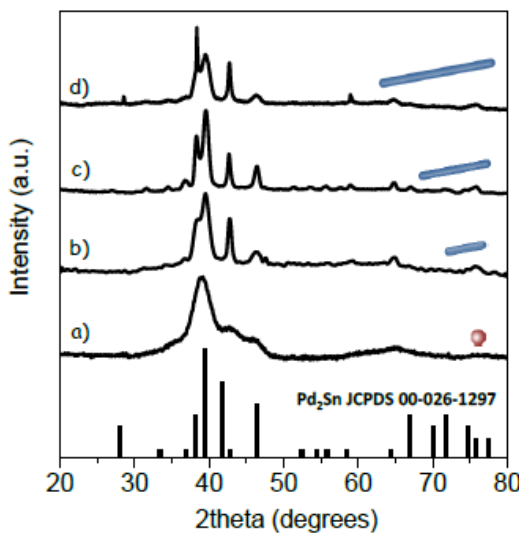


Figure 5.10. XRD pattern of a)  $4.3 \pm 0.2$  nm diameter Pd<sub>2</sub>Sn spherical NPs, b)  $83 \pm 2$  nm wide NRs, c)  $276 \pm 28$  nm long and  $15 \pm 2$  nm wide NRs, d)  $603 \pm 65$  nm long and  $32 \pm 3$  nm wide NRs, and reference pattern corresponding to orthorhombic Pd<sub>2</sub>Sn phase Pnma space group (JCPDS no. 00-26-1297)

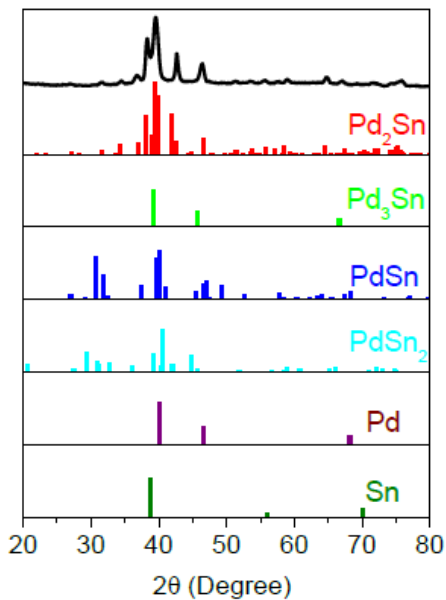


Figure 5.11. XRD pattern of  $276 \pm 28$  nm long and  $15 \pm 2$  nm wide NRs and reference pattern corresponding to orthorhombic  $Pd_2Sn$  (red) phase  $Pmna$  space group (JCPDS no. 00-0026-1297), cubic  $Pd_3Sn$  (green) phase  $Pm-3m$  space group (JCPDS no. 03-065-8225), orthorhombic  $PdSn$  (dark blue) phase  $Pnma$  space group (JCPDS no. 03-065-2603), tetragonal  $PdSn_2$  (light blue) phase space group (JCPDS no. 01-075-0892), cubic  $Pd$  (purple) phase  $Fm-3m$  space group (JCPDS no. 03-065-6174), and cubic  $Sn$  (dark green) phase  $Im-3m$  space group (JCPDS no. 03-065-0298)

TEM, HRTEM and STEM-HAADF micrographs of vertically aligned NRs probed NRs to be faceted and to show a rhombitruncated hexahedron geometry. Figures 5.11 and 5.12 display TEM and HAADF-STEM micrographs of vertically aligned  $Pd_2Sn$  NRs where it is clearly appreciated their non-circular cross section.

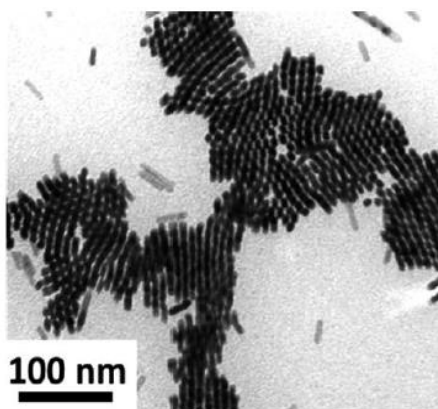


Figure 5.12. TEM micrograph of vertically aligned  $Pd_2Sn$  NRs

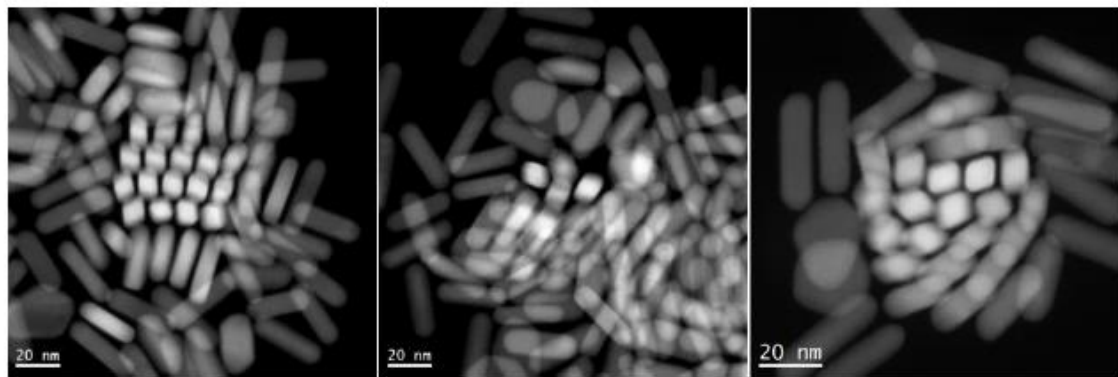


Figure 5.13. General STEM-HAADF micrographs showing Pd<sub>2</sub>Sn NRs aligned

The crystal phase, shape and faceting of the NRs were studied in more detail by HRTEM. Figure 1b in the main text shows HRTEM micrographs taken from vertically (along the growth axis) and horizontally aligned (lateral view) NRs, their corresponding power spectra and 3D structural models. As seen in the HRTEM micrograph taken from the vertically aligned NR, Pd<sub>2</sub>Sn NRs have at least 8 facets. This kind of structure is called rhombitruncated hexahedron and comprises {100} and {110} facets for cubic structures (Barnard et al. 2014). The power spectrum of the Pd<sub>2</sub>Sn NR revealed that it has an orthorhombic Pd<sub>2</sub>Sn phase (space group Pnma) with lattice parameters of  $a = 0.5635$  nm,  $b = 0.4283$  nm and  $c = 0.8091$  nm. The NR vertical view is visualized along its [010] zone axis, which is also the growth direction of the NR. For the orthorhombic system, {110} planes of the cubic rhombitruncated hexahedron structures are replaced by {102} planes, which are perpendicular planes to the <101> zone axes. Notice that the tips of the NR are also faceted. We could identify the Pd<sub>2</sub>Sn NR tip facets using different power spectra of Pd<sub>2</sub>Sn NRs aligned along [001] and [101] lateral zone axes. We created 3D structural models with the observed facets using the Rhodius software (Bernal et al. 1998) (Figure 5.13). It should be noted here that the experimentally observed facets are mostly truncated and in some cases may contain other high index facets. Power spectrum of horizontally aligned NR was also in good agreement with the orthorhombic Pd<sub>2</sub>Sn phase and confirmed the growth direction of the Pd<sub>2</sub>Sn NR as [010].

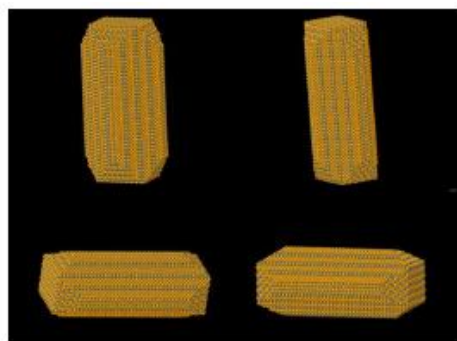


Figure 5.14. Additional images of the 3D structural model of a  $Pd_2Sn$  NR

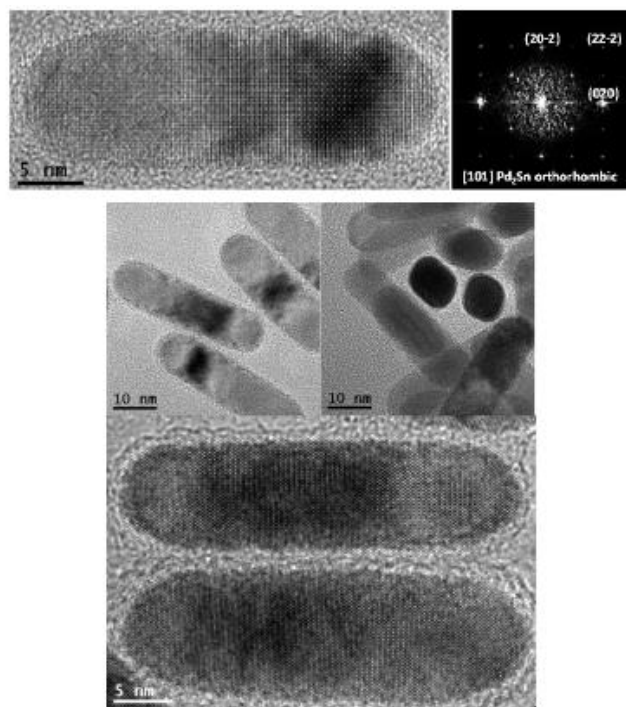


Figure 5.15. Additional HRTEM micrographs of orthorhombic  $Pd_2Sn$  NRs

Figure 5.15 shows a HRTEM micrograph revealing the presence of mostly single crystalline nanoparticles, where the presence of several twinned nanoparticles is also observed. Detail of the red squared nanoparticle and its corresponding power spectrum (FFT) are presented on the right. The power spectrum reveals that this 4.5 nm nanoparticle is composed of an orthorhombic  $Pd_2Sn$  phase (space group Pnma) with lattice parameters of  $a = 0.5635$  nm,  $b = 0.4283$  nm and  $c = 0.8091$  nm and it is visualized along its [010] zone axis. The phase is in good agreement with the previously studied  $Pd_2Sn$  nanorods.

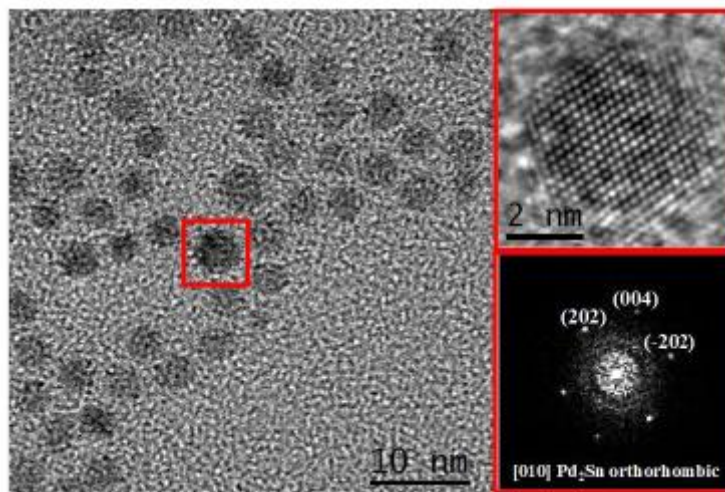


Figure 5.16. HRTEM micrograph showing several nanoparticles, detail of the red squared nanoparticle and its corresponding power spectrum

### 5.5.5 Summary of synthesis conditions of samples presented in Figure 5.2

Table 5.2. Synthesis conditions and geometrical parameters of the Pd<sub>2</sub>Sn NPs obtained

Sample	Pd(acac) <sub>2</sub> (mmol)	Sn(acac) <sub>2</sub> (mmol)	TOP (ml)	OLA (ml)	Cl- precursor	Cl content (mmol)	Length (nm)	Width (nm)	Aspect Ratio (nm)
a	0.075	0.025	0.25	5	----	0	$\delta=4.3 \pm 0.2$		1
b	0.075	0.025	0.25	5	HDA·HCl	0.15	$9 \pm 1$	$6.8 \pm 0.6$	1.3
c	0.075	0.025	0.25	5	HDA·HCl	0.18	$15 \pm 1$	$7 \pm 1$	2.1
d	0.075	0.025	0.25	5	MAH	0.2	$24 \pm 2$	$7 \pm 1$	3.4
e	0.075	0.025	0.5	5	HDA·HCl	0.2	$44 \pm 4$	$10 \pm 2$	4.4
f	0.075	0.025	0.25	5	HDA·HCl	0.25	$98 \pm 8$	$9 \pm 1$	10.8
g	0.075	0.025	0.50	5	HDA·HCl	0.5	$130 \pm 10$	$24 \pm 4$	5.4
h	0.075	0.025	0.25	5	HDA·HCl	0.5	$290 \pm 20$	$12 \pm 3$	24.2

### 5.5.6 Control experiments

To understand the role of each compound in the reaction mixture, a series of control experiments was carried out. We observed that the presence of chlorine ions and TOP was essential to obtain Pd<sub>2</sub>Sn NRs.

In the absence of any of these two compounds, no NRs were produced. As a source of chlorine ions, we initially tested the use of CHCl<sub>3</sub>. The addition of chloroform in the reaction mixture

containing an amine resulted in elongated Pd<sub>2</sub>Sn NPs, but repetitivity was very poor due to a lack of control on the chlorine ion concentration in solution. In this regard, chloroform decomposes to give a number of chlorine substituted organic compounds (mostly C<sub>2</sub>Cl<sub>4</sub>, C<sub>2</sub>HCl<sub>3</sub>, etc.) and HCl as a main product (Semeluk et al. 1954, 1957). Subsequently, HCl reacts with amine to provide the chlorine ions. Note that the yield of CHCl<sub>3</sub> decomposition to HCl is quite low at relatively high temperatures, although CHCl<sub>3</sub> decomposition can be catalyzed by the presence of the small Pd<sub>2</sub>Sn NPs. Instability of the Ar flow rate adds an additional uncertainty in the final hydrochloride concentration and thus the corresponding amount of chlorine ions present in the solution. A much more convenient strategy to introduce controlled amounts of chlorine ions was the addition of amine hydrochlorides. Different amine hydrochlorides were prepared as detailed in the previous section. The introduction of controlled amounts of amine hydrochloride allowed a precise control of the NR dimensions with a relatively high repetitivity from batch to batch. It should be pointed out that we observed no large differences on the results obtained using different amine hydrochlorides as chloride sources.

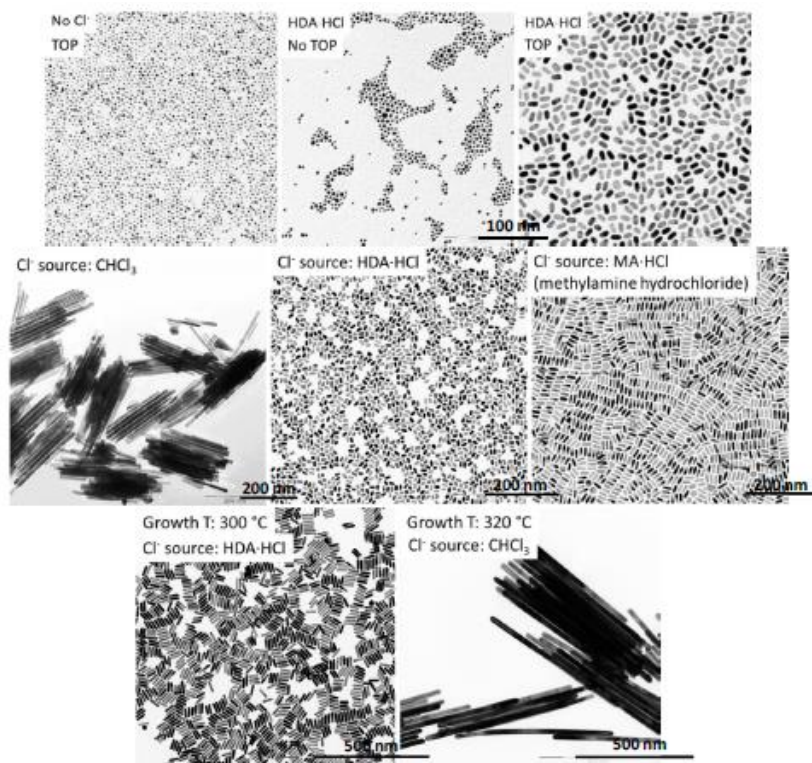


Figure 5.17. TEM micrographs of the Pd<sub>2</sub>Sn obtained from the control experiments. In each TEM image the parameter changed with respect to the standard Pd<sub>2</sub>Sn NR synthesis conditions is pointed out

The reaction temperature also played an important role in the control of the size of the NRs obtained. Larger temperatures and chloroform as a chlorine ion source resulted in the largest NRs,  $600 \pm 65$  nm x  $32 \pm 3$  nm.

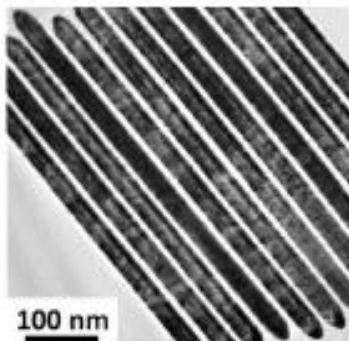


Figure 5.18. TEM micrograph of  $\sim 600 \pm 60$  nm x  $32 \pm 3$  nm Pd<sub>2</sub>Sn NRs

The use of OLA as a coordinating solvent systematically resulted in much better quality NP ensembles. As pointed out before, the presence of amines was also key to introduce chlorine ions when using CHCl<sub>3</sub> as the chlorine source. Thus the use of absolutely no amines resulted in spherical nanoparticles (Figure 5.18).

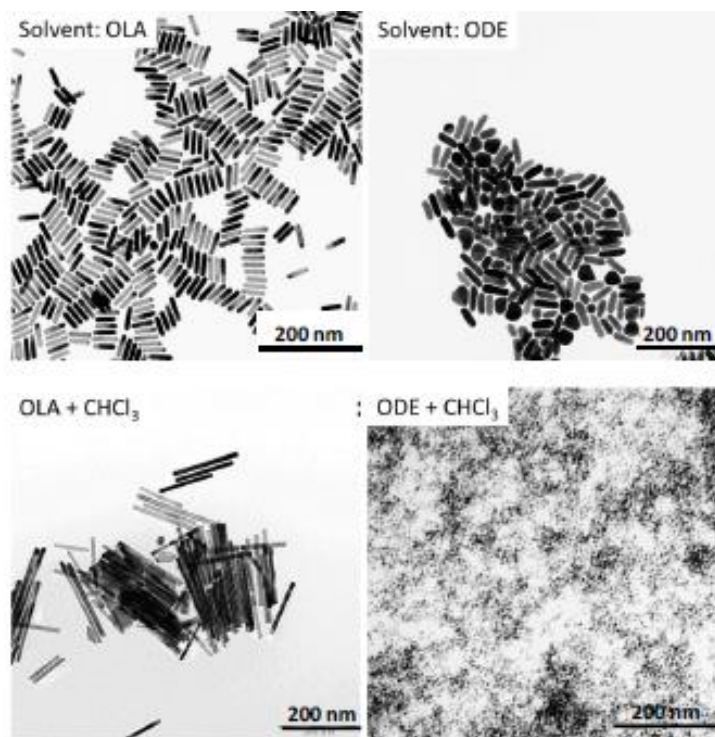


Figure 5.19. TEM micrographs of the Pd<sub>2</sub>Sn NPs obtained from control experiments. Noted in each TEM image the parameter changed with respect to the standard Pd<sub>2</sub>Sn NR synthesis conditions

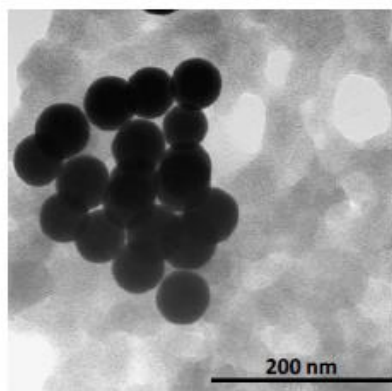


Figure 5.20. TEM micrograph of the Pd NPs obtained when no  $Pn(acac)_2$  and HDA·HCl were added

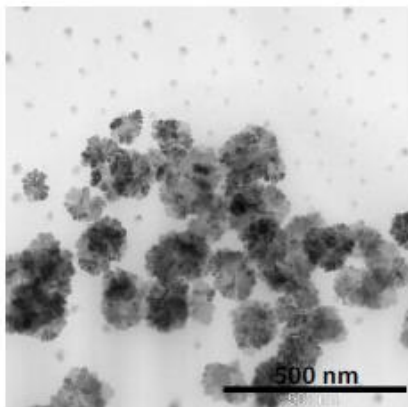


Figure 5.21. TEM micrograph of the NPs obtained when no  $Pn(acac)_2$  and HDA·HCl were added

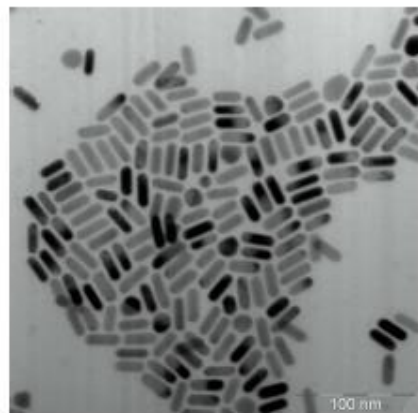


Figure 5.22. TEM micrograph of the NPs obtained for Pd/Sn ratio equal to 2

### 5.5.7 Estimation of nanorods and nanospheres concentration in NPs/mL

Concentrations of NPs per ml were estimated considering the NPs geometry and the density for bulk Pd<sub>2</sub>Sn and Pd. NRs geometry was approximated as cylinders. The length and radius of the cylinder were obtained from TEM analysis and correspond to the length and the half width of the NR respectively. In the case of spheres, the radius was also estimated by means of TEM analysis.

Pd<sub>2</sub>Sn NRs volume (V) is  $V_{NR} = L\pi r^2$ , where r is the radius and L is the length. Pd and Pd<sub>2</sub>Sn nanospheres (NE) volume:  $V_{NE} = \frac{4}{3} \cdot \pi \cdot r^3$ , where r is radius.

To estimate the amount of NPs (n) in a certain mass we used the values provide in literature for the density ( $\rho$ ) of Pd<sub>2</sub>Sn and Pd:  $n = m / \rho \cdot V$ .

### 5.5.8 p-Nitrophenol Reduction

The kinetics of catalytic reduction of *p*-nitrophenol to *p*-aminophenol was monitored by the color change involved in the reaction. Aqueous solutions of *p*-nitrophenol (1.4 mM) and NaBH<sup>4</sup> (0.42 M) were freshly prepared as separate stock solutions. Deionized water (13.0 mL) was mixed with 1.5 mL of *p*-nitrophenol stock solution. Then, 5 mL of MPA-coated Pd<sub>2</sub>Sn NR catalysts in water containing 0.1 mL of 0.2 M NaOH solution was added to the mixture with a final concentration of 0.05 mg/mL or  $1.4 \times 10^8$  NRs/mL. After mixing, 19.5 mL of the reaction solution was quickly transferred to a quartz cuvette. Then, 0.5 mL of NaBH<sub>4</sub> stock solution was injected into the quartz cuvette, and the absorbance spectra were successively recorded with a 5 s period using an ultraviolet-visible (UV-vis) spectrometer until the pale brown solution became colorless. To properly compare each type of catalyst, we keep the same amount for all catalysts (0.05 mg/mL). A total of 5 mL of Pd (3.1 nm in size) and Pd<sub>2</sub>Sn (4.9 nm in size) NP catalyst aqueous solution separately was used with a final concentration of  $3.4 \times 10^{11}$  and  $6.8 \times 10^{11}$  NPs/mL, respectively.

An initial evaluation of the functional properties of the new Pd<sub>2</sub>Sn NP geometry detailed in section 5.4 was obtained using the reduction of *p*-nitrophenol by sodium borohydride as a model catalytic system (Hayakama et al. 2003) (Figure 5.22). To evaluate and compare NP activity, spherical Pd<sub>2</sub>Sn and Pd NPs and Pd<sub>2</sub>Sn NRs with three different lengths were rendered soluble in water through ligand exchange with MPA (5.6.7.1). Figure 5.23 displays the kinetic of *p*-nitrophenol reduction to *p*-aminophenol in the presence of 3.0 nm Pd (160 m<sup>2</sup>/g), 4.3 nm Pd<sub>2</sub>Sn

spheres ( $110 \text{ m}^2/\text{g}$ ),  $15 \times 8 \text{ nm}$  Pd<sub>2</sub>Sn NRs ( $50 \text{ m}^2/\text{g}$ ),  $44 \times 10 \text{ nm}$  Pd<sub>2</sub>Sn NRs ( $37 \text{ m}^2/\text{g}$ ), and  $130 \times 24 \text{ nm}$  Pd<sub>2</sub>Sn NRs ( $15 \text{ m}^2/\text{g}$ ) (Zeng et al. 2009). In the presence of an excess of sodium borohydride and sufficient catalysts, the reaction rate could be fitted to a pseudo-first-order reaction,  $\ln(A^0/A) = kt$ , where  $k$  is the apparent rate constant (Figure 5.24) (Lee et al. 2008). Using the exact same total amount (5 mg) and concentration (0.05 mg/mL) of catalytic NPs,  $15 \times 8 \text{ nm}$  Pd<sub>2</sub>Sn NRs showed the highest reaction rates,  $38 \text{ s}^{-1} \text{ g}^{-1}$  ( $0.7 \text{ s}^{-1} \text{ m}^{-2}$ ). This value was clearly above that measured for spherical Pd<sub>2</sub>Sn ( $23 \text{ s}^{-1} \text{ g}^{-1}$ ;  $0.2 \text{ s}^{-1} \text{ m}^{-2}$ ) and spherical Pd ( $4.6 \text{ s}^{-1} \text{ g}^{-1}$ ;  $0.03 \text{ s}^{-1} \text{ m}^{-2}$ ) NPs. With normalization for the different surface areas of NRs and spherical NPs, the performance enhancement associated with Pd<sub>2</sub>Sn NRs was even more notable, with 3.5- and 28-fold reaction rate increases over spherical Pd<sub>2</sub>Sn and Pd NPs, respectively. Such an enhancement of the reaction rates with this particular NR geometry indicates that highly active catalytic sites are located at the NR (100) and/or (102) facets or at the corners between these facets. The reaction rates for longer NRs were  $22 \text{ s}^{-1} \text{ g}^{-1}$  ( $0.6 \text{ s}^{-1} \text{ m}^{-2}$ ) for  $44 \times 10 \text{ nm}$  Pd<sub>2</sub>Sn NRs and  $11 \text{ s}^{-1} \text{ g}^{-1}$  ( $0.8 \text{ s}^{-1} \text{ m}^{-2}$ ) for  $130 \times 24 \text{ nm}$  Pd<sub>2</sub>Sn NRs. When the NR length was increased, similar reaction rates per surface area unit were obtained. However, when the decrease of the surface area is taken into account with the increase of the NR size, lower reaction rates per mass unit were measured when increasing the NR size.

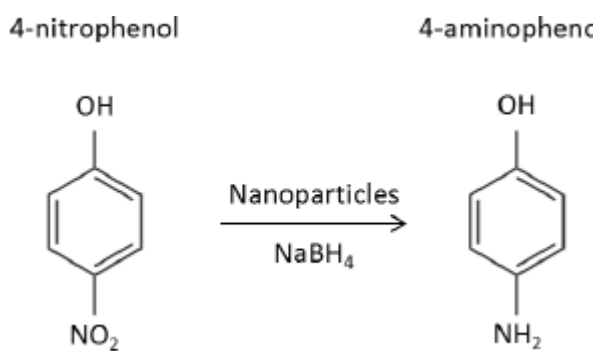


Figure 5.23. Scheme of the p-nitrophenol reaction

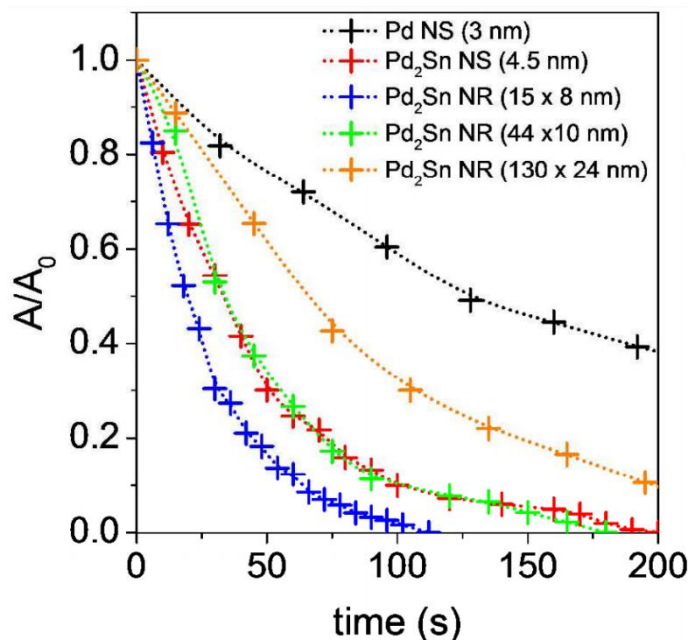


Figure 5.24. Sodium-borohydride-driven degradation of p-nitrophenol over 3 nm Pd and 4.3 nm Pd<sub>2</sub>Sn spheres, 15 x 8 nm Pd<sub>2</sub>Sn NRs, 44 x 10 nm Pd<sub>2</sub>Sn NRs, and 130 x 24 nm Pd<sub>2</sub>Sn NRs

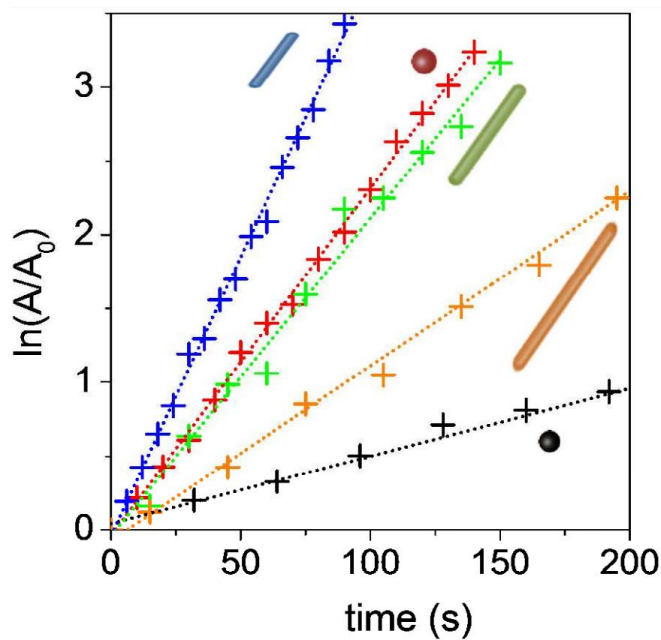


Figure 5.25. Sodium borohydride-driven degradation of p-nitrophenol over 3 nm Pd (black) and 4.3 nm Pd<sub>2</sub>Sn spheres, 15 nm x 8 nm Pd<sub>2</sub>Sn NRs, 44 nm x 10 nm Pd<sub>2</sub>Sn NRs, and 130 nm x 24 nm Pd<sub>2</sub>Sn NRs

### 5.5.8.1 Ligand Exchange with Mercaptopropionic Acid (MPA)

Pd<sub>2</sub>Sn NPs dispersed in hexane (~50 mg in 5 mL) and were mixed with 5 mL of MPA and 5 mL of cyclohexanone. The mixture was sonicated for 30 min. Subsequently, NPs were centrifuged, and the precipitate was further washed with 10 mL of cyclohexanone, chloroform, and ethanol, successively. Finally, NPs were dissolved in 2.25 mL of deionized water with 0.25 mL of 0.2 M NaOH solution.

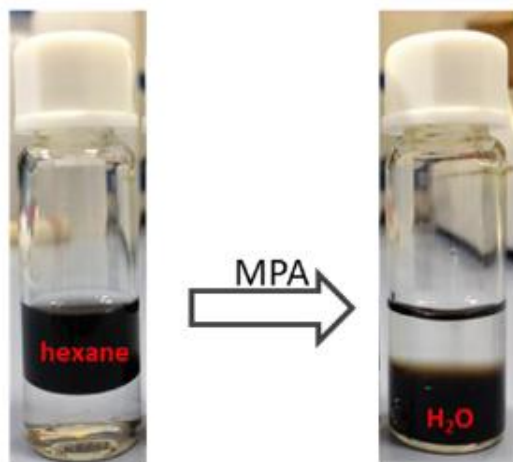


Figure 5.26. Picture of the solution of Pd<sub>2</sub>Sn NRs before and after MPA treatment

## 5.6 References

- www.gaen.cat/research/240.
- Aristizábal, A., S. Contreras, N. J. Divins, J. Llorca, F. Medina. 2012. “Pt–Ag/activated carbon catalysts for water denitration in a continuous reactor: Incidence of the metal loading, Pt/Ag atomic ratio and Pt metal precursor”. *Appl. Catal., B*, 127, 351–362.
- Aristizábal, A., S. Contreras, N. J. Divins, J. Llorca, F. Medina. 2014. “Effect of impregnation protocol in the metallic sites of Pt–Ag/activated carbon catalysts for water denitration”. *Appl. Surf. Sci.*, 298, 75–89.
- Barbosa, D. P., P. Tchiéta, M. D. C. Rangel, F. Epron. 2013 “The use of a cation exchange resin for palladium–tin and palladium–indium catalysts for nitrate removal in water”. *J. Mol. Catal. A: Chem.*, 366, 294–302.
- Barnard, A. S., E. Osawa. 2014. “The impact of structural polydispersivity on the surface electrostatic potential of nanodiamond”. *Nanoscale*, 6, 1188–1194.
- Bernal, S.; F. J. Botana, J. J. Calvino, C. López-Cartes, J. A. Pérez- Omil, J. M. Rodríguez- Izquierdo. 1998. The interpretation of HREM images of supported metal catalysts using image simulation: Profile view images”. *Ultramicroscopy*, 72, 135–164.
- Cathcart, N., A. J. Frank, V. Kitaev. 2009. “Silver nanoparticles with planar twinned defects: Effect of halides for precise tuning of plasmon resonance maxima from 400 to >900 nm<sup>2</sup>”. *Chem. Commun.*, 7170–7172.
- Dodouche, I., D. P. Barbosa, M. d. C. Rangel, F. Epron. 2009. “Palladium–tin catalysts on conducting polymers for nitrate removal”. *Appl. Catal., B*, 93, 50–55.
- Du, W., K. E. Mackenzie, D. F. Milano, N.A. Deskins, D. Su, X. Teng. 2012. “Palladium– Tin alloyed catalysts for the ethanol oxidation reaction in an alkaline medium. *ACS Catal.*, 2, 287-297.
- DuChene, J. S., W. Niu, J. M. Abendroth, Q. Sun, W. Zhao, F. Huo, W. D. Wei. 2012. “Halide anions as shape-directing agents for obtaining high-quality anisotropic gold nanostructures”. *Chem. Mater.*, 25, 1392–1399.

- Flox, C., J. Rubio-Garcia, R. Nafria, R. Zamani, M. Skoumal, T. Andreu, J. Arbiol, A. Cabot, J. R. Morante. 2012. “Active nano-CuPt<sub>3</sub> electrocatalyst supported on graphene for enhancing reactions at the cathode in all-vanadium redox flow batteries”. *Carbon*, 50, 237–2374.
- Gao, Q., Y. M. Ju, D. An, M.R. Gao, C.H. Cui, J.W. Liu, H.P. Cong, S.H. Yu. 2013. “Shape-controlled synthesis of monodisperse PdCu nanocubes and their electrocatalytic properties”. *ChemSusChem*, 6, 1878–1882.
- Garron, A., K. Lázár, F. Epron. 2005. “Effect of the support on tin distribution in Pd–Sn/Al<sub>2</sub>O<sub>3</sub> and Pd–Sn/SiO<sub>2</sub> catalysts for application in water denitration”. *Appl. Catal., B*, 59, 57–69.
- Gómez-Graña, S., B. Goris, T. Altantzis, C. Fernández-López, E. Carbó-Argibay, A. Guerrero-Martínez, N. Almora-Barrios, N. López, I. Pastoriza-Santos, J. Pérez-Juste, S. Bals, G. Van Tendeloo, L. M. Liz- Marzán. 2013. “Au@Ag nanoparticles: Halides stabilize {100} facets”. *J. Phys. Chem. Lett.*, 4, 2209–2216.
- Hayakawa, K., T. Yoshimura, K. Esumi. 2003. “Preparation of gold – dendrimer nanocomposites by laser irradiation and their catalytic reduction of 4-nitrophenol”. *Langmuir*, 19, 5517 – 5521.
- Herranz, T., M. Ibáñez, J. L. Gómez de la Fuente, F. J. Pérez-Alonso, M. A. Peña, A. Cabot, S. Rojas. 2014. “In situ study of etanol electrooxidation on monodispersed Pt<sub>3</sub>Sn nanoparticles”. *ChemElectroChem*, 1, 885–895.
- Heemeier, M., A. F. Carlsson, M. Naschitzki, M. Schmal, M. Bäumer, H. J. Freund. 2002. “Preparation and characterization of a model bimetallic catalyst: Co–Pd nanoparticles supported on Al<sub>2</sub>O<sub>3</sub>”. *Angew. Chem., Int. Ed.*, 41, 4073–4076.
- Hokenek, S., C. Bennett, J. N. Kuhn. 2013. “Synthesis of Ni–Pd nanocubes and nanorods with high selectivity through a modified polyol process”. *J. Cryst. Growth*, 374, 18–22.
- Horold, S., K. D. Vorlop, T. Tacke, M. Sell. 1993. “Development of Catalysts for a Selective Nitrate and Nitrite Removal from Drinking-Water”. *Catal. Today*, 17, (1-2), 21-30.
- Iacono, F., C. Palencia, L. de la Cueva, M. Meyns, L. Terracciano, A. Vollmer, M.J. de la Mata, C. Klinke, J. M. Gallego, B. H. Juarez, R. Otero. 2013.“Interfacing quantum dots and graphitic surfaces with chlorine atomic ligands”. *ACS Nano*, 7, 2559–2565.

- Jin, M., H. Zhang, J. Wang, X. Zhong, N. Lu, Z. Li, Z. Xie, M. J. Kim, Y. Xia. 2012. “Copper can still be epitaxially deposited on palladium nanocrystals to generate core–shell nanocubes despite their large lattice mismatch”. ACS Nano, 6, 2566–2573.
- Jou, L.H., J. K. Chang, T. J. Whanga, I. W. Sun. 2010. “Electrodeposition of palladium–tin alloys from 1-ethyl-3-methylimidazolium chloride–tetrafluoroborate ionic liquid for ethanol electro-oxidation”. J. Electrochem. Soc., 157, D443–D449.
- Kariuki, N. N., X. Wang, J. R. Mawdsley, M. S. Ferrandon, S. G. Niyogi, J. T. Vaughey, D. J. Myers. 2010. “Colloidal synthesis and characterization of carbon-supported Pd–Cu nanoparticle oxygen reduction electrocatalysts”. Chem. Mater. 22, 4144–4152.
- Kim, S. W., M. Kim, W. Y. Lee, T. Hyeon. 2002. “Fabrication of hollow palladium spheres and their successful application to the recyclable heterogeneous catalyst for Suzuki coupling reactions”. J. Am. Chem. Soc., 124, 7642–7643.
- Kim, M. R., K. Miszta, M. Povia, R. Brescia, S. Christodoulou, M. Prato, S. Marras, L. Manna. 2012. “Influence of chloride ions on the synthesis of colloidal branched CdSe/CdS nanocrystals by seeded growth”. ACS Nano, 6, 11088–11096.
- Lee, J., J. C. Park, H. Song. 2008. “A nanoreactor framework of a Au@ SiO<sub>2</sub> yolk/shell structure for catalytic reduction of p-nitropheno”l. Adv. Mater., 20, 1523–1528.
- Lemaignen, L., C. Tong, V. Begon, R. Burch, D. Chadwick. 2002. “Catalytic denitrification of water with palladium-based catalysts supported on activated carbons”. Catal. Today, 75, 43–48.
- Lohse, S. E., N. D. Burrows, L. Scarabelli, L. M. Liz-Marzán, C. J. Murphy. 2013. “Anisotropic noble metal nanocrystal growth: The role of halides”. Chem. Mater. 26, 34–43.
- Long, R., K. Mao, X. Ye, W. Yan, Y. Huang, J. Wang, Y. Fu, X. Wang, X. Wu, Y. Xie, Y. Xiong. 2013. “Surface facet of palladium nanocrystals: A key parameter to the activation of molecular oxygen for organic catalysis and cancer treatment”. J. Am. Chem. Soc., 135, 3200–3207.
- Lim, S. J., W. Kim, S. Jung, J. Seo, S. K. Shin. 2011. “Anisotropic etching of semiconductor nanocrystals”. Chem. Mater., 23, 5029– 5036.

- Mazumder, V., M. Chi, M. N. Mankin, Y. Liu, Ö. Metin, D. Sun, K. L. More, S. Sun. 2012. “A facile synthesis of MPd (M = Co, Cu) nanoparticles and their catalysis for formic acid oxidation”. *Nano Lett.*, 12, 1102–1106.
- Meyns, M., N. G. Bastus, Y. Cai, A. Kornowski, B. H. Juarez, H. Weller, C. Klinke. 2010. “Growth and reductive transformation of a gold shell around pyramidal cadmium selenide nanocrystals”. *J. Mater. Chem.*, 20, 10602–10605.
- Millstone, J. E., W. Wei, M. R. Jones, H. Yoo, C. A. Mirkin. 2008. “Iodide ions control seed-mediated growth of anisotropic gold nanoparticles”. *Nano Lett.*, 8, 2526–2529.
- Narayanan, R., M. A. El-Sayed. 2005. “Effect of colloidal nanocatalysis on the metallic nanoparticle shape: The Suzuki reaction”. *Langmuir*, 21, 2027–2033.
- Palencia, C., K. Lauwaet, L. de la Cueva, M. Acebron, J. J. Conde, M. Meyns, C. Klinke, J. M. Gallego, R. Otero, B. H. Juarez. 2014. “Cl- Capped CdSe nanocrystals via in situ generation of chloride anions”. *Nanoscale*, 6, 6812–6818.
- Palomares, A. E., C. Franch, A. Corma. 2011. “A study of different supports for the catalytic reduction of nitrates from natural water with a continuous reactor”. *Catal. Today*, 172, 90–94.
- Porter, N. S., H. Wu, Z. Quan, J. Fang. 2013. “Shape-control and electrocatalytic activity-enhancement of Pt-based bimetallic nanocrystals”. *Acc. Chem. Res.*, 46, 1867–1877.
- Prüsse, U., M. Hähnlein, J. Daum, K. D. Vorlop. 2000. “Improving the catalytic nitrate reduction”. *Catal. Today*, 55, 79–90.
- Rochefort, A., J. Andzelm, N. Russo, D. R. Salahub. 1990. “Chemisorption and diffusion of atomic hydrogen in and on cluster models of palladium, rhodium and bimetallic palladium tin, rhodium tin, and rhodium zinc catalysts”. *J. Am. Chem. Soc.*, 112, 8239–8247.
- Rupprechter, G., C. Weilach. 2007. “Mind the gap! Spectroscopy of catalytically active phases”. *Nano Today*, 2, 20–29.
- Semeluk, G. P., R. B. Bernstein. 1957. *Journal American Chemical Society*, 79, 46-49.
- Semeluk, G. P., R. B. Bernstein. J. 1954. *Journal American Chemical Society*, 76, 3793-3796.
- Shao, M. H., K. Sasaki, R. R. Adzic. 2006. “Pd–Fe nanoparticles as electrocatalysts for oxygen reduction”. *J. Am. Chem. Soc.*, 128, 3526–3527.

- Shao, M., P. Liu, J. Zhang, R. Adzic. 2007. “Origin of enhanced activity in palladium alloy electrocatalysts for oxygen reduction reaction”. *J. Phys. Chem. B*, 111, 6772–6775.
- S.I-No.106. (2007). European Communities Drinking Water Regulations.
- Tanielyan, S. K., R. L. Augustine. 1994. “Acetoxylation of toluene catalyzed by supported Pd–Sn catalysts2. *J. Mol. Catal.*, 87, 311–328.
- Son, S. U., Y. Jang, J. Park, H. B. Na, H. M. Park, H. J. Yun, J. Lee, T. Hyeon. 2004. “Designed synthesis of atom-economical Pd/Ni bimetallic nanoparticle-based catalysts for Sonogashira coupling reactions”. *J. Am. Chem. Soc.*, 126, 5026–5027.
- Tang, W., L. Zhang, G. Henkelman. 2011. “Catalytic activity of Pd/Cu random alloy nanoparticles for oxygen reduction”. *J. Phys. Chem. Lett.*, 2, 1328–1331.
- Wiley, B., T. Herricks, Y. Sun, Y. Xia. “Polyol synthesis of silver nanoparticles: Use of chloride and oxygen to promote the formation of single-crystal, truncated cubes and tetrahedrons”. *Nano Lett.* 2004, 4, 1733–1739.
- Xia, Y., Y. Xiong, B. Lim, S. E. Skrabalak. 2009. “Shape-controlled synthesis of metal nanocrystals: Simple chemistry meets complex physics?” *Angew. Chem., Int. Ed.*, 48, 60–103.
- Yang, X., J. Hu, J. Fu, R. Wu, B. E. Koel. 2011. “Role of surface iron in enhanced activity for the oxygen reduction reaction on a Pd<sub>3</sub>Fe(111) single-crystal alloy”. *Angew. Chem., Int. Ed.*, 50, 10182–10185.
- Yin Liebscher, J. 2006. “Carbon–carbon coupling reactions catalyzed by heterogeneous palladium catalysts”. *Chem. Rev.*, 107, 133–173.
- Zeng, J., Q. Zhang, J. Chen, Y. Xia. 2009. “A comparison study of the catalytic properties of Au-based nanocages, nanoboxes, and nanoparticles”. *Nano Lett.*, 10, 30–35.
- Zhang, L., F. Hou, Y. Tan. 2012a. “Shape-tailoring of CuPd nanocrystals for enhancement of electro-catalytic activity in oxygen reduction reaction”. *Chem. Commun.*, 48, 7152–7154.
- Zhang, H., M. Jin, Y. Xiong, B. Lim, Y. Xia. 2012b. “Shape-controlled synthesis of Pd nanocrystals and their catalytic applications”. *Acc. Chem. Res.*, 46, 1783–1794.

**CHAPTER 6:**

**General conclusions and  
Future recommendations**

## **6. General conclusions and Future recommendations**

### **6.1 General conclusions**

Lot of work has been done during these last ten years in collaboration between the groups of Tarragona (CaTheter, URV) and Montpellier (MACS-ICGM, ENSCM) on the catalytic reduction of nitrate in water, particularly using bimetallic catalysts obtained from LDH precursors. The stake is highly relevant and among the most worrying problems of the environmental catalysis nowadays. The high levels of nitrates ( $> 50 \text{ mg/L } \text{NO}_3^-$ ) in drinking water are indeed very risky to human health. Unfortunately, the nitrate concentration in groundwater, an important source of potable water, is continuously rising in the EU and other countries. Its presence is due to farmer, agricultural and many industries sources. The previous works of the two groups allow obtaining a wide knowledge on the mechanism of the reaction and on the required properties of the catalysts able to give high conversions and few toxic intermediates and by-products, such as nitrite ( $\text{NO}_2^-$ ), ammonium ( $\text{NH}_4^+$ ), and  $\text{NO}_x$  gases. In spite of the good results previously obtained following conventional catalytic routes, it is still a challenge to develop more ecofriendly processes with low energy consumption, total selectivity to  $\text{N}_2$  and  $\text{H}_2\text{O}$  (a requirement for drinking water), and high stability of the catalysts. This actually means obtaining efficient processes operating at lower total costs.

In this frame, this thesis represents an approach able to improve some of these points. Its aim was indeed to study the nitrate removal by a photocatalytic process using solar irradiation which is a very promising and ecofriendly technique. This has been scarcely performed until now and more research on highly efficient catalysts is still needed.

Based on a large survey of the literature and on the wide expertise of the groups of Tarragona and Montpellier on the preparation of catalysts, their composition has been first defined. This lead us to prepare monometallic and bimetallic heterogeneous catalysts based on silver and/or platinum supported on commercial Aerioxide Titania P25. This support is well known for its photocatalytic properties, which can be improved by metal(s) doping. On the other hand, silver and platinum are highly efficient for nitrate and nitrite reduction, respectively. Silver as co-catalyst is excellent at trapping photogenerated conduction band electrons. Pt is also one of the most active metals for photocatalytic enhancement producing the highest Schottky barrier. Pt thus facilitates electron capture producing a longer electron-hole separation lifetime hindering

their recombination. Furthermore, Pt has the ability to dissociate hydrogen. The Ag-Pt bimetallic pair supported on Titania, which can combine the interesting properties of both, has not been already investigated in the denitration reaction.

The comparative study between the catalytic and photocatalytic behavior of the same catalysts is an original aspect of this work. It is due to the specific composition of the samples that make them potentially active in the two processes. Therefore, it was an important feature to establish the part taken by each of these processes.

The bimetallic pair Pd-Sn used for catalytic nitrate abatement in water has been also studied. Both metals are well-known to be efficient in water denitration. Pd has the ability to reduce the nitrite to N<sub>2</sub> and to dissociate the H<sub>2</sub>, and the Sn is a co-catalyst known to reduce the nitrate towards nitrite. The influence of the morphology of the 5% Pd<sub>2</sub>Sn/P25 catalyst as spherical Nanoparticles and Nanorods has been tested. The nanocatalysts were synthesized by the IREC group.

Our objective was to determine the effect of the metal loading (Ag, Pt), the platinum precursor (H<sub>2</sub>PtCl<sub>6</sub>·6H<sub>2</sub>O, K<sub>2</sub>PtCl<sub>6</sub>), the impregnation order of both noble metals (Ag-Pt, Pt-Ag) and the morphology (Pd<sub>2</sub>Sn spherical NPs and NRs) onto the titania support for an overall and better understanding in the activity using different catalyst formulations and type.

The catalysts have been synthesized and characterized by a large range of physico-chemical methods (XRD, N<sub>2</sub> physisorption, TEM, DRUV-Vis, XPS, H<sub>2</sub>-TPR and H<sub>2</sub>-Chemisorption). Their activity for nitrate abatement for drinking water purpose has been investigated under non-photocatalytic and photocatalytic hydrogenation conditions. Pure hydrogen flow was used as the reducing agent. No hole scavenger such as organic acids (i.e. formic or oxalic acid) have been used in the photocatalytic process to avoid harmful radicals that could be formed in water and are potentially risky to the human health.

The main conclusions obtained from the studies performed all along this thesis are the following:

- Commercial Aerioxide Titania P25 and Pt based monometallic catalysts were almost inactive for the non-photocatalytic or photocatalytic reduction of nitrate under the experimental conditions used in the work.

- Ag(2)/P25, inactive in non-photocatalytic conditions, is in contrast the most efficient photocatalyst. However, the nitrite amounts have to be diminished to reach the EU Normative. The silver loading of 2 wt.% was used in the bimetallic catalysts because it was the optimum value observed in the monometallic catalysts leading to the higher N<sub>2</sub> yield and lower NO<sub>2</sub><sup>-</sup> yield.
- The best photocatalytic conditions were interestingly obtained under the ultraviolet irradiation of  $\lambda = 365$  nm (UV-A) (closer to solar light) and in presence of pure H<sub>2</sub> flow. Photocatalytic activity was enhanced in presence of H<sub>2</sub> due to synergetic effect induced by light between photogenerated electrons and dissociation of hydrogen on Pt. Therefore, all bimetallic catalysts were tested under these conditions.
- The mechanical mixture of monometallic Ag(2)/P25 + Pt(4)/P25(H) catalysts were active under catalytic condition but led to high NO<sub>2</sub><sup>-</sup> yield. They were poorly active in photocatalytic conditions due to probably lower synergetic light effect.
- Silver allows the reduction step from nitrate to nitrite intermediate product, and Pt from nitrite to nitrogen non-toxic gas product.
- Smaller mean nanoparticles sizes were obtained when using H<sub>2</sub>PtCl<sub>6</sub>·6H<sub>2</sub>O (ca. 2.3 nm) than K<sub>2</sub>PtCl<sub>6</sub> (ca. 4 nm) as Pt precursor, leading to higher reducibility and nitrate conversions but worse nitrogen selectivity and nitrate reduction rates.
- Bimetallic catalysts presented versatility under both catalytic and photocatalytic conditions.
- Better photocatalytic activities (higher NO<sub>3</sub><sup>-</sup> conversion, NO<sub>2</sub><sup>-</sup> selectivity and nitrate reductions rates) were obtained when impregnating Pt first and silver second (Pt-Ag) than in the reverse order (Ag-Pt), and using K<sub>2</sub>PtCl<sub>6</sub> as Pt precursor, attributed to better silver active sites accessibility and stronger interaction between both metals in the nanoparticles.
- The wt. 4 % platinum loading led to higher conversions and yields to nitrogen.

- The bimetallic catalysts Pt(4)-Ag(2)/P25 impregnated with K<sub>2</sub>PtCl<sub>6</sub> presented the highest photocatalytic activity among all the nanocatalysts synthesized. Nevertheless, ammonium levels have to be still diminished to be into the European normative limits, as well as the final pH (ca. 9).
- Decreasing the initial pH solution using as nitrate source nitric acid instead of sodium nitrate increased slightly the nitrogen selectivity but decreased the conversions and dramatically the final pH (ca. 2.5).
- The Pd<sub>2</sub>Sn growth mechanism was based on the selective desorption of TOP by chlorine ions.
- The Pd<sub>2</sub>Sn/P25 Nanorods showed higher catalytic performance than smaller spherical NPs towards water denitrification. The enhanced catalytic properties are attributed to the more active surface facets of Pd<sub>2</sub>Sn NRs.

## **6.2 Future recommendations**

Further studies must be done to improve the nitrate conversions and selectivity to reach the European legal limits.

- Using a continuous buffered solution in the media (i.e. CO<sub>2</sub>) could allow controlling the reaction to improve the activity obtaining a neutral pH.
- The AgPt-based catalysts show visible light range absorption, thus they can be used as photocatalysts. The proper combination of an ultraviolet irradiation ( $\lambda = 365$  nm) for the photoexcitation of the electrons in the titania and a visible light irradiation for the silver and platinum plasmons excitation ( $\lambda = \text{ca. } 530$  nm) could make the process potentially much more efficient.
- The metal loading of Pd<sub>2</sub>Sn particles has to be optimized.

- From an economical point of view, the amount of catalyst introduced in the reactor would be another important factor to take into account. It must be reduced by a further optimization of the catalyst, particularly improving the dispersion of the metals and their interaction.
- The photocatalytic nitrate reduction in water should be studied in continuous flow reactor.
- A non-metal co-catalyst would make the process cheaper (i.e. magnetite).
- The Aeroxide Titania P90 (anatase/rutile: 90/10) would be an interesting support to apply as an increase in the amount of anatase could benefit the catalyst activity.

## ANNEXES

**Annex A:**

**Scientific contributions**

### **A.1. Articles**

Title: Size and aspect ratio control of Pd<sub>2</sub>Sn Nanorods and their water denitration properties.

Authors: ZhiShan Luo, Maria Ibáñez, Ana M. Antolín, Aziz Genç, Alexey Shavel, Sandra Contreras, Francesc Medina, Jordi Arbiol, and Andreu Cabot.

DOI: 10.1021/la504906q

Journal Langmuir 31, 3952-3957 (9<sup>th</sup> March 2015). Impact Factor : 4.38 [*Published*]

Title: Silver/Platinum supported on TiO<sub>2</sub> P25 nanocatalysts for non-photocatalytic and photocatalytic denitration of water.

Authors: Ana M. Antolín, Sandra Contreras, Francesc Medina, Didier Tichit.

Journal Chemosphere (October 2016) [*Submitted*]

Title: Effect of metal loading, Pt precursor, and synthesis protocol in the catalytic and photocatalytic nitrate reduction towards nitrogen in water.

Authors: Ana M. Antolín, Sandra Contreras, Francesc Medina, Didier Tichit. [*To be submitted*]

### **A.2. Oral communications**

Title: Photocatalytic nitrate reduction with AgPt/TiO<sub>2</sub> catalysts.

Authors: Ana M. Antolín, Sandra Contreras, Francesc Medina, Didier Tichit.

3<sup>rd</sup> Symposium on Catalysis for Clean Energy and Sustainable Chemistry (CCESC 2016). Madrid, Spain. 7<sup>th</sup> – 9<sup>th</sup> September 2016.

Title: AgPt on Aeroxide P25 photocatalysts for nitrate abatement in ground water.

Authors: Ana M. Antolín, Sandra Contreras, Didier Tichit, Francesc Medina.

25<sup>èmes</sup> Journées Grand Sud-Ouest (GSO 2015). Montpellier, France. 27<sup>th</sup> November 2015.

Title: Water denitrification by heterogeneous photocatalytic reduction.

Authors: Ana M. Antolín, Sandra Contreras, Didier Tichit, Francesc Medina.

3<sup>rd</sup> Mediterranean Young Researchers Days (JMJC 2015). Montpellier, France. 12<sup>th</sup> – 14<sup>th</sup> October 2015.

### **A.3. Poster communications**

Title: Optimización de catalizadores de Ag/Pt soportados en Titania P25 para la reducción fotocatalítica de nitratos en agua de boca.

Authors: Ana M. Antolín, Sandra Contreras, Francesc Medina, Didier Tichit.

XXII Reunión de la Mesa Española de Tratamiento de Aguas (META2016). Madrid, Spain. 20<sup>th</sup> – 22<sup>th</sup> June 2016.

Title: Optimization of Ag/Pt supported on Titania P25 nanocatalysts for photocatalytic nitrate reduction.

Authors: Ana M. Antolín, Sandra Contreras, Francesc Medina, Didier Tichit.

9th European meeting on Solar Chemistry and Photocatalysis: Environmental Applications (SPEA9). Strasbourg, France. 13<sup>th</sup> – 17<sup>th</sup> June 2016.

Title: Fotocatálisis heterogénea en la reducción de nitratos en aguas.

Authors: Ana M. Antolín, Sandra Contreras, Francesc Medina.

Catálisis, confluencia interdisciplinar: modelos, catalizadores y reactores. Sociedad Española de Catálisis (SECAT'15). Barcelona, Spain. 13<sup>th</sup> – 15<sup>th</sup> July 2015.

Title: Water denitration by heterogenous (photo)catalytic reduction.

Authors: Ana M. Antolín, ZhiShan Luo, Andreu Cabot, Sandra Contreras, Francesc Medina.

7<sup>th</sup> European Meeting on Chemical Industry and Environment (EMCHIE 2015). Tarragona, Spain. 10<sup>th</sup> – 12<sup>th</sup> June 2015.

Title: Nitrate reduction by heterogeneous photocatalysis [1<sup>st</sup> Prize 2<sup>nd</sup> year students].

Authors: Ana M. Antolín, Sandra Contreras, Francesc Medina.

12<sup>th</sup> Doctoral Day. Chemical Engineering Department, Universitat Rovira i Virgili. Tarragona, Spain. 12<sup>th</sup> May 2015.

## **Annex B:**

### **Article submitted**

Title: Silver/Platinum supported on TiO<sub>2</sub> P25 nanocatalysts for non-photocatalytic and photocatalytic denitration of water.

Authors: Ana M. Antolín, Sandra Contreras, Francesc Medina, Didier Tichit

Journal Chemosphere (October 2016)

## B.1. Abstract

Denitration of water was investigated by non-photocatalytic and/or photocatalytic processes (UV irradiation at 365 nm) using Ag/P25 + Pt/P25 and Ag-Pt(Pt-Ag)/P25 bimetallic catalysts (2 wt% Ag; 4 wt% Pt) prepared by impregnation of TiO<sub>2</sub> P25. Influences of the Pt precursor (H<sub>2</sub>PtCl<sub>6</sub>·6H<sub>2</sub>O; K<sub>2</sub>PtCl<sub>6</sub>) and the impregnation order in the bimetallic samples were examined. The highest N<sub>2</sub> yield (42.6%) in the non-photocatalytic process was achieved with the Ag/P25 + Pt/P25 mixture with ca. 13% NO<sub>2</sub><sup>-</sup> yield. Photocatalytic activity was enhanced in presence of H<sub>2</sub>, in comparison to H<sub>2</sub>-free condition. Ag/P25 alone is the most active photocatalyst but with high NO<sub>2</sub><sup>-</sup> yield (32.5%). The bimetallic samples exhibit high versatility being active in the non-photocatalytic and the photocatalytic processes. Low NO<sub>3</sub><sup>-</sup> conversion and high NO<sub>2</sub><sup>-</sup> selectivity results were obtained from impregnation of Ag first. In contrast, impregnation of Pt from K<sub>2</sub>PtCl<sub>6</sub> first effectively promoted NO<sub>3</sub><sup>-</sup> reduction with N<sub>2</sub> yield of 36% instead of 4.6% with H<sub>2</sub>PtCl<sub>6</sub>·6H<sub>2</sub>O benefitting from the strong Pt and Ag interaction in the nanoparticles.

Keywords: Denitration; Photocatalyst; Silver; Platinum; Titania

## B.2. Introduction

The presence of nitrate ion (NO<sub>3</sub><sup>-</sup>) in drinking water is risky to human health (Rao et al. 2003). High concentration of highly soluble NO<sub>3</sub><sup>-</sup> (> 50 ppm) causes methemoglobinemia, cancer or can be an endocrine disruptor (Mori et al. 1999; Thompson 2001; Guillette et al. 2005; Mahler et al. 2007; European Union 2010). Several methods allow abatement of NO<sub>3</sub><sup>-</sup> from water and particularly by heterogeneous catalytic hydrogenation to obtain N<sub>2</sub>. It leads frequently to toxic side products, e. g. nitrite (NO<sub>2</sub><sup>-</sup>), and ammonium (NH<sub>4</sub><sup>+</sup>) ions (Hörold et al. 1993). Generally, the most efficient catalysts in NO<sub>3</sub><sup>-</sup> reduction also lead to the final lowest NO<sub>2</sub><sup>-</sup> production (Marchesini et al. 2012). Bimetallic catalysts associating a metal promoter with suitable redox properties (Cu, Sn, Ag) and a noble metal able to chemisorb hydrogen (Pt, Pd, Rh) allow obtaining efficient catalysts for denitration. Pt-Cu, Pd-Ag, Ag-Pt supported on Al<sub>2</sub>O<sub>3</sub> (Gauthard et al. 2003), Pt-Cu on hydrotalcite (Aristizábal et al. 2011), Pt-Cu and Pt-Ag on active carbon (Barrabés et al. 2006; Aristizábal et al. 2012) lead to high NO<sub>3</sub><sup>-</sup> conversions, however undesirable NO<sub>2</sub><sup>-</sup> and/or NH<sub>4</sub><sup>+</sup> by-products are present.

Heterogeneous photocatalysis is a promising route for denitration being a friendly technique due to the possibility of using solar irradiation (Ibhodon et al. 2013). Aerioxide Titania P25 (TiO<sub>2</sub> P25) is extensively applied in the photocatalysis field due to its low-cost, non-toxicity,

high stability and redox efficiency. Nevertheless, due to its limited band gap (3.2 eV) and the high recombination rate between photogenerated electrons and holes limiting the photocatalytic efficiency, TiO<sub>2</sub> is generally doped with noble metals enhancing the electron-hole separation and shifting the light absorption into the visible-light range (Soria et al. 1991; Asahi et al. 2001; Behnajady et al. 2008; Gomathi et al. 2010; Zhu et al. 2012). Silver is among the most largely metal used as dopant of the photocatalytic activity of TiO<sub>2</sub> (Gauthard et al. 2003; Zhang et al. 2005; Behnajady et al. 2008; Doudrick et al. 2013; Sowmya et al. 2014). Recently, few studies using silver catalyst supported on TiO<sub>2</sub> P25 applying ultraviolet light at 254 nm and 365 nm wavelengths and using different hole scavengers such as formic, acetic or oxalic acids as well as sodium formate or acetate, have been reported with good NO<sub>3</sub><sup>-</sup> conversion to N<sub>2</sub> (up to 95 %) (Sá et al. 2009; Aristizábal et al. 2011). These hole scavengers have different efficiencies due to the modification of the surface charge of the catalyst and, after dissociation, to the presence of anions competing with NO<sub>3</sub><sup>-</sup> for adsorption (Zhang et al. 2007; Sá et al. 2009; Barrabés et al. 2011). Their main drawbacks to achieve the requirements for drinking water are the remnant amounts in solution and the too low pH. However, it can be pointed out that formic acid which is decomposed into H<sub>2</sub> and CO<sub>2</sub> is attractive because H<sub>2</sub> is a very efficient hole scavenger (Sá et al. 2009). Recent studies showed that Ag-Pt/TiO<sub>2</sub> is highly efficient in the photo-conversion of CO<sub>2</sub> to CH<sub>4</sub> (Mankidy et al. 2013). To the best of our knowledge, there is no study dealing with the photocatalytic reduction of NO<sub>3</sub><sup>-</sup> with this type of catalyst. Nevertheless, it is noteworthy that Pt-Ag/AC or Pt-Ag/Al<sub>2</sub>O<sub>3</sub> have been reported for the non photocatalytic NO<sub>3</sub><sup>-</sup> reduction under H<sub>2</sub> (Aristizábal et al. 2012).

Our aim was to use Ag supported on TiO<sub>2</sub> P25 for the photocatalytic removal of NO<sub>3</sub><sup>-</sup> from aqueous solution with H<sub>2</sub> as hole scavenger. Besides, presence of Pt both able to dissociate H<sub>2</sub> and reduce NO<sub>2</sub><sup>-</sup> (Prusse et al. 2000) appears necessary to improve the photocatalytic efficiency. This led us to investigate a system associating the monometallic Ag/TiO<sub>2</sub> and Pt/TiO<sub>2</sub> photocatalysts and also bimetallic Ag-Pt/TiO<sub>2</sub> photocatalysts obtained by impregnation. Being the impregnation protocol and the nature of the metal precursors relevant parameters for the activity and selectivity, we have varied the addition order of the salts and used H<sub>2</sub>PtCl<sub>6</sub>·6H<sub>2</sub>O or K<sub>2</sub>PtCl<sub>6</sub> as Pt precursors (Aristizábal et al. 2014). To establish the non-photocatalytic and the photocatalytic contributions in the reduction of NO<sub>3</sub><sup>-</sup>, experiments were done without UV irradiation in presence of H<sub>2</sub> (non photocatalytic process), under irradiation in H<sub>2</sub>-free condition and lastly under UV irradiation and presence of H<sub>2</sub> (photocatalytic process).

### B.3. Materials and methods

#### B.3.1. Catalysts synthesis

Pt- (4 wt%) and Ag (2 wt%)-containing bimetallic catalysts were prepared by incipient-wetness of Aerioxide TiO<sub>2</sub> P25 support varying the order of addition of the Ag and Pt precursors and the nature of this latter (H<sub>2</sub>PtCl<sub>6</sub>·6H<sub>2</sub>O (H) or K<sub>2</sub>PtCl<sub>6</sub> (K)), followed by reduction with NaBH<sub>4</sub> (SI-1). Bimetallic catalysts are noted e.g. Ag-Pt/P25(H) meaning that Ag is impregnated first, P25 is the support and H is the H<sub>2</sub>PtCl<sub>6</sub>·6H<sub>2</sub>O precursor.

Physical mixture was prepared by mixing of the monometallic Ag/P25 and Pt/P25 catalysts (50/50 : wt/wt) and named as Ag/P25 + Pt/P25.

#### B.3.2. Catalysts characterization

Powder X-Ray diffraction (XRD) patterns (Bruker D8 Advance Diffractometer) were recorded using monochromatic Cu-K $\alpha$  radiation ( $\lambda_{\alpha} = 1.54184 \text{ \AA}$ , 40 kV, 50 mA) and LynxEye detector. The surface areas were calculated applying the BET method to the N<sub>2</sub> adsorption isotherm at 77 K performed on samples previously outgassed 10 h at 120 °C (Micromeritics ASAP 2010). Pore volumes and pore diameter sizes were obtained from desorption isotherm by the BJH method. TEM characterizations were operated at 100 kV (Jeol 1200 EXII). The DRUV-Vis spectras (Perkin Elmer Lambda 40 UV/VIS spectrometer) were registered between 300-800 nm with an integrating sphere accessory, using BaSO<sub>4</sub> powder as reference. Surface characterization of selected samples was achieved by X-ray photoelectron spectroscopy (XPS) (ESCALAB 250 spectrometer). A 400 μm surface was analyzed with monochromatic Al K $\alpha$  source ( $h\nu$ ) of 1486.6 eV. Binding energies (BE) are referenced to the carbon 1s signal at 284.8 eV and the load is compensated by an electron beam (-2 eV). Hydrogen consumption was measured by H<sub>2</sub> temperature programmed reduction (H<sub>2</sub>-TPR) (Autochem II 2920 V 4.03 Micromeritics equipped by a thermal conductivity detector (TCD)). 0.2 g of sample was located in a quartz reactor and reduced in a 20 ml/min of 10% vol. H<sub>2</sub>/Ar current within -80 – 400°C at 10 °C/min.

#### B.3.3. Denitration experiments

The reactions were carried out as described previously with 0.2 g of catalyst introduced in the 100 ppm NO<sub>3</sub><sup>-</sup> solution for 6 hours (Luo et al. 2015). The UV-A irradiation ( $\lambda = 365 \text{ nm}$ ; P = 4 W) was placed on the top of the reactor. Samples were withdrawn at regular time intervals to

analyze  $\text{NO}_3^-$ ,  $\text{NO}_2^-$  and  $\text{NH}_4^+$  ions measured by Ionic Chromatography (DIONEX ICS-900) (*B.6.2*). The catalyst powders were removed by filtration (0.45  $\mu\text{m}$  PTFE filter) before analysis.

## B.4. Results and discussion

### B.4.1. X-Ray Diffraction Powder

XRD patterns of  $\text{TiO}_2$  P25 (ca. 80 anatase/20 rutile, % w/w) and of the reduced catalysts (Figure B.3 in *B.6.4* SI) show the characteristic and most intense peaks at  $2\Theta = 25.28^\circ$  and  $27.44^\circ$  of the anatase (JCPDS 021-1272) and rutile (JCPDS 021-1274) phases. No additional peaks due to metallic particles are observed because of the sensitivity of XRD analysis at such metal loadings and/or the low size and high dispersion of the particles (Matos et al. 2012; Talat-Mehrabad et al. 2015). Characteristic peaks of  $\text{K}_2\text{PtCl}_6$  are observed in the XRD patterns of the samples impregnated with this salt indicating that oxidized Pt is present, as will be confirmed by XPS analysis.

### B.4.2. $\text{N}_2$ Physisorption

The  $\text{TiO}_2$  P25 support and the catalysts exhibit type IV nitrogen adsorption-desorption isotherms of mesoporous materials. The surface area for  $\text{TiO}_2$  P25,  $55 \text{ m}^2\text{g}^{-1}$ , in agreement with literature data, decreases to  $50 \text{ m}^2\text{g}^{-1}$  after calcination at  $400^\circ\text{C}$ . The surface areas of the catalysts are in the range from  $42$  to  $50 \text{ m}^2\text{g}^{-1}$ . Their pore volume is about  $0.3 \text{ cm}^3\text{g}^{-1}$  with a mean pore diameter of  $25 \text{ nm}$ .

### B.4.3. Transmission Electron Microscopy

The morphology of the monometallic and bimetallic catalysts is analyzed by TEM and the images are displayed in Figures B.4 and B.5 in section *B.6.5*. The TEM image of bare  $\text{TiO}_2$  P25 also reported displays spherical-shape particles ranging from  $20$  to  $70 \text{ nm}$  (Figure B.4). In  $\text{Ag}/\text{P25}$  the spherical Ag particles with average crystallite size of  $3.1 \text{ nm}$  are heterogeneously distributed on the surface of P25 particles. The behavior of the monometallic Pt-containing catalysts differs slightly depending on the precursor. Using  $\text{K}_2\text{PtCl}_6$  the particles present an average size of  $2.2 \text{ nm}$  and are larger and more agglomerated than using  $\text{H}_2\text{PtCl}_6 \cdot 6\text{H}_2\text{O}$ , which leads to higher dispersion with an average particle size of  $1.5 \text{ nm}$ . Moreover, in this latter case the Pt particles are found on the overall surface of the support but with a preferential distribution at the boundaries of the particles. Due to the composition of P25 (anatase/rutile: 80/20), the particles are mostly on the anatase phase as previously demonstrated by Sclafani et al. (Sclafani

et al. 1997, 1998). The influence of the precursor on the Pt dispersion can be explained based on the IEP for TiO<sub>2</sub> P25 of ~ 6.2 (Suttiponparnit et al. 2011) and the pH of aqueous H<sub>2</sub>PtCl<sub>6</sub>·6H<sub>2</sub>O and K<sub>2</sub>PtCl<sub>6</sub> solutions of ca. 1 and 2, respectively. The electrostatic interaction between [PtCl<sub>6</sub>]<sup>2-</sup> species and TiO<sub>2</sub> is higher and the dispersion is enhanced using H<sub>2</sub>PtCl<sub>6</sub>·6H<sub>2</sub>O (Kanda et al. 2009). Moreover, the chlorine-containing mobile species [Pt<sub>y</sub>O<sub>x</sub>Cl<sub>y</sub>] probably formed increase the Pt dispersion onto the support (Antos et al. 2004).

Remarkably, the same influence of the Pt precursor is observed in the micrographs of the bimetallic catalysts with smaller particles (2.3 nm) mostly present at the boundaries of the TiO<sub>2</sub> P25 support with H<sub>2</sub>PtCl<sub>6</sub>·6H<sub>2</sub>O, instead of more agglomerated with a larger average size (~ 4 nm) and deposited on all the surface with K<sub>2</sub>PtCl<sub>6</sub>.

#### B.4.4. Diffuse Reflectance UV-Vis spectroscopy

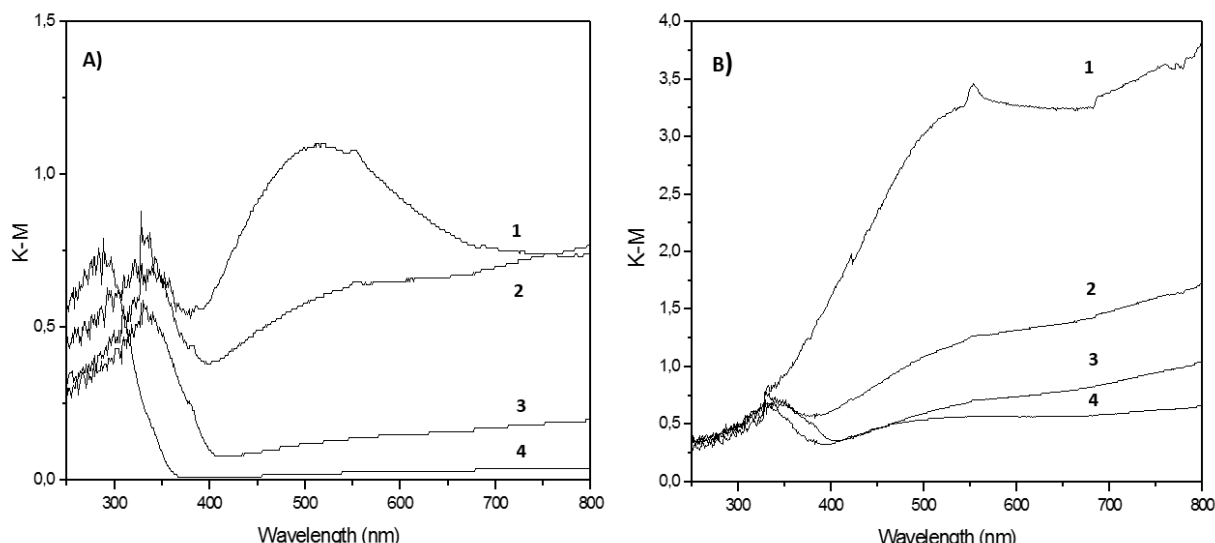


Figure B.1. DRUV-Vis spectra of: A): 1) Ag/P25, 2) Pt/P25(H), 3) Pt/P25(K), 4) P25; and B): 1) Pt-Ag/P25(H), 2) Ag-Pt/P25(H), 3) Pt-Ag/P25(K), 4) Ag-Pt/P25(K).

From the reflectance UV-Vis spectra of TiO<sub>2</sub> P25 and of the catalysts the optical absorbance is shown in Figure B.1 in terms of Kubelka-Munk equivalent absorbance units. TiO<sub>2</sub> P25 exhibits the fundamental absorbance stopping edge at ~ 400 nm due to charge-transfer transitions between the oxygens and the titanium ions. It shows a very moderate light absorption capability from 400 to 700 nm. As a general trend, the visible light absorption capability is largely enhanced from 400 to 700 nm in Ag/P25 and the bimetallic samples. The broad band centered at around 500 nm can be attributed to the localized surface plasmon resonance (LSPR) effect of the silver particles exhibiting generally characteristic absorption bands whose maximum are

reported at very different position in the literature; e. g. 440, 470 and 530 nm (Sobana et al., 2006; Rupa et al., 2009; Pulido Melián et al., 2012). The broadening of the peak can be due to the different sizes and shape of the particles. It is indeed strongly attenuated in Pt-Ag/P25(K) and Ag-Pt/P25(K) exhibiting the larger mean particle size of 3.5 and 4.4 nm, respectively.

#### B.4.5. X-Ray Photoelectron Spectroscopy

The surface of the reduced Ag/P25, Ag-Pt/P25(K) and Pt-Ag/P25(K) catalysts was analyzed by XPS to examine the valence state and the chemical environment of the active noble metals impregnated in different order. The Ti 2p and O 1s XPS peaks of all samples have very similar BE (Table B.3 in section B.6.6). The BE of  $\text{Ti}^{4+}$   $2\text{p}_{1/2}$  and  $\text{Ti}^{4+}$   $2\text{p}_{3/2}$  centered at 458.3 eV and 464.2 eV, respectively, well correspond to the standard values (Sowmya et al. 2014). The O<sub>1s</sub> peaks were deconvoluted in three species. The BE of 529.5 eV is assigned to Ti-O bonds. The BE of 531.3 eV is generally associated to the presence of oxygen vacancies in the TiO<sub>2</sub> lattice, and that of 532.9 eV to chemisorbed or dissociated oxygen on the surface (Sowmya et al. 2014).

Table B.1. BE of Ag and Pt recorded by XPS.

Catalyst	BE (eV)					
	$\text{Ag}^0$ $3\text{d}_{5/2}$	$\text{Ag}^0$ $3\text{d}_{5/2}$	$\text{Ag}^0$ $3\text{d}_{3/2}$	$\text{Pt}^0$ $4\text{f}_{7/2}$	$\text{Pt}^0$ $4\text{f}_{5/2}$	Pt(II) $4\text{f}_{7/2}$
Ag/P25	367.2	368	373.2	-	-	-
Ag-Pt/P25(K)	367.1	-	373.2	70	74.5	72.8
Pt-Ag/P25(K)	366.9	367.9	373.2	69.9	74.3	72.1

According to the literature, the Ag species show two peaks owing to Ag 3d<sub>5/2</sub> and Ag 3d<sub>3/2</sub> transitions and then to Ag<sup>0</sup> as main species (Table B.1). The BE of Ag 3d<sub>5/2</sub> and Ag 3d<sub>3/2</sub> are of ca. 367.2 and 373.2 eV, respectively, in Ag/P25 and Ag-Pt/P25(K). These values are shifted in comparison to those reported in the literature at 369.1 and 375.1 eV, respectively (Rodríguez-González et al. 2010; Sowmya et al. 2014), accounting for several concurrent features such as strong interaction between Ag<sup>0</sup> and TiO<sub>2</sub> and in Ag-Pt/P25(K), for the presence of an environment of chlorine provided by K<sub>2</sub>PtCl<sub>6</sub> (Aristizábal et al. 2014); finally electron transfer from Ag to Pt might occur. The Ag 3d<sub>5/2</sub> peak in Ag/P25 is slightly asymmetric and after deconvolution gives a component with BE of 368 eV, suggesting that part of Ag forms nanoparticles in different interaction with TiO<sub>2</sub> (Wodka et al. 2010). It is noteworthy that the

Ag 3d<sub>5/2</sub> BE is most largely shifted at 366.9 eV for Pt-Ag/P25(K). This can be assigned, like for Pt-Ag particles supported on activated carbon (Pt-Ag/AC), to a larger electron transfer from Ag to Pt in Pt-Ag solid solution (Aristizábal et al. 2014). It will be likely formed when Ag is secondly impregnated, then deposited on Pt with strong interaction. Furthermore, the Ag 3d<sub>5/2</sub> peak in Pt-Ag/P25(K) is slightly asymmetric and its deconvolution reveals a weak component at 367.9 eV due to nanoparticles in agreement with the large size distribution observed for these mono- and bimetallic samples by TEM. Such nanoparticles are not observed in Ag-Pt/P25(H), probably due to the decoration of the Ag particles impregnated first by Pt. The Pt spectra show the two Pt 4f<sub>7/2</sub> and Pt 4f<sub>5/2</sub> peaks with BE of ca. 70 and 74.4 eV related to Pt<sup>0</sup> particles. These BE are close to the literature for Pt<sup>0</sup> in Pt/TiO<sub>2</sub> at 70.5 and 73.9 eV (Ohtani et al. 1997), and in bimetallic Pt-Ag/AC at ca. 71.1 and 74.4 eV (Aristizábal et al. 2014).

It is noteworthy that the BE of Pt<sup>0</sup> are more largely shifted toward lower values at 69.9 eV and 74.3 eV in Pt-Ag/P25(K) according to the behavior of Ag<sup>0</sup> and assigned to the main formation of a solid solution. Furthermore, a shoulder appears at BE of ca. 72.5 eV, which can be assigned to a positively charged form due to K<sub>2</sub>PtCl<sub>6</sub> species detected by XRD.

Summarizing, Ag is almost totally reduced, while in addition to Pt<sup>0</sup>, slight amount of non-reduced platinum is present in the bimetallic samples following the NaBH<sub>4</sub> treatment. Ag and Pt appear mainly involved in a solid solution when Pt is impregnated first, with also the presence of silver nanoparticles as observed in Ag/P25. Ag impregnated first is probably decorated by Pt. In this case the electronic properties of Ag<sup>0</sup> in the bimetallic Ag-Pt/P25(K) sample are close to those in Ag/P25.

#### B.4.6. H<sub>2</sub>-Temperature Programmed Reduction

The TPR profiles of the samples are reported in Figure B.2 and the H<sub>2</sub> consumptions in Table B.4. in B.6.7 Ag/P25 presents a weak peak at ~ 100 °C and a low H<sub>2</sub> consumption (0.14 mmol g<sup>-1</sup>) both showing that AgNO<sub>3</sub> is photoreduced during impregnation (Aristizábal et al. 2014). Peaks at 12, 170 and 310 °C are observed in Pt/P25(H) shifted at 22, 157 and 231 °C in Pt/P25(K). The peak below 25 °C is assigned to highly dispersed Pt<sup>0</sup> particles. Those at higher temperature are due to particles interacting more strongly with the support. In Pt/P25(K) the shift toward lower temperature of the peaks situated above 150 °C in comparison to Pt/P25(H), and the significant decrease in H<sub>2</sub> consumption might be related to the larger particle size and the presence of residual K<sub>2</sub>PtCl<sub>6</sub>.

Remarkably the TPR profiles of the bimetallic samples where Pt was secondly impregnated (Ag-Pt/P25(H) and Ag-Pt/P25(K)) are closely related to those of the monometallic samples with the corresponding Pt precursor with the same peaks assigned to the reduction of these precursors, being Ag therefore reduced during impregnation. The decrease of ca. 25% of the H<sub>2</sub> consumption in comparison to the corresponding Pt/P25 samples is due to the large increase of the mean particle sizes and confirms that there is probably no contribution due to Ag reduction. A quite different feature is observed when Ag was secondly impregnated. H<sub>2</sub> consumptions decrease to 0.20 – 0.30 mmol g<sup>-1</sup>, suggesting that decoration of Pt particles by Ag hinders Pt reduction. Reduction occurs below room temperature in Pt-Ag/P25(H) showing that the metal particles might be highly dispersed and interact weakly with the support when situated at the boundaries of the anatase particles (Fig B.5 in section B.6.5). Pt-Ag/P25(K) exhibits very weak peaks of Pt at 30 and 232 °C and the lower H<sub>2</sub> consumption of the bimetallic samples due to the large particles size, the presence of residual K<sub>2</sub>PtCl<sub>6</sub> and the strong Ag-Pt interaction revealed by XPS.

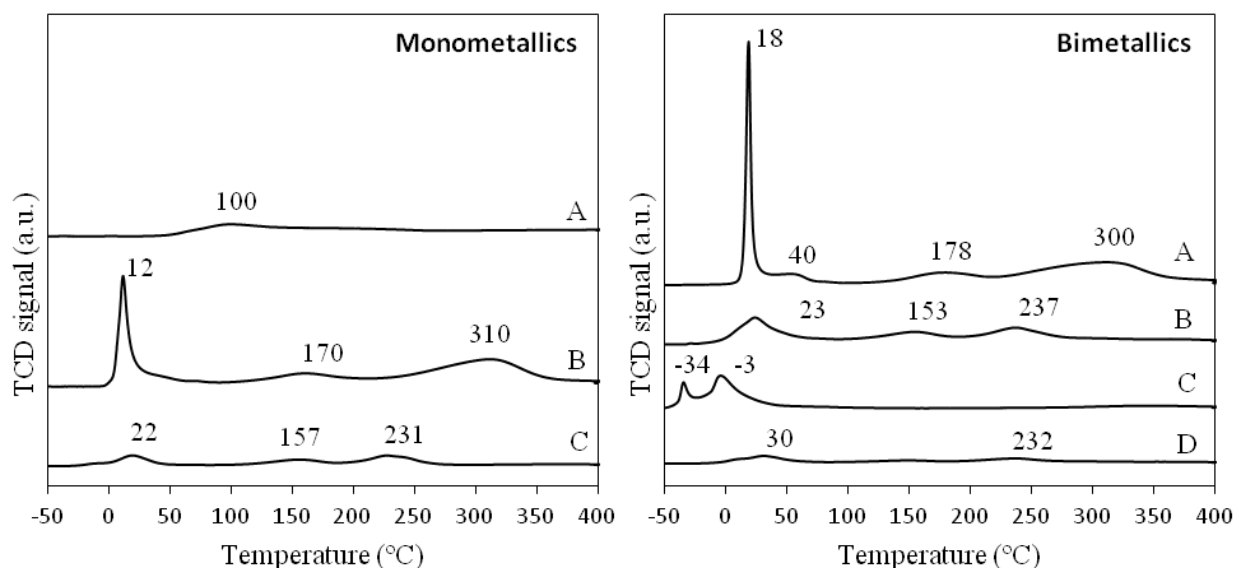


Figure B.2. H<sub>2</sub>-TPR profiles of: Monometallic: A) Ag/P25, B) Pt/P25(H), C) Pt/P25(K); and Bimetallic: A) Ag-Pt/P25(H), B) Ag-Pt/P25(K), C) Pt-Ag/P25(H), and D) Pt-Ag/P25(K).

#### B.4.7. Catalytic results

The catalytic activity of TiO<sub>2</sub> P25 was tested under dark or irradiated condition and no NO<sub>3</sub><sup>-</sup> reduction occurs.

NO<sub>3</sub><sup>-</sup> conversion and selectivity to products obtained with Ag/P25 and Pt/P25(H/K) for the non-photocatalytic (presence of H<sub>2</sub>; no irradiation) and the photocatalytic reduction (presence/absence of H<sub>2</sub>; irradiation) after 6h are shown in Table B.2.

Ag/P25, poorly active for the non-photocatalytic reduction (entry 1) is in contrast the most active photocatalyst (entry 6). Its photocatalytic activity is improved in presence of H<sub>2</sub> acting as hole scavenger where N<sub>2</sub> yield reaches 24.5% (entry 11), while NH<sub>4</sub><sup>+</sup> is not formed but NO<sub>2</sub><sup>-</sup> yield reaches 24.5%. The enhancement of the photocatalytic activity of the TiO<sub>2</sub> P25 support doped with Ag is consistent with the higher absorbance capability observed by DRUV-Vis (Fig. 1). There is an increase of NO<sub>3</sub><sup>-</sup> conversion and N<sub>2</sub> selectivity for the photocatalytic reduction in presence of H<sub>2</sub> in comparison to the H<sub>2</sub>-free condition. This accounts from a synergetic effect already reported with bimetallic Pd-Cu/TiO<sub>2</sub> catalyst. The oxidized metals are being reduced by both the photogenerated electrons and H<sub>2</sub> dissociated on Pt, as the irradiation promotes the electron availability on the metal particles in presence of H<sub>2</sub> (Soares et al. 2014).

The photocatalytic activity exhibited by Ag/P25 in presence of H<sub>2</sub> is in agreement with that reported using Ag/TiO<sub>2</sub> prepared by photodeposition in presence of oxalic acid (Sowmya et al. 2014) or sodium oxalate (Gekko et al. 2012). However, it disagrees with the results reported using formic acid where complete NO<sub>3</sub><sup>-</sup> removal and residual NO<sub>2</sub><sup>-</sup> and NH<sub>4</sub><sup>+</sup> amounts were obtained with no significant improvement compared to bare TiO<sub>2</sub> P25 (Sá et al. 2009), and with Ag-TiO<sub>2</sub> thin films leading to NO<sub>3</sub><sup>-</sup> removal of 70% with complete selectivity toward N<sub>2</sub> (Kobwittaya et al. 2014). These differences emphasize the role of the reaction conditions and the preparation method of the photocatalyst.

Our results, particularly the high NO<sub>2</sub><sup>-</sup> yields, are consistent with the low photoreduction ability to reduce NO<sub>2</sub><sup>-</sup> on Ag/TiO<sub>2</sub> with only a slight enhancement compared to bare TiO<sub>2</sub> (Zhang et al. 2007).

The NO<sub>3</sub><sup>-</sup> rate consumption,  $0.165 \pm 0.065 \text{ h}^{-1}$  (Table B.5 in B.6.8), of Ag/P25 for the photocatalytic reduction in presence of H<sub>2</sub> is about 10 to 30 times higher than that of Pt/P25 samples in the same conditions (entries 12 and 13); although using K<sub>2</sub>PtCl<sub>6</sub> (entry 13) leads to higher NO<sub>3</sub><sup>-</sup> conversion and selectivity to N<sub>2</sub> (97%), with NH<sub>4</sub><sup>+</sup> as only other by-product,

suggesting high activity for  $\text{NO}_2^-$  reduction. This was checked performing the photocatalytic  $\text{NO}_2^-$  reduction with Pt/P25(H) and Pt/P25(K) (Table B.6 in B.6.9) which reveals higher  $\text{N}_2$  yield with Pt/P25(K) and concurrent oxidation of  $\text{NO}_2^-$  to  $\text{NO}_3^-$ .

When the reaction was carried out with the Ag/P25+Pt/P25(H) mixture better non-photocatalytic activity (entry 3) than with each monometallic catalyst was obtained;  $\text{NO}_3^-$  conversion and  $\text{N}_2$  yield reached 56% and 42.5%, respectively. However, the  $\text{NO}_2^-$  yield of ca. 13% does not satisfy the requirements for drinking water (European Union 2010). These results show, following the redox mechanism for  $\text{NO}_3^-$  reduction into  $\text{NO}_2^-$  with concurrent oxidation of the Ag promoter then reduced by  $\text{H}_2$  adsorbed and dissociated on Pt, that this latter step and the migration of  $\text{H}_2$  is efficient, improving  $\text{NO}_3^-$  conversion. Pt is efficient for  $\text{NO}_2^-$  reduction, but this is not observed using Ag/P25+Pt/P25(H) suggesting that migration of  $\text{NO}_2^-$  to the Pt sites is not effectively achieved.

The photocatalytic activity of the Ag/P25 + Pt/P25 mixture in  $\text{H}_2$ -free condition (entry 8) is very low and below that of Ag/P25 (entry 6) mainly accounting for the decrease in the number of  $\text{Ag}^0$  sites. Although conversion is low, it is noted that  $\text{NO}_2^-$  and  $\text{NH}_4^+$  are not formed. As reduction is only due to the photoexcited electrons transferred from  $\text{TiO}_2$  P25 to the metal particles, this shows that it is limited without  $\text{H}_2$ .

It is remarkable that the photocatalytic activity of Ag/P25 + Pt/P25 in presence of  $\text{H}_2$  (entry 14) is lower than the non-photocatalytic activity (entry 3) with an increase of  $\text{NO}_2^-$  selectivity at the expense of  $\text{N}_2$ . This fact can suggest that the higher  $\text{H}_2$  coverage on Pt/P25 due to additional  $\text{H}_2$  evolved by photoreduction of water inhibits the reaction (Hirayama et al. 2012).

To conclude on the mixture Ag/P25 + Pt/P25, it is more efficient for the non-photocatalytic than for the photocatalytic reaction, although leading to  $\text{NO}_2^-$ , which does not satisfy the requirements of drinking water.

We will now examine the behavior of the impregnated bimetallic samples. Like the mixture Ag/P25 + Pt/P25 they are poorly active in the  $\text{H}_2$ -free photocatalytic reduction (entries 9 and 10). The solution pH is  $\sim 5$ , the reaction being performed in non-buffered media. At pH values lower than the  $\text{pH}_{\text{PZC}}$  of the support ( $\sim 6.2$ ), the positively charged surface weakly adsorbed  $\text{NO}_3^-$  and normally favors conversion. However, it has been observed that  $\text{NO}_3^-$  reduction does not occur if pH is too low, although this is controversial in literature (Sá et al. 2009; Soares et al. 2014).

In the non-photocatalytic reaction and the photocatalytic reaction with H<sub>2</sub> a fruitful comparison is done with the samples derived from H<sub>2</sub>PtCl<sub>6</sub>·6H<sub>2</sub>O precursor. It is worth emphasizing on the dramatic influence of the impregnation order on the conversion, and particularly on the selectivity. When Pt is first impregnated, Pt-Ag/P25(H) (entries 5 and 16), NO<sub>3</sub><sup>-</sup> conversion is slightly higher and NO<sub>2</sub><sup>-</sup> yield is enhanced at the expense of N<sub>2</sub> in comparison to the reverse impregnation order, Ag-Pt/P25(H) (entries 4 and 15). When Pt is impregnated in a second time it is probably involved both in individual particles and deposited on the Ag particles thus decreasing the number of sites available for NO<sub>3</sub><sup>-</sup> reduction. But NO<sub>2</sub><sup>-</sup> reduction to N<sub>2</sub> is improved benefiting from the high ability of the accessible Pt. This more likely occurs in non-photocatalytic reduction (entry 4). At the reverse, NO<sub>2</sub><sup>-</sup> reduction is inhibited in all conditions when Ag decorates Pt particles in Pt-Ag/P25(H) as suggested from the TPR characterization (entries 5 and 16).

Besides, in the non-photocatalytic reduction, Pt-Ag/P25(H) (entry 5) and the Ag/P25 + Pt/P25 mixture (entry 3) exhibit closer NO<sub>3</sub><sup>-</sup> conversion, but NO<sub>2</sub><sup>-</sup> conversion to N<sub>2</sub> is not favored with the former sample accounting for its lower accessibility to Pt decorated with Ag. In the photocatalytic reduction with H<sub>2</sub> the two bimetallic samples (entries 15 and 16) are more active than the Ag/P25 + Pt/P25 mixture (entry 14), suggesting a higher synergistic effect by light similar to that observed for Ag/P25.

The influence of the Pt precursor already reported (Hörold et al., 1993; Aristizábal et al., 2012, 2014), is established from the results obtained with the impregnated samples in the photocatalytic reaction with H<sub>2</sub> (entries 15 – 18). Higher NO<sub>3</sub><sup>-</sup> conversion is achieved in Ag-Pt/P25(H) than in Ag-Pt/P25(K) due to the smaller mean particle size of the former observed by TEM (2.1 nm versus 4.4 nm) and then to the higher number of accessible active sites. The larger particles also favor NH<sub>4</sub><sup>+</sup> selectivity in Ag-Pt/P25(K). The dramatic influence of the Pt precursor on the selectivity observed with Pt-Ag/P25 samples deserves comments as they exhibit similar conversion showing that it is probably not related to their different mean particle size. The higher N<sub>2</sub> selectivity of Pt-Ag/P25(K) and its reaction rate ( $0.104 \pm 0.022 \text{ h}^{-1}$ ), two times higher than in the other bimetallic catalysts, must be related to the large extent of Pt and Ag in strong interaction in solid solution shown by XPS. These species enhance NO<sub>2</sub><sup>-</sup> reduction, although NH<sub>4</sub><sup>+</sup> is still formed in too large amount (European Union 2010). A N<sub>2</sub> yield of 36% is thus obtained in the photocatalytic process which compares well with those reach with Ag-Pt/P25(H) and the mixture Ag/P25 + Pt/P25 ranging from 36 to 42% in the catalytic process.

Table B.2. Non-photocatalytic and photocatalytic results in the reduction of  $\text{NO}_3^-$ .

Entry	Catalyst	$\text{H}_2$	Irrad.	Conv. (%)	Sel. (%)		
					$\text{NO}_2^-$	$\text{NH}_4^+$	$\text{N}_2$
1	Ag/P25	Y	N	3	4	0	96
2	Pt/P25(H)	Y	N	1	0	3	97
3	Ag/P25+Pt/P25(H)	Y	N	56	23	1	76
4	Ag-Pt/P25(H)	Y	N	44	16	1	83
5	Pt-Ag/P25(H)	Y	N	58	81	2	17
6	Ag/P25	N	Y	10	89	8	3
7	Pt/P25(H)	N	Y	1	8	3	92
8	Ag/P25+Pt/P25(H)	N	Y	3	0	0	100
9	Ag-Pt/P25(H)	N	Y	7	1	0	99
10	Pt-Ag/P25(H)	N	Y	7	2	0	98
11	Ag/P25	Y	Y	57	57	0	43
12	Pt/P25(H)	Y	Y	1	0	33	67
13	Pt/P25(K)	Y	Y	10	0	3	97
14	Ag/P25+ Pt/P25(H)	Y	Y	20	60	3	37
15	Ag-Pt/P25(H)	Y	Y	38	32	3	65
16	Pt-Ag/P25(H)	Y	Y	46	88	2	10
17	Ag-Pt/P25(K)	Y	Y	17	31	16	53
18	Pt-Ag/P25(K)	Y	Y	45	6	14	80

## B.5. Conclusions

Ag (2 wt.%) and /or Pt (4 wt.%) supported on  $\text{TiO}_2$  P25 materials synthesized by drop-wise wetness impregnation either as mixture of monometallic catalysts or as co-impregnated catalysts promoted both the non-photocatalytic and the photocatalytic (365 nm UV irradiation; presence/absence of  $\text{H}_2$ ) removal of  $\text{NO}_3^-$  from water. In comparison to  $\text{H}_2$ -free condition, the photocatalytic activity was highly enhanced in presence of  $\text{H}_2$ .

Ag/P25 alone, inactive in non-photocatalytic conditions, is in contrast the most efficient photocatalyst. Conversion is improved in presence of  $\text{H}_2$  due to synergistic effect induced by

light between photo-generated electrons and H<sub>2</sub> dissociated on Pt. However NO<sub>2</sub><sup>-</sup> selectivity is too high.

The Ag/P25 + Pt/P25 (50/50 : wt/wt) mixture is more efficient in the non-photocatalytic process with N<sub>2</sub> yield of 42.5% than for the photocatalytic process (N<sub>2</sub> yield = 7.4%), probably due in this latter case to inhibition by H<sub>2</sub> produced by photoreduction of H<sub>2</sub>O over Pt/P25.

The impregnated samples are highly versatile. They are indeed active both in the non-photocatalytic and the photocatalytic processes with a clear influence of the impregnation order and the Pt precursor. Pt impregnated first leads to higher conversion due to improved accessibility of NO<sub>3</sub><sup>-</sup> to Ag<sup>0</sup> sites partially covering Pt, and high NO<sub>2</sub><sup>-</sup> selectivity at the expense of N<sub>2</sub> due to low Pt accessibility. Higher synergetic effect by light probably occurs in the most active bimetallic impregnated photocatalysts than in the Ag/P25 + Pt/P25 mixture. Using K<sub>2</sub>PtCl<sub>6</sub> instead of H<sub>2</sub>PtCl<sub>6</sub>·6H<sub>2</sub>O as Pt precursor increases the mean particle size accounting for the decrease of photocatalytic NO<sub>3</sub><sup>-</sup> conversion when Ag is first impregnated. When Pt is first impregnated the closer interaction between the metals observed using K<sub>2</sub>PtCl<sub>6</sub> (Pt-Ag/P25(K)) leads to a great improvement of N<sub>2</sub> yield reaching 36%. It is equivalent to that obtained in the catalytic reaction with Ag-Pt/P25(H) which exhibits higher NO<sub>2</sub><sup>-</sup> selectivity (16%). Bimetallic Ag-Pt(Pt-Ag)/P25 photocatalysts are very promising for denitration of water in presence of H<sub>2</sub> and studies are currently performed to improve activity and selectivity varying particularly metal loadings.

## B.6 Supplementary Information

### B.6.1 Nanocatalysts synthesis

AgNO<sub>3</sub> (Johnson Matthey), H<sub>2</sub>PtCl<sub>6</sub>·6H<sub>2</sub>O (Alfa Aesar), K<sub>2</sub>PtCl<sub>6</sub> (Aldrich) and NaBH<sub>4</sub> (Aldrich), are used without any further purification. The support Aerioxide Titania P25 (TiO<sub>2</sub> P25) is purchased from Acros Organics. NaNO<sub>3</sub> (Riser S.A.) is used as the nitrate source for denitration experiments. Ethanol (absolute PRS) is purchased from Panreac. Milli-Q water type (18.2 Ω) is used in all synthesis, experiments and analysis. The Ag/P25 and Pt/P25 (2 wt.% Ag; 4 wt.% Pt) monometallic and (Ag-Pt(Pt-Ag)/P25) bimetallic catalysts are synthesized by drop-wise wetness impregnation of TiO<sub>2</sub> P25 with AgNO<sub>3</sub> and/or H<sub>2</sub>PtCl<sub>6</sub>·6H<sub>2</sub>O or K<sub>2</sub>PtCl<sub>6</sub> followed by a reduction step with NaBH<sub>4</sub> varying the impregnation order of the precursors in the case of the bimetallic samples.

## *Annexes*

In the case of the monometallic Ag/P25 catalyst, 0.063 g AgNO<sub>3</sub> is dissolved in 0.5 mL of water and deposited drop by drop over 2g of TiO<sub>2</sub> P25. The obtained powder is dried at 100 °C overnight, and then calcined at 400°C, getting the metal oxides and avoiding the rutilation of P25 (Viswanathan et al. 2009). Preparation of the Pt/P25 monometallic catalysts followed the same impregnation protocol using aqueous solutions of 0.168 g of H<sub>2</sub>PtCl<sub>6</sub>·6H<sub>2</sub>O or 0.203 g of K<sub>2</sub>PtCl<sub>6</sub> dissolved in 0.5 mL of water. The samples are noted as Pt/P25(H) and Pt/P25(K) when H<sub>2</sub>PtCl<sub>6</sub> (H) and K<sub>2</sub>PtCl<sub>6</sub> (K) are respectively used.

Afterwards, the desirable amount of catalyst is stirred in 20 ml of EtOH and 20 mg of NaBH<sub>4</sub> drop-wise added, firstly stirred in 5 ml of EtOH. The solution color turns out to dark yellow-slight grey (Ag) and grey (Pt). Thereupon, catalyst is filtered under vacuum and washed with EtOH several times. As Ag gets oxidized fast, catalyst is immediately introduced inside the reactor or characterized.

In the bimetallic catalysts the impregnation order of the Ag and Pt salts and the Pt precursor are varied. In a typical experiment, the Ag-Pt/P25(H) catalyst is obtained by firstly drop-wise impregnation of 2 g of TiO<sub>2</sub> P25 powder by a solution of 0.063 g AgNO<sub>3</sub> in 0.5 mL of H<sub>2</sub>O, then dried overnight at 100 °C. On this dried powder, a solution of 0.168 g of H<sub>2</sub>PtCl<sub>6</sub>·6H<sub>2</sub>O in 0.5 mL of H<sub>2</sub>O is secondly drop-wise added, then dried again at 100 °C and calcined at 400 °C overnight. The bimetallic catalysts are named as Ag-Pt/P25(H) or Ag-Pt/P25(K) indicating that firstly Ag and secondly Pt with H<sub>2</sub>PtCl<sub>6</sub> (H) or K<sub>2</sub>PtCl<sub>6</sub> (K) precursors were impregnated. Pt-Ag/P25(H) and Pt-Ag/P25(K) correspond to the reverse impregnation order of the Ag and Pt salts.

### B.6.2 Nitrate, nitrite and ammonium detection by Ionic Chromatography

The Ionic Chromatography technique (DIONEX ICS-900) is used for nitrate (NO<sub>3</sub><sup>-</sup>), nitrite (NO<sub>2</sub><sup>-</sup>) and ammonium (NH<sub>4</sub><sup>+</sup>) ions analysis. Before analysis samples were filtered (0.45 µm PTFE filter). The system works at isocratic flow.

#### B.6.2.1 Nitrate and nitrite detection

For the NO<sub>3</sub><sup>-</sup> and NO<sub>2</sub><sup>-</sup> ions detection the guard column (DIONEX IonPac<sup>TM</sup> AG9-HC RFIC<sup>TM</sup> 4 x 50 mm, Thermo Scientific), anionic column (DIONEX IonPac<sup>TM</sup> AS9-HC RFIC<sup>TM</sup> 4 x 250 mm, Thermo Scientific) and anionic suppressor (DIONEX ACRS 500 4 mm, Thermo Scientific) are used. The eluent solution is 9 mM Na<sub>2</sub>CO<sub>3</sub> (0.5 M, Thermo Scientific) and the regenerant solution 25 mM H<sub>2</sub>SO<sub>4</sub> (2 N, Thermo Scientific). The retention times for NO<sub>3</sub><sup>-</sup> and

$\text{NO}_2^-$  are c.a. 16.5 min and 10.6 min, respectively. Calibrations curves match linear type with a correlation coefficient of  $R^2 = 0.991$  ( $\text{NO}_3^-$ ) and  $R^2 = 0.995$  ( $\text{NO}_2^-$ ).

#### B.6.2.2 Ammonium detection

For the ammonium ion detection is used the cationic suppressor system of guard column (DIONEX IonPac<sup>TM</sup> CG12A RFIC<sup>TM</sup> 4 x 50 mm, Thermo Scientific), cationic column (DIONEX IonPac<sup>TM</sup> CS12A RFIC<sup>TM</sup> 4 x 250 mm, Thermo Scientific) and cationic suppressor (DIONEX CCRS 500 4 mm, Thermo Scientific). The eluent solution is 20 mM  $\text{CH}_4\text{SO}_3$  (Sigma-Aldrich) and 100 mM  $\text{C}_{16}\text{H}_{37}\text{NO}$  (1.5 M, Acros Organics) as regenerant solution. The retention time for  $\text{NH}_4^+$  is c.a. 5.6 min. Calibration curve fits quadratic second order type with a correlation coefficient of  $R^2 = 0.999$ .

#### B.6.3 Nitrate conversion, selectivity and yield calculations

Nitrate conversion (Conv), selectivity (Sel) and yield (Yield) in percentage toward nitrite, ammonium and nitrogen gas are calculated by the following equations:

$$\text{Conv}_{\text{NO}_3^-} = \frac{[\text{NO}_3^-]_0 - [\text{NO}_3^-]_i}{[\text{NO}_3^-]_0} \times 100 \quad (\text{Eq.B.1})$$

$$\text{Sel}_{\text{NO}_2^-} = \frac{[\text{NO}_2^-]_i}{[\text{NO}_3^-]_0 - [\text{NO}_3^-]_i} \times 100 \quad (\text{Eq.B.2})$$

$$\text{Sel}_{\text{NH}_4^+} = \frac{[\text{NH}_4^+]_i}{[\text{NO}_3^-]_0 - [\text{NO}_3^-]_i} \times 100 \quad (\text{Eq.B.3})$$

$$\text{Sel}_{\text{N}_2} = 100 - (\text{S}_{\text{NO}_2^-} + \text{S}_{\text{NH}_4^+}) \quad (\text{Eq.B.4})$$

Where  $i$  points out the concentration of the substance (nitrate, nitrite or ammonium) at the moment of taking sample, and  $0$  the concentration at initial time.

$$\text{Yield}_i = \frac{\text{Conv}_{\text{NO}_3^-}}{100} \times \text{Sel}_i \quad (\text{Eq.B.5})$$

Where  $i$  indicates the nitrate, nitrite or ammonium.

B.6.4 X-ray diffraction patterns (XRD)

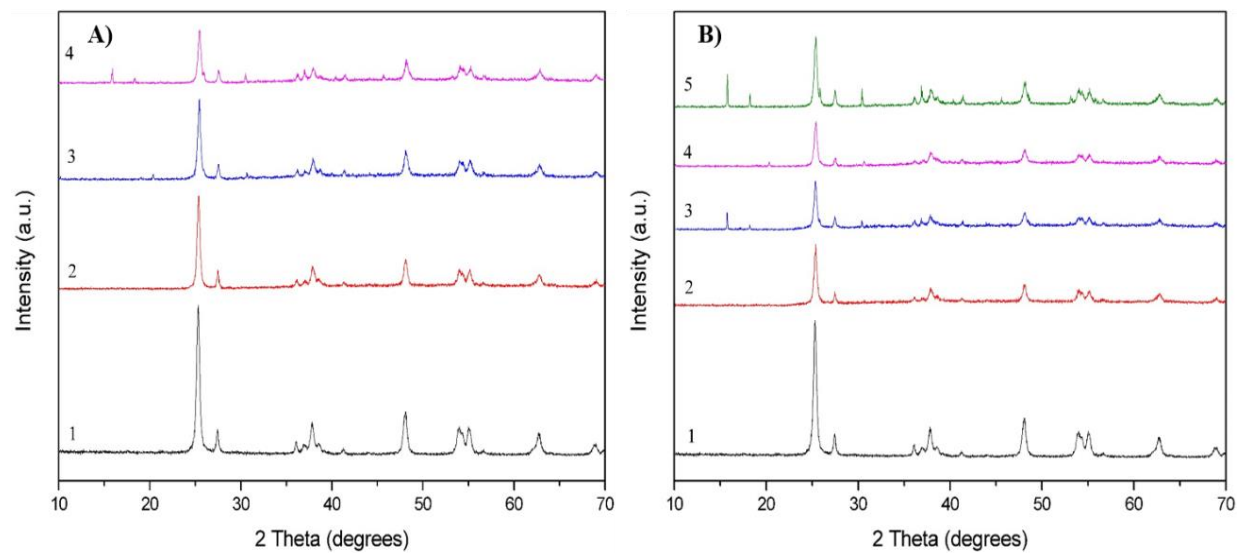


Figure B.3. XRD diffraction patterns of: A): 1) TiO<sub>2</sub> P25 2) Ag/P25, 3) Pt/P25(H) and 4) Pt/P25(K); and B) : 1) P25 2) Ag-Pt/P25 (H), 3) Ag-Pt/P25(K), 4) Pt-Ag/P25 (H) and 5) Pt-Ag/P25(K).

B.6.5 Transmission Electron Microscopy (TEM)

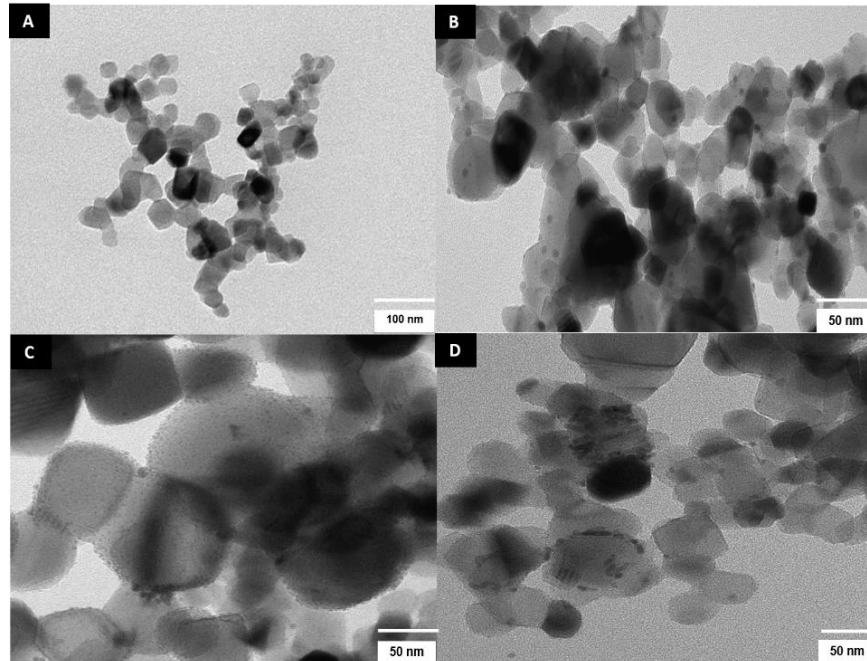


Figure B.4. TEM images of: A) TiO<sub>2</sub> P25, B) Ag/P25, C) Pt/P25(H), and D) Pt/P25(K).

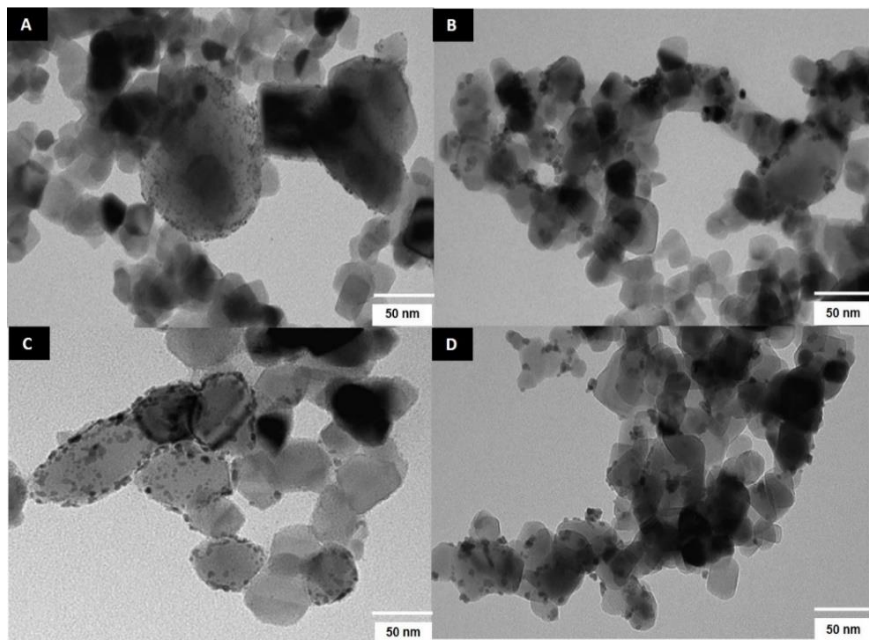


Figure B.5. TEM images of: A) Ag-Pt/P25(H), B) Ag-Pt/P25(K), C) Pt-Ag/P25(H), and D) Pt-Ag/P25(K).

#### B.6.6 X-ray photoelectron spectroscopy (XPS)

Table B.3. Binding energies of oxygen and titanium species obtained by XPS.

Catalyst	BE (eV)				
	O1s	O1s	O1s	Ti <sup>4+</sup> 2p <sub>1/2</sub>	Ti <sup>4+</sup> 2p <sub>3/2</sub>
Ag/P25	529.5	531.2	533	458.3	464.2
Ag-Pt/P25(K)	529.6	531.3	533	458.4	464.2
Pt-Ag/P25(K)	529.5	531.1	532.8	458.3	464.2

### B.6.7 Thermal programmed reduction (TPR)

Table B.4. Hydrogen consumption of mono- and bimetallic catalysts.

Catalyst	H <sub>2</sub> TPR (mmol/g)
Ag/P25	0.14
Pt/P25(H)	0.95
Pt/P25(K)	0.45
Ag-Pt/P25(H)	0.73
Ag-Pt/P25(K)	0.33
Pt-Ag/P25(H)	0.29
Pt-Ag/P25(K)	0.20

### B.6.8 Photocatalytic nitrate reaction rates

The photocatalytic nitrate reduction rate from all nanocatalysts were fitting pseudo-first order kinetics at a constant initial nitrate concentration of 100 mg/L. The equation used for their calculations was (Sowmya et al. 2014):

$$\ln \frac{C_0}{C_t} = kt \quad (\text{Eq.B.6})$$

Where  $k$  is the pseudo-first photocatalytic reaction constant ( $\text{h}^{-1}$ ),  $t$  the time of UV irradiation (h),  $C_0$  the initial nitrate concentration (mg/L), and  $C_t$  the nitrate concentration after a time  $t$  of UV irradiation.

Table B.5. Pseudo-1<sup>st</sup> order nitrate reaction rates and correlation coefficients of mono- and bimetallic catalysts ( $\lambda = 365$  nm irradiation; 150 mL/min H<sub>2</sub>; 6 hours).

Catalyst	k (h <sup>-1</sup> )	R <sup>2</sup>
Ag/P25	0.165 ± 0.065	0.987
Pt/P25(H)	0.005 ± 0.001	0.987
Pt/P25(K)	0.013 ± 0.003	0.976
Ag-Pt/P25(H)	0.055 ± 0.004	0.999
Ag-Pt/P25(K)	0.073 ± 0.018	0.991
Pt-Ag/P25(H)	0.065 ± 0.020	0.988
Pt-Ag/P25(K)	0.104 ± 0.022	0.999

Experimental conditions: 0.2g catalyst/350 mL; 100 ppm NO<sub>3</sub><sup>-</sup>; 120 mL/min Ar

#### B.6.9 Photocatalytic nitrite reduction

To verify the platinum addition effect, tests with Pt monometallic catalysts were performed using NaNO<sub>2</sub> (Riser S.A.) as nitrite source, under  $\lambda = 365$  nm UV irradiation and hydrogen current conditions. The Pt loading was 4% wt. and precursors were varied. Initial nitrite solution was fixed to 50 mg/L, because it was the highest nitrite concentration obtained in the catalytic nitrate reduction tests.

Table B.6. Catalytic performances of Pt/P25(H) and Pt/P25(K) in the reduction of NO<sub>2</sub><sup>-</sup> ( $\lambda = 365$  nm irradiation; 150 mL/min H<sub>2</sub>; 6 hours).

Catalyst	Conv <sub>NO<sub>2</sub><sup>-</sup></sub> (%)	Sel <sub>NO<sub>3</sub><sup>-</sup></sub> (%)	Sel <sub>NH<sub>4</sub><sup>+</sup></sub> (%)	Sel <sub>N<sub>2</sub></sub> (%)
Pt/P25(H)	19	20	28	52
Pt/P25(K)	34	12	43	46

Experimental conditions: 0.2g catalyst/350 mL; 50 ppm NO<sub>2</sub><sup>-</sup>; 120 mL/min Ar

Nitrite conversions are higher when increasing the amount of Pt, and using K<sub>2</sub>PtCl<sub>6</sub> instead of H<sub>2</sub>PtCl<sub>6</sub>. Although conversions are not high enough to reach the EU Normative, it could be seen a tendency toward nitrogen selectivity against intermediate and by-product compounds. Thus, Pt addition benefits the selectivity to desired N<sub>2</sub> gas.

## B.7 References

- Antos, G.J., A.M. Aitani, J.M Parera. 2004. Catalytic Naphta Reforming, ed. Marcel Dekker, New York.
- Sclafani, A., M.N. Mozzanegra, JM.Herrmann. 1997. "Influence of Silver Deposits on the Photocatalytic Activity of Titania." *Journal of Catalysis* 120:117–20.
- Aristizábal, A., S. Contreras, N. Barrabés, J. Llorca, D. Tichit, and F. Medina. 2011. "Catalytic Reduction of Nitrates in Water on Pt Promoted Cu Hydrotalcite-Derived Catalysts: Effect of the Pt-Cu Alloy Formation." *Applied Catalysis B: Environmental* 110:58–70.
- Aristizábal, A., S. Contreras, N. J. Divins, J. Llorca, and F. Medina. 2012. "Pt-Ag/activated Carbon Catalysts for Water Denitration in a Continuous Reactor: Incidence of the Metal Loading, Pt/Ag Atomic Ratio and Pt Metal Precursor." *Applied Catalysis B: Environmental* 127:351–62.
- Aristizábal, A., S. Contreras, N. J. Divins, J. Llorca, and F. Medina. 2014. "Effect of Impregnation Protocol in the Metallic Sites of Pt-Ag/activated Carbon Catalysts for Water Denitration." *Applied Surface Science* 298:75–89.
- Asahi, R., T. Mikawa, T. Ohwaki, K. Aoki, and Y. Taga. 2001. "Visible Light Photocatalysis in Nitrogen-Doped Titanium Oxides." *Science* 293(July):269–71.
- Barrabés, N., J. Just, A. Dafinov, F. Medina, J. L. G. Fierro, J. E. Sueiras, P. Salagre, and Y. Cesteros. 2006. "Catalytic Reduction of Nitrate on Pt-Cu and Pd-Cu on Active Carbon Using Continuous reactorThe Effect of Copper Nanoparticles." *Applied Catalysis B: Environmental* 62:77–85.
- Barrabés, N., and J. Sá. 2011. "Catalytic Nitrate Removal from Water, Past, Present and Future Perspectives." *Applied Catalysis B: Environmental* 104:1–5.
- Behnajady M.A., N. Modirshahla, M.Shokri, and B. Rad. 2008. "Enhancement of Photocatalytic Activity of TiO<sub>2</sub> Nanoparticles by Silver Doping: Photodeposition versus Liquid Impregnation Methods." *Global Nest Journal* 10(1):1–7.
- Doudrick, K., T. Yang, K. Hristovski, and P. Westerhoff. 2013. "Photocatalytic Nitrate Reduction in Water: Managing the Hole Scavenger and Reaction by-Product Selectivity." *Applied Catalysis B: Environmental* 136–137:40–47.
- European Union. 2010. "The EU Nitrates Directive." 1–4.
- Gauthard, F., F. Epron, and J. Barbier. 2003. "Palladium and Platinum-Based Catalysts in the Catalytic Reduction of Nitrate in Water: Effect of Copper, Silver, or Gold Addition." *Journal of Catalysis* 220:182–91.

- Gekko, H., K. Hashimoto, and H. Kominami. 2012. "Photocatalytic Reduction of Nitrite to Dinitrogen in Aqueous Suspensions of Metal-Loaded Titanium(iv) Oxide in the Presence of a Hole Scavenger: An Ensemble Effect of Silver and Palladium Co-Catalysts." *Physical Chemistry Chemical Physics* 14(22):7965.
- Gomathi Devi, L., and K. Mohan Reddy. 2010. "Enhanced Photocatalytic Activity of Silver Metallized TiO<sub>2</sub> Particles in the Degradation of an Azo Dye Methyl Orange: Characterization and Activity at Different pH Values." *Applied Surface Science* 256(10):3116–21.
- Guillette, L. J., and T. M. Edwards. 2005. "Is Nitrate an Ecologically Relevant Endocrine Disruptor in Vertebrates?" *Integrative and comparative biology* 45(1):19–27.
- Hirayama, J., H. Kondo, Y. K. Miura, R. Abe, and Y. Kamiya. 2012. "Highly Effective Photocatalytic System Comprising Semiconductor Photocatalyst and Supported Bimetallic Non-Photocatalyst for Selective Reduction of Nitrate to Nitrogen in Water." *Catalysis Communications* 20(3):99–102.
- Hörhold, S., K. D. Vorlop, T. Tacke, and M. Sell. 1993. "Development of Catalysts for a Selective Nitrate and Nitrite Removal from Drinking Water." *Catalysis Today* 17:21–30.  
2):21–30.
- Ibhadon, A., and P. Fitzpatrick. 2013. "Heterogeneous Photocatalysis: Recent Advances and Applications." *Catalysts* 3(1):189–218.
- Kanda, Y., A. Seino, T. Kobayashi, Y. Uemichi, and M. Sugioka. 2009. "Catalytic Performance of Noble Metals Supported on Mesoporous Silica MCM-41 for Hydrodesulfurization of Benzothiophene." *Journal of the Japan Petroleum Institute* 52(2):42–50.
- Kobwittaya, K., and S. Sirivithayapakorn. 2014. "Photocatalytic Reduction of Nitrate over TiO<sub>2</sub> and Ag-Modified TiO<sub>2</sub>." *Journal of Saudi Chemical Society* 18(4):291–98.
- Luo, Z., M. Ibáñez, A. M. Antolín, A. Genç, A. Shavel, S. Contreras, F. Medina, J. Arbiol, and A. Cabot. 2015. "Size and Aspect Ratio Control of Pd<sub>2</sub>Sn Nanorods and Their Water Denitration Properties." *Langmuir* 31(13):3952–57.
- Mahler, R. L., A. Colter, and R. Hirnyck. 2007. "Nitrate and Groundwater." Cis 1–4.
- Mankidy, B. D., B. Joseph, and V. K. Gupta. 2013. "Photo-Conversion of CO<sub>2</sub> Using Titanium Dioxide: Enhancements by Plasmonic and Co-Catalytic Nanoparticles." *Nanotechnology* 24(40):405402.
- Marchesini, F. A., N. Picard, and E. E. Miró. 2012. "Study of the Interactions of Pd,In with SiO<sub>2</sub> and Al<sub>2</sub>O<sub>3</sub> Mixed Supports as Catalysts for the Hydrogenation of Nitrates in Water." *Catalysis Communications* 21:9–13.

- Matos, J., T. Marino, R. Molinari, and H. García. 2012. "Hydrogen Photoproduction under Visible Irradiation of Au-TiO<sub>2</sub>/activated Carbon." *Applied Catalysis A: General* 417–418:263–72.
- Mori, T., J. Suzuki, K. Fujimoto, M. Watanabe, and Y. Hasegawa. 1999. "Reductive Decomposition of Nitrate Ion to Nitrogen in Water on a Unique Hollandite Photocatalyst." *Applied Catalysis B: Environmental* 23(4):283–89.
- Ohtani, B., K. Iwai, S. I. Nishimoto, and S. Sato. 1997. "Role of Platinum Deposits on Titanium (IV) Oxide Particles : Structural and Kinetic Analyses of Photocatalytic Reaction in Aqueous Alcohol and Amino Acid Solutions." *Society* 101(Iv):3349–59.
- Priusse, U., M. Hähnlein, J. Daum, and K. D. Vorlop. 2000. "Improving the Catalytic Nitrate Reduction." *Catalysis Today* 55(2):79–90.
- Pulido Melián, E., O. González Díaz, J. M. Doña Rodríguez, G. Colón, J. A. Navío, M. Macías, and J. Pérez Peña .2012. "Effect of Deposition of Silver on Structural Characteristics and Photoactivity of TiO<sub>2</sub>-Based Photocatalysts." *Applied Catalysis B: Environmental* 127:112–20.
- Rao, K. V. S., B. Lavédrine, and P. Boule. 2003. "Influence of Metallic Species on TiO<sub>2</sub> for the Photocatalytic Degradation of Dyes and Dye Intermediates." *Journal of Photochemistry and Photobiology A: Chemistry* 154:189–93.
- Rodríguez-González, V., S. Obregón Alfaro, L. M. Torres-Martínez, S. H. Cho, and S. Wohn Lee. 2010. "Silver-TiO<sub>2</sub> Nanocomposites: Synthesis and Harmful Algae Bloom UV-Photoelimination." *Applied Catalysis B: Environmental* 98(3–4):229–34.
- Rupa, A.V., D. Divakar, and T. Sivakumar. 2009. "Titania and Noble Metals Deposited Titania Catalysts in the Photodegradation of Tartazine." *Catalysis Letters* 132(1–2):259–67.
- Sá, J., C. Alcaraz Agüera, S. Gross, and J. A. Anderson. 2009. "Photocatalytic Nitrate Reduction over Metal Modified TiO<sub>2</sub>." *Applied Catalysis B: Environmental* 85(3–4):192–200.
- Sclafani, A., and J. M. Herrmann. 1998. "Influence of Metallic Silver and of Platinum-Silver Bimetallic Deposits on the Photocatalytic Activity of Titania (Anatase and Rutile) in Organic and Aqueous Media." *Journal of Photochemistry and Photobiology A: Chemistry* 113:181–88.
- Soares, O. S. G. P., M. F. R. Pereira, J. J. M. Órfão, J. L. Faria, and C. G. Silva. 2014. "Photocatalytic Nitrate Reduction over Pd–Cu/TiO<sub>2</sub>." *Chemical Engineering Journal* 251:123–30.
- Sobana, N., M. Muruganadham, and M. Swaminathan. 2006. "Nano-Ag Particles Doped TiO<sub>2</sub> for Efficient Photodegradation of Direct Azo Dyes." *Journal of Molecular Catalysis A: Chemical* 258(1–2):124–32.

- Soria, J., J. C. Conesa, V. Augugliaro, L. Palmisano, M. Schiavello, and A. Sclafani 1991. “Dinitrogen Photoreduction to Ammonia over Titanium Dioxide Powders Doped with Ferric Ions.” *The Journal of Physical Chemistry* 95(1):274–82.
- Sowmya, A., and S. Meenakshi. 2014. “Photocatalytic Reduction of Nitrate over Ag–TiO<sub>2</sub> in the Presence of Oxalic Acid.” *Journal of Water Process Engineering* 4–11.
- Suttiponparnit, K., J. Jiang, M. Sahu, S. Suvachittanont, T. Charinpanitkul, and P. Biswas. 2011. “Role of Surface Area, Primary Particle Size, and Crystal Phase on Titanium Dioxide Nanoparticle Dispersion Properties.” *Nanoscale Research Letters* 6(1):1–8.
- Talat-Mehrabad, J., M. Khosravi, N. Modirshahla, and M. A. Behnajady. 2015. “Synthesis, Characterization, and Photocatalytic Activity of Co-Doped Ag-, Mg-TiO<sub>2</sub>-P25 by Photodeposition and Impregnation Methods.” *Desalination and Water Treatment* 1–11.
- Thompson, T. S. 2001. “Nitrate Concentrations in Private Rural Drinking Water Supplies in Saskatchewan, Canada.” *Bulletin of Environmental Contamination and Toxicology* 66(1):64–70.
- Viswanathan, B., and K. Joseph Antony Raj. 2009. “Effect of Surface Area, Pore Volume and Particle Size of P25 Titania on the Phase Transformation of Anatase to Rutile.” *Indian Journal of Chemistry - Section A Inorganic, Physical, Theoretical and Analytical Chemistry* 48(October):1378–82.
- Wodka, D., E. Bielanska, R. P. Socha, M. Elzbieciak-Wodka, J. Gurgul, P. Nowak, P. Warszynski, and I. Kumariki. 2010. “Photocatalytic Activity of Titanium Dioxide Modified by Silver Nanoparticles.” *ACS Applied Materials and Interfaces* 2(7):1945–53.
- Zhang, F., R. Jin, J. Chen, C. Shao, W. Gao, L. Li, and N. Guan. 2005. “High Photocatalytic Activity and Selectivity for Nitrogen in Nitrate Reduction on Ag/TiO<sub>2</sub> Catalyst with Fine Silver Clusters.” *Journal of Catalysis* 232:424–31.
- Zhang, F., Y. Pi, J. Cui, Y. Yang, X. Zhang, and N. Guan. 2007. “Unexpected Selective Photocatalytic Reduction of Nitrite to Nitrogen on Silver-Doped Titanium Dioxide.” *Journal of Physical Chemistry C* 111(9):3756–61.
- Zhu, S., S. Liang, Q. Gu, L. Xie, J. Wang, Z. Ding, and P. Liu. 2012. “Effect of Au Supported TiO<sub>2</sub> with Dominant Exposed {001} Facets on the Visible-Light Photocatalytic Activity.” *Applied Catalysis B: Environmental* 119–120:146–55.

## **Annex C:**

### **Photometer methods**

## C.1. Nitrate detection method

2    6    5

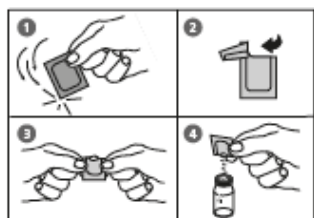
### Nitrate with Tube Test

1 – 30 mg/l N



Insert the adapter for 16 mm Ø vials.

1. Open one white capped vial (Reagent A), add **1 ml of the water sample** and close tightly with the cap.
2. Place the vial in the sample chamber making sure that the marks are  aligned.
3. Press **ZERO** key.
4. Remove the vial from the sample chamber.
5. Add the contents of **one Vario Nitrate Chromotropic Powder Pack** straight from the foil into the same water sample.
6. Close the vial tightly with the cap and invert gently several times (10 x) to mix the contents (Note 1).



7. Place the vial in the sample chamber making sure that the marks are  aligned.

Zero accepted  
prepare Test  
press TEST  
Countdown  
5:00

8. Press **TEST** key.  
Wait for a **reaction period of 5 minutes**.

After the reaction period is finished the measurement starts automatically.

The result is shown in the display in mg/l Nitrate.

**Notes:**

1. Some solids may not dissolve.
2. To optimise the readings an optional batch related calibration can be performed. Follow the procedure using 1 ml deionised water in place of the sample and subtract the reagent blank value from the final result.
3. Conversion:  
$$\text{mg/l NO}_3 = \text{mg/l N} \times 4.43$$
4.  $\Delta$  N  
 $\nabla$   $\text{NO}_3$

Reagent	Form of reagent/Quantity	Order-No.
<b>Set</b> VARIO Nitrate Chromotropic VARIO Nitra X Reagent tube VARIO deionised water	<b>Set</b> Powder Pack / 50 Reaction tube / 50 100 ml	535580

## C.2. Nitrite detection method

2 7 0

### Nitrite with Tablet

0.01 – 0.5 mg/l N



1. Fill a clean vial (24 mm Ø) with **10 ml of water sample**, close tightly with the cap.
2. Place the vial in the sample chamber making sure that the marks are aligned.
3. Press **ZERO** key.
4. Remove the vial from the sample chamber.
5. Add **one NITRITE LR tablet** straight from the foil to the water sample and crush the tablet using a clean stirring rod.
6. Close the vial tightly with the cap and swirl several times until the tablet is dissolved.
7. Place the vial in the sample chamber making sure that the marks are aligned.

Zero accepted  
prepare Test  
press TEST

8. Press **TEST** key.  
Wait for a **reaction period of 10 minutes**.

Countdown  
10:00

After the reaction period is finished the measurement starts automatically.

The result is shown in the display in mg/l Nitrite.

**Notes:**

1. The following ions can produce interferences since under the reaction conditions they cause precipitation:  
Antimony (III), Iron (III), Lead, Mercury (I), Silver, Chloroplatinate, Metavanadate and Bismuth.  
Copper (II)-ions may cause lower test results as they accelerate the decomposition of the Diazonium salt.  
It is unlikely in practice that these interfering ions will occur in such high concentrations that they cause significant reading errors.
2. Conversion:  
 $\text{mg/l NO}_2 = \text{mg/l N} \times 3.29$
3.  $\begin{array}{ccc} \blacktriangle & N \\ \blacktriangledown & \text{NO}_2 \end{array}$

Reagent	Form of reagent/Quantity	Order-No.
NITRITE LR	Tablet / 100	512310BT

### C.3. Ammonia detection method

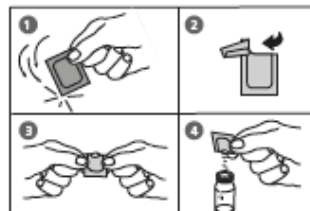
6      5

#### Ammonia LR with Vario Tube Test

0.02 – 2.5 mg/l N



Insert the adapter for 16 mm Ø vials.



1. Open one white capped reaction vial and add **2 ml deionised water** (this is the blank).
2. Open another white capped reaction vial and add **2 ml of water sample** (this is the sample).
3. Add the contents of **one Vario Ammonia Salicylate F5 Powder Pack** straight from the foil into each vial.
4. Add the contents of **one Vario Ammonia Cyanurate F5 Powder Pack** straight from the foil into each vial.
5. Close the vials tightly with the caps and swirl several times to dissolve the powder.
6. Press **[.J]** key.  
Wait for a **reaction period of 20 minutes**.

Countdown 1  
20:00  
start: ↴

After the reaction period is finished proceed as follows:

7. Place the vial (the blank) in the sample chamber making sure that the marks are aligned. Place the cover on the adapter.

prepare Zero  
press ZERO

8. Press **ZERO** key.

9. Remove the vial from the sample chamber.

10. Place the vial (the sample) in the sample chamber making sure that the marks are aligned. Place the cover on the adapter.

Zero accepted  
prepare Test  
press TEST

11. Press **TEST** key.

The result is shown in the display in mg/l Ammonia as N.

**Notes:**

1. Strong alkaline or acidic water samples must be adjusted to approx. pH 7 before analysis (use 1 mol/l Hydrochloric acid resp. 1 mol/l Sodium hydroxide).
2. Iron interferes with the test. The interferences will be eliminated as follows:  
Determine the amount of total iron present in the water sample. To produce the blank add an iron standard solution with the same iron concentration to the vial (point 1) instead of deionised water
3. Conversion:  
 $\text{mg/l NH}_4 = \text{mg/l N} \times 1.29$   
 $\text{mg/l NH}_3 = \text{mg/l N} \times 1.22$
4.  $\blacktriangle \text{ N}$   
 $\blacktriangledown \text{ NH}_4$   
 $\blacktriangledown \text{ NH}_3$

Reagent	Form of reagent/Quantity	Order-No.
<b>Set</b>		
VARIO Ammonia Salicylate F5	Powder Pack / 50	
VARIO Ammonia Cyanurate F5	Powder Pack / 50	
VARIO Am Diluent Reagent LR	Reaction tube / 50	
VARIO deionised water	100 ml	

## **Annex D:**

### **Reactor design**

## Annexes

The experimental PTFE batch reactor design planes (Figures D.1 and D.2) were made using the SolidWorks software by the Tècnic SRCT at Universitat Rovira i Virgili (Tarragona, Spain).

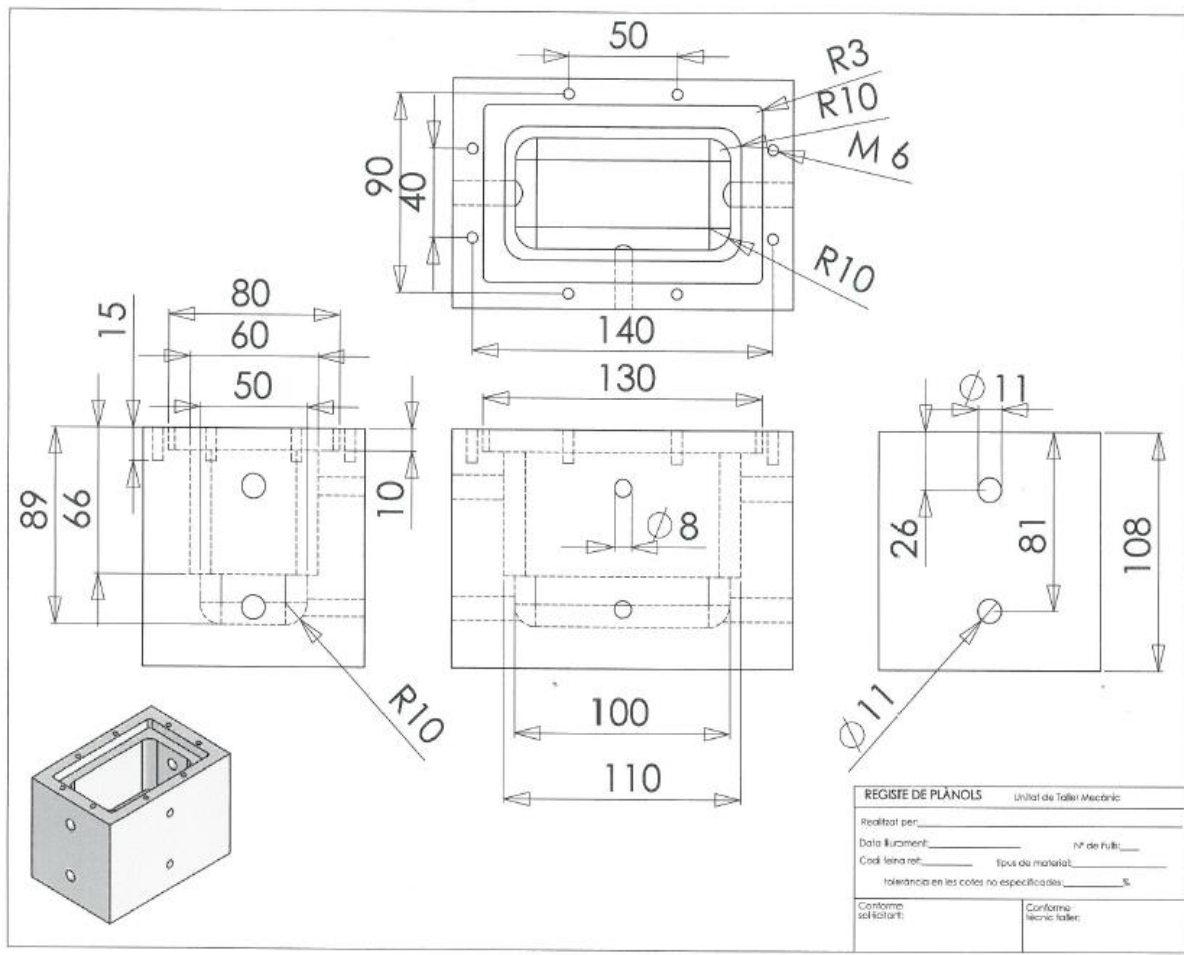


Figure D.1. PTFE reactor body design

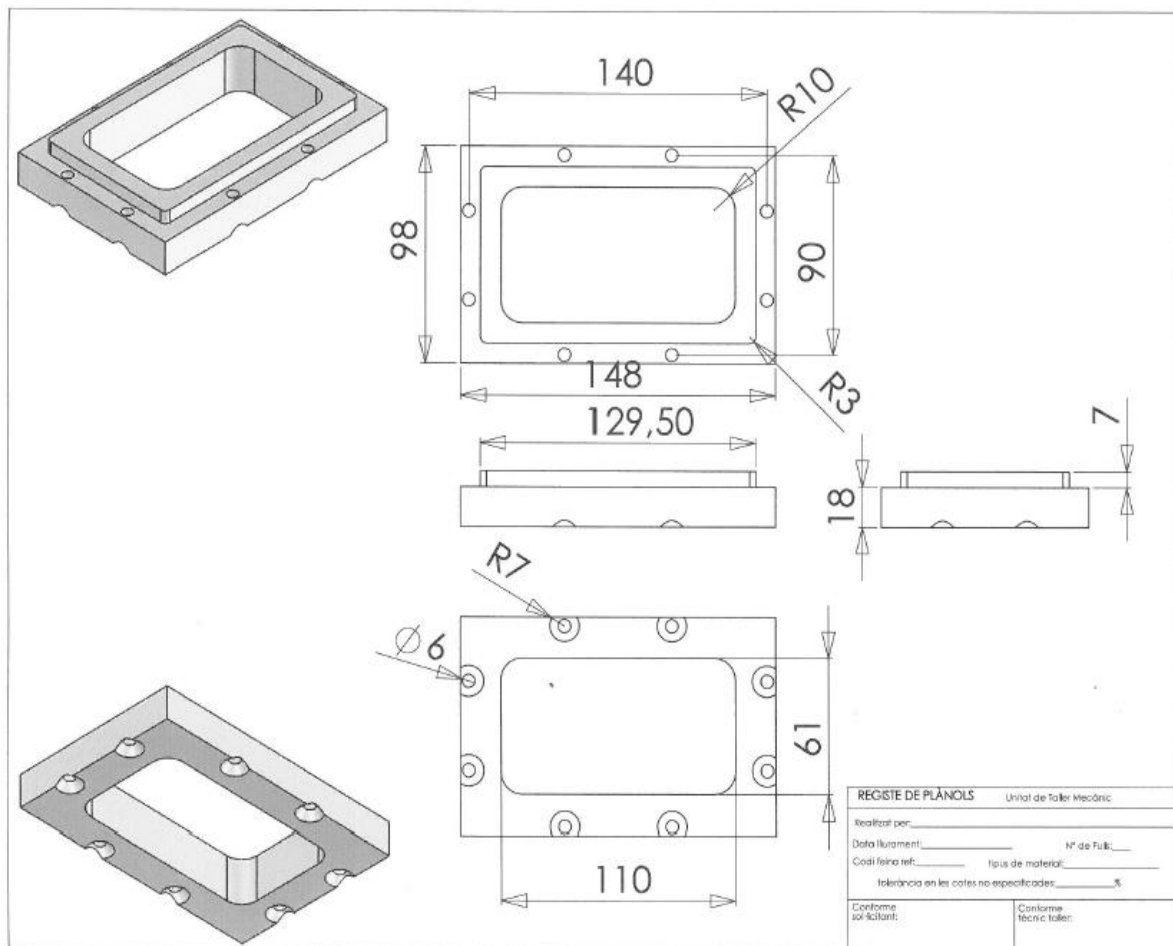


Figure D.2. PTFE reactor cover design

